January 2015

Observations of variability of TeV gamma-ray blazars

Qi Feng
Purdue University

PURDUE UNIVERSITY
GRADUATE SCHOOL
Thesis/Dissertation Acceptance

This is to certify that the thesis/dissertation prepared

By Qi Feng

Entitled
OBSERVATIONS OF VARIABILITY OF TEV GAMMA-RAY BLAZARS

For the degree of Doctor of Philosophy

Is approved by the final examining committee:

Wei K. Cui
Chair

John P. Finley

Dimitrios Giannios

Martin Kruczenski

To the best of my knowledge and as understood by the student in the Thesis/Dissertation Agreement, Publication Delay, and Certification Disclaimer (Graduate School Form 32), this thesis/dissertation adheres to the provisions of Purdue University's "Policy of Integrity in Research" and the use of copyright material.

Approved by Major Professor(s): Wei K. Cui

Approved by: Mark P. Haugan 04/10/2015

Head of the Departmental Graduate Program Date

OBSERVATIONS OF VARIABILITY OF TEV GAMMA-RAY BLAZARS

A Dissertation

Submitted to the Faculty

of

Purdue University

by

Qi Feng

In Partial Fulfillment of the

Requirements for the Degree

of

Doctor of Philosophy

August 2015

Purdue University

West Lafayette, Indiana

To my family

ACKNOWLEDGMENTS

I thank my advisor, Wei Cui, for the ultimate support and guidance over the course of my graduate study and professional development. I am grateful for his mentoring style that encouraged me to think independently.

I thank the professors, researchers, and students at Purdue University, John Finley, Glenn Sembroski, Daniel Gall, Ben Zitzer, Angelo Varlotta, Miguel Araya-Arguedas, Joey Richards, Maria Petropoulou, Dimitrios Giannios, Matt Lister, Maxim Lyutikov, Talvikki Hovotta, James Tucci, and Brett McArthur for the helpful discussions, which cover a wide range of topics and benefit both specific topics in my research and the breadth of knowledge in astrophysics in general.

I thank the VERITAS collaborators, Martin Schroeder, Ken Gibbs, Nicola Galante, Dave Staszak, David Hanna, Pat Moriarty, Jim Buckley, Jeff Grube, Lucy Fortson, Rene Ong, Pascal Fortin, Simon Archambault, Jack Musser, and George Jones for the extremely helpful interactions and wonderful memories at the VERITAS base camp, through which I have learned a variety of useful skills like drilling holes on a metal plate, operating a man lift, and using an oscilloscope. Thanks to them, I learned about and contributed to the versatility of the VERITAS.

I thank Su-Ju Wang for the unlimited personal support and interesting discussions on the other side of physics (theoretical atomic/molecular and condensed matter physics). I thank King Triton for the warm companion during the nights that I was typing this thesis. I thank my parents for the everlasting support and encouragement.

TABLE OF CONTENTS

Page

LIST OF TABLES

LIST OF FIGURES

Figure Page

Figure Page

ABSTRACT

Feng, Qi Ph.D., Purdue University, August 2015. Observations of variability of TeV gamma-ray blazars . Major Professor: Wei Cui.

The boom in ground-based gamma-ray astronomy since the beginning of the 21st century has enabled a new probe of the universe using very-high-energy photons. The Very Energetic Radiation Imaging Telescope Array System (VERITAS) is an array of four 12-m imaging Cherenkov telescopes that is sensitive to gamma rays in the energy range between ∼100 GeV and ∼30 TeV.

Among all known TeV sources, blazars, a particular type of active galactic nuclei, have shown exceptional variabilities over a wide range of timescales and energies. The observations of such variabilities have been previously limited at lower energies, ranging from radio to X-ray. However, the superior sensitivity of VERITAS has made the detection of fast TeV gamma-ray variability of blazars possible. The studies of their gamma-ray variability can, in a relatively model-independent way, shed significant light on the emitting regions and production mechanisms in blazars. This thesis describes my work on blazar variability, based primarily on the VERITAS observations but are interpreted in a multi-wavelength context.

One of the most exceptional phenomena observed in blazars with VERITAS is the fast variability of the TeV gamma rays. The short duration of these flares strongly constrains the size of the emitting region, and provides insights to the kinetics and location of the emitting region. We describe the fast TeV flare of BL Lacertae as an example, and discuss the connection between TeV flares and multi-wavelength observations that may help localize the TeV emitting region.

To study the persistent variability of TeV blazars, we examine a variety of statistical properties in the time and frequency domains. We study both local properties

of time series, e.g. time lags between different energy bands and spectral hysteresis during flares, and global properties, e.g. variability amplitude and power spectrum. These properties are connected to the physical processes in blazars, although they are also limited by the time resolution and sampling of the observations. We also test the statistical methods to obtain these properties with simulated light curves to study their effectiveness under different circumstances.

1. Introduction to very high energy (VHE) astrophysics

⋯ a fun analogy to try to get some idea of what we're doing here to try to understand nature is to imagine that the gods are playing some great game like chess. ⋯ and you don't know the rules of the game, but you're allowed to look at the board from time to time, in a little corner, perhaps. And from these observations, you try to figure out what the rules are of the game, what are the rules of the pieces moving.
— Richard P. Feynman

In the multi-messenger era of astronomy, the ability to detect different types of information carriers has been improving. These messengers include (i) photons, (ii) charged particles called cosmic rays (CRs), (iii) neutrinos, (iv) gravitational waves, and (v) dark matter particles. Different physics processes can produce a combination of these messengers with distinct signatures. From the observation of these signatures, we can learn about the underlying physics processes. However, difficulties arise in detecting many of these messengers. CRs are deflected in magnetic field and lose information about their origin; neutrinos, gravitational waves and dark matter particles are difficult to detect because of their weak interactions. Thus the photon is the most common type of messenger. A photon carries information about its arrival time, direction, energy and polarization. Again, "signatures" are imprinted in these four dimensions from different physical processes in different environments. By counting photons in these four simple dimensions, time series, images and spectra are constructed, which are the basic tools to study astrophysics.

Human eyes are photon detectors sensitive to light in a narrow band of wavelengths from ~4000 $\AA$ to ~7000 $\AA$ (called visible light), in which the Sun emits most of its radiation. Within the visible band, different colors appear when wavelengths of the photons change. Going from longer to shorter wavelengths, color changes from red to blue, frequency ν becomes higher because $\nu = c/\lambda$, where c is the speed of light and λ is the wavelength, and energy E also becomes higher since $E = h\nu$ for a single photon, where h is Planck's constant. Thus wavelength, frequency, and energy of the electromagnetic radiation are equivalent. The energy unit of electronvolt (eV) is commonly used in high energy astrophysics. A photon with an energy of 1 eV has a wavelength of $\sim$1240 nm, and a frequency of $\sim 2.4\times10^5$ GHz. Conventionally, high energy astrophysics is further divided into high energy (HE) between $\sim$30 MeV to $\sim$100 GeV, very high energy (VHE) between $\sim$100 GeV to $\sim$100 TeV, and ultra-high energy $\gtrsim$100 TeV.

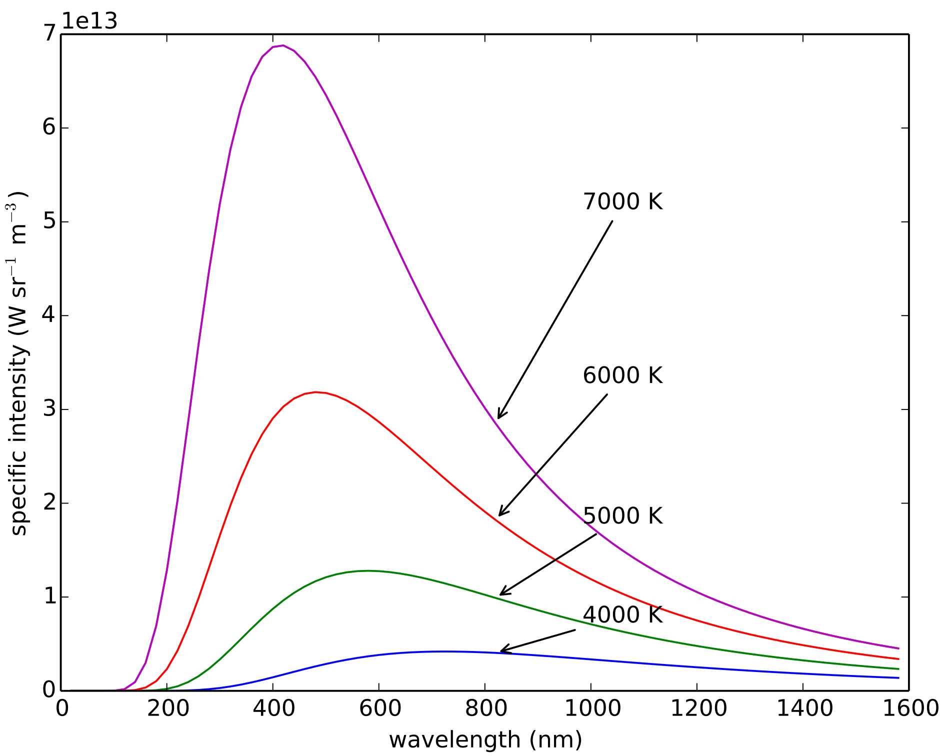

Figure 1.1.: Blackbody radiation calculated from Planck's law.

By building telescopes, we can break the limits of human eyes and probe a wider range of energy. Since the 20th century, telescopes in radio, X-ray, IR, and gamma-ray wavelengths have been expanding our knowledge of astrophysics vastly. This is important since many violent astrophysical sources are "hiding" themselves as ordinary stars in visible light, although their physics processes are drastically different. Stars and galaxies emit light via thermal processes. The resulting blackbody spectrum can be described by Planck's law, covering a frequency range from radio up to X-ray (see Figure 1.1). By extending to a much broader range of frequencies, a quite different picture of the universe emerges. At energies higher than X-ray, the observed radiation is dominated by the non-thermal processes from relativistic particles in magnetized plasma. These relativistic particles may escape and reach the Earth as observed CR particles, or emit light in the presence of magnetic field, or through interactions with other particles and/or photons (see section 1.1.3). The locations and mechanisms by which the highest energy CR particles are produced still remain an interesting puzzle related to gamma-ray astronomy.

Modern telescopes not only cover a wide range of energy, but also provide high angular resolutions. To illustrate the power of multiwavelength (MWL) observation, images of 3C 273 are shown in Figure 1.2. 3C 273 is the first quasar discovered in 1963 Schmidt (1963). The top panel of Figure 1.2 shows an optical image taken by the Small & Moderate Aperture Research Telescope System (SMARTS) (Bonning et al., 2012). The quasar and a comparison star, both of which were labeled in the image, share a very similar point-like morphology. However, the images of high angular resolution in the lower panels revealed an elongated and highly-collimated jet structure that is nothing like a star. Moreover, redshift measurement from the optical spectrum in the top panel of Figure 1.3 indicates 3C 273 is located at a large distance from us ($\sim$750 Mpc), and therefore extremely luminous. More recently, the broadband spectral energy distribution (SED) of 3C 273 in the bottom panel of Figure 1.3 shows non-thermal emission across the electromagnetic spectrum, from radio to gamma rays. By expanding wavelength coverage and improving angular resolution, we were able to identify the "signature" of the peculiar nature of 3C 273.

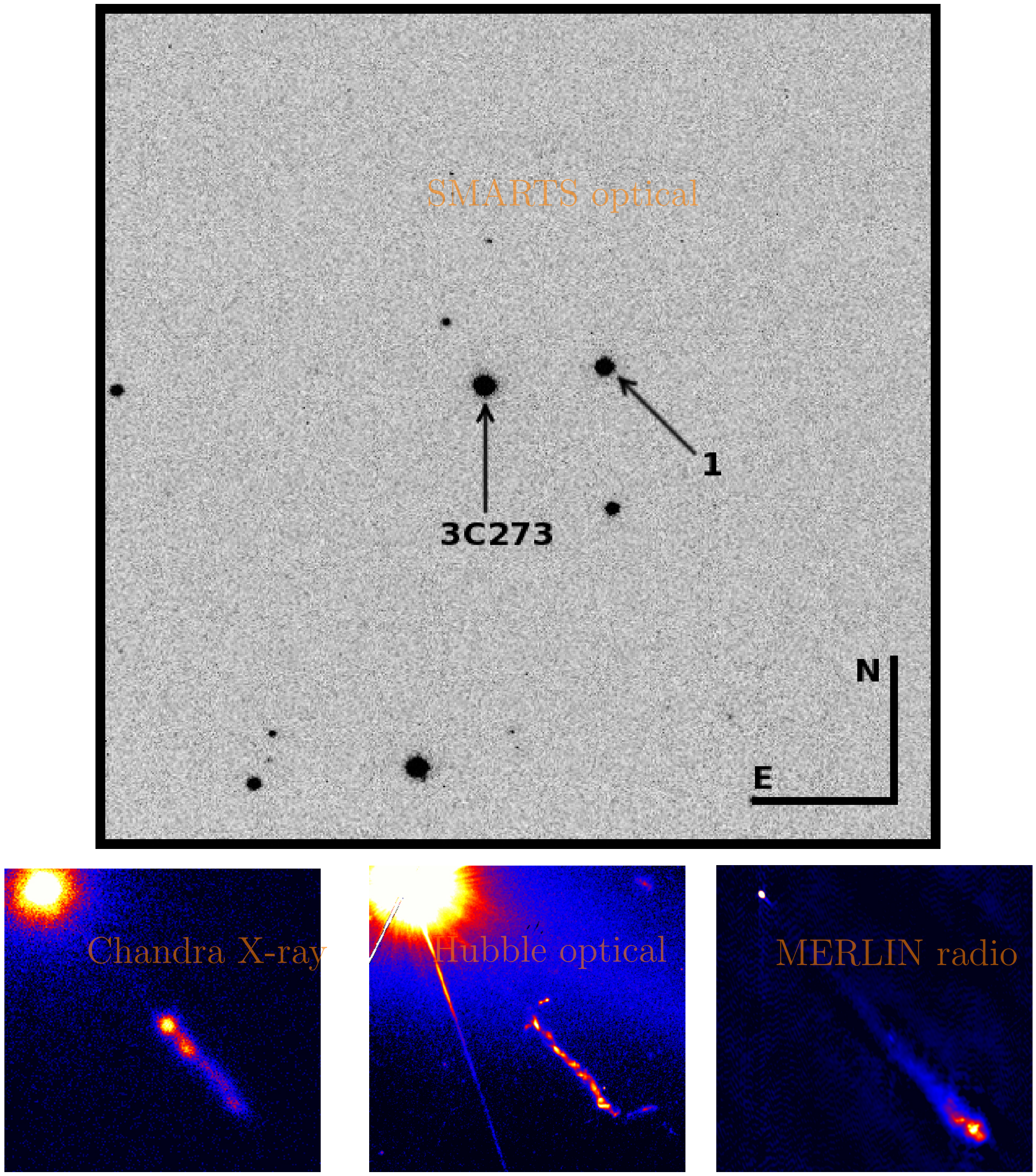

Figure 1.2.: Multiwavelength images of quasar 3C 273. Top image is a finding chart taken from SMARTS program, the quasar 3C 273 and the comparison star labeled as 1 both show up as a star-like point source. Bottom panels are high resolution images taken in X-ray band by Chandra (left), in optical band by Hubble Space Telescope, and in radio band by the Multi-Element Radio Linked Interferometer Network (MERLIN) `http://chandra.harvard.edu/photo/2000/0131/index.html`. An elongated and highly-collimated jet structure is resolved. Image courtesy of SMARTS `www.astro.yale.edu/smarts/glast/home.php`, NASA/CXC/SAO/H. Marshall et al. Marshall et al. (2001), NASA/STScI, and MERLIN.

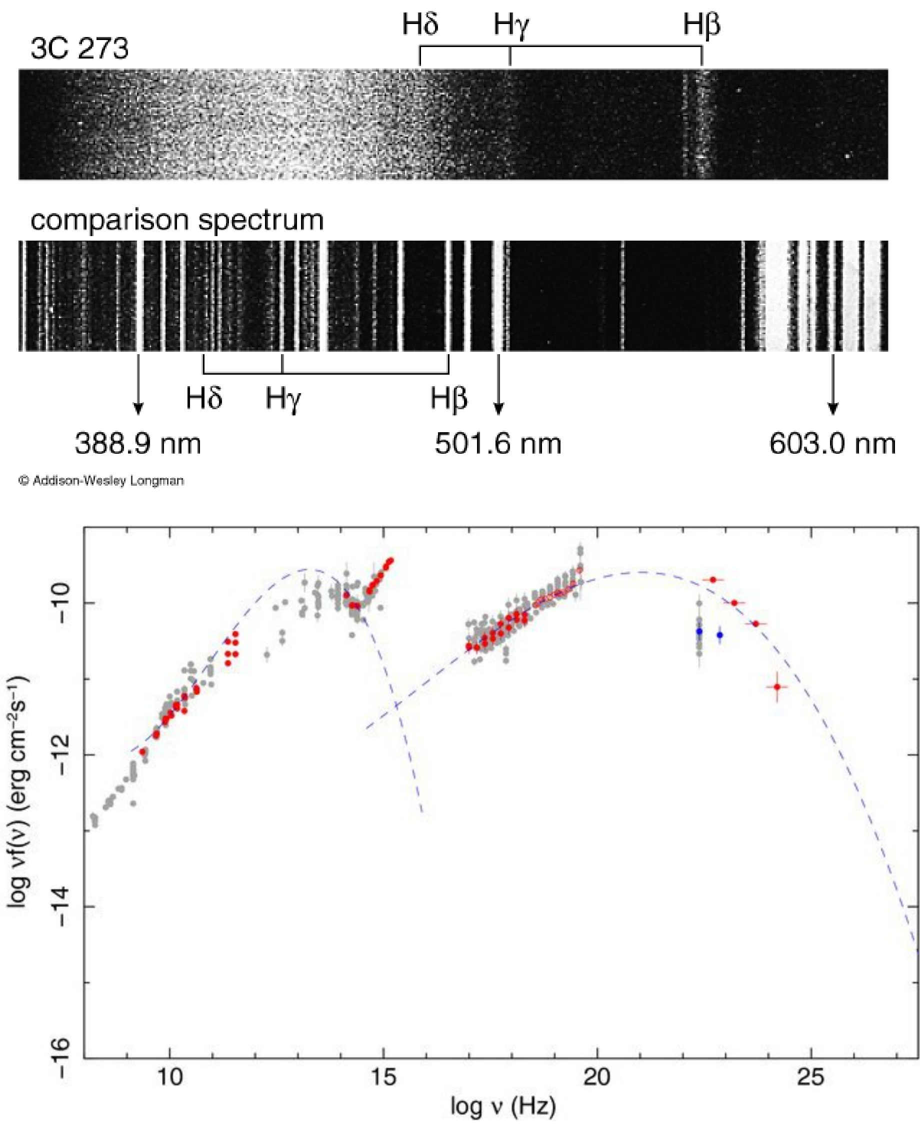

Figure 1.3.: Optical (top panel) and broadband (lower panel) spectra of 3C 273. The redshift can be determined from optical spectrum. Broadband spectral distribution indicate non-thermal processes from relativistic particles. Image courtesy of Maarten Schmidt (Schmidt, 1963) and *Fermi*-LAT (Abdo et al., 2010).

Although MWL observations are important, not all of the radiations and particles reach the ground of the Earth thanks to the atmosphere. Figure 1.4 shows the atmospheric opacity to the electromagnetic radiations. Only radiations within the visible band, a fraction of the infra-red (IR) band, and most of radio band pass through the "atmospheric window". Atoms in the atmosphere strongly absorb UV and X-ray photons, while molecules absorb most of the near-IR and some radio photons of particular frequencies. For high energy particles, only cosmic neutrinos and secondary muons in extensive air showers of cosmic hadrons frequently reach the ground.

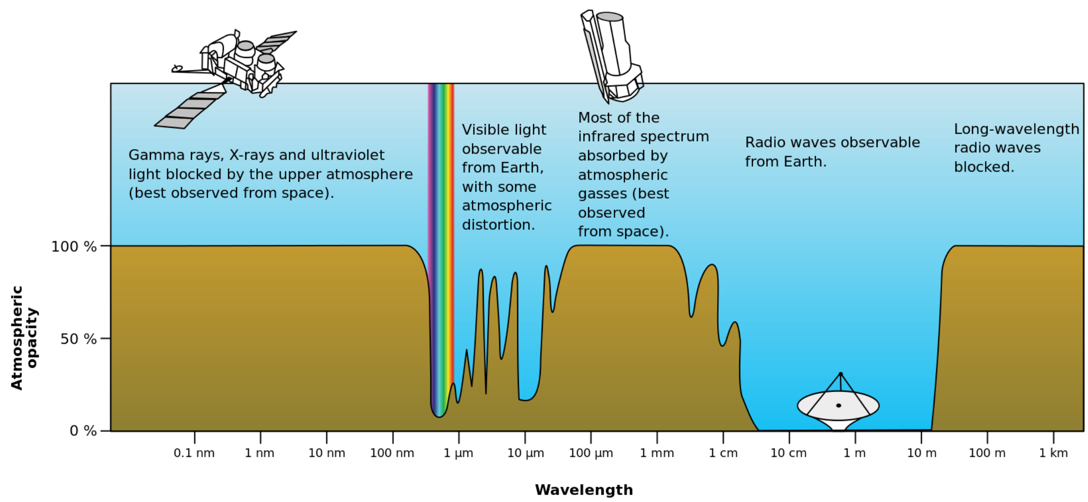

Figure 1.4.: Cartoon showing atmospheric transparency at different wavelengths. Image courtesy of Wikipedia.

As a result of atmosphere opacity, observatories are divided in to space telescopes onboard satellites (or similarly, sounding rockets and balloons) and ground-based telescopes. Space telescopes not only avoid the atmospheric absorption, but also the blurring caused by the turbulent air (seeing). Therefore, they are usually capable of providing a better angular resolution than ground-based ones at the same frequency. However, space telescopes are usually limited in size and weight, leading to a limited collection area (e.g. *Fermi*-LAT), requiring long exposure to study weak signals. This can be compensated by the ground-based telescopes with much larger collecting area (e.g. VERITAS), which is ideal for studying fast-varying and weak signals. VHE gamma rays are electromagnetic radiation of the shortest wavelengths, i.e. highest frequencies/energies. The atmosphere is completely opaque to VHE gamma rays. However, as they penetrate into the atmosphere, gamma rays produce a shower of particles that are traveling faster than the speed of light in the air, resulting in a bright but fast (on the order of 10 ns) flash of blue Cherenkov light. Therefore VHE gamma rays can be detected by taking pictures of these Cherenkov flash with a very fast camera. Beginning in the 1960s, this possibility to detect Cherenkov flashes and therefore high-energy gamma rays has been pursued and realized. After a long journey of exploration and persistent effort of many physicists, the first VHE source, the Crab Nebula, was detected by the Whipple telescope by Weekes et al. (1989).

VHE gamma-ray astrophysics has been growing rapidly since the beginning of the 21st century. Imaging atmospheric Cherenkov telescope arrays have pushed the VHE gamma-ray sensitivity to a new level and greatly expanded the zoo of known VHE sources (see section 1.2). These sources can be divided into galactic ones, including supernova remnants (SNRs), pulsars, pulsar wind nebulae (PWN), X-ray binaries (XRBs), as well as the Galactic Center (GC); and extragalactic ones, almost exclusively active galactic nuclei (AGN), with the exception of a few starburst galaxies. Potential VHE sources have been proposed and observed, e.g. gamma-ray bursts, candidate sources of dark matter annihilation or decay (e.g. clusters of galaxies and dwarf spheroidal galaxies), and primordial black holes, but no firm detections have been reported so far.

With the help of the larger collecting area of ground-based gamma-ray observatories and simultaneous monitoring campaign from space X-ray telescopes (e.g. Swift-XRT), studies of variable sources in the time-domain at high energies have been made possible and are becoming increasingly important.

This thesis focuses on the variability of a particular type of AGN, TeV blazars, and uses the Very Energetic Radiation Imaging Telescope Array System (VERITAS) as the main instrument. In this chapter, I give a brief overview of VHE gamma-ray astronomy. In chapter 2, I describe how VERTAS detects VHE gamma rays. In chapter 3, I describe the observations of TeV blazars, present the results of their variability studies, and discuss the interpretations in a multi-wavelength context.

In the following sections of this chapter, I will first briefly describe the acceleration mechanisms (section 1.1.1) and the propagation for CR (section 1.1.2), as well as their radiative processes (section 1.1.3), all of which are closely related to gamma-ray astronomy. Then I will briefly introduce the VHE gamma-ray emitting sites (section 1.2).

1.1 Relation between cosmic ray particles and VHE gamma rays

VHE gamma ray astronomy was originally intended to help search for CR sources, since only a few places in the universe are able to produce TeV photons, which requires relativistic charged CR particles of higher energies >TeV. CRs were discovered by Victor Hess with balloon experiments in 1912, when he observed increasing ionization rate at higher altitude (F. Hess, 1912). They are deflected in the galactic and inter-galactic magnetic field, and they consequently lost the information of their original direction. Thus identifying their origins remained an outstanding goal in astroparticle physics and the gamma ray counterpart needs to be studied. A good understanding of the particle acceleration, radiative mechanism, escape, and propagation in astrophysical sources are needed to infer the cosmic ray origin from the VHE gamma ray observations.

CRs consist of protons, alpha particles and heavier nuclei, as well as electrons and positrons (hereafter electrons). The particle energy distribution satisfies the continuity equation with the general form of:

$$\frac{\partial}{\partial t}\frac{dN}{d\gamma} + \frac{\partial}{\partial \gamma}\left(\dot{\gamma}\frac{dN}{d\gamma}\right) = Q(\gamma, t), \tag{1.1}$$

where γ is the Lorentz factor of the particle, $dN/d\gamma$ is the time-dependent particle spectrum, $\dot{\gamma}dN/d\gamma$ describes all energy loss processes, and $Q(\gamma, t)$ is the source function. Although the general solution of this continuity equation depends on each term, a power-law form solution $dN/d\gamma \propto \gamma^{-p}$ can be found in many cases. For example, by assuming a stationary system $\partial/\partial t = 0$ with no source $Q(\gamma, t) = 0$, a power law distribution with index $p = 2$ can be found.

Figure 1.5 shows a measured energy spectrum of CRs over 13 orders of magnitude in energy, from GeV to ZeV (10^9 to 10^{21} eV). The well measured spectrum follows a power law with a few features: the slope flattens significantly at below ~1 GeV, steepens slightly from a spectral index of ~2.7 to ~3.0 at the "knee" between 3 to 4 PeV (1 PeV=10^{15} eV), steepens again at around 500 PeV to an index of ~3.3, and finally flattens again to an index of ~2.7 at above the "ankle" around 4 EeV (1 EeV=10^{18} eV). The "knee" and "ankle" may indicate different CR particle compositions and/or sources (see Blandford et al. (2014) for a review).

Independent of any model, the energy of the observed CR immediately puts a constraint on the size of the accelerator. The accelerator has to be larger than the gyro radius of the CR particle, in order to contain them for a sufficiently long period of time for acceleration. This constraint is captured by the Hillas formula (Hillas, 1984):

$$R_{\rm size} \geqslant \frac{2R_{\rm gyro}}{\beta} \approx 2.16 \left(\frac{E}{10^{15}{\rm eV}}\right) Z^{-1} \left(\frac{B}{1\mu{\rm G}}\right)^{-1} \beta^{-1}{\rm pc}, \tag{1.2}$$

$$\text{or } \frac{E}{10^{15}{\rm eV}} \leqslant \frac{E_{\rm max}}{10^{15}{\rm eV}} \approx 0.46 Z\beta \left(\frac{B}{1\mu{\rm G}}\right) \left(\frac{R_{\rm size}}{1{\rm pc}}\right), \tag{1.3}$$

where $R_{\rm size}$ is the size of the accelerator, $R_{\rm gyro}$ is the gyroradius of the particle, $E = \gamma mc^2$ and Ze is the energy and charge of the particle, respectively, $E_{\rm max}$ is the maximum energy of a particle that can be contained in the accelerator, B is the magnetic field of the source, and βc is the velocity of the scattering center (e.g. shock front). Applying the Hillas formula, one can find that in order to accelerate particles to higher energies, a larger value of BR is needed. For example, plug in the galactic magnetic field strength $B \approx 6\mu$G at the Earth, and the distance between the Earth and the Galactic center ~8 kpc, one may estimate the highest energy particles that can be contained by the Milky Way galaxy is roughly $5Z \times 10^{18}$ eV, which cannot account for the highest observed CR energies.

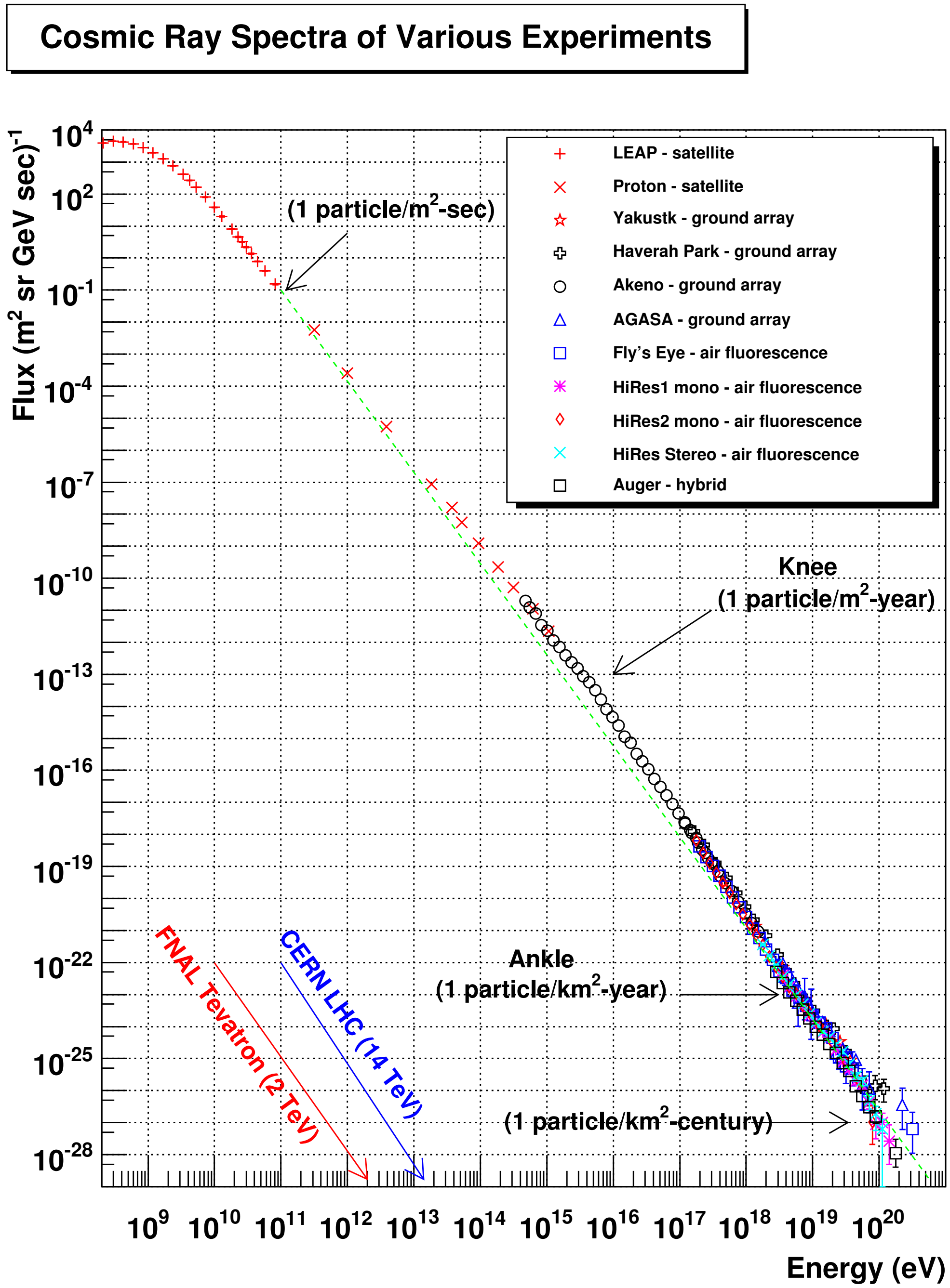

Figure 1.5.: Cosmic-ray spectrum between 10^8 to 10^{21} eV. Image courtesy of Dr. William Hanlon.

At below $\sim$2 GeV, the observed CRs are almost exclusively from the Sun, since these CRs cannot penetrate the solar wind. The propagation of these low energy CR particles is governed by the diffusion coefficient in the interplanetary magnetic field (Palmer, 1982). Going toward higher energies, (i) a large fraction of the observed CRs between $\sim$GeV and the spectral "knee" ($\sim$PeV) are believed to come from galactic SNRs; (ii) CRs with energies between the "knee" and the "ankle" are from larger shock structures associated with pulsars and PWNe; and (iii) the Ultra High Energy Cosmic Rays (UHECRs; >EeV) most likely have extragalactic origin, possibly coming from AGN, GRBs, or other exotic objects (like magnetars or intergalactic shocks).

1.1.1 Particle acceleration mechanisms

The observed CRs reach ultra high energies up to 10^{21} eV as mentioned in the previous section. An immediate question to ask is how these CR particles are accelerated. Gravity is usually the ultimate power source, e.g. from core collapse of massive stars or accretion in supermassive black holes. But the gravitational energy released in astrophysical processes is not directly converted to the energy of the observed particles. Instead, the particles exist in the from of magnetized plasma in the extreme astrophysical environments, and can be efficiently accelerated to relativistic speed through electromagnetic interactions. A static magnetic field does no work, therefore either a regular electric field ($\langle\vec{E}\rangle \neq 0$) on large scales or a stochastic electric field ($\langle\vec{E}\rangle = 0$, $\langle\vec{E}^2\rangle \neq 0$) on small scales is needed in order to accelerate charged particles. Note that regular E field is rare, since freely moving charged particles in the highly conductive plasma are able to redistribute and compensate the original E field. However, Blandford & Znajek (1977) have demonstrated how to extract energy electromagnetically from a Kerr black hole, which makes use of a large scale induced E field and should be applicable for any spinning magnetic field (so called "unipolar inductor"). Focusing on the more specific processes, two popular acceleration mechanisms have been long proposed: shock acceleration (with stochastic E field) and magnetic reconnection (with regular E field). I now briefly describe these two mechanisms.

Shock acceleration Shocks are ubiquitous in the universe. Physical properties, e.g. pressure, velocity, temperature, are almost discontinuous between the two sides of the shock front dividing the shocked and unshocked material. Astrophysical shocks are usually collisionless due to the low density of the medium, therefore particles do not interact with each other via Coulomb collision, but instead collide with massive magnetic "clouds" and may gain energy when crossing the shock front. Such a diffusive shock acceleration mechanism (first-order Fermi acceleration) was proposed by Fermi (1949). Note that at each crossing a particle may gain or lose energy depending on the frame of reference, since only head-on collisions result in an energy gain. However, the probability for a head-on collision is larger due to the larger relative speed, and the net change of the energy of the particle is positive. A loop of two shock crossings will always result in an energy gain.

The particle distribution function $f(\mathbf{x}, \mathbf{p}; t)$ in a diffusive shock satisfies the Vlasov equation (a simplified version of the Fokker-Planck equation without collision):

$$\frac{\partial f}{\partial t} + \mathbf{v} \cdot \frac{\partial f}{\partial \mathbf{x}} + \frac{\partial}{\partial \mathbf{p}} \cdot (\mathbf{F} f) = 0, \tag{1.4}$$

where $\mathbf{x}$, $\mathbf{v}$, $\mathbf{p}$, and $\mathbf{F} = d\mathbf{p}/dt$ are the position, velocity, momentum of the particle, and force acting on the particle, respectively, and t is time. The third term in the Vlasov equation can be written as multiple terms describing diffusion, compression, advection, energy loss, injection, and escape, and form the transport equation:

$$\frac{\partial f}{\partial t} = \nabla \cdot \{\mathbf{n}\mathbf{D}(\mathbf{n} \cdot \nabla) f\} - \mathbf{v} \cdot \nabla f + \frac{1}{3}(\nabla \cdot \mathbf{v})\mathbf{p}\frac{\partial f}{\partial \mathbf{p}} + Q(\mathbf{x}, \mathbf{p}; t). \tag{1.5}$$

The first term on the right hand side of equation 1.5 describes diffusion, where the diffusion coefficient $\mathbf{D}$ is a tensor, the second term describes advection, the third term describes compression, and the last term describes injection. More specific terms describing other energy loss, injection, and escape processes may be added to the right hand side of the equation. Equation 1.5 is fundamental for solving for particle distributions, and are extensively used in simulations in astrophysical sources. Note that different directions of the average magnetic field at the shock will affect the parallel and perpendicular (with respect to the shock normal direction) components of the diffusion coefficient, therefore having strong effect on the transport and acceleration of particles (e.g. perpendicular shocks Jokipii, 1987). In general, random magnetic fluctuations both upstream and downstream of the shock are assumed.

The average energy gain of shock crossings in first-order Fermi acceleration is estimated by Gallant & Achterberg (1999). A particle on average gains energy by a factor of Γ_s^2 in the first shock crossing, where Γ_s is the Lorentz factor of the shock, and by a factor of ~ 2 in each subsequent one. The difference comes from the lack of time for the particle to relax into an isotropic distribution of velocity after the first shock crossing.

Following Tammi & Duffy (2009), we can estimate the energy-gain rate $\langle d\gamma/dt \rangle$, and subsequently the acceleration timescale $t_{acc} \approx \gamma / \langle d\gamma/dt \rangle$, where γ is the Lorentz factor of the particle. Assuming the mean free path λ of the particle is equal to its gyroradius $r_{gyro} = \gamma mc^2/(eB)$, the acceleration timescale in comoving frame is

$$\tau_{Fermi\_I} \gtrsim 6\beta_s^{-2}\frac{\lambda}{c} \approx 6\beta_s^{-2}\frac{r_{gyro}}{c} \approx 3.4\left(\frac{\gamma}{10^4}\right)\left(\frac{B}{1\mathrm{G}}\right)^{-1}\beta_s^{-2}\ \mathrm{ms},$$

where β_s is the speed of the shock. The acceleration timescale increases linearly as a function of the Lorentz factor (or energy) of the particle, i.e. it takes longer to accelerate particles to higher energies. The acceleration time is on the order of ms for a $\gamma \sim 10^4$ particle in a 1 G magnetic field for a relativistic shock, which can often be considered instantaneous. However, we note that to reach ultra-high energies, (i) a large number of scatterings or shock crossings are needed, and (ii) radiative cooling (e.g. synchrotron radiation) may become important as the cooling time becomes shorter at higher energies. Both effect may make the acceleration slower and less efficient.

In addition to the first-order Fermi acceleration, there are two other types of acceleration which may be related to shocks: second-order Fermi acceleration and converter mechanism (Tammi & Duffy, 2009).

Second-order Fermi acceleration is the stochastic scattering between particle and random magnetic fields, which does not necessarily require a shock. Second-order Fermi process is only important when the shock speed is almost as low as the Alfvén speed (low Mach number), and the diffusion in momentum space becomes prominent. The acceleration time for second-order Fermi process in comoving frame is

$$\tau_{Fermi\_II} \gtrsim \frac{3}{4}\left(\frac{v_A}{c}\right)^{-2}\frac{\lambda}{c} \approx \frac{3}{4}\frac{r_{gyro}c}{v_A^2} \tag{1.6}$$

$$\approx \begin{cases} 0.425\left(\frac{\gamma}{10^4}\right)\left(\frac{B}{1\mathrm{G}}\right)^{-3}\left[1.9\times 10^3\left(\frac{n_p}{10^5\mathrm{cm}^{-3}}\right)+\left(\frac{B}{1\mathrm{G}}\right)^2\right]\ \mathrm{ms}, & \text{for protons;} \\ 0.425\left(\frac{\gamma}{10^4}\right)\left(\frac{B}{1\mathrm{G}}\right)^{-3}\left[1.0\left(\frac{n_e}{10^5\mathrm{cm}^{-3}}\right)+\left(\frac{B}{1\mathrm{G}}\right)^2\right]\ \mathrm{ms}, & \text{for electrons;} \end{cases} \tag{1.7}$$

where $v_A = Bc/\sqrt{(4\pi\rho c^2 + B^2)}$ is the relativistic Alfvén speed, n_p or n_e is the number density of the protons or electrons in the plasma. The timescale for second-order Fermi acceleration depends on the number density of the particles and the strength of the magnetic field. For higher density plasma in weaker magnetic field, the timescale is rather long; for low density plasma in strong magnetic field, which may happen in AGN jets, the acceleration is fast. It is also much faster to accelerate electrons via Fermi II process. Taking the value of $n_e = n_p = 10^5\mathrm{cm}^{-3}$ and $B = 1\mathrm{G}$, the acceleration time for electrons is $\sim$1 ms, and for proton is $\sim$1 s.

Converter mechanism is a modified version of the first-order Fermi acceleration, in which charged particles only cross the shock from upstream to downstream. An accelerated charged particle can then be converted into a neutral particle (e.g. neutron or a synchrotron photon) downstream, recrosses the shock from downstream to upstream, decays into or produces a pair of charged particles in the upstream, and continues the cycle. Converter mechanism offers an energy gain of a factor of Γ^2 every shock crossing, in contrast to the first-order Fermi mechanism where the factor of Γ^2 is only for the first cycle. In ultrarelativistic shocks, converter mechanism with synchrotron photon as the neutral form can be as fast as the first-order Fermi process, and can reach a higher maximum energy.

Shock acceleration has an advantage for being able to produce a particle energy distribution that follows a power-law

$$\frac{dN}{dE} \propto E^{-(1+\tau_{acc}/\tau_{esc})},$$

assuming that a particle gains energy at a rate $dE/dt = E/\tau_{acc}$, where τ_{acc} and τ_{esc} are the timescales related to particle acceleration and escape. However, shock acceleration also has its limitations. For example, the power law index (p in $dN/dE \propto E^{-p}$) achieved from shock accelerations are usually larger than 2, and with non-linear effect the particle distribution deviates from power law. Moreover, Fermi acceleration can be rather inefficient, since it may take many shock crossings to accelerate particles to very high energies.

In relativistic outflows, the extreme environment usually lead to relativistic shocks. In this setting, the maximum energy that can be achieved is

$$E \leqslant \gamma_{shock} q v B_{background} R,$$

where γ_{shock} is the Lorentz factor of the shock, and $B_{background}$ is the unamplified background magnetic field (Plotnikov et al., 2013). Although the extra γ_{shock} comparing to the Hillas formula 1.2 leads to a higher energy upper limit, but the background magnetic field is much weaker than the turbulent magnetic field (by a factor of a few to 100 depending on different amplification mechanism and field geometry). Therefore the resultant maximum energy may still be much lower than the highest observed UHECRs.

Magnetic reconnection Magnetic reconnection is an abrupt change of magnetic field topology, from a higher magnetic energy field configuration to a lower magnetic energy one. It is observed in the Sun (e.g. solar flares, coronal mass ejection) and in the Earth's magnetosphere. It is believed to occur in many astrophysical environments, from the formation of stars to AGN and GRB. A magnetic field has tension along the field lines ($(\mathbf{B} \cdot \nabla)\mathbf{B}/4\pi$) and transverse pressure ($B^2/8\pi$). The magnetic tension tries to straighten bent field lines, and magnetic pressure resists when field lines come too close. However, in the highly conductive environment where the assumption of ideal magnetohydrodynamics (MHD) holds, the magnetic field lines are "frozen in" or "attached to" the plasma. When magnetic field lines with opposite directions convect toward each other with a particle inflow, magnetic reconnection occurs as particles "unfreeze" in a small central "X-line" region (see Fig 1.6 for a qualitative illustration). During this process, (i) strong localized transient E field and current layers are formed, leading to the formation of magnetic islands (e.g. Drake et al., 2006b); and (ii) magnetic energy is converted into plasma kinetic energy efficiently, e.g. through the first-order Fermi mechanism particles bounce repeatedly within and between magnetic islands in the current layer (e.g. Drake et al., 2006a; Guo et al., 2014). More in-depth reviews on magnetic reconnection can be found in Zweibel & Yamada (2009); Yamada et al. (2010).

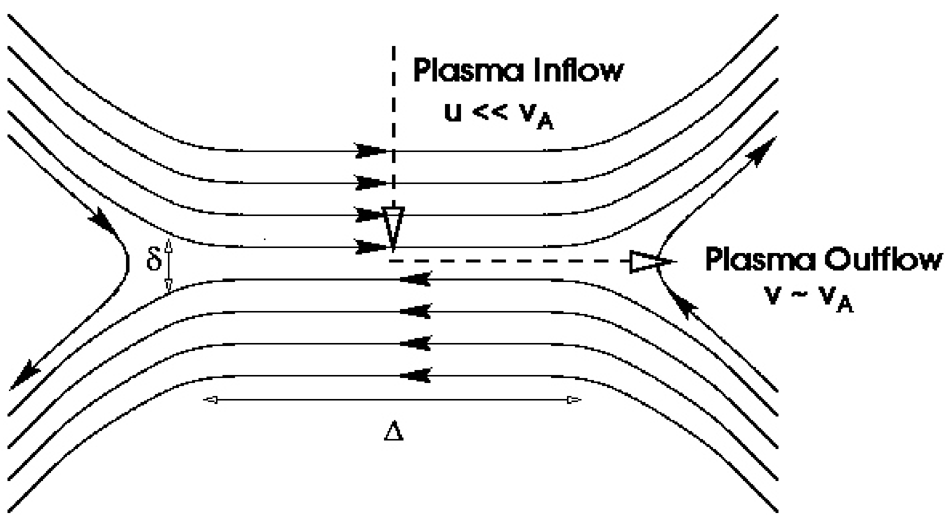

Figure 1.6.: A cartoon qualitatively illustrating two-dimensional magnetic reconnection. Image courtesy of MRX at PPPL.

Magnetic reconnection is a self-organized process that happens on all scales, and it can be fast. These properties are useful for explaining some of the observed phenomena in energetic astrophysical sources. The energy-gain rate, acceleration timescale, and maximum energy depend on the relative velocity of the two inflow regions with opposite magnetic field directions, as well as the geometry and scale of the reconnecting region. However, a rather generic estimation of the acceleration timescale was given by Giannios (2010) as

$$\tau_{\mathrm{acc\_recon}}(\gamma) = \frac{2\pi\gamma mc^2}{(1-1/A)eBc},$$

where γ is the Lorentz factor of the accelerated particle, B is the strength of magnetic field, amplification A is the energy-gain ratio each time the particle bounces around the reconnection layer, $\langle A\rangle \sim \gamma_r^2(1+3/4\beta_r+1/2\beta_r^2)$, and γ_r and $\beta_r c$ are the Lorentz factor and speed of the relative motion of the two inflow regions. For $A \sim 2$, this acceleration timescale is comparable to the gyration time $t_g = 2\pi\gamma mc^2/eBc \sim 1\times 10^{-6}\gamma(B/1\mathrm{G})^{-1}$ s, which is very fast.

Moreover, magnetic reconnection may produce a power-law particle energy distribution $dN/dE \propto E^{-p}$, where p may reach 1 in highly magnetized plasma (i.e. the magnetization parameter $\sigma \equiv B^2/(4\pi nmc^2) \gg 1$). Guo et al. (2014) has demonstrated the formation of such a hard power-law energy distribution of particles in magnetic reconnections. This is considerably harder than the first-order Fermi process, where the particle distribution with a spectral index of $\gtrsim$2 may be achieved.

It is worth noting that both shocks and magnetic reconnection can contribute to particle acceleration in the same source, e.g. in Earth's magnetosphere, or between plasmoids in reconnection region. Besides shocks and magnetic reconnection, there are other acceleration mechanisms proposed as well, e.g. shear acceleration (Rieger & Duffy, 2004), wakefield acceleration (Tajima & Dawson, 1979).

1.1.2 Cosmic ray propagation

After they are accelerated, a fraction of CR particles may escape and propagate to the Earth for us to directly observe them. These CR particles first need to survive radiative loss, which is particularly severe for electrons. Then the turbulent magnetic field at the source may produce a CR "halo", where the CRs are injected into the interstellar/intergalactic medium (ISM/IGM). In the ISM/IGM, the propagation of galactic cosmic rays is affected by (i) the transport along the magnetic field, (ii) the diffusion in pitch angle and consequently in space due to irregular magnetic field, (iii) nuclear fragmentation/spallation, and (iv) radioactive decay of unstable isotopes. Moreover, more prominent for extragalactic CRs, they can (i) interact with the ambient radiation field, e.g. cosmic microwave background (CMB) or extragalactic background light (EBL), producing a cascade of secondary particles and VHE photons, and therefore get absorbed; (ii) generate electrons from the cascade described above which produce synchrotron radiation as they transport along the intergalactic magnetic field (IGMF) or galactic magnetic field (GMF), (iii) are deflected by the structured IGMF/GMF and observed as an elliptical halo.

Focusing on UHECRs, they are believed to have extragalactic origin, and they experience less deviation by the magnetic field compared to lower energy counterparts. Thus, there is a potential to search directly for their anisotropy and pinpoint their sources. Evidence for UHECR anisotropy has been claimed before (e.g. Takeda et al., 1999; Pierre Auger Collaboration et al., 2007), showing possible correlations between UHECRs and known extragalactic sources (e.g. a nearby AGN, Cen A). But this correlation has become weaker in subsequent studies. Most recently, The Pierre Auger Collaboration (2014) has used UHECR events with energy $E > 5$EeV in a 0.25 rad region around those with $E > 60$EeV to study (i) energy-energy correlations, which provide information about turbulent magnetic field near the source, and (ii) principal axes decomposition, in which the first principal axis represents the strength of clustering, and the second principal axis may contain the deflection pattern caused by structured IGMF/GMF. Their studies showed no evidence of characteristic patterns and anisotropy of UHECRs (see Figure 1.7).

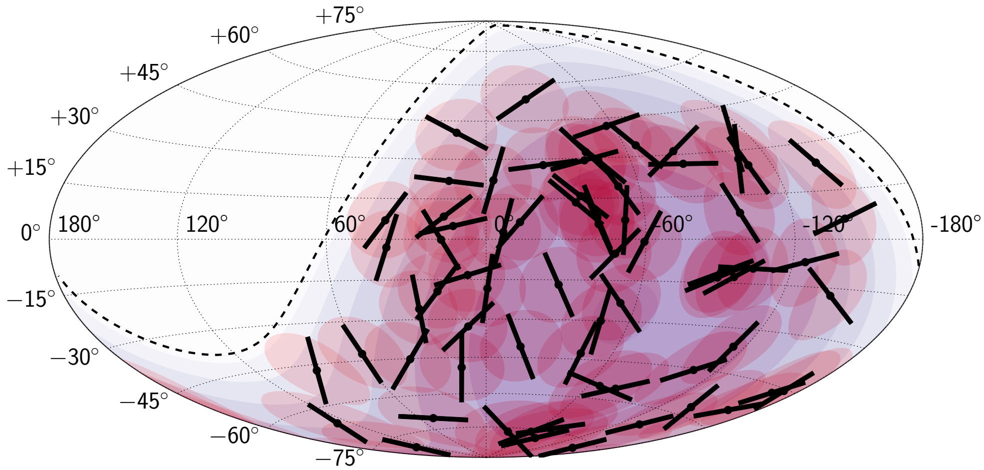

Figure 1.7.: Map of principal axes of directional energy distribution measured by the Pierre Auger observatory (The Pierre Auger Collaboration, 2014). The black dots and black solid lines represent the first and second principal axes, respectively. The first principal axis comes out of the plane of the page and represents the strength of clustering, and the second principal axis may contain the deflection pattern caused by the IGMF/GMF.

One important implication of the interaction between UHECRs and CMB radiation is the Greisen-Zatsepin-Kuzmin (GZK) cutoff (Greisen, 1966; Zatsepin & Kuz'min, 1966), through photon pion production processes

$$p + \gamma_{CMB} \rightarrow \Delta^+ \rightarrow p + \pi^0, \tag{1.8}$$

$$p + \gamma_{CMB} \rightarrow \Delta^+ \rightarrow n + \pi^+. \tag{1.9}$$

With a precise knowledge of the CMB spectrum one can calculate the cross section of the above processes, and reach the conclusion that the characteristic distance a proton of energy $E \gtrsim 10^{20}$eV can travel before interacting with a CMB photon is $\lesssim$50 Mpc. UHECRs with energy $\gtrsim 10^{20}$eV from further away ($z \gtrsim 0.01$) sources should be severely absorbed. Note that the pions produced in the above process will further decay into gamma rays (1.41) or muons and neutrinos (1.42), this leads to the so called GZK neutrino signal of the highest energies ($> 10^{16}$eV).

1.1.3 Radiative processes

The deflection from IGMF/GMF makes the CR distribution isotropic, and UHECR with a high redshift origin cannot reach us due to the GZK cutoff, posing challenges to studying the CR origin. However, the same sources that produced UHECRs can also produce gamma rays. Therefore observations of their gamma-ray counter part is important. An understanding of how charged particles radiate and interact with photons is necessary. In this section I briefly describe some radiative processes that are relevant to VHE astrophysics, following the discussions in Rybicki & Lightman (1979) and Longair (1992).

Basic radiative transfer The luminosity L of a source is simply defined as the power, or energy per unit time, emitted by the entire source. For an observer at distance r, the flux, defined as the total energy arrived per unit time per unit area from the source, is $F = L/(4\pi r^2)$. For telescopes that are only sensitive to a particular frequency of light, it is useful to define flux density (or specific flux) as the flux per frequency $F_\nu = F(\nu, \nu + d\nu)/d\nu$. To study the source of the emission, another quantity describing the flux within a solid angle $d\Omega$ called specific intensity (or surface brightness) can be defined as $I_\nu = dF_\nu/(cos\theta d\Omega)$, where θ is the angle between the the line of sight and the direction of the solid angle.

Radiative transfer generally describe the change of specific intensity when light travels through matter. The basic radiative transfer equation is given in Rybicki & Lightman (1979) as

$$\frac{dI_\nu}{ds} = -\alpha_\nu I_\nu + j_\nu, \tag{1.10}$$

where ds is the distance increment that the light travels through, $j_\nu = P_\nu/4\pi$ and $\alpha_\nu = n\sigma_\nu$ are the emission and absorption coefficient, respectively. P_ν in the emission coefficients j_ν describes the total power per volume per frequency; σ_ν and n in the absorption coefficient α_ν is the cross section for absorption processes for a single particle, and the number density of the particle, respectively. Note that α_ν is related to the optical depth τ_ν and the mean free path l_ν by

$$
\begin{aligned}
d\tau_\nu = \alpha_\nu(s)ds \Rightarrow dI_\nu &= -\alpha_\nu I_\nu ds = -I_\nu d\tau_\nu, \\
\tau_\nu &= \int_{s1}^{s2} \alpha_\nu(s')ds', \\
l_\nu &= \frac{1}{\alpha_\nu}.
\end{aligned}
$$

The optical depth τ_ν describes the amount of attenuation that the radiation of a certain frequency suffers between $s1$ and $s2$. When $\tau_\nu > 1$, the attenuation reduces the specific intensity by a factor of $> 1/e$ resulting in $I'_\nu < I_\nu/e$, and it is called optically thick; similarly, when $\tau_\nu < 1$, it is called optically thin.

With the help of the radiative transfer equation, we can obtain the spectrum of a process from the emitting power per unit frequency from a particle of a certain energy, the number density of particles at each energy, and the absorption processes between photons and particles. First, in the non-relativistic regime, the total power emitted by a charged particle can be described by Larmor's formula:

$$
\frac{dP}{d\Omega} = \frac{q^2a^2}{4\pi c^3} sin^2\theta, \tag{1.11}
$$

$$
P = \frac{2q^2a^2}{3c^3}, \tag{1.12}
$$

where q and a are the charge and acceleration of the particle, θ is the angle between the direction of acceleration and the direction to the point of interest, and c is the speed of light. Note that the radiation is strongest in the direction perpendicular to the acceleration. For a small cloud (size L) of non-relativistic charged particles, at distances far away from the cloud, Larmor's formula can be approximated by dipole radiation with power $P_{dipole} = 2\ddot{\vec{d}}^2/(3c^2)$, where the dipole is defined as $\vec{d} = \sum_i q_i \vec{r}_i$.

In the relativistic regime, assuming the total emitted power is Lorentz invariant, Larmor's formula becomes

$$P = \frac{2q^2}{3c^3}\gamma^4(a_\perp^2 + \gamma^2 a_\parallel^2), \tag{1.13}$$

where γ is the Lorentz factor of the particle, $a_\perp$ and $a_\parallel$ are the perpendicular and parallel component of the acceleration with respect to the particle direction. Note that the radiation is beamed, and stronger by a factor of γ^2 in the direction the particle motion. The beaming effect leads to linear polarization in the case of synchrotron radiation, the fraction of which can be expressed as $(P_\perp - P_\parallel)/(P_\perp + P_\parallel)$, where now $P_\perp$ and $P_\parallel$ are the specific power perpendicular and parallel to the direction of the magnetic field.

Relativistic effect When an emitter moves at relativistic speed toward the observer, in the lab frame (i) the apparent luminosity is higher (Doppler boosting or aberration), (ii) the apparent size of the emitting region is smaller (length contraction), (iii) the apparent time intervals are longer (time dilation), and (iv) the apparent frequency of the light is shorter (blue-shift). The effect is the opposite when the source is moving away.

Assume the source is moving along x-direction at the speed of u (or $\beta = u/c$) in the lab frame (unprimed frame S), the four-vector $x'^\mu = (ct', x', y', z')$ in the comoving frame (primed frame S') and that in the lab frame $x^\mu = (ct, x, y, z)$ are connected by the Lorentz transformation

$$\begin{pmatrix} ct' \\ x' \\ y' \\ z' \end{pmatrix} = \begin{pmatrix} \gamma & -\gamma\beta & 0 & 0 \\ -\gamma\beta & \gamma & 0 & 0 \\ 0 & 0 & 1 & 0 \\ 0 & 0 & 0 & 1 \end{pmatrix} \begin{pmatrix} ct \\ x \\ y \\ z \end{pmatrix}, \tag{1.14}$$

and inverse transformation:

$$\begin{pmatrix} ct \\ x \\ y \\ z \end{pmatrix} = \begin{pmatrix} \gamma & \gamma\beta & 0 & 0 \\ \gamma\beta & \gamma & 0 & 0 \\ 0 & 0 & 1 & 0 \\ 0 & 0 & 0 & 1 \end{pmatrix} \begin{pmatrix} ct' \\ x' \\ y' \\ z' \end{pmatrix}. \quad (1.15)$$

From the inverse Lorentz transformation we immediately get:

$$\begin{aligned} cdt &= \gamma(cdt' + \beta dx'), && (1.16) \\ dx &= \gamma(dx' + \beta cdt'), && (1.17) \\ dy &= dy', && (1.18) \\ dz &= dz'. && (1.19) \\ & && (1.20) \end{aligned}$$

Since the velocity is the time derivative of the coordinates, we have the velocity transformation:

$$\begin{aligned} u_x = \frac{dx}{dt} &= \frac{u'_x + \beta c}{1 + \beta u'_x/c}, && (1.21) \\ u_y = \frac{dy}{dt} &= \frac{u'_y}{\gamma(1 + \beta u'_x/c)}, && (1.22) \\ u_z = \frac{dz}{dt} &= \frac{u'_z}{\gamma(1 + \beta u'_x/c)}. && (1.23) \\ & && (1.24) \end{aligned}$$

The aberration effect can be now derived from the velocity transformation

$$tan\theta = \frac{u_\perp}{u_\parallel} = \frac{u' sin\theta'}{\gamma(u' cos\theta' + \beta c)}. \quad (1.25)$$

In the limit of $\theta' = \pi/2$, we have $sin\theta_c = \frac{1}{\gamma}$. When $\gamma \gg 1$, the above angle can be approximated by $\theta_c \sim 1/\gamma$. This means the radiation in the lab frame of a relativistic emitter, which radiates isotropically in its comoving frame, will be confined into a cone with a narrow opening angle $\theta_c \sim 1/\gamma$. This effect is called relativistic beaming, or aberration.

Taking into account the different viewing angles with respect to the direction of motion of the source, it is useful to define the Doppler factor as

$$\delta = \frac{1}{\Gamma(1 - \beta cos\theta)}, \tag{1.26}$$

where βc is the speed of the emitting region, $\Gamma = 1/\sqrt{1-\beta^2}$ is the Lorentz factor, and θ is the viewing angle between the line of sight and the direction of the source. Following Urry & Shafer (1984), it can be calculated that in the lab frame (i) the apparent luminosity density is boosted by a factor of δ^2 due to aberration, and another factor of δ due to time dilation, which also makes the emitting frequency different, therefore $L(\nu) = \delta^3 L'(\nu')$, and similarly the apparent flux density becomes $F(\nu) = \delta^3 F'(\nu')$; (ii) the apparent size of the emitting region becomes $R = R'/\delta$; (iii) the apparent time interval becomes $t = t'/\delta$; and (iv) the apparent frequency of the light becomes $\nu = \delta\nu'$.

Bremsstrahlung radiation Bremsstrahlung radiation happens when a charged particle is accelerated in the Coulomb field of another charged particle. Although the Bremsstrahlung from a UHECR particle can reach the VHE regime, it is usually not the dominant process of producing VHE gamma rays. However, it is an important process in the air shower development when a VHE gamma ray enters the atmosphere. Of particular relevance to air showers is the electron-ion bremsstrahlung. In this case, electrons can be treated as moving in a stationary Coulomb field of the ion, since the mass of the electron is much smaller than that of the ion.

Synchrotron radiation When charged particles gyrate around the magnetic field, they will radiate. In the non-relativistic regime, such radiation is called cyclotron radiation. The frequency of this radiation is the gyrating frequency of the particle $\omega_{gyro} = qB/mc$ (cgs unit). Since the acceleration always points radially inward, the cyclotron radiation at a given time is a dipole radiation along the tangential direction, following Larmors formula. In the relativistic regime, such radiation is heavily beamed along the line of sight (see the illustration in Fig 1.8), and is called synchrotron radiation. The relativistic gyrofrequency becomes $\omega_r = qB/\gamma mc = (1/\gamma)\omega_{gyro}$, and the acceleration becomes $a_\perp = \omega_r v_\perp$ and $a_\parallel = 0$. Applying equation 1.13, the total emitted power of synchrotron radiation by a particle is

$$P_{syn} = \frac{2}{3} r_0^2 c \beta_\perp^2 \gamma^2 B^2, \tag{1.27}$$

where $r_0 = e^2/(m_e c^2)$ is the classical electron radius, $\beta_\perp$ is the particle's gyrating speed perpendicular to the field line, and B is the magnetic field strength. Assuming an isotropic velocity (therefore pitch angle) distribution, the above total power becomes

$$P_{syn} = \frac{4}{3} \sigma_T c \beta^2 \gamma^2 U_B, \tag{1.28}$$

where $\sigma_T = 8\pi r_0^2/3$ is the Thomson cross section, and $U_B = B^2/8\pi$ is the magnetic energy density.

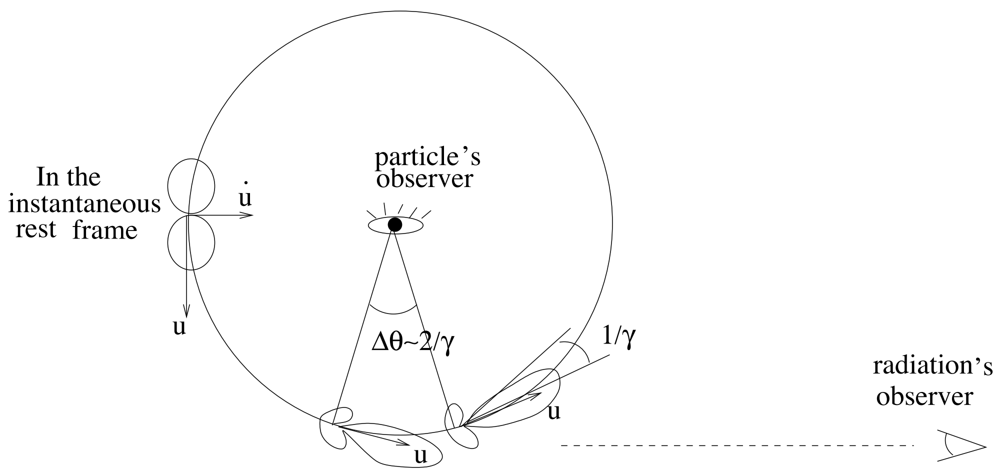

Figure 1.8.: A cartoon illustrating synchrotron radiation and beaming effect towards the observer. The magnetic field is perpendicular to the plane of the paper, and only the projection in the plane of the paper is shown. Image courtesy of J. Poutanen.

To study the spectrum of the synchrotron radiation for a single particle, we need to know the emitting frequency in addition to the total power. Taking into account the beaming effect, the critical frequency, around which most of the synchrotron radiation is emitted, can be worked out as

$$\omega_c = \frac{3q\gamma^2 B sin\alpha}{2mc}, \tag{1.29}$$

where α is the pitch angle. For electrons, the peak emitting energy can be estimated by $E_{syn} \approx 5 \times 10^{-9} B_{\perp}\gamma^2$eV, or in terms of frequency $\nu_{syn} \approx 3.7 \times 10^6 B_{\perp}\gamma^2$Hz.

Note that the above results are for a single particle. In reality, it is typically expected that the particle distribution follows a power law $dN/d\gamma \propto \gamma^{-p}, \gamma_{min} < \gamma < \gamma_{max}$, or a broken power law $dN/d\gamma \propto \gamma^{-p1}, \gamma_{min} < \gamma < \gamma_{br}$ and $dN/d\gamma \propto \gamma^{-p2}, \gamma_{br} < \gamma < \gamma_{max}$. For a power-law distributed electron population, the synchrotron radiation spectrum also follows a power law $f(\nu) \propto \nu^{-s}$ and the spectral index of the particle distribution and photon distribution satisfies

$$s = \frac{p-1}{2}. \tag{1.30}$$

Note that the spectral index s is different from the photon index Γ in $dN/dE \propto E^{-\Gamma}$. Since the specific flux density $f(\nu) \approx EdN/dE$, s and Γ are related by $s = \Gamma - 1$ for a power-law distribution. So the photon index for synchrotron radiation from particle distribution with index p should be $\Gamma = (p+1)/2$. The polarization fraction for such a particle population was calculated by Rybicki & Lightman (1979) to be $(p+1)/(p+7/3)$. For $p = 2$, the polarization fraction is $\sim$70%; for $p = 1$, it is 60%.

However, this power-law radiation does not extend to arbitrarily low energies, because of the self-absorption process. A synchrotron photon may interact with an electron and lose its energy to the electron. At lower energies ($E < E_{abs}$), the optical depth for this self-absorption process becomes large due to the increase number density of electrons. The source function can be calculated as $S_\nu \propto \nu^{-5/2}$, which is independent of the injection particle spectrum. Note that the index $-5/2$ is steeper than the Rayleigh-Jeans limit in blackbody radiation, because the effective temperature of the electrons is different as different energies.

An interesting timescale in an energy loss process is the radiative cooling timescale. For any given energy loss process with an energy-loss rate dE/dt (or power $P =$

$-dE/dt$), the cooling timescale for a particle at energy E is given by $t_{\rm cool} = -E/(dE/dt)$. Consider an electron with a Lorentz factor γ (therefore $E = \gamma m_e c^2$), the total power of the synchrotron radiation is given by equation 1.28. Thus the synchrotron radiation has a characteristic cooling time of

$$t_{syn} = \frac{E}{P_{syn}} = \frac{6\pi m_e c}{\sigma_T \gamma B^2} \approx 7.74 \times 10^8 \left(\frac{B}{1\mathrm{G}}\right)^{-2} \gamma^{-1} \mathrm{s}. \tag{1.31}$$

The above equation shows that the higher energy electrons cool faster through synchrotron radiation. The cooling time through synchrotron loss decreases linearly with the particle Lorentz factor γ. This fact has important implications on how the electron population evolves.

The relations between (i) cooling timescale, (ii) the acceleration timescale as discussed in the previous section 1.1.1, and (iii) the dynamical timescale, characterize a few interesting quantities in a system.

The first quantity is the maximum Lorentz factor $\gamma_{\rm max}$ that a particle can be accelerated to. (i) As discussed previously in the Hillas formula 1.2, the gyroradius of the particle cannot exceed the size of the source, therefore the magnetic field and size of the source put an upper limit on $\gamma_{\rm max}$. (ii) For a given acceleration and cooling process, by equating the cooling time t_{syn} with the acceleration timescale t_{acc}, the $\gamma_{\rm max}$ of the particle limited by the cooling mechanism can be found. For example, considering synchrotron cooling and non-relativistic first-order Fermi acceleration with the assumption that the mean free path λ of the particle is equal to its gyroradius $r_{gyro} = \gamma mc^2/(eB)$, the maximum comoving Lorentz factor is given by Rieger et al. (2007) as:

$$\gamma_{\rm max\_Fermi\_I} \approx 9 \times 10^9 \left(\frac{B}{1\mathrm{G}}\right)^{-1/2} \left(\frac{m}{m_p}\right) \left(\frac{\beta_s}{0.1}\right),$$

where B is the strength of magnetic field, m is the mass of the particle, and $\beta_s c$ is the velocity of the shock. Similarly, the maximum energy considering synchrotron cooling and second-order Fermi acceleration is:

$$\gamma_{\rm max\_Fermi\_II} \approx 2 \times 10^8 \left(\frac{B}{1\mathrm{G}}\right)^{-1/2} \left(\frac{m}{m_p}\right) \left(\frac{v_A}{0.001c}\right),$$

where v_A is the Alfén velocity.

By comparing the cooling time t_{syn} with the dynamical timescale $t_{dyn} = R/c$, where R is the size of the emitting region, the electrons can be divided into (i) the so-called fast-cooling regime, where $t_{syn} < t_{dyn}$ and the majority of the electrons can cool through synchrotron radiation on the dynamic timescale; and (ii) the slow-cooling regime, where $t_{syn} > t_{dyn}$ and only the electrons with highest energy can cool on the timescales of t_{dyn} (Sari & Esin, 2001). The critical energy can be found when $t_{syn} \approx t_{dyn}$:

$$\gamma_c = \frac{6\pi m_e c^2}{\sigma_T R B^2}. \tag{1.32}$$

In the slow cooling regime, $\gamma_{min} < \gamma_c < \gamma_{max}$, where γ_{min} and γ_{max} are the minimum and maximum energy of the injected power-law electrons $dN/d\gamma \propto \gamma^{-p}$, a cooling break will occur in the particle spectrum at γ_c, leading to a steeper spectrum $dN/d\gamma \propto \gamma^{-(p+1)}$ between γ_c and γ_{max}. Applying equation 1.30, the resulting radiation spectrum will become:

$$\frac{dN}{dE} \propto \begin{cases} E^{-(p-1)/2}, & E_{min} < E < E_{br} \\ E^{-p/2}, & E_{br} < E < E_{max}; \end{cases}$$

where the photon spectral break energy E_{br} is determined by the break Lorentz factor γ_c of the particles distribution. The break in photon spectrum occurs smoothly around E_{br} because electrons with a given γ emit over a range of energies. The difference in index below and above E_{br} is 0.5. Note that if the minimum energy E_{min} (corresponding to γ_{min}) is higher than the characteristic self-absorption energy E_{abs} in slow-cooling regime: (i) the peak of the radiation spectrum will be at E_{min}, (ii) a break on the rising edge of the spectrum occurs at E_{abs}, (iii) a cooling break occurs at E_{br} as in equation 1.1.3, and (iv) a spectral cutoff at E_{max} corresponding to γ_{max}.

In the fast cooling regime, most of the electrons are able to cool and lose energy. Therefore, a cooled electron population below the minimum injection energy γ_{min} is formed, and we have $\gamma_c < \gamma_{min} < \gamma_{max}$. Since there is no injection at $\gamma < \gamma_{min}$, solving the continuity equation 1.1 yields the electron spectrum between γ_c and γ_{min}

to be $dN/d\gamma \propto \gamma^{-2}$; and between γ_{min} and γ_{max} to be $dN/d\gamma \propto \gamma^{-(p+1)}$. Similar to the slow cooling regime, the radiation spectrum in the fast cooling regime is given by

$$\frac{dN}{dE} \propto \begin{cases} E^{-1/2}, & E_{br} < E < E_{min} \\ E^{-p/2}, & E_{min} < E < E_{max}. \end{cases}$$

Note that now $E_{br} < E_{min}$, and the radiation spectral index between E_{br} and E_{min} is constant at 0.5, while the spectrum above E_{min} is similar to that above E_{br} in the slow cooling regime.

Besides electrons, protons can produce synchrotron emission. As Böttcher et al. (2013) pointed out, if protons dominate the observed radiation, plug in the typical value for the highest proton energy 10^{19}eV and emitting region size 10^{15}cm into Hillas formula 1.2, the magnetic field is found to be $\gtrsim$ 30G. Proton synchrotron radiation may easily be the dominating energy loss channel in such a strong magnetic field. However, due to the large mass of protons $m_p \approx 1836 m_e$, the consequent small gyrofrequency and long cooling time often requires extreme Doppler factor and/or magnetic field to achieve fast variability in radiation. For example, Mücke & Protheroe (2001) demonstrated that for proton synchrotron model to produce a flare on the timescale of 12 hours, a Doppler factor $\delta = 10$ and a magnetic field $B = 20$G, or $\delta = 50$ and $B = 5$G, are needed; similarly for a flare on the timescale of 3 hours, $\delta = 10$ and $B = 50$G are needed. The proton synchrotron radiation has a characteristic cooling time of

$$t_{p\_syn} = \frac{6\pi m_p^3 c}{\sigma_T m_e^2 \gamma_p B^2} = \left(\frac{m_p}{m_e}\right)^3 \left(\frac{\gamma_p}{\gamma_e}\right)^{-1} t_{e\_sync} \approx 4.79 \times 10^{18} \left(\frac{B}{1\mathrm{G}}\right)^{-2} \gamma_p^{-1}\mathrm{s}, \quad (1.33)$$

where γ_p is the Lorentz factor of the proton. Assuming energy equilibrium between protons and electrons $\gamma_p m_p c^2 = \gamma_e m_e c^2$, we found protons generally have much smaller Lorentz factor comparing to electrons $\gamma_p = (m_e/m_p)\gamma_e$. Plug this relation back to equation 1.33, we have $t_{p\_syn} \approx (m_p/m_e)^4 t_{e\_syn} \approx 1.14 \times 10^{13} t_{e\_syn}$, which quantifies the extremely long synchrotron cooling time for a proton with respect to an electron of the same energy in the same magnetic field.

Inverse-Compton scattering (see below) also affects the observed synchrotron radiation spectrum, since (i) a fraction of the synchrotron photons become the seed photons for the IC process, and therefore are not observed in the synchrotron peak, and (ii) electrons lose energy through IC process, therefore less energy is available for synchrotron radiation. A more detailed description of synchrotron self-Compton (SSC) is given in the context of blazars in chapter 3.

Inverse-Compton radiation When a relativistic electron collides with a photon, it can transfer energy to the photon. This process is called inverse-Compton (IC) scattering. It is an important process to produce high energy photons.

First consider a photon with a low energy $\epsilon \ll m_e c^2$ approaches an electron at rest. The electron will oscillate at the same frequency of the incident photon, and produce dipole radiation. The photon is effectively scattered elastically with no change in energy. This process is called Thomson scattering, for which the Thomson differential cross section is

$$\frac{d\sigma}{d\Omega} = \frac{1 + \cos^2\theta}{2} r_0^2,$$

and the integrated cross section is $\sigma_T = 8\pi r_0^2/3$ with $r_0 = e^2/(m_e c^2)$.

Now consider a photon with an energy ϵ approaches a relativistic electron with an energy $\gamma m_e c^2$. In the rest frame of the electron, the above Thomson scattering results can still be applied when $\epsilon\gamma \ll m_e c^2$, noting that the energy of the photon in the electron's frame becomes ϵ/δ, where the Doppler factor $\delta = 1/\gamma(1 - \beta cos\theta)$.

However, when the incident photon has a high energy in the electron's frame $\epsilon\gamma \gtrsim m_e c^2$, quantum effect needs to be considered and the differential scattering cross section is described by the Klein-Nishina (KN) formula

$$\frac{d\sigma}{d\Omega} = \frac{r_0^2}{2} \frac{1 + \cos^2\theta}{[1 + \gamma(1 - \cos\theta)]^2} \left[1 + \frac{\gamma^2(1 - \cos\theta)^2}{(1 + \cos^2\theta)[1 + \gamma(1 - \cos\theta)]}\right]. \tag{1.34}$$

The total cross section is obtained by integrating the above differential cross section:

$$\sigma_{KN} = \frac{\pi r_0^2}{\epsilon} \left(\left[1 - \frac{2(\epsilon + 1)}{\epsilon^2}\right] \ln(2\epsilon + 1) + \frac{1}{2} + \frac{4}{\epsilon} - \frac{1}{2(2\epsilon + 1)^2} \right).$$

The Klein-Nishina formula gives a much smaller cross section than the σ_T, meaning that the inverse-Compton process is very inefficient, when the photon energy is high.

Note that when $\epsilon\gamma$ is small, the KN cross section is well approximated by the Thomson cross section.

Importantly, an inverse-Compton scattering between a low energy photon and a relativistic electron boosts the photon energy by a factor of γ^2, as long as it is still in the Thomson regime $\gamma\epsilon \ll m_e c^2$.

To get the power of inverse-Compton scattering, consider an electron with a Lorentz factor γ and a seed photon population with an isotropic energy distribution $dN/d\epsilon$. The power of inverse Compton radiation from this electron is

$$P_{IC} = \frac{4}{3}\sigma_T c \beta^2 \gamma^2 U_{ph}, \tag{1.35}$$

where $U_{ph} = \int \epsilon dN/d\epsilon d\epsilon$ is the energy density of the seed photon field. It should be kept in mind that the inverse-Compton process provides another energy loss channel for the electrons. The IC cooling time for a electron can be worked out similarly as before:

$$t_{IC} = \frac{\gamma m_e c^2}{P_{IC}} \approx \frac{3 m_e c}{4\sigma_T \gamma U_{ph}}. \tag{1.36}$$

Comparing the results from equation 1.35 and equation 1.28, we have the relation between the emitting power by a electron through synchrotron and inverse-Compton process:

$$\frac{P_{IC}}{P_{syn}} = \frac{U_{ph}}{U_B}. \tag{1.37}$$

The equation above indicates that when the magnetic energy density dominates over the energy density of the radiation field, synchrotron dominates over inverse-Compton, and vice versa. A similar parameter called “Compton dominance” are defined as the ratio of peak luminosities for blazar population studies. Note that an additional correction that makes P_{IC} smaller needs to be applied when the scattering is in the Klein-Nishina regime.

If a population of electrons follow a power law distribution $dN/d\gamma \propto \gamma^{-p}$, inverse-Compton radiation also follows a power law distribution $f(\nu) = \nu^{-s}$ with a spectral index of $s = (p-1)/2$. Note that this result is the same as the synchrotron radiation as shown in equation 1.30.

Pion decays from hadronic processes Pions are direct products of hadronic processes, e.g. photomeson production ($p\gamma$) or proton-proton collisions (pp). pp collision has been proposed as a potential gamma ray production mechanism in blast waves in GRBs and AGN (e.g. Pohl & Schlickeiser, 2000), starburst galaxies (Lacki et al., 2011), and star-jet interactions in AGN (e.g. Barkov et al., 2010). It often requires a high density of target cloud material, since the cooling time of pp collision is

$$t_{pp} \approx 10^{15} \left(\frac{n_c}{\mathrm{cm}^{-3}}\right)^{-1} \mathrm{s},$$

where n_c is the density of the target proton cloud. In situations like jet-star interaction, the material provided by the star can lead to an extremely dense target proton field $n_c \sim 10^{10}\mathrm{cm}^{-3}$, and the relatively short cooling time $t_{pp} \sim 10^5$s makes pp collision dominate over proton synchrotron and $p\gamma$ process.

On the other hand, $p\gamma$ process usually dominates over pp collisions in most of the blazar hadronic models. Similar to the interaction between UHECRs and CMB photons that leads to the GZK cutoff mentioned in previous sections 1.8, $p\gamma$ processes produce neutral and charged pions through:

$$p + \gamma \rightarrow \Delta^+ \rightarrow p + \pi^0, \text{fraction } 2/3; \tag{1.38}$$

$$p + \gamma \rightarrow \Delta^+ \rightarrow n + \pi^+, \text{fraction } 1/3. \tag{1.39}$$

Note that protons can become neutrons in $p\gamma$ interactions, making it possible to form neutron beams that can carry kinetic energy to large distances from the site of acceleration. The threshold of the Lorentz factor γ_p of a proton to interact with a photon of energy ϵ_{ph} through $p\gamma$ interaction is

$$\gamma_{p\_thresh} = \frac{m_\pi c^2}{2\epsilon_{ph}} \left(1 + \frac{m_\pi}{2m_p}\right), \tag{1.40}$$

where m_π is the mass of a pion $\approx 134.98\mathrm{MeV}/c^2$ for π^0 and $\approx 139.57\mathrm{MeV}/c^2$ for $\pi^\pm$. Following Aharonian (2000), the cooling time for $p\gamma$ process, assuming a broad-band photon field with a flat spectrum, can be written as

$$t_{p\gamma} \approx \left[c\langle\sigma_{p\gamma} f\rangle n(\epsilon^*)\epsilon^*\right]^{-1},$$

where $\langle\sigma_{p\gamma}f\rangle \approx 10^{-28}\text{cm}^2$ is the cross section of $p\gamma$ process weighted by inelasticity, $\epsilon^* = 0.03E_{19}^{-1}\text{eV}$ and $n(\epsilon^*)$ are the energy and the number density of the target photon, respectively. The cooling time $t_{p\gamma}$ depends on the low-energy target photon distribution, thus is related to the photon-photon optical depth $\tau_{\gamma\gamma}$ (see equation 1.47 and 3.12). For a power-law distribution of target photon field with a spectral index of $\alpha = 1$, the $p\gamma$ cooling time $t_{p\gamma} \approx 10^6\Delta t_{3h}\tau_{1TeV}^{-1}E_{19}^{-1}\text{s}$. As the spectrum of the target photon field becomes harder, $t_{p\gamma}$ becomes longer.

Note that neutrons can also interact with photons through photohadronic interactions:

$$n + \gamma \rightarrow \pi \rightarrow \gamma + \nu + e.$$

A π^0 consists of $u\overline{u}$ or $d\overline{d}$, and will almost immediately decay into gamma-ray photons, with a lifetime of $\sim 8 \times 10^{-17}s$:

$$\pi^0 \rightarrow 2\gamma. \tag{1.41}$$

A π^+ consists of $u\overline{d}$ and a π^- of $\overline{u}d$, and will decay into a muon and a muon-neutrino, with a lifetime of $\sim 3 \times 10^{-8}s$:

$$\pi^+ \;\rightarrow\; \mu^+ + \nu_\mu, \tag{1.42}$$

$$\pi^- \;\rightarrow\; \mu^- + \nu_\mu. \tag{1.43}$$

A muon also decays into an electron and two neutrinos, however, with a life time of $\sim 2.2\mu s$:

$$\mu^+ \rightarrow e^+ + \overline{\nu}_e + \nu_\mu,$$

$$\mu^- \rightarrow e^- + \nu_e + \overline{\nu}_\mu.$$

The life time of a muon is considered to be very long. This is the reason that they penetrate the atmosphere, and even reach as deep as many kilometers under the ground, causing background for neutrino detectors like ICECUBE. Muons are charged and may also produce synchrotron radiation. However, its cooling timesacle is usually much longer than its decay time, therefore many models make the assumption that all muons decay to electrons immediately. This assumption breaks down when the magnetic field is very strong $B \gtrsim 6\times10^{10}$G (Böttcher et al., 2013). Similar arguments applies to charged pions. When $B \gtrsim 8 \times 10^{12}$G, synchrotron emission from charged pions becomes fast enough and needs to be considered.

1.1.4 Gamma-ray absorption processes

In the previous section, I briefly introduced some important radiative mechanisms through which gamma rays can be produced. However, gamma rays can also be absorbed both at the emitting region and on their path of propagation to the Earth. The absorption processes for gamma rays at the source are mainly photon-photon pair production and Bethe-Heitler pair production; while on the path of propagation the most important process is the photon-photon pair production with extragalactic background light (EBL).

Photon-photon ($\gamma\gamma$) pair production as an absorption channel As illustrated in Fig 1.9, when a high energy (ϵ_h) photon and and low energy (ϵ_l) photon collide at an angle θ (in lab frame), if the energies exceed the threshold of the sum of the rest mass energy of two electrons (m_ec^2 in their center of mass frame) $\epsilon_h\epsilon_l \gtrsim 2m_e^2c^4/(1-cos\theta)$, $e^\pm$ pair production may occur (Gould & Schréder, 1966). The cross section for this pair production process is given by Jauch & Rohrlich (1955) as

$$\sigma_{\gamma\gamma}(\epsilon_h,\epsilon_l,\theta) = \frac{3\sigma_T}{16}(1-\beta^2)\left[(3-\beta^4)\ln\frac{1+\beta}{1-\beta} - 2\beta(2-\beta^2)\right], \tag{1.44}$$

$$\beta(\epsilon_h,\epsilon_l,\theta) = \sqrt{1-\frac{\epsilon_{l\_thresh}}{\epsilon_l}}, \tag{1.45}$$

$$\epsilon_{l\_thresh}(\epsilon_h,\theta) = \frac{2m_e^2c^4}{\epsilon_h(1-cos\theta)}, \tag{1.46}$$

where σ_T is the Thomson cross section. Note that for a head-on collision $\theta = \pi$, the energy threshold is minimized to $\epsilon_h\epsilon_{l\_thresh} \approx m_ec^2 \approx (511\text{keV})^2$, and for an isotropic low energy photon field $\epsilon_h \epsilon_{l\_thresh} \approx 2m_e c^2 \approx (723\text{keV})^2$. The cross section is maximized to $\sigma_{\gamma\gamma} \sim 0.256\sigma_T$ when $\beta \approx 0.7$, corresponding to $\epsilon_l \approx 1.96\epsilon_{l\_thresh}$.

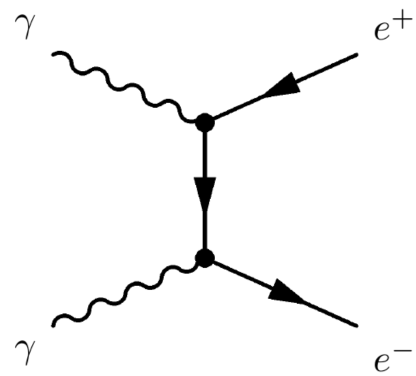

Figure 1.9.: An illustration of photon-photon pair production process. An e$^{\pm}$ pair is produced.

Dondi & Ghisellini (1995) used the approximation of $\sigma_{\gamma\gamma} \sim \sigma_T/5$, and derived the optical depth for photons at energy ϵ_h' in the frame of emitting region (labeled with prime) as follows:

$$\tau_{\gamma\gamma}(\epsilon_h') = \frac{\sigma_T}{5} n'(\epsilon_l') \frac{\epsilon_l'}{m_e c^2} R' = \frac{\sigma_T}{5} \frac{L'(\epsilon_l')}{4\pi m_e c^3 R'}, \tag{1.47}$$

where $n'(\epsilon_l')$ is the comoving density of lower energy photons, R' is the comoving radius of the spherical emitting region, and $L'(\epsilon_l')$ is the comoving luminosity at energy ϵ_l'. From equation 1.47 an important parameter "injection compactness" L'/R' arises: the effective absorption on VHE gamma rays from photon-photon pair production becomes increasingly important at larger L'/R'. Sometimes a dimensionless parameter called "compactness parameter" is defined as $l' = L'\sigma_T/(R' m_e c^3)$, and the optical depth in equation 1.47 becomes $\tau_{\gamma\gamma}(\epsilon_h') \approx l'(\epsilon_l')/20\pi$. Considering the relativistic Doppler effect following the discussion in previous sections, the luminosity in the observer's frame is $L(\epsilon_l) = \delta^3 L'(\epsilon_l')$, and the radius can be constrained by the fastest observed variability timescale Δt by $R' = c\Delta t\delta/(1+z)$. This implies that with knowledge of the lower energy photon field at the emitting region, the Doppler factor

δ can be constrained by the shortest variability timescale from the observations. A detailed discussion of this implication in the context of observations of TeV blazars is included in chapter 3.

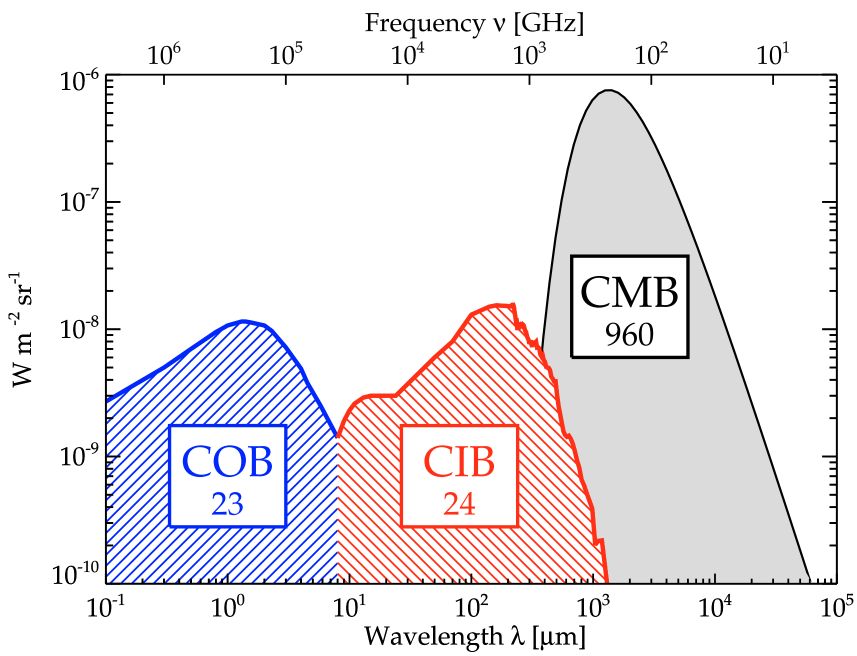

Figure 1.10.: Spectral energy distribution of the EBL and the CMB radiation field. The blue bump shows the cosmic optical background (COB) with an intensity of ∼23 nW m^{-2} sr^{-1}; the red bump shows the cosmic infrared background (CIB) with an intensity of ∼24 nW m^{-2} sr^{-1}; and the gray bump is the cosmic microwave background (CMB) with an intensity of ∼960 nW m^{-2} sr^{-1}. Plot taken from Dole et al. (2006).

After the gamma rays escape the emitting region, they travel through the EBL photon field before they reach the Earth. EBL is the diffuse radiation field over the history of star and galaxy formation, ranging from UV to far infrared wavelengths. The spectral energy distribution of EBL measured by *Spitzer* (Dole et al., 2006) is shown in Figure 1.10 together with the CMB radiation. The infrared bump that peaks at $\sim 150\mu$m is mainly contributed by the dust reemission of starlight, called the "cosmic infrared background" (CIB); and the optical bump that peaks at $\sim 1.3\mu$m is mainly the contribution from the starlight, called "cosmic optical background" (COB). Many other EBL models have been proposed (see e.g. Dwek & Krennrich, 2013, for a recent review), both based on observations and analytical approaches (e.g. Domínguez et al., 2011). Note that the EBL distribution is different at different redshift, depending on the evolution history of different contributing sources; and there may be an anisotropy in its distribution (Zemcov et al., 2014).

The EBL inevitably absorbs TeV gamma rays through pair production 1.47. The optical depth of EBL absorption of TeV photons depend on both energy of the photon ϵ_h and the redshift of the TeV source z, and can be formalized following Dwek & Krennrich (2013):

$$\tau(\epsilon_h, z) = \int_0^z \frac{dl}{dz'}dz' \int_{-1}^{+1} \frac{1-\mu}{2} d\mu \int_{\epsilon_{th}}^{\infty} n_{\epsilon_l}(\epsilon_l', z')\sigma_{\gamma\gamma}(\epsilon_h', \epsilon_l', \mu) d\epsilon_l', \tag{1.48}$$

where $n_{\epsilon_l}(\epsilon_l', z')$ is the comoving number density of EBL photons, and $\sigma_{\gamma\gamma}$ is given in equation (1.44). The characteristic wavelength that yields the maximum absorption of high energy photons, assuming an isotropic distributions of EBL photons, is $\lambda_l \approx 1.23(\epsilon_h/\mathrm{TeV})\mu$m following equation 1.44. The optical depth increases as z gets larger, therefore an energy-dependent effective "horizon" of TeV gamma rays (where $\tau \sim 1$) should be present (e.g. Fazio & Stecker, 1970). The existence of such a "horizon" would lead to a spectral break at gamma-ray energies, and no gamma rays should have an origin with a much higher redshift.

However, it is difficult, if not impossible, to distinguish intrinsic curvature of distant TeV sources and the imprints (gamma-ray spectral break) of EBL absorption. Nevertheless, the knowledge (or assumptions) of one can constrain the other. With a reasonable assumption on the limit of intrinsic spectral shape, blazar spectra at TeV energies can set an upper limit of the EBL density. On the other hand, the minimal amount of EBL density can be given by integrating light from all resolved galaxies (Madau & Pozzetti, 2000), leading to a minimum amount of EBL correction that needs to be applied to an observed blazar. The most distant TeV object detected by far is PKS 1424+240 at a redshift of $z \gtrsim 0.6$ (Furniss et al., 2013; Archambault et al., 2014). Even after applying only the minimum amount of EBL correction, the VHE spectrum shows an upturn at a few hundred GeV. Similar upturn features have also been observed in several other blazars (e.g. Aharonian et al., 2006b; MAGIC Collaboration et al., 2008), the energy of which is redshift-dependent. Such unexpected spectral hardening/upturn suggests that either the universe is more transparent to gamma rays than we previously thought (i.e. the EBL density is over-estimated or the gamma rays are produced at closer distances), or there are some mechanisms that produces such an upturn at the location of the source.

Several proposed exotic models put the location of the gamma ray production closer to the Earth, and ameliorate the absorption problem, e.g. through the coupling between TeV gamma-ray photons and axion-like particles in the intergalactic magnetic field (e.g. Sánchez-Conde et al., 2009; Meyer et al., 2013), or the line-of-sight interaction between ultrahigh energy cosmic rays and CMB/EBL photons (e.g. Essey et al., 2010, 2011; Aharonian et al., 2013; Zheng & Kang, 2013; Inoue et al., 2014). The CR line-of-sight interaction model requires a weak magnetic field ($B < 10^{-14}$G), has a more prominent effect for distant sources ($z > 0.15$) at high energies ($E > 1$TeV), and predicts a delay between higher- and lower-energy gamma rays that washes out any fast variability (e.g. Prosekin et al., 2012).

Alternatively, the spectral upturn may be produced at the location of the source. For example, proton synchrotron blazar model produces another spectral component above TeV energies (e.g. Mannheim, 1993; Aharonian, 2002; Dimitrakoudis et al., 2014), the rising edge of which may emerge at the tail of the observed TeV spectrum. But note that it is difficult for such models to produce fast variability. The upturn may also be explained by the pair-production between TeV gamma rays and narrow band low-energy local photons at the source, which is somewhat unrealistic (Aharonian et al., 2008b).

Another effect related to VHE gamma-ray propagation is the Lorentz invariance violation (LIV), which modifies the energy threshold of the soft photons that can pair-produce with TeV gamma rays (e.g. Kifune, 1999; Jacob & Piran, 2008). Such modification can lead to significantly less absorption of TeV gamma rays. The Lorentz symmetry breaking predicted by quantum gravity and effective field theory are only prominent at the Planck scale (e.g. Planck energy $E_P \approx 1.22 \times 10^{28}$eV). One effect of LIV is the proposed energy dependence of the speed of light, the measurement of which has been attempted (e.g. see Aharonian et al., 2008a, and references therein). The modification of the speed light at different energies can be expressed as

$$c(E) = c\left(1 + \xi\frac{E}{E_P} + \zeta\frac{E^2}{E_P^2}\right),$$

where ξ and ζ are parameters in the models. The time delay Δt between two energies ΔE after traveling a distance corresponding to redshift z satisfies

$$\frac{\Delta t}{\Delta E} \approx \frac{\xi}{E_P H_0}\int_0^z dz' \frac{(1+z')}{\sqrt{\Omega_m(1+z')^3 + \Omega_\Lambda}}, \tag{1.49}$$

$$\frac{\Delta t}{\Delta E^2} \approx \frac{3\zeta}{2E_P H_0}\int_0^z dz' \frac{(1+z')^2}{\sqrt{\Omega_m(1+z')^3 + \Omega_\Lambda}}, \tag{1.50}$$

where H_0 is the Hubble constant, Ω_m is the density of matter, and Ω_Λ is the cosmological constant. From the above equations we can see: (i) the difference in arrival time is very small because E_P is much higher than the currently measurable energies; (ii) the difference in arrival time increases with energy and distance, making VHE measurements of distant sources ideal for such studies. By measuring the spectral time-delay $\Delta t/\Delta E$ and $\Delta t/\Delta E^2$, one may constrain parameters ξ and ζ in the models.

As a direct consequence of the photon-photon pair production between VHE gamma rays and EBL photons, the resulting $e^{\pm}$ pairs can initiate an electromagnetic cascade in the presence of the intergalactic/extragalactic magnetic field (IGMF/EGMF). The cascade produces lower-energy GeV photons, with an energy-dependent spatially-broadened "halo" shape due to the deflection of the electrons in IGMF/EGMF in a similar fashion of the UHECR "halo" discussed previously. By studying the energy-dependent morphology of a distant blazar in the gamma-ray band, constraints on the strength of the IGMF/EGMF may be derived. For example, Taylor et al. (2011) derived an lower limit of the IGMF/EGMF of $B \gtrsim 10^{-15}$G or $B \gtrsim 10^{-17}$

from the non-detection of such cascade emission, depending on two different assumptions of the reason for suppression of the cascades. However, Broderick et al. (2012) argued that with the plausible assumption of plasma beam instability dominating over inverse-Compton scattering, previous lower limits on the strength of the magnetic field are no longer valid. Instead, a stringent upper limit of $B \lesssim 10^{-12}$G was given.

Bethe-Heitler pair production A photon in the field of a nucleus can undergo pair production $Z + \gamma \rightarrow Z + x^+ + x^-$, where Z stands for a charged nucleus and $x^\pm$ stands for the pair, e.g. a muon or electron pair. A common example of such process is the Bethe-Heitler (BH) pair production $p + \gamma \rightarrow p + e^+e^-$. The energy threshold of BH process in the center of mass frame satisfies $m_p^2c^4 + 2\epsilon_p\epsilon_\gamma(1 - \beta_p cos\theta) \gtrsim (m_pc^2 + 2m_ec^2)^2 \approx 0.88\text{GeV}^2$, where β_p and ϵ_p are the speed and energy of the proton, ϵ_γ is the energy of the photon, and θ is the angle between the two. Note that the energy threshold for BH process is lower than $p\gamma$ interaction, and BH pair production can be the dominant process that serves as (i) a proton energy loss channel, (ii) an electron injection channel, and (iii) a gamma-ray absorption process at the source (Mastichiadis et al., 2005). At above the energy threshold for photomeson interaction in equation 1.40, BH process can often be neglected.

A similar process, magnetic pair production $\gamma + B \rightarrow e^+ + e^-$, becomes non-negligible when the magnetic field becomes extremely strong $B > 10^9$G (see Daugherty & Harding, 1983, and references therein).

1.2 TeV gamma-ray emission sites

As mentioned in previous sections, only a handful of proposed candidate sources can manufacture UHECRs. VHE gamma-rays sources are also quite rare, with the number of all known sources amounting to ∼150, from both within and out of the Milky Way Galaxy. In this section, I will briefly describe the detected and candidate types of VHE sources.

1.2.1 Galactic sources

Supernova remnants A substantial amount of the stellar materials are ejected into the interstellar medium during the violent supernova explosion when (i) the accreted mass onto a white dwarf in a binary system exceed a limit (type Ia), or (ii) a massive star collapses as the nuclear fusion ceases at its center (type Ib, Ic, and II). The ejecta from the explosion blast through the ISM at supersonic speed and form shock structures, which can accelerate particles efficiently through e.g. first-order Fermi acceleration mechanism. These particles may then radiate through e.g. synchrotron, IC, or hadronic processes, observed as a shell-like supernova remnant (SNR) with filament structures tracing the shock fronts. A compact source may be left at the center depending on the progenitor type.

After the initial supernova explosion, the SNR may experience different phases of expansion, going from the freely expanding blast wave phase with constant velocity lasting for $\sim$100 yrs, to the adiabatically expanding Sedov-Taylor explosion phase with constant energy lasting for $\sim 10^4$ yrs, then to a radiative cooling snowplow phase with constant momentum until $\sim 10^5$yrs, finally reaching a stop of expansion and starting to merge with the ISM (Rosswog & Brüggen, 2007). The expansion velocity and magnetic field strength in each phase is different. Therefore different age-dependent radius and shock velocity needs to be taken into account when estimating the highest energy that SNRs can accelerate particles to using the Hillas formula 1.2. Plug in conservative values $B \approx 10\mu$G and $R_{\rm size} \approx 20$pc, we get a very rough estimation of $E_{\rm max} \approx 2Z \times 10^{17}$eV. More detailed model-dependent calculations of the maximum energy has been carried out many times, the results of which scatter across a range of values. For example, a limit of $Z \times 10^{15}$eV is given by Berezhko (1996), while a higher limit of $Z \times 10^{17}$eV is given by Bell & Lucek (2001) taken into account of the non-linear magnetic field amplification, and a even higher speculation of $Z \times 10^{19}$eV was given by Voelk & Biermann (1988) assuming a strongly inhomogeneous medium.

It is generally believed that the galactic SNRs are at least responsible for most of the high-energy cosmic rays below the "knee" in the CR spectrum, and probably extending up to the "ankle" (Blandford et al., 2014). To account for the flux density observed in this energy range, a rough estimation of the efficiency of the accelerating mechanism can be made, with reasonable assumptions of the escape timescale and the rate of supernova explosions in the galaxy. Assuming a 5% efficiency of first-order Fermi acceleration, the power required to maintain the observed flux is $P_{\text{GCR}} \approx \rho V_{\text{gal}}/t_{\text{esc}} \approx 10^{41}$erg/s, which is estimated from the energy density of the CR particles ~ 1 eV cm^{-3}, the volume of the galaxy $V \approx 4\pi R_{\text{disk}}^2 h_{\text{disk}} \approx 2 \times 10^{67}$cm^3, and the escape time of $\sim 10^7$ yrs. Considering an average energy of 10^{51}ergs^{-1} per supernova explosion, and an average rate of supernova explosion $\sim$2 per century in our galaxy, the efficiency of acceleration mechanism is estimated to be $\sim$10%.

SNRs form an important branch of TeV sources. They provide good environments for testing hadronic emission models. A few examples of the VERITAS detected SNRs are: Tycho (Acciari et al., 2011a), Cassiopeia A (Acciari et al., 2010a), and IC 443 (Acciari et al., 2009c).

Pulsars and pulsar wind nebulae Pulsars are rapidly spinning neutron stars with strong magnetic field, formed from a core-collapse supernova explosion (type Ib, Ic, II). Note that type Ia supernova explosions do not leave behind a pulsar. The rapid spin of the pulsar, the period P of which ranges from $\sim$1 ms to $\sim$10 s, is the consequence of the angular momentum conservation in the collapse of the stellar core. Although their spin period provides an extremely precise clock, they are found to slowly spin down on a long timescale at a rate $\dot{P} = dP/dt$ between $\sim 10^{-19}$ s s^{-1} and $\sim 10^{-15}$ s s^{-1}. The spin-down luminosity of a pulsar is $\dot{E} = -dE/dt = 4\pi^2 I\dot{P}/P$, where I is the moment of inertia of the pulsar. The observed spin-down luminosity ranges from the highest $\sim 5 \times 10^{38}$ ergs s^{-1} of the Crab pulsar to the lowest $\sim 3 \times 10^{28}$ ergs s^{-1} of PSR J2144-3933, with a typical value of $> 4 \times 10^{36}$ ergs s^{-1} (Gaensler & Slane, 2006, and references therein). Another consequence of the core collapse is that the magnetic field strength is amplified, reaching e.g. $\gtrsim 10^{12}$G for the Crab pulsar.

The only two pulsars with pulsed emission detected at TeV energies are the Crab pulsar and the Vela pulsar. The Crab pulsar was detected with MAGIC (Albert et al., 2008b) at ~25 GeV and with VERITAS at >120 GeV (VERITAS Collaboration et al., 2011). Recent MAGIC results presented at the 2014 Fermi Symposium show evidence of a power-law spectrum of the Crab Pulsar extending up to ~2 TeV without a cutoff. The High Energy Stereoscopic System (H.E.S.S.) II collaboration announced the detection of the Vela pulsar in July 2014 at >30 GeV with an 89 ms period. Another candidate TeV pulsar is the Geminga pulsar, which has been extensively observed without a detection so far (Aliu et al., 2015).

The detection of pulsed emission from a pulsar at TeV energies gives important insights into the radiative mechanism. The case of Crab pulsar is particularly interesting, since the lack of a spectral cutoff may indicate an inverse-Compton origin (in deep Klein-Nishina regime) instead of the commonly assumed curvature radiation that predict a break in the gamma-ray spectrum at $E_{\rm br} = 150{\rm GeV}\eta^{3/4}\xi^{1/2}$, where η is the efficiency and ξ is the curvature radius of the field lines (e.g. Lyutikov et al., 2012).

Pulsars accelerate particles through a unipolar conductor mechanism. As proposed by Goldreich & Julian (1969), an extremely strong induced electric field $E \sim 6 \times 10^{12} P^{-1}$ V m^{-1} caused by the rotation of the large-scale dipole magnetic field may strip off the material at the surface of the pulsar, since the Lorentz force is much stronger than the gravitational force, e.g. by a factor of $\sim 10^{12}$ for the Crab pulsar. These relativistic particles can propagate away from the pulsar in the form of "pulsar wind", and radiate through curvature radiation and/or inverse-Compton scattering. A pulsar is initially embedded in the SNR that resulted from the same explosion that gave birth to the pulsar itself. A termination shock, the so-called "pulsar wind nebula" (PWN) or "plerion", is naturally formed as the pulsar wind sweeps through the SNR. Note that a PWN may be embedded in a SNR, but usually on a much smaller scale. In some cases, a PWN may still be present after the SNR has already merged with the ISM and no longer visible.

Pulsars and PWNe are important sources of galactic CRs, especially $e^{\pm}$ pairs, see A. Weinstein for the VERITAS Collaboration (2014) for a recent review. Since the detection of the first TeV source, the Crab Nebula (Weekes et al., 1989), an increasing number of PWNe are detected in TeV band, e.g. CTA 1 (Aliu et al., 2013), G106.3+2.7 (Acciari et al., 2009a).

X-ray binaries X-ray binaries (XRB) are systems with a compact object (white dwarf, neutron star, or stellar-mass black hole) and a companion star orbiting each other. The matter falling from the companion star onto the compact object forms an accretion disk, in which gravitational energy is efficiently converted into heat in the plasma, leading to luminous disk thermal radiation in X-ray. A XRB containing a stellar-mass black hole is called a black hole binary (BHB). BHBs are believed to be similar to AGN, as they are both powered by the accretion of material onto a black hole. For example, a particular type of BHBs exhibits a superluminal jet feature that is analogous to radio-loud quasars, and therefore named as "microquasars". For example, the observations of GRS 1915+105 not only confirmed the existence of a black hole in the binary system, but also revealed the similarity between the accretion processes in stellar mass black holes and SMBHs.

BHBs are known to have different states. In "soft" (or "thermal") state the accretion disk is believed to be geometrically-thin and optically-thick, and emit a black-body spectrum; while in "hard" state, it is believed that a radio jet is switched on, leading to non-thermal radiation via e.g. the synchrotron process. In soft state, the accretion disk often gives rise to a red-noise type of variability, with a characteristic timescale that scales with the black hole mass and the accretion rate (e.g. Cui et al., 1997). The scaling relations among BHBs and AGNs have been extensively studied in the X-ray band (see e.g. McHardy, 2010, for a review). Since BHBs have much lower mass and consequently much shorter timescales, they are relatively easier to study. The understanding of BHBs may provide detailed insights into the accretion process around a black hole, and may be used to better understand the AGN.

There are already four binary systems detected at TeV energies, LS I +61 303 (Acciari et al., 2009b), HESS J0632+057 (Aliu et al., 2014b), PSR B1259-63/LS 2883 (H.E.S.S. Collaboration et al., 2013), and LS 5039 (Aharonian et al., 2006a). Most of these binaries are only detected at TeV energies during certain near-periastron orbital phases, possibly due to the enhanced accretion when the distance between the two companions are so close that the compact object is immersed in the wind of the star. The particles may be accelerated through diffusive shock acceleration, or possibly *pp* collision due to the dense target proton field provided by the stellar wind (see e.g. Cui, 2009, and references therein). TeV photons may then be produced via inverse-Compton scattering or neutral pion decay.

Besides the sources mentioned above, there are more complex regions that may contain multiple point-like and/or extended sources. For example, the Cygnus region, a nearby region with active star formation, is extensively observed by both ground-based gamma-ray telescopes (e.g. Weinstein, 2009; Aliu et al., 2014c), as well as by shower particle detectors (e.g. Amenomori et al., 2006). Multi-wavelength and multi-messenger observations of such regions allows potential identification of galactic CR sources and production mechanism.

Galactic Center The Galactic Center (GC) is a one-of-a-kind object that harbors the most nearby SMBH, showing up as a radio source Sgr A*. It is so close to us that precise measurements of the stellar orbits through long-term monitoring in the near-IR band can constrain its mass within 10% (e.g. Gillessen et al., 2009). A gamma-ray source is detected in spatial coincidence with the GC at energies up to 30 TeV by HESS (Aharonian et al., 2009d), although the angular resolution at such energies does not rule out other possibilities than the SMBH Sgr A*.

A pair of bubble-like structures along directions perpendicular to the disk plane extending to 55° away from the GC was detected by *Fermi*-LAT, known as “Fermi bubbles" (Ackermann et al., 2014). The gamma-ray production mechanisms in Fermi bubbles can be either IC from electrons, or synchrotron radiation produced by the secondary leptons and/or neutral pion decay in the hadronic model. However, the large extension perpendicular to the disk without elongation along the disk plane, combined with a hard spectrum at below $\sim$1 GeV, is consistent with a dark matter annihilation scenario, rather than a hidden population of millisecond pulsars (Daylan et al., 2014).

1.2.2 Extragalactic sources

Extragalactic sources that have been established as VHE emitters are radio-loud AGN (including blazars and radio galaxies) and starburst galaxies. Potential candidates as TeV sources include gamma-ray bursts (GRBs), clusters of galaxies, and primordial black holes.

Radio-loud AGN An example of radio-loud AGN, 3C 273, was already given at the beginning of this chapter. In this section I briefly introduce the models of AGN. As the focus of this thesis, the detailed studies of AGN variability is presented in chapter 3.

As described in section 3.2 in chapter 3, a unified scheme of AGN is widely accepted (Urry & Padovani, 1995). We focus on radio-loud AGN, which consist of a central SMBH, an accretion disk, a jet, some ionized cloud with broad- or narrow-line emission depending on the distance to the center, and a distant dusty torus. Different subclasses of AGN arise as the manifestation of the viewing angle. For example, a subclass of radio-loud AGN, known as blazars, are characterized by highly variable non-thermal emission at almost all wavelengths. The lack of strong emission lines in their optical spectra, the double-peak non-thermal appearance of their broadband spectra, and the rapid variability suggest that blazar emission originates in relativistic jets closely aligned to our line of sight (e.g. Schlickeiser, 1996). These objects form the majority of the detected extragalactic TeV objects. However, several questions regarding gamma-ray emission from blazars remain open, for example, (i) the location of the emitting region (close to or far away from the black hole), (ii) the type of emitting particles (leptons or hadrons), (iii) the acceleration mechanisms that produces ultrarelativistic particles; and (iv) the radiative mechanisms through which the particles lose energy in the form of gamma-ray radiation.

The puzzles of AGN need to be addressed by the observations. As illustrated in Figure 1.3, the spectral energy distribution (SED) of a blazar invariably shows a double-humped feature, with a lower-energy peak located at up to X-ray energies and a higher-energy peak at up to TeV energies (e.g. Fossati et al., 1998). Although it is widely accepted that the lower-energy SED peak originates from the synchrotron radiation of relativistic electrons in the jet, the origin of the high energy emission is still under debate. Different emission models have been proposed that fall into two broad classes known as leptonic and hadronic models, both of which have been successful at explaining the average observed SEDs. In each model, a combination of the specific radiative processes and gamma-ray absorption processes should be considered carefully, and included into the source terms and energy loss terms in a set of kinetic equations 1.1. The basic elements of the acceleration and radiative mechanisms have been introduced in previous sections.

In leptonic models, the high-energy bump is explained by inverse-Compton scattering of photons with the same electron populations that produced the synchrotron radiation. The seed photons for inverse-Compton process can be (see e.g. Böttcher et al., 2013, and references therein):

1. the synchrotron photons, which is called synchrotron self-Compton (SSC); and/or
2. external photons (e.g. from accretion disks or dust tori), which is called external-Compton (EC).

Note that besides the simplest one-zone SSC model, multiple emitting zones or particle populations of SSC as well as EC can all exist in the same source, possibly with one of them dominating at different times.

Hadronic models propose that both electrons and protons are accelerated sufficiently in the jet, and the relativistic protons are responsible for the gamma-ray emission through the following scenarios:

1. π^0 decay: the lower energy tail of the SSC photons provide a target photon field for $p\gamma$ collision (as in 1.38), and the secondary π^0s decay into gamma ray photons between GeV and TeV energies (e.g. Sahu et al., 2013);

2. EM cascades initiated by absorption of VHE gamma-rays from photopion processes (e.g. Mannheim, 1993);

3. synchrotron radiation of secondary pairs from photopion processes (e.g. Dimitrakoudis et al., 2014);

4. proton synchrotron radiation (e.g. Aharonian, 2000);

5. proton-proton collision (e.g. Pohl & Schlickeiser, 2000).

All the models above can describe the stationary SED reasonably well.

The blazars are known to flare on a wide range of timescales, ranging from months down to minutes. There were five blazars exhibiting fast flares on sub-hour timescales at TeV energies: three high-frequency peaked BL Lac objects (HBLs) Mrk 421 (Gaidos et al., 1996), Mrk 501 (Albert et al., 2007b), PKS 2155-304 (Aharonian et al., 2007); a low-frequency peaked BL Lac object (LBL) BL Lacertae (Arlen et al., 2013); and a flat spectrum radio quasar (FSRQ) PKS 1222+216 (Aleksić et al., 2011). Such fast flares provide a unique probe to examine the jet and pose challenges to the theoretical understanding of gamma-ray production in blazars. Firstly, an upper limit of the comoving size of the emitting region R' can be estimated from the observed variability timescale Δt. According to causality, any variation from a source of size R' cannot be faster than the light crossing time, therefore

$$R' \lesssim c\Delta t\delta, \tag{1.51}$$

where δ is the Doppler factor of the emitting region defined in equation 1.26. Fast variability indicates compact emitting regions. For example, if $\Delta t = 10\mathrm{min}$, $R' \lesssim 2 \times 10^{11}\delta\mathrm{m}$, comparable to the Schwarzschild radius of a 10^8-10^9 solar mass black hole. Such compact regions are most likely associated with the vicinity of the black hole. However, TeV gamma-ray photons may interact with soft photons in the vicinity to produce electron-positron pairs, and thus be effectively absorbed. The optical depth of this absorption process depends on low energy photon field, as well as the comoving radius of the blob, as described in equation 1.47 in the previous section 1.1.4.

With the above two arguments, the fact that we detect a fast TeV flare from a blazar implies that (i) the size of the emitting region is small, and (ii) the pair production opacity of the jet must be sufficiently small. The second implication leads to two different scenarios: (i) if the lower energy photons are emitted in the same region as the gamma rays, the emitting region has a very large Doppler factor, or (ii) the gamma ray emitting region is further away from the black hole than the region that produces the low-energy photons. If we assume a single spherical emitting region that emits both the gamma-ray and low-energy radiation and is optically thin to photon-photon pair production, a *lower* limit on the Doppler factor can be given, usually significantly larger than the radio measurements. Models with either spatially or temporally separated emitting zones or particle populations are proposed to explain the discrepancy between TeV and radio Doppler factor measurements, e.g. structured jet (Ghisellini et al., 2005), jet deceleration (Stern & Poutanen, 2008), jets in a jet (Giannios et al., 2009).

Although some of these models do put the gamma-ray production region far away from the black hole, the same region, or the even further region that produces the slower radio emission, may also produce low-energy photons through e.g. synchrotron radiation. Moreover, it is also difficult to determine the location of the low energy emission from observations due to various reasons, e.g. low angular resolution of the instruments.

It is worth noting that hadronic models face another difficulty from fast flares due to the long cooling time of protons. However, recently Dermer et al. (2012) proposed that the 1/3 fraction of the secondary products of $p\gamma$ process are neutrons, which can escape in the form of a neutral beam together with gamma-ray photons and neutrinos. These neutrons and gamma-ray photons then interact with low-energy photons (e.g. IR photons from the dust torus) through photohadronic interactions and photon-photon pair production, respectively. The resulting electrons from these secondary processes can produce the observed VHE photons. Such radiation mechanism has a dramatic Doppler beaming factor of δ^5, in which a factor of δ^3 comes from the $p\gamma$ process, and a factor of δ^2 from the secondary photohadronic interactions or photon-photon pair productions. Therefore, with large Doppler factor $\delta \gtrsim 100$, the variability timescales of the observed fast flares may be accounted for.

Another interesting phenomena observed from blazars is that some of the TeV gamma-ray flares detected have no simultaneous X-ray counterparts (e.g. Krawczynski et al., 2004; Błażejowski et al., 2005), which presents a severe challenge to both the leptonic and hadronic models. Note that "orphan flares" are relatively rare among TeV blazars. A tight correlation between X-ray and TeV band during major flares of blazars are usually observed (e.g. Fossati et al., 2008; Aharonian et al., 2009b). However, the correlation between X-rays and VHE gamma-rays are found to be not as tight as predictions from one-zone SSC during low states of the same blazar (e.g. Błażejowski et al., 2005; Aharonian et al., 2009c), which again may indicate multiple zones with different emitting particle populations. Petropoulou (2014) found that a two-zone SSC model or proton synchrotron model are both consistent with the observed loose correlation at lower flux level, while a tight correlation emerges for two-zone SSC when one of the zone produces a significant flare via e.g. a sudden increase of the highest electron energy. Moreover, if such a correlation is present, the steepness of the correlation may be different on long (days) and short (hours) timescales (e.g. Fossati et al., 2008), and may depend on different emitting mechanisms (Mastichiadis et al., 2013). Some other models that are dedicated to explain "orphan flares" also invoke separate emitting regions, e.g. a hybrid hadronic synchrotron mirror model (Böttcher, 2005).

However, blazars are not the only AGN observed at VHE band. When the viewing angle with respect to the jet is large and the Doppler beaming effect is weak, an AGN shows up as a radio galaxy. There are two radio galaxies detected at TeV energies, Centaurus A (Aharonian et al., 2009a) and M87 (Acciari et al., 2008). The first observational evidence of an extragalactic jet was found in M87 (Curtis, 1918). More recently, blobs/knots in the jet were observed in multiple wavelengths, from the superluminal motions of which one can measure the viewing angles to be in the range of $\sim 20^\circ$ to $\sim 40^\circ$ (e.g. Biretta et al., 1999; Forman et al., 2007). Strong TeV flares from M87 on a timescale as short as 1 day was observed (e.g. Aharonian et al., 2006c; Albert et al., 2008a), such timescales are comparable to the dynamic timescale at the vicinity of the black hole. However, the TeV flare could also be related to superluminal knot HST-1, which put the emitting region downstream in the jet and far away from the black hole (e.g. Stawarz et al., 2006; Cheung et al., 2007).

Starburst galaxies The exceptionally intense star formation activities in starburst galaxies naturally lead to high supernova rates. The SNR associated with the supernova activities can accelerate particles and subsequently produce gamma-ray emission. Two starburst galaxies, M82 (VERITAS Collaboration et al., 2009) and NGC 253 (Acero et al., 2009), have been detected in TeV band so far. The main gamma-ray radiation channel in the starburst galaxies may be inelastic *pp* (or proton-hadron) collisions between the ultra-relativistic CR particles accelerated by the SNR and the dense ISM, although there may be other contributions e.g. from inverse-Compton and Bremsstrahlung from CR electrons and ions which will produce signatures at lower energy gamma-ray band (Lacki et al., 2011). With the assumption of inelastic *pp* collision being the main energy loss channel, constraints on the density of CR particles and the flux of neutrinos can be made (e.g. "proton calorimetry" Pohl, 1994). More gamma-ray observations of starburst galaxies, and other similar sources e.g. Ultra Luminous Infrared Galaxies (ULIRGs), are important for further distinguishing the particle population and the energy loss channel.

Gamma-ray bursts Gamma-ray bursts (GRBs) were discovered in the late 1960s (Klebesadel et al., 1973). They are the most luminous objects in the universe, releasing more than 10^{51}ergs of energy within a few seconds. Similar to AGN, despite that many models for GRBs have been proposed, their radiation mechanism remains an open question.

In the mainstream relativistic "fireball" model (see e.g. Piran, 1999, for a review), an ultra-relativistic "fireball" with Lorentz factor $\gtrsim 100$ (in a jet-like fashion similar to blazars) can create internal shocks that are responsible for the prompt emission through synchrotron mechanism, and external shocks between the outflowing material and the surrounding material that are responsible for the afterglow. Although alternative explanations for the GRB prompt emission exists, e.g. magnetic reconnection and photospheric models (see e.g. Mészáros, 2013, for a recent review).

GRBs are regularly detected at MeV to GeV energies by *Fermi*-GBM at a rate of ∼250 per year, since (i) the synchrotron radiation is usually strong in this energy range, and (ii) the field of view of *Fermi*-GBM is large (∼7°). It is expected that GRBs will produce inverse-Compton emission at TeV energies, which is delayed with respect to the synchrotron emission and at a lower flux. However, in spite of the large amount of effort, there has not been a detection of GRB emissions from ground-based VHE telescopes, maybe due to the low flux and the observation delay of roughly 1 to a few minutes. Upper limits of VHE emission of GRBs have been derived from VERITAS observations (Acciari et al., 2011c), which puts constraint on their emitting models. An exceptional example is the GRB130427A, which was observed by *Fermi*-LAT (Fermi-LAT collaboration & Fermi-GBM collaboration, 2013) with long lasting GeV emissions consistent with the inverse-Compton nature. Upper limits for this GRB derived from VERITAS observations put a strong constraint on the IC spectral peak (Aliu et al., 2014a).

1.2.3 Dark matter

Both direct and indirect searches for dark matter (DM) are being actively carried out, including the use of VHE gamma-ray observations. Many models of stable and weakly-interacting dark matter, as well as various annihilation or decay channels of dark matter have been proposed. For interacting dark matter, the two main unknown parameters are the mass and cross-section of a DM particle; while for decaying DM, the unknowns are the life time and mass of a DM particle.

However, since the expected gamma-ray flux from DM is a function of (i) DM spectrum, (ii) DM interaction cross-section (or life time), and (iii) astrophysical factor (J-factor) representing the DM column density along the line of sight, the measurement (or non-detection) of gamma rays can be used to constrain the DM interacting cross-section (or life time) for each different DM particle mass (see e.g. Cirelli, 2012, for a review).

The flux of the secondary products from DM annihilation/decay is expected to be higher from astrophysical sites with a higher DM density, usually in the form of halos around a gravitationally-bound objects. Due to the collisionless nature (in most DM models), DM particles in a gravitationally-bound system do not virialize and stay in a halo with a roughly smooth radial density distribution profile (e.g. the NFW profile Navarro et al., 1996). Such dark matter halos exist around galaxies and clusters of galaxies, extending to much further distance from the center than the baryonic matter. Gamma-ray observations of galactic center region, galaxy clusters and dwarf spheroidal galaxies may reveal dark matter annihilation or decay signals, although there are likely other possible production mechanisms in GC and galaxy clusters. For example, the observed radio halo and relic structures in clusters of galaxies indicate efficient particle acceleration, which may lead to gamma-ray radiation as well. The non-detections of Coma cluster from VERITAS and *Fermi*-LAT were used to put constraints on its CR, magnetic field, as well as DM (Arlen et al., 2012). The VHE gamma-ray emission from the galactic center region detected by HESS also has a likely baryonic origin (Aharonian et al., 2006d). Although the gamma-ray emission from dwarf galaxies are believed to be negligible, which is ideal for indirect DM searches, no significant gamma-ray emission has been detected (Acciari et al., 2010b; The Fermi-LAT Collaboration et al., 2013).

The most prominent spectral feature that DM can produce is a spectral line either from annihilation directly to gamma-ray pairs or from two-body decay into one or two gamma rays. The recent report of a tentative spectral line at $\sim$130 GeV around GC region seen by *Fermi*-LAT has brought much excitement (Weniger, 2012), although additional observations and confirmations from other instruments are needed to confirm the existence of the spectral line.

2. VERITAS

After a gamma-ray photon is produced in one of the sources described in the previous chapter, survives the absorption by lower energy photons along its path to the Earth, and enters the Earth's atmosphere, what happens before it ends up as an event detected by a Cherenkov telescope? In this chapter, I conceptually describe how VERITAS works. Other ground based air-shower telescopes work in a similar fashion. The content is arranged roughly following the journey of a gamma-ray photon from the top of the atmosphere to the electronics of VERITAS. In section 2.1, I briefly introduce the air shower development, the Cherenkov light production, and how the KASCADE simulation treat them. In section 2.3 I describe how VERITAS images an air shower to reconstruct the primary gamma-ray photon or cosmic ray particle, including some calibration work that I have helped in. In section 2.4, `KASCADE` simulations and `VEGAS` data analysis are described.

2.1 Gamma-ray initiated extensive air showers and Cherenkov radiation

In chapter 1, we already introduced that the Earth's atmosphere is opaque to gamma rays. However, gamma rays of VHE (100 GeV – 100 TeV) may interact with air nuclei, lose their energy, generate secondary particles, and initiate extensive air showers (EAS) which can be used to reconstruct the information of the original photon. Therefore, it is possible to build ground-based VHE gamma-ray telescopes. These telescopes rely on the characterization of EAS to reconstruct the information of the incident gamma-ray photon. Both gamma ray photons and CR particles produce EAS, the latter of which are considered background in gamma-ray astronomy.

When passing through the air, photons may lose energy mainly through three different processes: pari-production, Compton scattering, and photoelectric effect.

As illustrated by Figure 2.1, the cross section calculations show that pair-production is the dominating absorption process when the photon energy is higher than ∼100 MeV. At such energies, there is a high probability of a gamma-ray photon decaying into an electron (e^-) and a positron (e^+), in the presence of electromagnetic field from a nearby air nuclei (Bhabha & Heitler, 1937). On the other hand, the attenuation from photoelectric effect increases sharply at below ∼10 keV and dominates over other processes at lower energies.

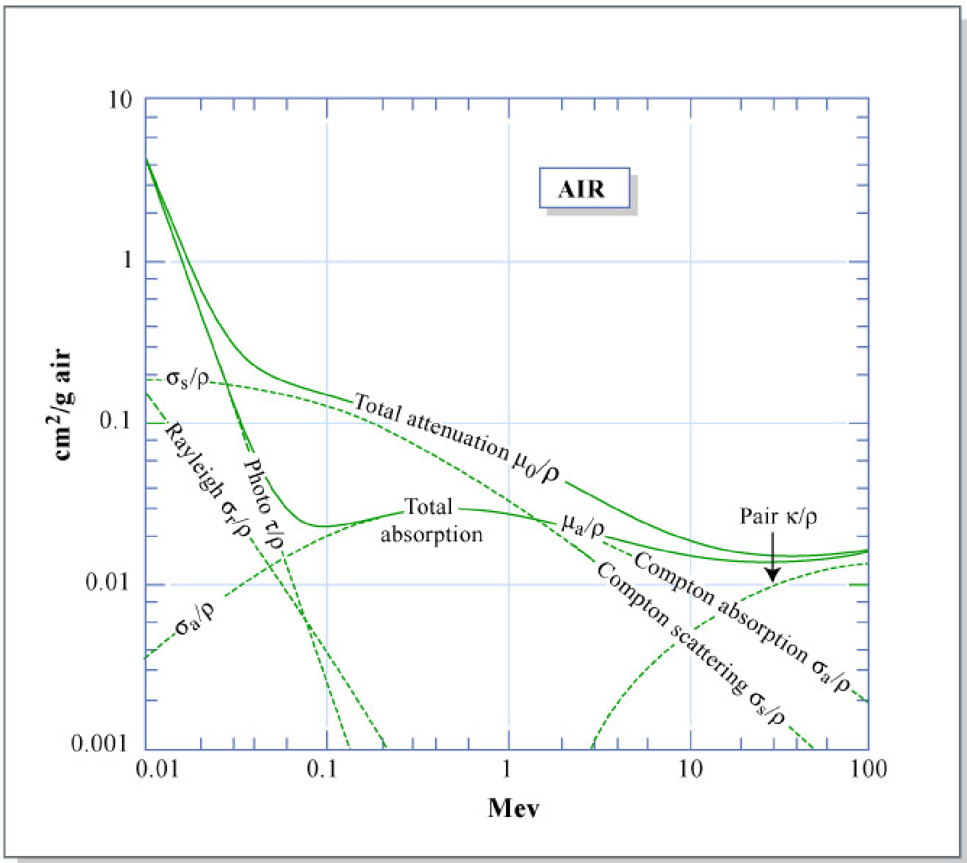

Figure 2.1.: The mass attenuation coefficient of photons in air, computed from cross sections of pair-production, Compton, and photoelectric processes. Figure by MIT OpenCourseWare `http://ocw.mit.edu/courses/nuclear-engineering/22-101-applied-nuclear-physics-fall-2006/`.

VHE gamma rays can penetrate into the atmosphere to an altitude of 10-20 km before the first interaction through pair-production. The resulting e^-/e^+ pair splits the energy of the original gamma ray photon, and are highly relativistic. They may interact with air nuclei and produce secondary gamma-ray photons via Bremsstrahlung process. The Bremsstrahlung photons repeat the pair-production process to generate more $e^{\pm}$ particles. A narrow and elongated particle cascade is formed as the iteration of pair-production and Bremsstrahlung carries on, as illustrated in the left subplot of Figure 2.2. As the cascade propagate further downward in the atmosphere, the

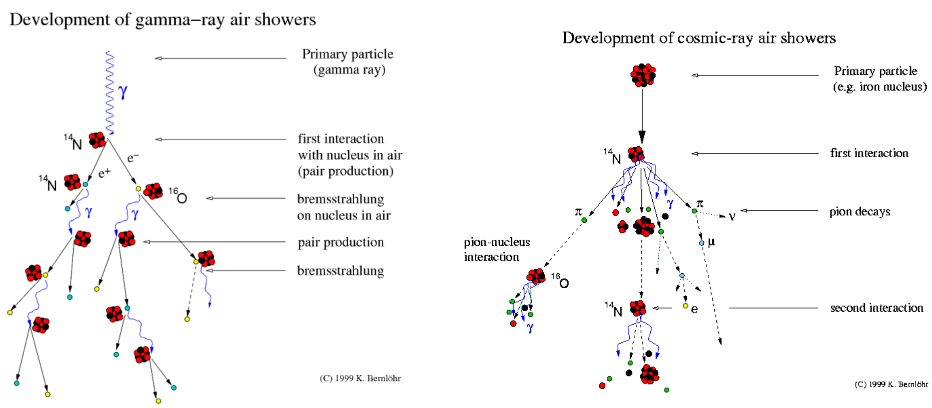

Figure 2.2.: Schematic illustration of estensive air showers from a gamma-ray photon and a cosmic-ray particle. Figure by Konrad Bernlöhr, taken from `http://www.mpi-hd.mpg.de/hfm/CosmicRay/Showers.html`.

number of particles increases exponentially, and the energy of each particle becomes so low that ionization and the photoelectric effect starts to dominate. This marks the end of an electromagnetic shower. Such electromagnetic showers have been proposed as early as in the 1930s (e.g. Bhabha & Heitler, 1937). Simulations show that a typical 300 GeV gamma ray shower has a shape that can be approximated by a three dimensional ellipse of about 10 to 15 km along the incident direction, and about 100 to 200 m across the direction perpendicular to the incident direction (see the top left panel in Figure 2.4). It is important to note that the major axis of the ellipse reflect the shower axis, therefore the incident direction of the gamma ray.

The secondary $e^{\pm}$ pairs in a EAS travel faster than the speed of light in air and emit Cherenkov light in UV or blue wavelengths. Assume a particle with speed $v = \beta c$, where c is the speed of light in vacuum, traveling in the air whose index of refraction is n. There is an induced charge displacement in the medium (air in this case) caused by the perturbation of the moving particle. When the particle travels slower than the speed of light in the medium c/n, the induced displacement (or polarization) (i) is symmetric and roughly perpendicular to the path of the particle, (ii) restores much faster than the time that the particle needs to pass through the local region, and (iii) results in an electromagnetic pulse that is collectively destructive, leading to no detectable net radiation. However, when the speed of the particle is larger than the speed of light in the air, i.e. $\beta > 1/n$ or $v > c/n$, the induced charge displacement (i) is symmetric but has a large net projection along the path of the particle, (ii) restores only after the charge moves further away, and (iii) results in an electromagnetic pulse that is collectively constructive, leading to a strong, polarized radiation, known as the Cherenkov radiation (see Figure 2.3 for illustrations).

The pair-production and Bremsstrahlung interactions in the cascade slightly randomize the directions of secondary particles with respect of the incident direction of the primary gamma ray. Therefore the Cherenkov photons from an EAS produce a roughly uniform light pool on the ground, illustrated by the bottom left panel of Figure 2.4 and Figure 2.8. These Cherenkov photons can be detected by the ground-based Cherenkov telescopes, and used to reconstruct information about the incident gamma-ray photon.

2.2 Cosmic-ray hadron initiated extensive air showers

A cosmic-ray hadron also produces an EAS and causes major background for ground-based gamma-ray telescopes. Fortunately, the properties of hadronic showers are usually very different from the electromagnetic shower from a gamma ray, because of the different nature of nuclear interactions.

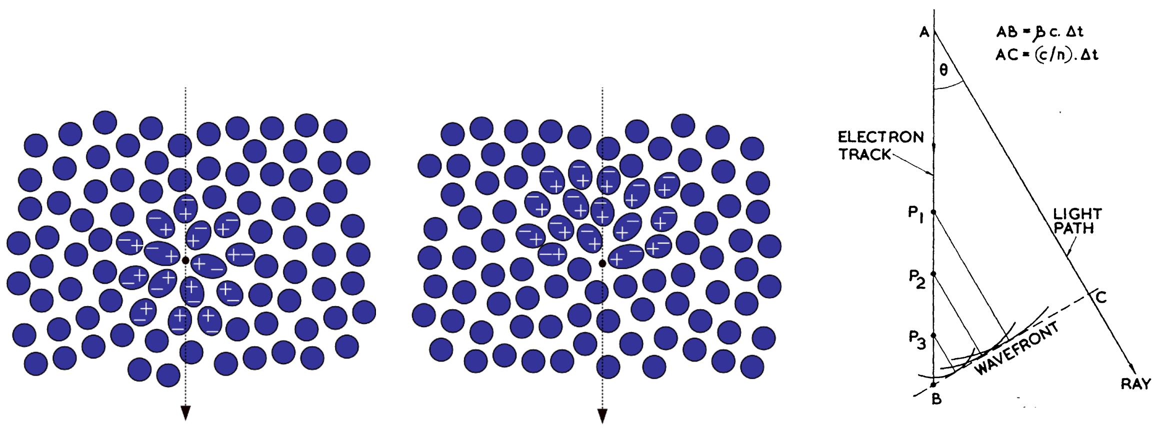

Figure 2.3.: Schematic illustration of the induced charge polarization in a medium caused by a moving negative charge. Left panel shows the effect of a non-relativistic moving particle: the electromagnetic wave emitted by the restoration of the polarized charge distribution is destructive in phase and results in no net radiation. Center panel shows the effect of a superluminal particle: the electromagnetic wave is emitted in a similar fashion as the non-relativistic case, but the resulting radiation constructively interfere in the direction at an angle of $\theta = arccos(1/\beta n)$, with respect to the direction of motion of the particle. Figures by Farzad Sadjadi, taken from `http://mxp.physics.umn.edu/s04/projects/s04cherenkov/theory.htm`. Right panel illustrates the relation between Cherenkov light path and the charge path, using Huygens' construction. Figure taken from Jelley & Porter (1963).

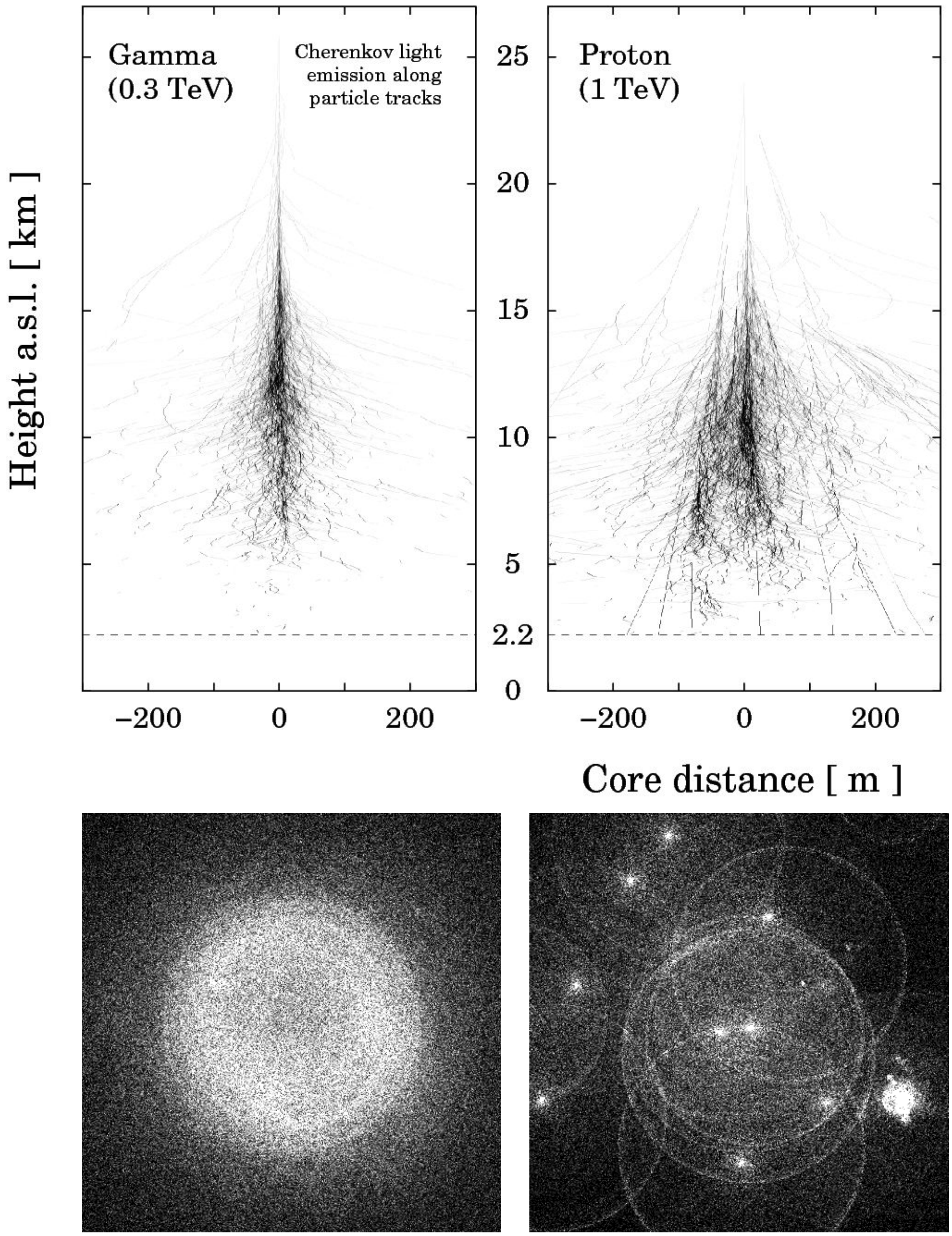

Figure 2.4.: Top panels: the traces of all secondary particles in an EAS from CORSIKA simulations of a 300 GeV gamma ray and a 1 TeV proton. Height and distance to the shower core are shown but not to scale. Darkness of the particle tracks are positively correlated with the emission of Cherenkov photons. Plot taken from Bernlöhr (2008). Bottom panel: the lateral distribution of Cherenkov photons at ground level from CORSIKA simulations of EAS of a 300 GeV gamma ray and a 1 TeV proton. Each plot shows a 400 m by 400 m region around the shower core. Atmospheric extinction is not considered. Figure by Konrad Bernlöhr, taken from `http://www.mpi-hd.mpg.de/hfm/CosmicRay/ChLight/ChLat.html`.

Consider a relativistic proton, the most abundant cosmic-ray particles. When it interacts with an air nucleus, phenomenological models (e.g. quark-gluon string fragmentation or bag of quarks model) can be used which give probabilities of secondary products and their parallel and transverse momenta. Pions (and kaons for higher energy showers) are a major product of hadronic showers, amounting to about 90% of all secondary particles. Roughly a third of the secondary pions are neutral π^0s, which immediately decay into secondary gamma rays (see 1.41); and the rest pions are charged $\pi^{\pm}$s, which can subsequently decay into muons (see 1.42). The secondary gamma rays $e^{\pm}$ pairs produce electromagnetic showers similar to that from a gamma-ray photon. A hadronic shower can produce multiple electromagnetic sub-showers, and the hadronic interactions lead to a much larger transverse momentum of the secondaries than gamma-ray showers. Therefore hadronic showers generally have a broader profile comparing to gamma-ray showers, especially at higher energies. This can be used as a criteria to separate CR hadronic showers and gamma-ray showers.

2.3 Gamma-ray detection using imaging atmospheric Cherenkov telescopes

In the following subsection, I first summarize the concept of the direction and energy reconstruction of the incident gamma ray, using the measurable properties of the EAS introduced in the previous section. Then I dabble through the components of VERITAS roughly following the journey of the Cherenkov photons: they are generated in the shower, some propagate through the atmosphere to the ground, a fraction hit one or more mirrors of VERITAS, an even smaller fraction are reflected to the camera plane and hit a cluster of photomultiplier tubes (PMTs), an even smaller fraction trigger signals from the PMT, finally some events further trigger a telescope and the entire array, and data are stored and analyzed.

2.3.1 The concept of imaging atmospheric Cherenkov technique

The details of shower development and Cherenkov radiation production were briefly covered in the previous section 2.1. An extensive air shower can help us measure the arrival time, direction, and energy of the primary VHE gamma ray, therefore we can construct a VHE gamma-ray detector by observing the air shower. We now introduce how we can use the properties of air shower to reconstruct VHE gamma rays.

Timing

First, the arrival time of an EAS, regardless of its origin (gamma rays or cosmic rays), can be determined accurately. As mentioned above in section 2.1, the body of a shower can be approximated by a three-dimensional ellipse of $\sim$10 km long and $\sim$100 m across. If the shower is illuminated instantaneously, the photons from the two ends of the shower are separated in time by $\sim$30 μs. However, note that the superluminal secondary particles travel faster than the Cherenkov photons, and the photons are "chasing" the particles as they propagate. The photons produced earlier in a shower (also at higher altitude) only slightly lag behind the photons produced later (at lower altitude). The resulting time span of the Cherenkov photons from an EAS is around 10 ns, corresponding to the duration of the detected pulses in PMTs. The exact duration depends on the direction of the shower axis and energy of the primary particle. This timescale can be considered instantaneous in VHE gamma-ray astrophysics. Although note that there are a few other longer timescales involved in atmospheric Cherenkov technique: (i) The time for Cherenkov photons to travel from the shower body to the ground, which can be calculated from the direction and the height of the shower. Note that there is a large uncertainty in the determination of the shower height, also called the shower maximum. This time is on the order of μs. (ii) The deadtime caused by the data readout after a trigger is received. The deadtime of VERITAS for a single event is $\sim$0.33 ms. At the array trigger rate of

∼400 Hz, the deadtime of the four-telescope array is around 15%. However, these two factors do not affect the relative timing of the source, and are corrected for in simulations and data analyses.

In order to accurately determine the trigger time of each telescope, a constant fraction discriminator (CFD) is used by VERITAS (see below in 2.3.2). When a shower triggers more than one telescope, the delay between each single-telescope event is calculated by the array trigger system and accounted for in the data acquisition process (see 2.3.2).

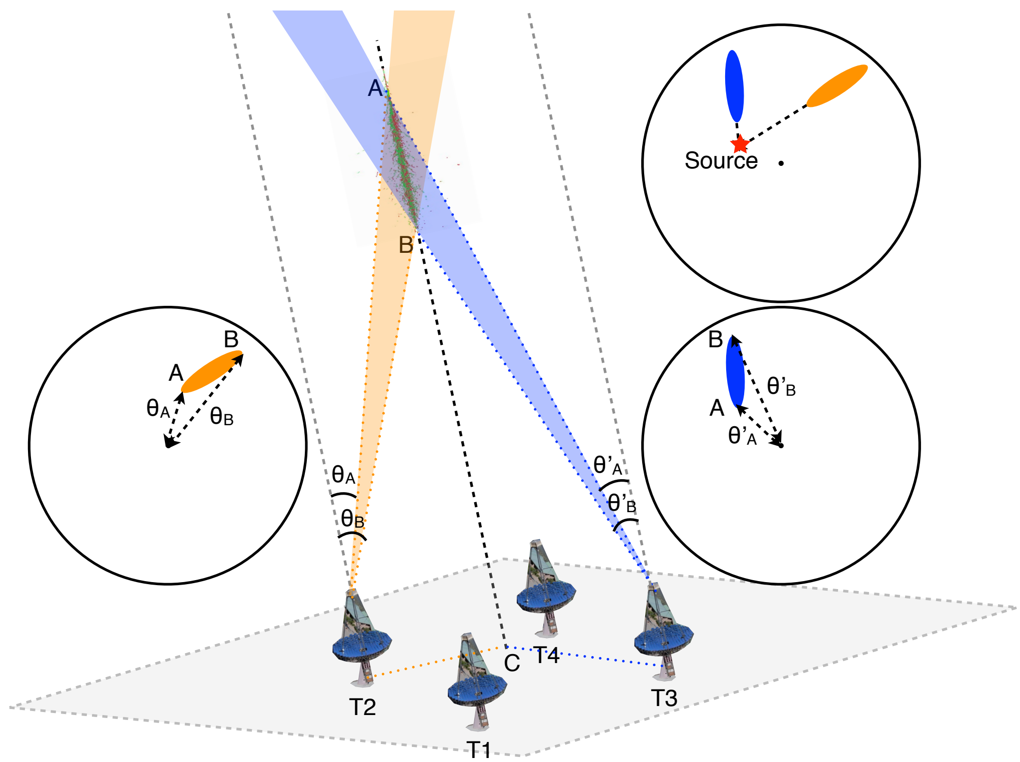

Figure 2.5.: Cartoon illustrating the principle of direction reconstruction from shower imaging. A and B are the two ends of an air shower, C is the shower core; θ_A, θ_B, θ'_A, and θ'_B are the angular distances from the optical axes of the two triggered telescopes. The images of the shower in each camera plane and a combined view are also shown. Note that the coordinates in the camera plane correspond to the angular position on the sky, with the center being the direction of the optical axis.

Direction reconstruction and image parameterization

Secondly, the direction of an incident gamma ray can be reconstructed through the images of the shower, since most gamma-ray showers have an narrow, elliptical shape, with a major axis parallel to the incident direction. Each telescope can only produce an image of a two-dimensional projection of the shower, which is an ellipse in the camera plane. Figure 2.5 illustrates the image of an EAS in two telescopes. It is important to remember that the coordinates in the camera plane correspond to directions of the incoming light. Therefore the coordinates of the two ends of a shower image along the major axis give the angular directions of the start and end of the shower, forming an angle with the location of the telescope being its apex (see Figure 2.5). The direction of the primary gamma ray lies in the plane defined by the two edges of this angle. In the camera plane, it corresponds to a line on the extension of the major axis. With only one telescope, it is impossible to know the exact direction of the shower axis, therefore the ability of direction reconstruction is limited. However, if there is a gamma-ray point source in the field of view, the extension of the major axes of the shower images produced by the source will all go through a point, corresponding to the coordinate of the source. This is an important criteria for single telescope gamma-ray detection.

Stereo imaging with multiple telescopes at different locations provides a much better direction reconstruction. Multiple images from different perspectives allows the identification of a unique direction, since the extensions of all the shower images in the sky coordinates should intersect at the position of the source. In reality, they do not always intersect at a single point due to measurement error. A geometric (geo) method finds a point that minimizes the sum of the weighted distances squared to the major axes of each shower, and treat it as the reconstructed shower direction. Different weights (e.g. the ellipticity of an image) can be used. An alternative displacement (disp) method reconstruct the incoming shower direction using a characteristic relation between (i) the length, width, and size of a shower image and

(ii) the displacement of the incoming shower direction and the center of the image (Beilicke & VERITAS Collaboration, 2012). The disp method is especially useful for large zenith observations, when the majority of the major axes of the shower image in all telescopes are parallel to each other. Currently, VERITAS achieves a (68% containment) point spread function (PSF) of $\sim 0.1°$ at ~ 1 TeV.

As described in the previous sections, a gamma-ray shower and a hadronic shower can be separated using the image shape. The shape of each image of a shower can be parameterized by width W and length L, characterizing angular distance along minor and major axes, respectively. Two more parameters are important for energy reconstruction (discussed below): (i) The first one is the total integrated charge from all PMTs in the unit of digital count (dc), usually called size S. Size is directly related to the number of photo electrons, which reflects the number density of Cherenkov photons. (ii) The second one is the distance between the shower core (where the extension of the shower axis hits the ground) and the telescope in the unit of meter, called impact distance D. A mean-scaled width (MSW) and a mean-scaled length (MSL) can be calculated by comparing each event with simulated gamma-ray events (Daum et al., 1997):

$$MSW(S,D) = \frac{1}{N_{tel}} \sum_{i=1}^{N_{tel}} \frac{W_i}{\langle W_{sim,i}(S,D) \rangle}, \tag{2.1}$$

$$MSL(S,D) = \frac{1}{N_{tel}} \sum_{i=1}^{N_{tel}} \frac{L_i}{\langle L_{sim,i}(S,D) \rangle}; \tag{2.2}$$

where W_i is the width of the image in the ith telescope, $\langle W_{sim,i}(S,D) \rangle$ is the average width of simulated gamma ray showers with the same size S and impact distance D (same for length). The MSW and MSL offer the most discriminatory power to separate gamma rays and cosmic ray showers, demonstrated by many studies including some recent machine learning results.

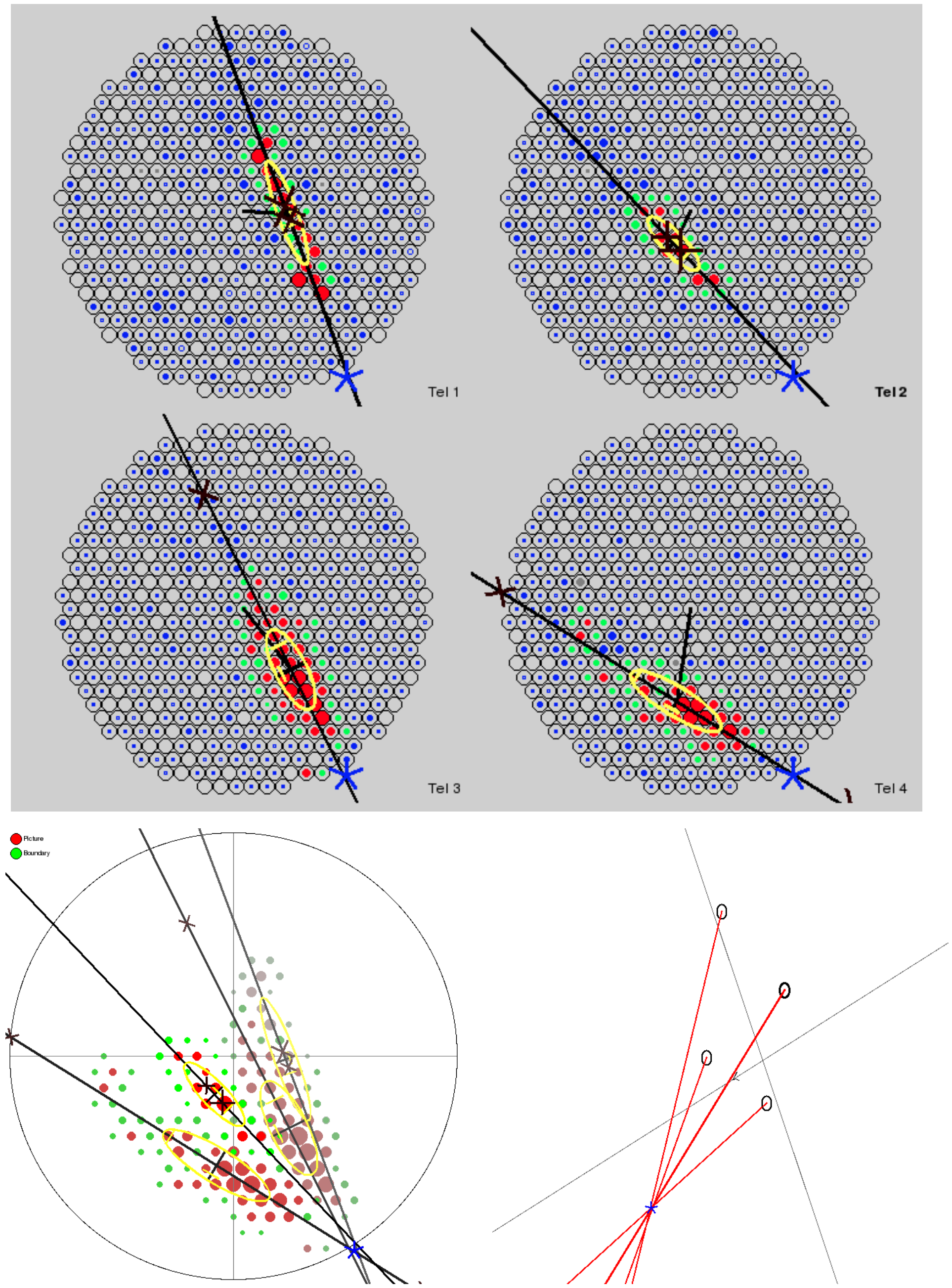

Figure 2.6.: VERITAS images of one gamma ray candidate event from an observation of Mrk 421. Top panel shows the actual image of the event in each telescope. Red pixels are imaging pixels that have digital counts more than 5 standard deviation higher than the noise pedestal variance; green pixels are boundary pixels that yield digital counts between 3 and 5 standard deviation higher than the pedestal variance and adjacent to a image pixel. Yellow ellipses and black lines show the best fit of an ellipse to the image. Bottom left panel shows the overlap of four images in the field of view on the sky. Bottom right panel shows the extension of the reconstructed image on the ground. All images were produced by the Quicklook tool ql_monitor.

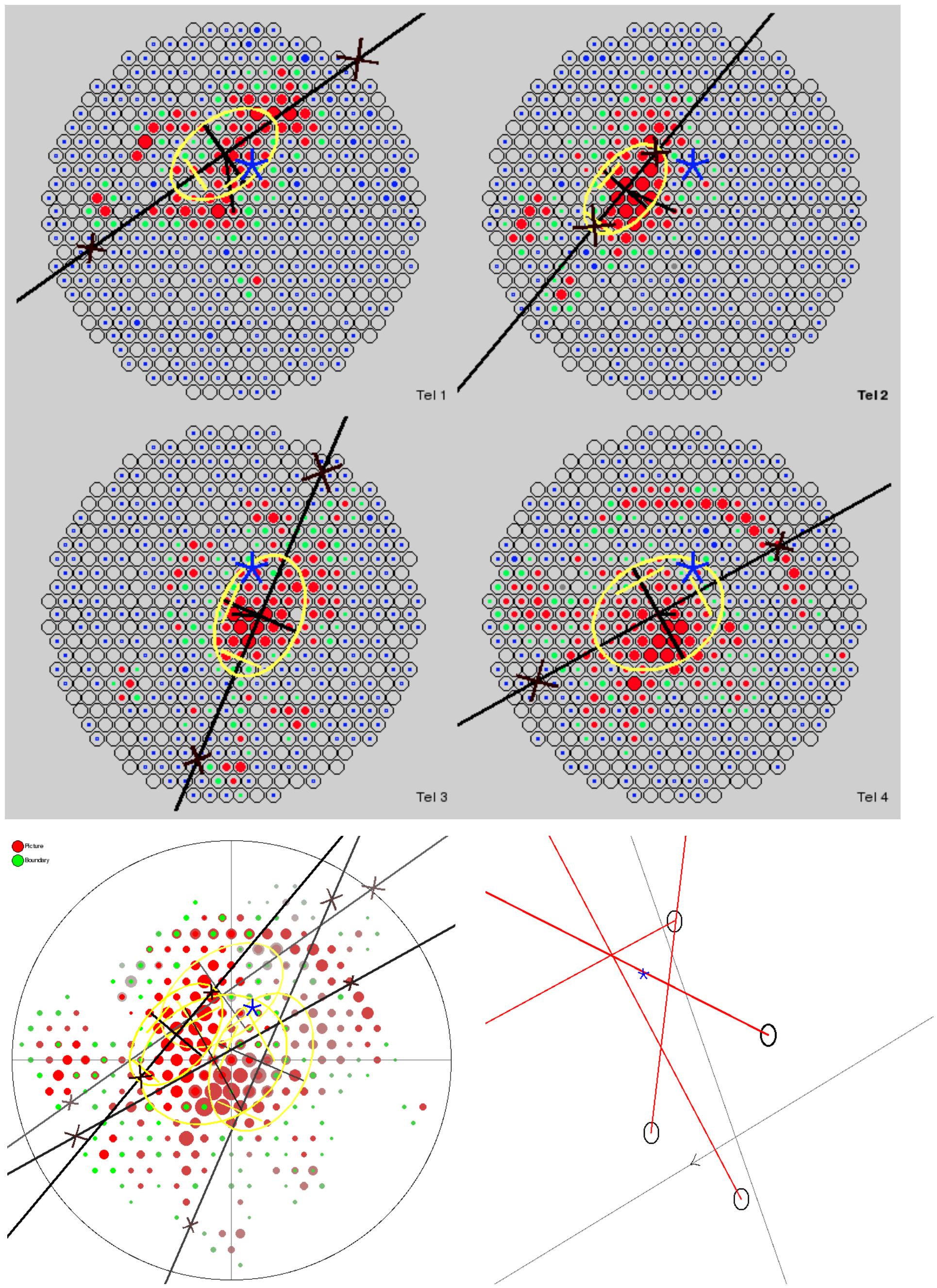

Figure 2.7.: VERITAS images of one cosmic ray candidate event from an observation of Mrk 421. See the caption in Figure 2.6 for detailed information of each panel.

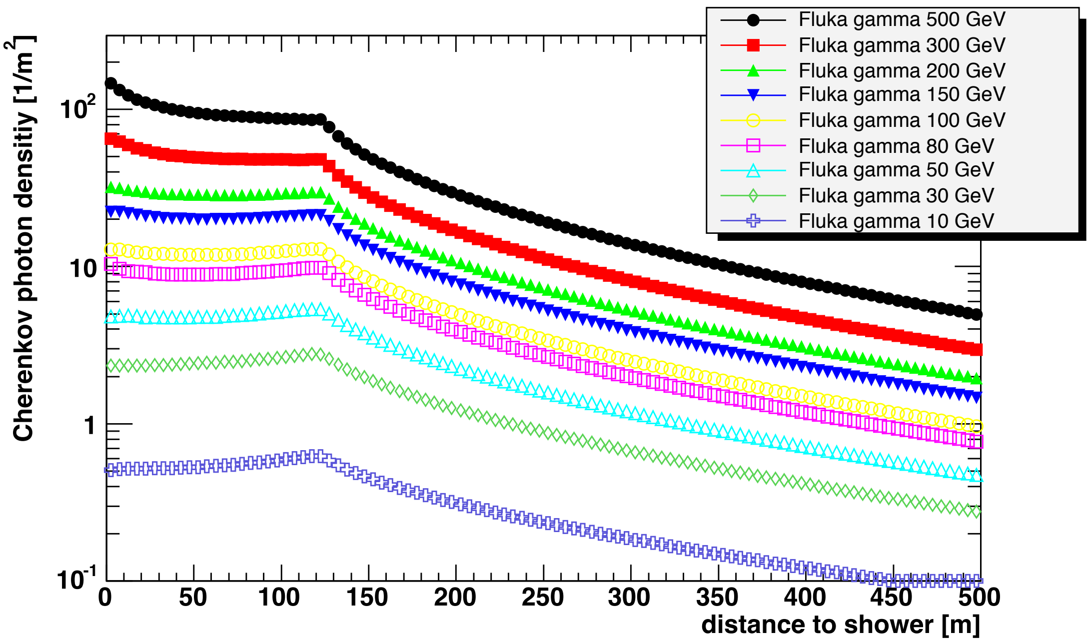

Figure 2.8.: Simulated Cherenkov photon density in the Cherenkov light pool as a function of distance from the shower core. Different colors correspond to different energies as shown in the legend. The Cherenkov photon density correlates with the energy of the incident gamma ray, and remains roughly constant within the light pool of a radius of ∼100 m. Figure taken from Maier (2013).

Energy reconstruction

Thirdly, the energy of a primary particle or gamma ray can be reconstructed by measuring the density of Cherenkov photons. Figure 2.8 shows results from CORSIKA numerical simulations illustrating (i) the relation between the energy of the incident gamma ray and the density of the Cherenkov photons, and (ii) the roughly constant Cherenkov photon density within the light pool of a radius of ∼100 m.

The directly measurable quantity related to the density of the Cherenkov photons is the size parameter S (total charge of the photoelectrons coming from all PMTs as mentioned above). However, there are a number of efficiencies affecting the relation between size and Cherenkov photon density: (i) atmospheric extinction, (ii) mirror reflectivity, (iii) light cone efficiency, and (iv) quantum efficiency of the PMTs.

In order to reliably measure the energy, we need to understand and calibrate the efficiencies mentioned above. I have participated in the calibration measurements of the gain and quantum efficiencies of the PMTs at Purdue, and the whole-dish mirror reflectivity lead by the McGill group.

VERITAS is sensitive to VHE radiation in the energy range from ∼100 GeV to ∼30 TeV. The energy resolution of VERITAS is around 15% above 300 GeV.

2.3.2 VERITAS

In this section, I briefly summarize the components of VERITAS that have appeared in the previous subsection.

Telescope mechanics and optics

Any imaging telescope needs to maintain the pointing direction toward the desired coordinates in the sky, and focusing the incoming light to the focal plane. The main mechanical structure of each telescope of VERITAS includes an elevation-azimuth positioner, and an optical support structure (OSS) mounted on the positioner. The telescope uses the Davies-Cotton design (Davies & Cotton, 1957) that consists of identical segmented mirrors.

Tracking software controls the telescopes individually or in array mode, with optional wobble offset (difference in angle between the pointing direction and the source coordinates). In wobble mode, the telescopes deliberately point off target (usually by $0.5°$) in order to use reflected regions for background estimation (see section 2.4.2 below). The pointing of the telescopes are constantly monitored during data taking. The results of the VERITAS pointing monitor (VPM) are saved and used in data analysis to compensate tracking errors. The telescopes slew at an angular speed of $\sim 1°\mathrm{s}^{-1}$. A special tracking wizard for GRBs immediately starts to slew the telescopes to the GRB trigger coordinates after a button click, to minimize delay in observations. In 2009, telescope 1, the original prototype of VERITAS, was relocated to the current position to improve the sensitivity and background rejection (Perkins et al., 2009).

About 345 small hexagonal mirrors, covering a hexagonal area of $\sim$110 m^2 (or diameter of $\sim$12 m) are mounted on the OSS of each telescope. The optical focal length is $\sim$12 m. The reflectivity of the mirrors peaks at $\sim$320 nm with a value of $\sim$90%. The natural degrading of the overall reflectivity is at a rate of $\sim$3% per year. Therefore, mirrors are recoated in batches on average every two years, to maintain an optimal reflectivity (Roache et al., 2008).

Camera

The cameras' job is to record the intensity of the Cherenkov pulses at each pixel.

Each VERITAS camera is equipped with 499 photomultiplier tubes (PMTs), covering a $3.5°$ field-of-view. A light cone plate sits in front of the PMTs, filling the area between neighboring PMTs. When a photon hits a PMT, a photoelectron may be released at the photocathode, accelerated by a high voltage, hits a series of dynodes, and produces a cascade of electrons. This process happens fast ($<$2 ns), so PMTs are ideal for detecting fast Cherenkov flashes. The most important two properties of a PMT is gain and quantum efficiency (QE).

The gain is defined as the number of photoelectrons on average produced at the final dynode by a single photoelectron. The gain can be characterized by a power-law function of the applied high voltage. The relation between gain and high voltage varies among different PMTs, therefore it is necessary to supply a customized high voltage (typically between 800 to 1100 V) for each PMT to keep a uniform gain (typically of 2×10^5) across the camera. Two commercial multichannel power supply crates provide high voltages to the PMTs of each telescope. A pre-amplifier is attached to the base of each PMT to amplify the output. Also current monitor system displays the real-time current from the PMTs, and provides safety features that automatically cut off the high voltage supplies if the current exceeds certain limits.

The QE of a PMT characterizes the probability of producing a photoelectron if the PMT is struck by a photon. The QE of VERITAS PMTs typically peak around the wavelength $\sim$300 nm at a value of $\sim$35%, which coincides with the wavelengths of Cherenkov light well. The QE is an important factor of efficiency, and are used in the simulations. Both gain and QE of the VERITAS PMTs are measured at Purdue University.

In 2012, a major upgrade to replace the original Photonis PMTs by the higher QE Hamamatsu PMTs (D. B. Kieda for the VERITAS Collaboration, 2013). The upgrade has brought the energy threshold down by $\sim$30% for gamma-ray events, and subsequently increased the effective area by about 20% to 30%.

Trigger systems

The abundant night sky background (NSB) light can produce signals in PMTs, leading to high trigger rates. Since the telescopes cannot record new shower events while the data is being read out, a certain fraction of the observing time (called dead-time) is ineffective. The higher the trigger rate is, the higher the dead-time fraction is. The three-level trigger system of VERITAS is designed to avoid triggering on NSB noise, control the trigger rate and dead-time at a hardware level.

The level 1 (L1; pixel level) trigger system sends a trigger only if the number of photoelectrons from a PMT exceeds a threshold. L1 trigger decisions come from the combination of the constant fraction discriminators (CFD) and a regular threshold discriminator associated with individual PMTs (Hall et al., 2003). The CFDs are able to trigger at the time when the pulse reaches a constant fraction of its maximum, through finding the zero crossing time of the sum of the original signal and an inverted and delayed signal. The advantage of CFDs over normal threshold discriminator is that they reduce the time jitter, and therefore makes it possible to have a narrower coincidence window for level 2 (L2; telescope level) triggers (see below).

The threshold of CFDs can be adjusted. At a lower threshold, the PMTs can trigger on dimmer showers (with lower energy), but also suffers more triggers from NSB noise and subsequently higher dead-time. Bias curves, which show the L1 or L2 trigger rates as a function of CFD threshold, are used to determine the optimal trigger threshold. L2 bias curves are regularly taken, thanks to the convenience of reading only one L2 rate from each telescope. On the other hand, the L1 bias curves are more difficult to take since the rates from each pixel needs to be read out. I have written a script `L1BiasCurve.pl` to take L1 level bias curves based on the VERITAS data acquisition programs and L2 bias curve script. A measurement was taken on Jun 21, 2011, and the results of averaged L1 rates for each telescope as a function of threshold is shown in Figure 2.9.

The level 2 (L2; telescope level) trigger system looks for clusters of L1 triggers from neighboring PMTs within a short coincidence window. A new FPGA-based L2 trigger system was installed in 2011, which provides programmable time delay adjustments between the signals from each PMT. The use of the 400 MHz FPGAs in the new L2 trigger board makes it possible to narrow the operational L2 coincidence window to $\sim$5 ns (comparing to previously $\sim$10 ns) that more effectively rejects the NSB noise, making it possible to operate at a lower CFD threshold (Zitzer

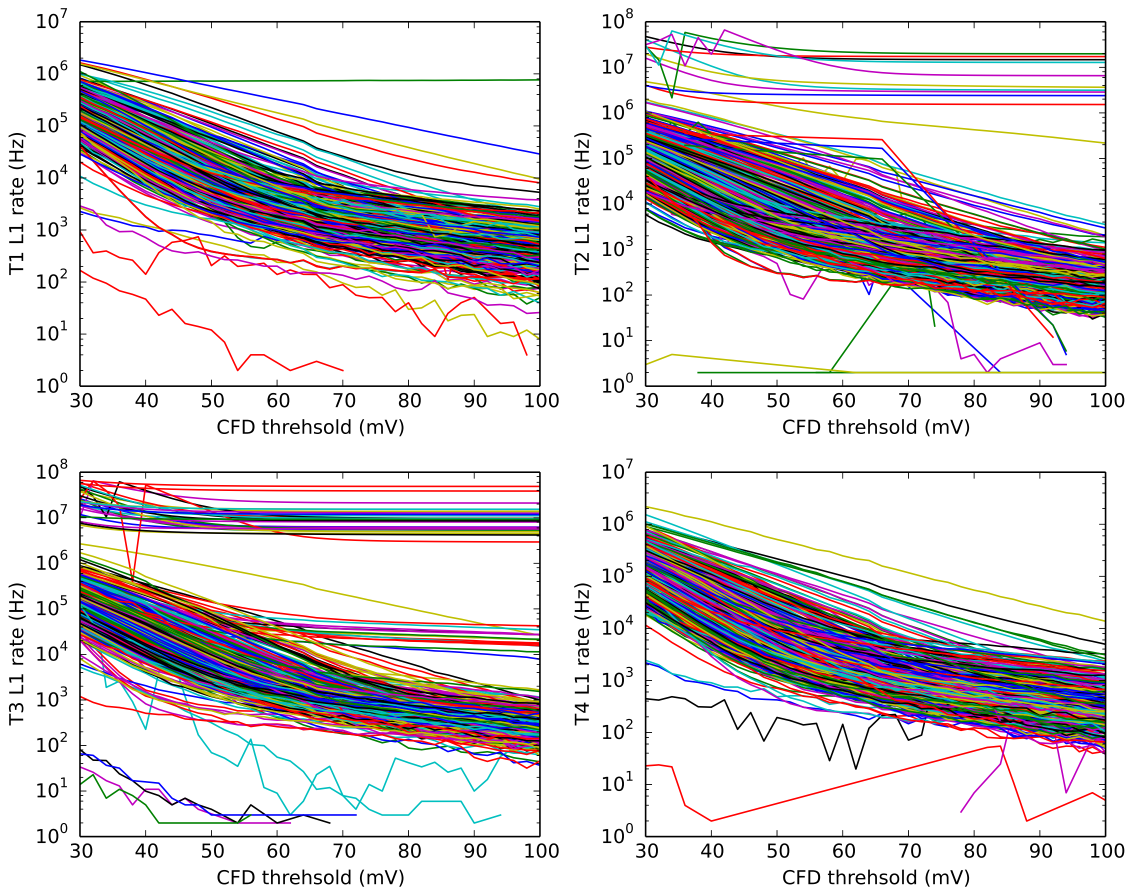

Figure 2.9.: The L1 bias curves for each channel and each telescope, taken on Jun 21, 2011, using the script `L1BiasCurve.pl`. The dead channels with constant zero readings are not plotted. Note that these plot contain a few channels that are used for L2 triggers, as well as bad channels that can be flagged and taken out by L2 software.

& for the VERITAS Collaboration, 2013b). A minimum of three contiguous pixels are required. The L2 trigger system significantly lowers the triggering rate on NSB noise. For example, the VERITAS array in 2011 (before the new L2 and high-QE PMTs) has a L2 trigger rate of ∼10 kHz at the CFD threshold of 45 mV, comparing to L1 rate which can reach ∼1 MHz.

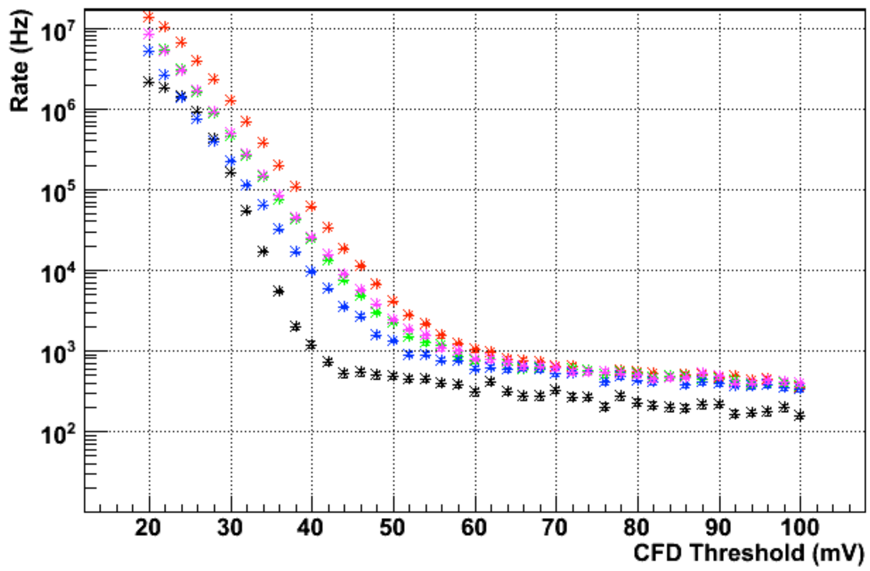

Figure 2.10.: The L2/L3 bias curves of VERITAS after the PMT upgrade in 2012. Figure taken from D. B. Kieda for the VERITAS Collaboration (2013). The colored markers show the L2 rates, and the black markers show the L3 rates.

An L2 bias curve after the VERITAS PMT upgrade is shown in Figure 2.10. An inflection point can be identified in the bias curve between 50 and 60 mV for the L2 rates (colored markers), and between 40 and 45 mV for the L3 rates (black). Below the inflection threshold, the trigger rates are dominated by the NSB as suggested by the steep slope of the bias curve; while above the inflection threshold, the rates are dominated by the CR as suggested by the flat slope. The optimal CFD threshold has increased comparing to pre-upgrade, since the new high-QE PMTs offer higher sensitivity to detect Cherenkov light. The operating CFD threshold has been determined to be 45 mV according to the L3 rate inflection point in the bias curve.

The level 3 (L3; array level) trigger system deals with another major background triggers coming from cosmic ray showers. One distinct feature of CR showers comparing to gamma ray showers is the existence of muons. A muon has a long life time and can penetrate to the ground and pass through the mirrors. Along its track, highly directional Cherenkov light at a roughly constant angle $\sim arccos(1/\beta n)$ is produced, leading to a ring (or partial arc) in the camera.

Fortunately, such muon images are usually only bright enough to be seen by one telescope. The L3 (array level) trigger system can further reject triggers on CR events by requiring more than one L2 trigger from individual telescopes within a coincidence window of 100 ns. Different delays due to (i) cable lengths between L2 and L3 hardware, and (ii) the locations of telescopes with respect to the wave front of the Cherenkov light are corrected by the L3 system. A delay between 100 ns and 6 μs can be set from the L3. The delay is different for different observing modes and pointing directions.

Now I recap the sequence of the VERITAS trigger system: (1) if enough photons hit a PMT, it sends an L1 trigger to the L2 system; (2) if the L2 system gets three or more contiguous L1 triggers within the L2 coincidence window, it sends an L2 trigger to the L3 system; (3) similarly, if the L3 system gets more than one L2 triggers within the L3 coincidence window, it generates an L3 trigger. The three-level trigger system helps VERITAS to keep the trigger rate and the dead-time at a manageable level.

Data acquisition systems

After an L3 trigger decision is made, the L3 system sends a trigger signal (along with a unique 32-bit event number and a look-back time) back to a data acquisition (DAQ) system at each telescope. The DAQ chain then raises a busy signal, reads out all relevant information regarding this triggered event from the FADCs, puts it in a buffer, and sends buffers of events to the Harvester that assembles single-telescope events into an array event and saves it in a data file and perform real-time analysis (Wakely et al., 2003).

In order to readout the entire Cherenkov pulse, a flash ADC (FADC) board samples the PMT signals at a rate of 500 MHz (2 ns intervals). The FADC uses 8 bits to store the digitized pulse intensity (0-255 digital counts) and a ring buffer with a depth of 32 μs. When the pulse is so bright that the peak intensity exceeds 255 digital counts, the FADC automatically delays the signal and sends it into a low-gain channel that offers 6 times more dynamic range up to 1500 digital counts. For normal VERITAS observing, 24 samples (48 ns) are read out for every event. Typical gamma-ray analysis uses a 7-sample (14 ns) integration window to calculate the total charge of an event.

The look-back time for each event quantifies the delay between the time of the L2 trigger and the time that L2 receives the L3 trigger (i.e. the time that an L2 trigger travels to the L3 system plus the time that the L3 trigger travels back to the L2 system). Upon receiving the L3 trigger, the DAQ reads out the corresponding buffer in the FADCs that contains the Cherenkov pulse of this event, after adjusting for the look-back time. Then the FADC traces for each event are sent to the Event-Builders for each telescope, where the single-telescope events are created, saved locally, and sent to the Harvester in buffers via ethernet. Each single-telescope event not only contains the digitized FADC charge trace coming out of the pixels, but also other information coming from the L3 including the telescope number, the event number which uniquely identifies one triggered event for all telescopes and the L3, the trigger mask that labels the active telescopes, the trigger type that indicates whether a particular telescope has sent an L2 trigger that participated the L3 trigger or not, the GPS time at which the trigger was created (different for each telescopes and the L3). The above information is crucial for the array data acquisition and data analysis.

The array data acquisition system (Harvester) is a combination of data collecting and analysis programs that runs as a daemon on the Harvester machine. It has four main tasks: (i) assembling data from multiple telescopes and the L3 system into a single data stream of array events; (ii) performing real-time diagnostics and analysis on the data via a package called Quicklook; (iii) saving the five streams of data into local chunk files and combining the chunks into a final VERITAS bank format (VBF) files or compressed VBF (CVBF) files, via a process called "purifier"; (iv) sending the data to the archive machine via a process called "archive".

Note that each single-telescope event may have a very different trigger time due to shower geometry and look-back time, therefore Harvester relies on the unique event number, instead of event GPS time, to assemble array events. The delay between single-telescope events may cause them to arrive at Harvester in different data buffers. Therefore, a data structure called "event table" is used to store single-telescope and L3 event streams. If events from one telescope is jumping ahead (or lagging behind) the other telescopes, the event table allows us to save the data streams in the memory until the other telescopes catch up in the future, after which all array events can be assembled. There is a limit on the amount of memory used by each telescope to prevent overuse of the computing resources on the Harvester machine.

The Harvester is designed to handle incoming data at rate higher than 15 MB/sec for at least 30 minutes. This rate roughly corresponds to a L3 trigger rate of $\sim$1.5 kHz, if each event from four individual telescopes and L3 has a size of 2048 bytes. However, for future ground-based telescopes like CTA, the large number of telescopes and possibly high trigger rates will impose a significantly heavier burden on array-level data collecting devices.

The real-time analysis system (Quicklook) is a component of the Harvester that is always running with the Harvester daemon, providing real-time analysis and diagnostic results. These results can be accessed by the observer through a set of `QLtools`. Two of the most used `QLtools` are `ql_monitor` that displays all the diagnostic and analysis results during or after a run via a GUI interface, and `nightsum` that prints out the gamma-ray rates and significance values for all finished observations.

The cuts and tables used in Quicklook analysis are stored in the file /usr/local/veritas/etc/qltools.conf on Harvester machine. It is also possible to specify cuts and tables for offline `QLtools` with the options -config and -msw-table. There are two offline `QLtools` programs, `ql_params` and `ql_wobble`, which can analyze a cvbf file and reproduce real-time Quicklook results.

To optimize the cuts, run `ql_params` and `ql_wobble` with different cutting values to find out the value that produces the greatest significance. The important cuts include: (i) the image cleaning cuts on minimum signal to noise ratio of the integrated charge from a picture pixel or a boundary pixel, respectively; (ii) the size cuts; and (iii) the MSW cuts.

I have analyzed a list of VERITAS Crab runs using `QLtools` to study the zenith angle dependence of the Quicklook results. I also optimized the size cuts for reduced high voltage observations and UV-filter observations during moon time after the PMT upgrade, and wrote an automated bash script that analyzes all runs using the optimized size cuts (200 dc and 400 dc comparing to the normal 700 dc) and stores the results into the VERITAS database for easy access. These results can be found in Appendix A.

2.4 Simulations and data analysis

As described above, numerical simulation plays an important part in VHE astronomy. Part of the reason is that there is no VHE "standard candle" (despite the existence of the Crab Nebulae, of which the true TeV flux is unknown and variability has been observed) in the sky for instrument calibration. Instead, a gamma ray point source of known flux needs to be simulated. This involves the simulation of the particle traces in an air shower, generation and propagation of Cherenkov photons, and the entire VHE optics, detectors and trigger systems on the ground.

The output files from simulations have similar format as data files from observations, containing triggered array events with know energy and direction. These files are processed through the data analysis chain (described below in section 2.4.2) to produce two important tables for real gamma-ray analysis: the look-up tables and effective area tables. These tables relate the observable quantities (e.g. the image parameters and total integrated charge) to the quantities that we want to measure (e.g. the energy and flux). Below I describe the `KASCADE` simulation package as an example of VERITAS simulations.

2.4.1 KASCADE

The Kertzman And Sembroski Cherenkov Airshower and Detector Emulation (`KASCADE`) (Kertzman & Sembroski, 1994) is a set of detailed, three-dimensional computer simulations, which (i) generates the particles (`ksKascade`) and subsequent Cherenkov photons (`ksLite`) produced by VHE gamma-ray and cosmic-ray air showers, and (ii) simulates the response of the optics (`ksAomega`) and triggers (`ksTrigger` and `ksArrayTrigger`) of the telescopes. It has the ability to simulate a wide range of primaries, including gamma rays, all ions from proton to iron, electrons and positions. It has been developed and maintained by Glenn Sembroski from Purdue University and Mary Kertzman from DePauw University since 1989. The `KASCADE` system has been designed as a general tool in investigating a variety of air-shower Cherenkov telescope designs with the goal of maximizing their gamma ray detection sensitivity. It is relatively easy to change telescope configurations as well as detector models.

The current settings of `KASCADE` simulates particles with 45 discrete energies evenly distributed (in steps of 0.1 log_{10} GeV) from 20 GeV to 52.265 TeV for each combination of azimuth, zenith angle, noise and offset. The number of simulated showers decreases roughly following a power law from a total of 1382 showers generated at 20 GeV, to 10 showers at 350 GeV, a constant number of 10 showers are simulated from 350 GeV to 25.56 TeV, and 5 showers are simulated from 30.565 TeV to 52.265 TeV.

The particle interactions (described in section 2.1 and section 2.2) in the shower is treated in `ksKascade` according to a QCD Monte Carlo algorithm proposed by Gaisser & Stanev (1989). This algorithm is also used in neutrino and particle accelerator experiments. The interaction or decay channel for different particles, as well as the "thickness" (in the unit of g cm^{-2}) that a particle can travel before interaction or decay, are considered. Each particle is tracked in segments of lengths of 0.2 radiation length, until it further interacts, or decays, or hits the ground, or loses enough energy and becomes sub-luminal. The effect of the geomagnetic field and the density profile of the atmosphere is taken into account. Cherenkov photons are generated in `ksLite` for each segment and traced to the ground. The atmosphere extinction of the Cherenkov light is considered. The location where the photon hits the ground, the time, and the direction of this photon are recorded. The photons are then sorted by their location and arrival time. `ksTrigger` and `ksArrayTrigger` divide the ground into grids, each of which roughly correspond to the dimension of a telescope. For each shower, a virtual telescope array is put at different locations (corresponding to different impact distances) on the grids, and trigger decision is made according to the number of Cherenkov photons within the telescope grid and a detailed detector model including the QE of PMTs and the jitter from the mirrors. Random photons are added to represent the NSB noise light, with the total amount reaching the desired noise level (characterized by the pedestal variance value).

The simulation results are processed through VEGAS (see below in section 2.4.2) to produce look-up tables and effective areas. A lookup table has a value of the mean energy/width/length of simulated gamma-ray events with a particular combination of size and impact distance. One sub look-up table is made for each combination of:

1. zenith angle of 1, 10, 20, 30, 40, 50, 60, and 70 deg,

2. azimuth angle of 0, 45, 90, 135, 180, 225, 270, and 315 deg,

3. offset angle (the angle between the incoming direction of the simulated particle and the optical pointing direction of the telescope) of 0, 0.25, 0.5, 0.75, 1.0, 1.25, 1.5, 1.75, and 2.0 deg, and

4. pedestal variance of 4.73, 5.55, 6.51, 7.64, 8.97, 10.52, 12.35, 14.49, and 17.00. Each all-offset KASCADE look-up table file for upgrade array configuration consists of these 5184 sub look-up tables above. Different look-up tables are made for different array configurations (before and after the relocation of T1 in 2009 and the PMT upgrade in 2012) and season (Winter ATM21 and Summer ATM22).

For all simulated events with a combination of the above parameters at each energy, an "effective area" is calculated based on the simulated triggered rate and the number of simulated events. With the help of lookup table and effective area, standard VERITAS analysis can be performed. One can reconstruct each shower and get the gamma ray map, light curve and spectrum of a source. I have participated in the `KASCADE` detector modeling (model name "MDL15") of the VERITAS new-array configuration. A good agreement between the effective area produced by `KASCADE` using this model and by `CORSIKA` simulation package is shown in Figure 2.11.

Electron simulation With the goal of study cosmic ray electrons, we generated a set of electron simulations with `KASCADE` using the detector model "MDL15" following the steps described above. Electrons produce electromagnetic air showers which are identical to gamma-ray showers. Thus it is very difficult, if not impossible, to separate CR electrons and gamma rays. The general strategy for studying electrons with IACTs is to take observations at a region free of any gamma-ray source, and assume that all gamma-ray like air showers are dominated by the diffuse CR electron emission. A comparison between the shape of the MSW distribution from simulated gamma rays, electrons, protons, and helium particles are shown in Figure 2.12. Different from gamma rays, CR electrons are diffuse. This introduces another major difficulty in background (hadronic background) rejection: the whole field of view is occupied

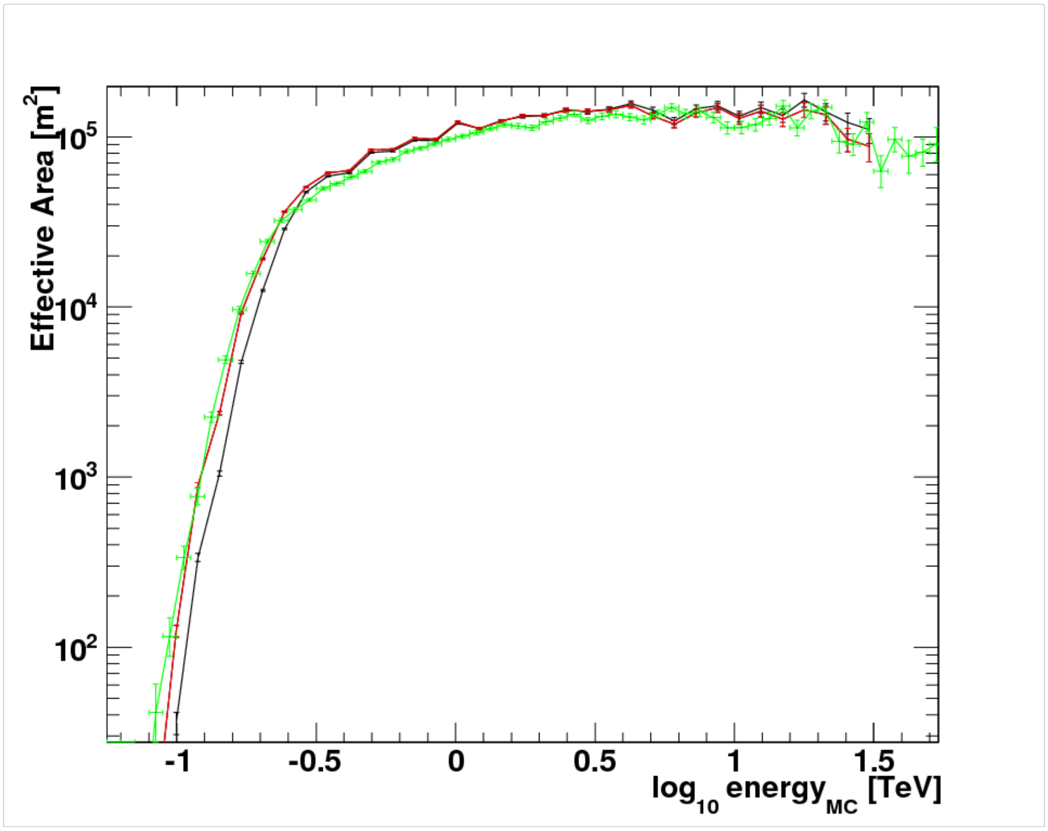

Figure 2.11.: A comparison between the `KASCADE` 7-sample (black), 12-sample (red), and `CORSIKA` 7-sample (green) effective areas for the VERITAS new-array configuration with medium cuts, using Winter atmosphere profile, at 20 deg zenith angle, 180 deg azimuth angle, 0.5 deg offset, and 5.5 σ above the pedestal variance.

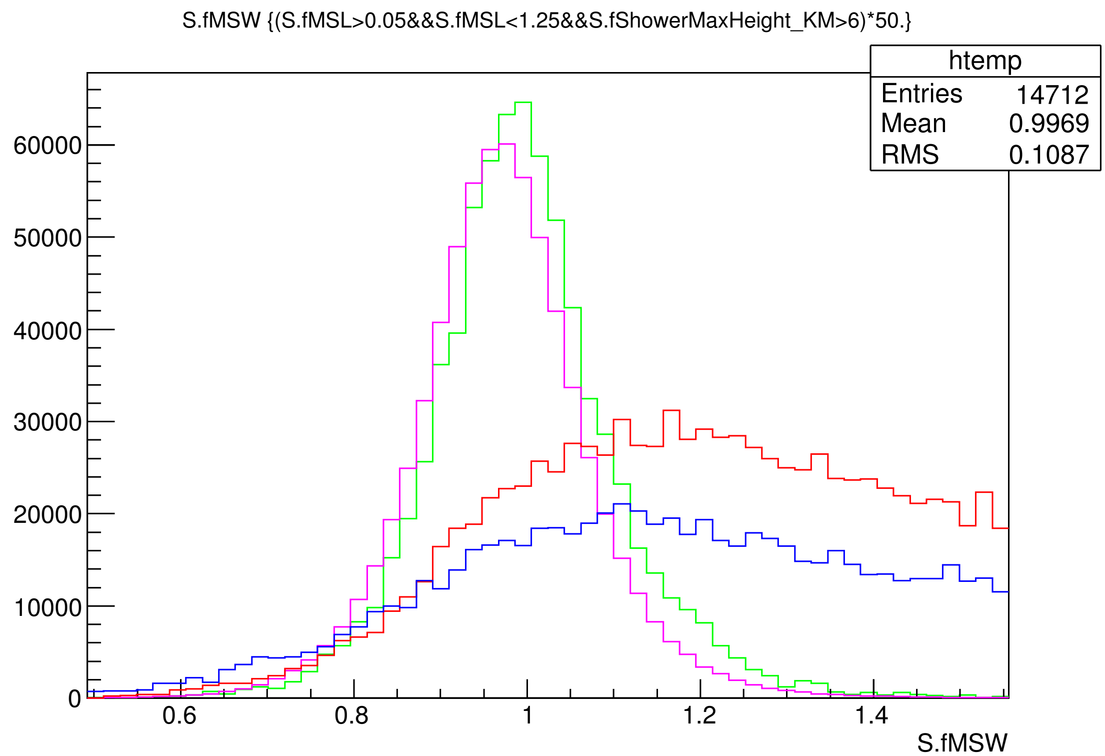

Figure 2.12.: A comparison between the MSW from (i) a fake Crab-like cosmic electron source (green), (ii) a simulated Crab-like gamma-ray source (magenta), (iii) simulated diffuse CR protons (red), and (iv) simulated CR helium cores (blue) using `KASCADE` simulations with the VERITAS new-array configuration, using Winter atmosphere profile, at 20 deg zenith angle and 180 deg azimuth angle. Cuts are made to select events with MSL between 0.05 and 1.25, and shower height greater than 6 km. The normalization is arbitrary.

by the “source” (CR electrons) and there is no possible background region. Thus background rejection has to be performed on a event by event basis. This is difficult because although the majority of CR protons and Helium ions produce different shower images, there are still a portion of CR hadronic showers that have similar air shower images after the cuts. The feasibility of selecting electron events based on image parameters is being studied. If this cannot be achieved, we should consider boosted decision tree (BDT) method to perform particle classification.

2.4.2 Data analysis

The two standard VERITAS data analysis packages are the VERITAS Gamma-ray Analysis Suite (VEGAS) (Cogan, 2008) and EventDisplay (Daniel, 2008).

VEGAS

I describe each stage of VEGAS analysis as follows. EventDisplay follows the same principles. VEGAS analysis is divided into 5 stages:

1. Stage 1 (calibration calculation) takes out the hardware dependencies from the raw CVBF data. The calibrations include (i) the flat-fielding of individual PMT gains, (ii) the NSB noise that fluctuates at each PMT (pedestal variance), (iii) the difference in time delay for signals to travel between PMTs and the FADCs, and (iv) optical pointing corrections. To help the relative gain corrections, a flasher run of a typical duration of 2 minutes is taken every observing night (Hanna et al., 2010), shining a uniform light on the PMTs from blue LEDs at seven alternating levels of intensities. Stage 1 produces a `ROOT` file for the data containing calibration results as well as the information of each event and the whole run. Another `ROOT` file is produced from the flasher run associated with the data. Both data and flasher `ROOT` files are fed to Stage 2.

2. Stage 2 (calibration application and image parameterization) applies the calibration results from stage 1 to each event and determines the parameters for this event. In stage 2, image cleaning is performed so that only pixels with a signal greater than 5 times the pedestal variance (picture pixels), or pixels with a signal greater than 2.5 times the pedestal variance (boundary pixels), are kept. The cleaned image is then parameterized. The parameters include distance, width, length, alpha, number of tubes, and size. Stage 2 saves the parameterization results and the calibrated events in a `ROOT` file.

3. Stage 4.2 (quality selection and shower reconstruction) reads in the image parameters from stage 2, apply quality cuts (size, number of tubes, and distance), and reconstruct the shower core, shower direction, and shower energy. The current pre-optimized quality cuts for the upgrade VERITAS array only select events with a minimum number of 5 picture and boundary pixels, a maximum distance of 1.43°, and a minimum size of 400 digital counts (dc) for soft-spectrum sources, or 700 dc for medium-spectrum sources, and 1200 dc for hard-spectrum sources. An energy look-up table produced by simulations is used in stage 4 for energy reconstruction. A look-up table containing separate sub look-up tables for different combinations of azimuth, zenith angle, offset, and noise level is made. In each sub look-up table, an energy value can be found providing an impact distance and a size. Similarly, a width look-up table and a length look-up table are used to find the mean (or median) value of the width and length of simulated gamma-ray showers, which is used to calculate MSW and MSL following equations 2.1 and 2.2. The shower reconstruction follows the principles described in the previous section 2.3. Stage 4 produces a `ROOT` file that contains the direction, time, energy, and image parameters (MSW/MSL etc.), ready for the analysis in the final Stage 6.

4. Stage 5 (shower cuts) performs shower-level cuts including MSW, MSL, shower height, and time cuts. If only a part of the run can be used due to weather

or hardware issues (L3 rates along with a series of diagnostic plots are used for data quality selections), it is necessary to use time cuts to select the usable period. Time cuts can only be applied in stage 5, while the rest of the cuts can be applied in stage 6 as well. Stage 5 is not mandatory in VEGAS analysis if there is no need for time cuts, but it reduces the files size and makes stage 6 run faster.

5. Stage 6 (results extraction) performs background estimations, flux estimation, and statistical calculations to produce sky maps, spectra, and light curves. Stage 6 reads in a Stage 4 or Stage 5 `ROOT` file that contains all gamma-ray-like events in the field-of-view for the entire run. It then selects an "On" region and one or more "Off" region for background subtraction (see below). Since the "On" and "Off" region may have different area and different offset, a parameter α is used to scale the "Off" number of counts to compensate this difference. Stage 6 looks for an effective area A associated with each event depending on its azimuth, elevation, offset, noise level, and energy. The effective area is determined from gamma-ray simulations. The live-time $\Delta t_{\rm live}$ is also estimated by correcting the difference in the elapsed time of the run between sequential events by the dead-time (monitored by L3 system). An "On" event is weighed by $1/(A\Delta t_{\rm live})$ to get a flux with the unit of photons m^{-2} s^{-1}; an "Off" event is weighed by $\alpha/(A\Delta t_{\rm live})$.

Background estimation

Although after three levels of triggers and multiple quality and shower cuts based on image parameters, the majority of cosmic ray showers are rejected, there are still a small fraction of gamma-ray like cosmic-ray showers that have passed all cuts. A final background estimation at the results extraction stage is necessary for testing whether there is a gamma-ray source at a particular "On" region, usually a circular region with a radius of 0.1° or 0.3° for point sources. We take full use of a prior assumption that the background cosmic rays are isotropic, and assume that the background flux in the “Off” regions is the same as that in the “On” regions. In observations taken

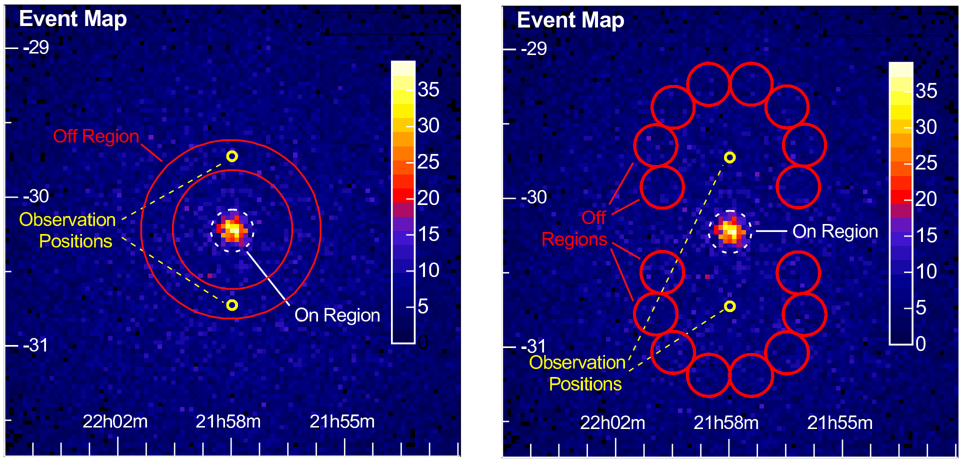

Figure 2.13.: A cartoon illustrating the “ring background mode” (left) and “wobble” mode (right). Plot taken from Berge et al. (2007).

in the “wobble” (or “reflected-region”) mode, the telescopes point at a direction that has a constant offset angle (usually 0.5°) with respect to the source. As a result, the “On” region around the source is 0.5° away from the center of the field of view, and “Off” regions can be chosen at “reflected” regions at the same offset so that both “On” and “Off” regions have the same acceptance (which is a function of offset) (Aharonian et al., 2001; Berge et al., 2007). More than one “Off” regions are usually used for better statistics, and a parameter $\alpha = area_{On}/area_{Off}$ is used to normalize the number of “Off” events N_{Off} to the same scale of the “On” events. The gamma-ray excess is then:

$$N_{Excess} = N_{On} - \alpha N_{Off}. \tag{2.3}$$

Different background region may be chosen (e.g. ring background mode; RBM), the difference in acceptance and area may both contribute to the α parameter.

The excess of gamma-rays can be converted to flux by weighing it with the inverse of effective area and exposure time. However, to examine the confidence level of the hypothesis that the gamma-ray excess comes from a source, rather than random fluctuation of background noise, we can calculate a significance value following equation 17 in Li & Ma (1983):

$$S = \sqrt{-2\ln\lambda} = \sqrt{2}\left\{N_{on}\ln\left[\frac{1+\alpha}{\alpha}\left(\frac{N_{on}}{N_{on}+N_{off}}\right)\right] + N_{off}\ln\left[(1+\alpha)\left(\frac{N_{on}}{N_{on}+N_{off}}\right)\right]\right\}^{\frac{1}{2}}. \tag{2.4}$$

The significance in the above equation is calculated from maximum likelihood ratio method, and is valid as long as N_{on} and N_{off} are not too few ($\gtrsim$10).

Other statistical inferences

The list of "On" events and "Off" events, together with all information associated with them (the key ones are the arrival time, the energy, the effective area, and the live exposure time), can be used for density estimations in time, direction, and energy domains to produce light curves, maps, and spectra. The most common way for such density estimation is a histogram. This part of the data analysis is independent of the particular type of instrument used. I describe some related concepts, especially focusing on time domain (and frequency domain) in the next chapter 3.

Recent development in alternative analyses

Several new alternative methods to separate gamma-ray events and cosmic ray events are being developed, each of them can improve the current analysis dramatically in certain circumstances at the expense of more computational resources. I list a few examples (by no means complete) as follows:

1. Machine learning methods (e.g. boosted decision trees Ohm et al., 2009) using Hillas parameters as training features were used. They are helpful for extended

or isotropic sources e.g. cosmic electrons, since they do not rely on background regions.

2. Image template analyses (e.g. Fancy Reconstruction by Optimization over Gamma ray Simulations, FROGS; or "HFit" method) that directly compares a shower image with a semi-analytical prediction based on a large database of simulated images (e.g. Le Bohec et al., 1998; de Naurois & Rolland, 2009) are being studied. These template analyses are more accurate when a shower image falls near the edge of the camera, and is partially cut off.

3. A displacement (disp) method (see section 2.3.1), an alternative to the currently used geometric (geo) method, for determining the shower direction (Beilicke & VERITAS Collaboration, 2012) is used. The disp method offers a more reliable shower direction reconstruction when the shower images are parallel to each other. This is especially useful for large-zenith-angle observations.

4. A three-dimensional model of the shower is being studies, as a better alternative to the two-dimensional Hillas parameters. The 3D model improves the accuracy in the reconstruction on the shower height, which becomes the most important discriminator at lower energies since MSW becomes less powerful at lower energies (low-energy CR showers bare more resemblance to gamma-ray showers).

5. A complex maximum likelihood method (MLM) is being studied, which can greatly improve the sensitivity for extended emission.

6. A crescent background model is used in Dwarf galaxy studies to maximize the statistics (Zitzer & for the VERITAS Collaboration, 2013a).

3. Variabilities of gamma-ray active galactic nuclei

In section 3.1 and 3.2, I briefly describe the background of AGN, including the history and unified scheme. In section 3.3, I introduce the simplest blazar model, one-zone SSC model, based on section 1.1.3 of chapter 1. In section 3.4, I describe the multiwavelength observations on two blazars, BL Lacertae and Mrk 421. In section 3.5, I describe some common formats of astronomical time series, present interesting results from the observations described in section 3.4, including a fast TeV flare from BL Lacertae, and simultaneous X-ray and TeV observations of Mrk 421, and discuss what we can learn from flares of these two blazars. In section 3.6, I describe the global variability on longer timescales, focusing on the frequency domain.

3.1 History

In the 1950s, a large amount of discrete radio "stars" were discovered but difficult to be associated with optical sources, mainly due to uncertainties in their positions and angular sizes Baade & Minkowski (1954). With radio data alone, the distances of many of these objects could not be unambiguously determined. In 1963, the study of optical Balmer lines from 3C 273 yielded a redshift of $\sim$0.158 (see Figure 1.3 in chapter 1). This observation strongly suggests that 3C 273 is the compact nuclear region, which has a diameter of less than 1 kpc, of a galaxy $\sim$600 Mpc away. The inferred luminosity of this nuclear region was $\sim 10^{40}$W, which is $\sim$1000 times brighter than the entire Milky Way galaxy. 3C 273 was then famously established as the first quasar Schmidt (1963).

The zoo of AGNs expanded rapidly with the development of telescopes with increasing angular and spectral sensitivity in different wavelengths. By the early 1990s, there were more than 10 types of AGNs based on the different observed properties:

(i) based on the radio loudness AGNs are divided into radio-loud ones and radio-quiet ones; (ii) based on optical emission line width, they are divided into type I AGNs with broad emission lines and type II AGNs with narrow emission lines. These two criteria roughly divide all AGNs into four subsets. Each subset may be further divided into more subclasses depending on other observed features. For example, radio-loud Type I AGNs are narrow-line radio galaxies (NLRGs), but are further divided into Fanaroff Riley I (FRI) and II (FRII) radio galaxies based on radio morphology.

Since the detection of Mrk 421 with the Whipple 10 m telescope (Punch et al., 1992), AGN have been established as TeV sources (see chapter 1 for an brief introduction of AGN as TeV sources). They are the most promising sources of UHECRs and high energy cosmic neutrinos.

3.2 Unified scheme of AGN

AGNs collectively exhibit a list of extreme properties:

1. high luminosities,
2. compact sizes,
3. broad-band, non-thermal emission,
4. radio jets and lobes,
5. strong variability in all wavelengths on all timescales,
6. bright UV or X-ray emissions,
7. polarized emission in radio and optical bands, and
8. weak but very broad optical emission lines.

Each property in this list can be explained by a component of an AGN. A supermassive black hole in the center powers the entire AGN through accretion process. A hot accretion disk is formed due to the conservation of angular momentum. The material

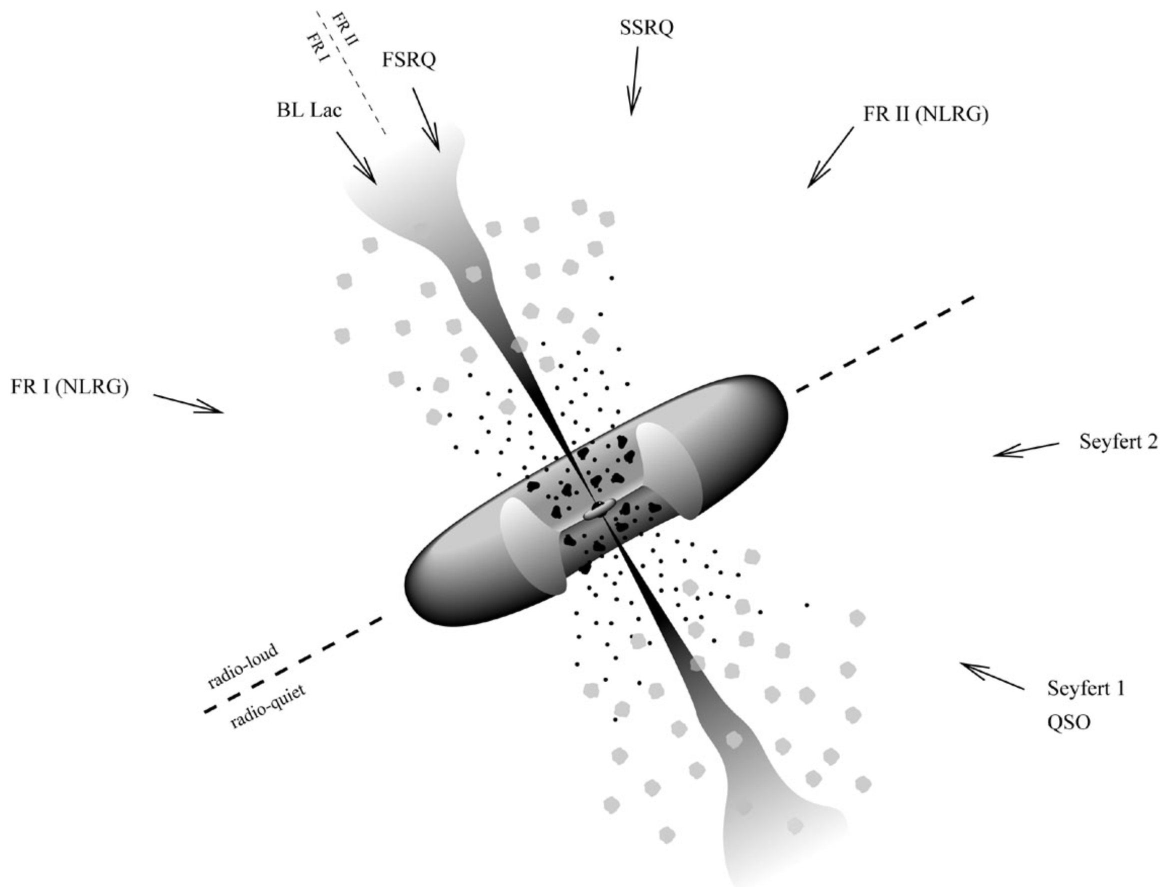

Figure 3.1.: A cartoon of the unified scheme of AGN Urry & Padovani (1995). In this scheme, an AGN is composed of a central SMBH (shown as the central black dot) surrounded by a compact and hot accretion disk (shown as the small grey contour around the central black dot), some hot corona (shown as small black blobs) around the disk, a broad-line region (BLR; shown as large black dots) of fast-moving gas clouds close to the center, a narrow-line region (NLR; shown as larger grey dots) of much farther and slower gas, a torus (shown as the large grey torus) made of cold dust far away from the center in the plane of the disk, and a relativistic jet in some cases. Note this cartoon is not to scale. Image courtesy of NASA/IPAC Extragalactic Database (NED).

in the accretion disk loses angular momentum slowly as a result of viscosity or turbulence. The lost angular momentum is converted into heat, therefore the accretion disk appears to be hot and produces thermal emission in ultraviolet (UV) or X-ray wavelengths. The material is ionized to a plasma state in the hot rotating accretion disk, and produces an electromagnetic field which then leads to non-thermal radiation observed from the AGN. The magnetic field near the black hole is very strong, since the magnetic flux is frozen into the material being accreted. Up to 10% of the vast amount of gravitational potential energy of a SMBH is eventually converted to electromagnetic radiation. The strong radiation from the accretion disk ionizes the gas cloud around the central SMBH that forms the broad-line region (BLR). Some

TABLE 1
AGN Taxonomy

Optical Emission Line Properties

Radio Loudness	**Type 2** (Narrow Line)	**Type 1** (Broad Line)	**Type 0** (Unusual)	
Radio-quiet:	Sy 2 NELG IR Quasar?	Sy 1 QSO	 BAL QSO?	Black Hole Spin?
Radio-loud:	NLRG { FR I, FR II }	BLRG SSRQ FSRQ	Blazars { BL Lac Objects, (FSRQ) }	

Decreasing angle to line of sight

Table 3.1.: AGN Taxonomy by Urry & Padovani (1995).

AGN ($\sim$ 10%) exhibit highly-collimated bipolar jet features that transport material from the center to up to thousands of light years away. Particles, both leptons and hadrons, are accelerated to extremely relativistic speed at the base of the jet, and produce strongly beamed radiation. By combining these components spatially together, a unified scheme of AGN was proposed by Urry & Padovani (1995) (a cartoon is shown as Fig. 3.1). However, the detailed properties (shape, size, formation, evolution etc) of the components of AGN are not completely understood.

This thesis focuses on blazars, a dramatic subclass of AGN with their jets pointing at the observers. The lack of strong emission lines in their optical spectra, the non-thermal appearance of their broadband spectra and the rapid variability suggest that blazar emission originates in relativistic jets closely aligned to our line of sight (e.g. Schlickeiser, 1996). Under the unified scheme, the differences between subclasses of AGNs can be explained by the presence of the jet and difference in viewing angle. Therefore, the studies of blazars may help the understanding of all AGNs.

3.3 Theoretical models of radiative mechanisms - the simplest case

A couple of key questions are still open regarding the studies of TeV blazar jets:

1. What type of particles are emitting VHE gamma rays observed in blazar jets? Are they UHE cosmic ray and neutrino sources?

2. How are the particles accelerated? How do they radiate?

3. Where is the VHE emission produced in blazar jets?

4. How does VHE emissions escape the absorption caused by pair production with lower energy photons?

These questions ultimately need to be addressed by the observations. Many models are proposed to explain the observed features from blazars, mainly the two-peak SED, the fast variability, polarizations, and flickr-noise power spectrum.

SSC model In section 1.1.3 of chapter 1, I briefly introduced relevant radiative processes in VHE astronomy, and listed a few detailed models in the context of blazars. In this section, I describe the simplest model of blazars: one-zone synchrotron self-Compton (SSC) model (e.g. Jones et al., 1974; Ghisellini et al., 1985; Bloom & Marscher, 1996; Finke et al., 2008). This model assumes one homogeneous emitting zone of a radius R moving relativistically in the jet with a bulk Lorentz factor of Γ at an angle of θ with respect to the observer. The Doppler factor of the emitting region $\delta = 1/(\Gamma(1-\beta cos\theta))$ captures the relativistic beaming effect (see section 1.1.3 in chapter 1). The emitting region contains a magnetic field with strength B, and a single population of relativistic electrons with energy density w_e, the number density distribution of which follows a broken power-law $dN/d\gamma \propto \gamma^{-p1}, \gamma_{min} < \gamma < \gamma_{br}$ and $dN/d\gamma \propto \gamma^{-p2}, \gamma_{br} < \gamma < \gamma_{max}$. Here γ is the Lorentz factor of the electrons (the energy of the electron is therefore $\gamma m_e c^2$), and γ_{min}, γ_{br}, and γ_{max} correspond to the minimum, break, and maximum energies, respectively. These electrons loses energy through synchrotron radiation with the presence of magnetic field, producing a synchrotron photon population corresponding to the low-energy SED peak (see Figure 3.2). These synchrotron photons subsequently inverse-Compton scatter upon the same population of electrons (so-called SSC), producing the higher-energy photons that also forms a peak in the SED. The break in the electron distribution is a consequence of the radiative cooling, though note that the actual electron distribution may have more than one cooling break corresponding to different cooling channels (synchrotron and IC in this model). The energy of the electrons are restricted between E_{min} and E_{max}. The maximum electron energy E_{max} is determined by the cooling time, acceleration time, and R, and it governs the highest energy of the photon.

Figure 3.2 shows the SEDs of the radiation from the electrons following a static SSC model described in Krawczynski et al. (2002). The double-peak is apparent, the same as observed SEDs from blazars. Different parameters in the SSC model are changed independently for visualization of their effect on the shape of the SED, e.g. the peak frequencies of synchrotron emission ν_{syn} and SSC emission ν_{SSC}, and the ratio between SSC peak and synchrotron peak η (or Compton dominance). Li & Kusunose (2000) suggests that the relation is different in fast-cooling regime and slow-cooling regime, the definition of which can be found in section 1.1.3 in chapter 1. Following the studies of Li & Kusunose (2000), a unique set of solutions of the SSC model can be found in the slow-cooling time regime assuming SSC happens in the Klein-Nishina regime. Some relations are given below:

$$\begin{aligned}
\nu_{syn} &\approx 2.8 \times 10^{-6} \delta \gamma_{max}^2 B, && (3.1)\\
\nu_{SSC} &\approx 1.236 \times 10^{-20} \delta \gamma_{max}, && (3.2)\\
B &\approx 5.46 \times 10^{33} \delta \frac{\nu_{syn}}{\nu_{SSC}^2}, && (3.3)\\
\eta &\propto \frac{U_{ph}}{U_B} \propto \delta^8, && (3.4)
\end{aligned}$$

where B is in the unit of Gauss, U_{ph} is the energy density of the synchrotron photon field, and U_B is the magnetic energy density. In slow-cooling regime, only emission from the highest energy electrons (i.e. the falling edge of the synchrotron and SSC peak) can undergo fast variations.

However, several important predictions are made by Li & Kusunose (2000) in the fast-cooling time regime:

1. the SSC model is able to produce fast variabilities in all wavelengths;

2. the spectrum is soft and curved at highest observed photon energies ($\gtrsim$TeV) due to the combination of Klein-Nishina effect and the fast cooling (therefore soft) electrons;

3. spectral variation is fast at the tails of the peaks (e.g. keV and TeV), and much slower at the rising edges of the spectral peaks;

4. hysteresis patterns should exist, and the direction of the hysteresis loops depends on the injected energy of the electrons;

5. during a decay (or flare), the peak energies ν_{syn} and ν_{SSC} shifts at different rates of γ^2 and γ, respectively.

There are many other models of blazars, assuming e.g. more emitting regions and electron populations, different photon sources for IC scattering (external Compton models), and other type of emitting particles (hadronic models). Considering the large number of parameters in these models, their differences in the resulting SED are usually subtle. As described in the above SSC model, dynamic changes in spectra and light curves can be a very effective method to discriminate among models.

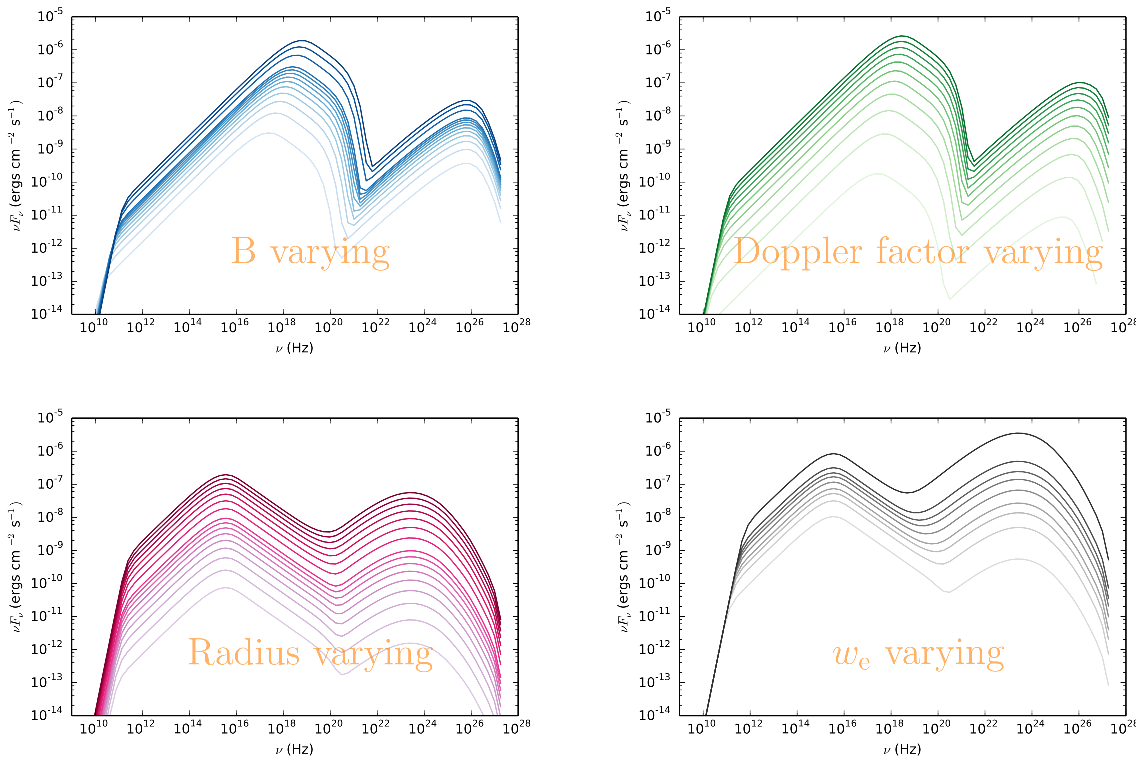

Figure 3.2.: Theoretical predictions of broadband SED from a one-zone static SSC model. Each panel corresponds to a series of SED with one parameter varying. From lighter to darker color, the value of the parameter increases. Top left panel: SEDs with the magnetic field B varying from 0.1 to 2.5 μG; top right panel: SEDs with the Doppler factor ranging from 5 to 55; bottom left panel: SEDs with the radius of emitting region R changing from 4×10^{13} to 5.5×10^{14} m; bottom right panel: SEDs with the electron energy density w_e varying from 0.001 to 0.08 erg cm^{-3}.

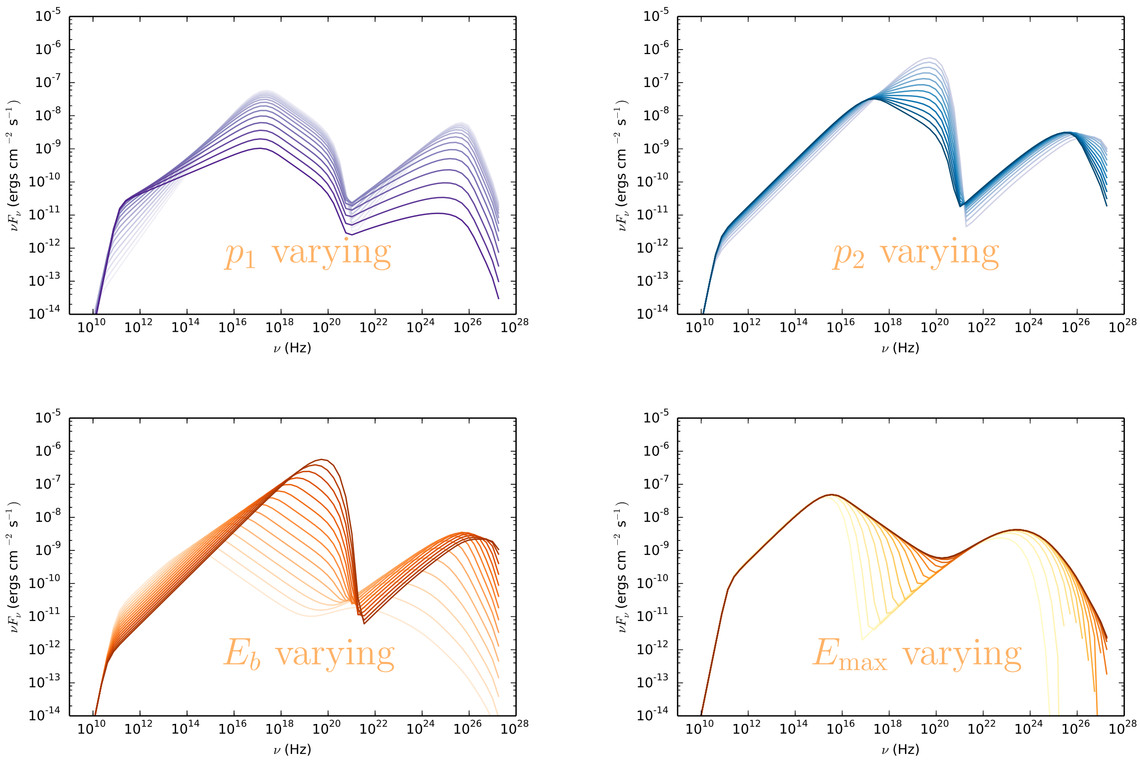

Figure 3.3.: Theoretical predictions of broadband SED from a one-zone static SSC model similar to Figure 3.2. Each panel corresponds to a series of SED with one parameter varying. From lighter to darker color, the value of the parameter increases. Top left panel: SEDs with the electron spectral index before the break p_1 varying from 1.0 to 2.4; top right panel: SEDs with the electron spectral index after the break p_2 varying from 1.6 to 3.8, while p_1 is fixed at 1.6, and E_b at $10^{10.5}$ eV; bottom left panel: SEDs with the breaking energy E_b changing from $10^{9.0}$ to $10^{11.8}$ eV, corresponding to the Lorentz factor of electrons from 2×10^3 to 1.2×10^6; bottom right panel: SEDs with the maximum energy $E_{\rm max}$ varying from $10^{9.6}$ to $10^{12.8}$ eV, corresponding to Lorentz factor from 7.8×10^3 to 1.2×10^7.

3.4 Multiwavelength AGN observations

One of the most interesting features observed from blazars is the fast variability at very high energies. In the most extreme cases, the timescale of gamma-ray variability can be as short as a few minutes at VHE. Such variability has been detected in three HBLs (Mrk 421 (Gaidos et al., 1996), Mrk 501 (Albert et al., 2007b), and PKS 2155-304 (Aharonian et al., 2007)), an LBL (BL Lacertae (Arlen et al., 2013)), and a FSRQ (PKS 1222+21 (Aleksić et al., 2011)). As described in chapter 1, variability of blazars could be related to different particle acceleration models, e.g. internal shocks in the jets (Rees, 1978; Spada et al., 2001), to major ejection of new components of relativistic plasma into the jet (e.g. Böttcher et al., 1997; Mastichiadis & Kirk, 1997), and to magnetic reconnection events (similar to solar flares, see e.g. Lyutikov, 2003).

The SED of a TeV blazar often evolves significantly during a major flare. It is believed that the two SED peaks are usually correlated (Fossati et al., 1998), although the correlation is not always apparent. For instance, some of the TeV gamma-ray flares detected have no simultaneous X-ray counterparts (Krawczynski et al., 2004; Błażejowski et al., 2005), which presents a severe challenge to the leptonic and hadronic models alike (see section 1.1.3 in chapter 1).

Since blazars are broadband emitters, observations need to cover a wide range of wavelengths. Due to their highly variable nature, the MWL observations need to be simultaneous in order to catch the broad-band spectra at the same flux level. There are many MWL campaigns dedicated to simultaneous observations on the few brightest TeV blazars. The X-ray and TeV bands are especially focused on, since they are both produced by the electrons with the highest energies (as described in previous section). However, fast flares on the timescale of minutes have been observed from blazars at VHE band, revealing some of their most interesting properties, while challenging the strategies of the observations as well.

Firstly, it is difficult, if not impossible, to predict when a blazar will flare, due to the stochastic nature of its emission. Secondly, it takes time to coordinates target-of-opportunity (ToO) observations with X-ray satellites and ground based telescopes in response of a spontaneous flaring event, giving rise to risks of actual observations missing the flares. Thirdly, most of the current X-ray satellites have a relatively short orbital period, and are frequently interrupted by Earth occultation and South Atlantic Anomaly (SAA) passage; and the observations from ground based Cherenkov telescopes may be affected by the weather.

In this section, I describe observations of BL Lacertae and Mrk 421 in different wavelengths. In the next section, I describe the temporal and spectral analysis of the data and present the results.

3.4.1 BL Lacertae

BL Lacertae (also known as 1ES 2200+420 or VER J2202+422) is the prototype of the class "BL Lac object". It was originally discovered in optical by Hoffmeister (1929). The host galaxy of BL Lacertae is most likely an elliptical galaxy located at a redshift of $z = 0.069$ (Miller et al., 1978). The mass of the central black hole in BL Lacertae was measured to be $\sim 1.3 \times 10^{8} M_{\odot}$ using stellar velocity dispersion (Barth et al., 2003). Early multiwavelength observations of BL Lacertae from the year 1968 to 1988 were summarized by Bregman et al. (e.g. 1990), showing some typical blazar features including (i) variable and polarized optical and IR emissions; (ii) synchrotron cooling spectral break at optical IR wavelengths, and possibly SSC spectral peak at higher energies; (iii) polarized, superluminal components, including a core and knots, identified at radio frequencies.

As described in section 3.2, blazars consist of BL Lac objects and FSRQs, both are radio-loud AGNs with a jet pointing towards the observer. The difference between BL Lac objects and FSRQ is based on the equivalent width (EW) of the broad-line emission, which is < 5Å for BL Lacs and > 5Å for FSRQs. Although BL Lacertae was long thought to be the archetypical BL Lac object, Vermeulen et al. (1995) found in the observations in 1995 that the $H\alpha$ line in BL Lacertae was stronger than previous observations, reaching $6-7$Å. The classification of BL Lacertae is thus very ambiguous, we adopt the class of low-frequency peaked BL Lac object for it in this work. However, due to the variable nature of blazars, the EW of their broad-line emission is also variable mainly due to the variance of the continuum emission, and several sources including BL Lacertae have “transitioned” between BL Lac and FSRQ. Therefore, it may be more appropriate to call these sources “transition” blazars (Ruan et al., 2014).

BL Lacertae exhibits high variabilities at all wavelengths. As mentioned above, at optical wavelengths the source varies both in continuum and line emissions. Corbett et al. (1996) confirmed the $H\alpha$ results mentioned above, and observed a rapid decrease of V-band magnitude by ∼0.1 mag in 30 minutes.

BL Lacertae was originally identified as a radio source by Schmitt (1968), and has been extremely variable in radio frequencies. For example, four major outbursts at 4.8, 8.0, and 14.5 GHz were observed from 1980 to 1984, two of which were accompanied with a simultaneous rise in polarization percentage and swing of polarization angle (Aller et al., 1985). Note that in these observations the polarization fraction increases as the the flux increases.

At VHE energies, the Crimean Observatory reported a detection of the source at >100% of the steady Crab Nebula flux (Crab Unit; C. U.) above 1 TeV In 1998 (Neshpor et al., 2001). Subsequently, the MAGIC Collaboration reported another detection during an active state in 2005, but at a much lower flux level (only about 3% of the steady C. U.) (Albert et al., 2007a).

BL Lacertae entered an active period since 2011, exhibiting a series of major outbursts in many wavelengths (see e.g. Raiteri et al., 2013). Triggered by activities seen with the *Fermi* LAT (Cutini, 2011) and AGILE (Piano et al., 2011) at GeV gamma-ray energies, as well as in the optical (Larionov et al., 2011), near-IR (Carrasco et al., 2011), and radio (Angelakis et al., 2011) bands in 2011 May, we began to monitor BL Lacertae more regularly at TeV gamma-ray energies with VERITAS.

The source was detected by VERITAS during a rapid, intense VHE gamma-ray flare on MJD 55740 (2011 June 28).

In the following subsections, I describe the MWL observations of BL Lacertae around the time of the 2011 flare. The results and discussions of these observations are presented in later sections. This part of the work was published in Astrophysical Journal (Arlen et al., 2013).

VHE-gamma-ray observations of BL Lacertae

Prior to the intensified MWL monitoring campaign in 2011, BL Lacertae had also been observed by VERITAS on a number of occasions, mostly with the full array. The data from those observations are also used in this work to establish a longer baseline. The total exposure time (after quality selection) amounts to 20.3 hrs from 2010 September to 2011 November, with zenith angles ranging from 10 to 40 degrees. The source was not detected throughout the time period, except for one night on MJD 55740 (2011 June 28), when the automated realtime analysis revealed the presence of a rapidly flaring gamma-ray source in the direction of BL Lacertae. On that night, BL Lacertae was observed only with three telescopes in the "wobble" mode (see section 2.4.2) with $0.5°$ offset, because one telescope was temporarily out of commission. Starting at 10:22:24 UTC, two 20-minute runs were taken on the source under good weather conditions, with the zenith angle varying between 10 and 13 degrees. No additional runs were possible due to imminent sunrise. The total exposure time was 34.6 minutes.

The data were analyzed using the VEGAS package (described in section 2.4.2 of chapter 2). The standard data quality cuts (identical for the four- and three-telescope configuration), which were previously optimized for a simulated soft point source of $\sim$6.6% of the C. U. at 200 GeV and a photon index of 4, were applied to the shower images. The cuts used were: an integrated charge lower cut of 45 photoelectrons, a distance (between the image centroid and the center of the camera) upper cut of 1.43 degrees, a minimum number of pixels cut of 5 for each image, inclusive, mean scaled width and length cuts $0.05 < \mathrm{MSW} < 1.15$, and $0.05 < \mathrm{MSL} < 1.3$, respectively. A cut of $\theta^2 < 0.03\ \mathrm{deg}^2$ on the size of the point-source search window was made, where θ is the angle between the reconstructed gamma-ray direction and the direction to the source. A specific effective area corresponding to these cuts and the relevant array configuration was generated from simulations and was used to calculate the flux. The reflected-region background model (Berge et al., 2007) was applied for background estimation, a generalized method from Li & Ma (1983) was used for the calculation of statistical significance, and upper limits were calculated using the method described by Rolke et al. (2005). The results were confirmed by an independent secondary analysis with the EventDisplay package, as described in Daniel (2008).

The VERITAS analysis showed an excess of 212 γ-like events, corresponding to $11.0 \pm 0.8\ \gamma/\mathrm{min}$ and a 21.1 standard deviation (σ) detection of BL Lacertae in the first observation run on MJD 55740 (2011 June 28), with an effective exposure of 19.3 minutes starting at 10:22:24 UTC. The second run, with an effective exposure of 15.3 minutes, yielded an excess of only 33 γ-like events, corresponding to a 4.1σ detection. The VERITAS analysis of 19.7-hour data from 2010 September to 2011 November, excluding the two flaring runs, showed an excess of 21 γ-like events, and a statistical significance of 0.28σ.

High-energy-gamma-ray of BL Lacertae

The *Fermi* Large Area Telescope (LAT) is a pair-conversion high-energy gamma-ray telescope covering an energy range from about 20 MeV to more than 300 GeV (Atwood et al., 2009). It has a large field-of-view of 2.4 sr, and an effective area of $\sim 8000\ \mathrm{cm}^2$ for > 1 GeV. In its nominal (survey) mode, the *Fermi*-LAT covers the full sky every 3 hours.

During the time window when VERITAS detected a rapid flare on MJD 55740 (2011 June 28), BL Lacertae was in the field of view of the LAT for about 16 minutes (MJD 55740.431 - 55740.442). In analyzing the simultaneous LAT data, we selected *Diffuse* class photons with energy between 0.2 and 10 GeV in a $16° \times 16°$ region of interest (ROI) centered at the location of BL Lacertae. Only events with rocking angle $< 52°$ and zenith angle $< 100°$ were selected. The data were processed using the publicly available *Fermi*-LAT tools (`v9r23p1`) with standard instrument response functions (`P7SOURCE_V6`). For such a short exposure, a very simple model containing the source of interest and the contribution of the galactic (using file `gal_2yearp7v6_v0.fits`) and isotropic (using file `iso_p7v6source.txt`) diffuse emission was used. The contribution of the other known gamma-ray sources in the ROI is assumed to be negligible compared to that of BL Lacertae and the diffuse emission.

The model is fitted to the data using a binned likelihood analysis (`gtlike`), where the only free parameters are the spectral normalization and the power-law index of BL Lacertae. The contribution of the galactic and isotropic diffuse emission was fixed to a normalization of 1.0, which is compatible with the values obtained when analyzing the same field of view during longer timespans. The results are used to construct an energy spectrum of BL Lacertae. We also performed an unbinned likelihood analysis and obtained similar spectral results.

For comparison, we repeated the analyses for a longer period (of 24 hours) centered at the time of the VERITAS observations, as well as for times prior to the VERITAS-detected flare (between 2011 May 26 and 2011 June 26, or MJD 55707–55738). For the latter, we adopted a source model that incorporates all sources in the 2FGL catalog within the ROI and within 5 degrees of the ROI edges. The spectral results were extracted by adopting a custom spectral code (`SED_scripts`) available on the *Fermi*-LAT website. In all cases, the LAT spectrum of BL Lacertae can be well described by a power law, which justifies the assumption made in the likelihood analyses.

A daily-binned light curve integrated above 0.1 GeV was derived covering the period MJD 55652-55949 (2011 April 01 - 2012 Jan 23) using the likelihood method described above. In each 1-day bin, the flux and the corresponding 1σ error are calculated if the test statistic (TS) value is greater than 1, otherwise an upper limit is calculated.

X-ray and ultraviolet observations of BL Lacertae

BL Lacertae was also observed with the XRT and UVOT instruments on board the *Swift* satellite (Gehrels et al., 2004) contemporaneously with the gamma-ray flare in 18 exposures between MJD 55704 (2011 May 23) and MJD 55768 (2011 July 26), including six $\sim$2 ks Target of Opportunity (ToO) observations on six nights following the VHE flare on MJD 55740. The combination of the X-ray telescope (XRT) and UV/optical telescope (UVOT) provided useful coverage in soft X-rays and UV, although none of the observations were simultaneous with the VERITAS observations during the flare.

We analyzed the XRT data using the `HEASOFT` package (version 6.11). The event files are calibrated and cleaned using the calibration files from 2011 September 5. The data were taken in the photon-counting (PC) mode, and were selected from grades 0 to 12 over the energy range 0.3-10 keV. Since the rates did not exceed 0.5 counts per second, pile-up effects were negligible. Source counts were extracted with a 20 pixel radius circle centered on the source, while background counts were extracted from a 40 pixel radius circle in a source-free region. Ancillary response files were generated using the `xrtmkarf` task, with corrections applied for the point-spread function (PSF) losses and CCD defects. The corresponding response matrix from the XRT calibration files was applied. The spectrum was fitted with an absorbed power law model, allowing the neutral hydrogen (HI) column density (N_H) to vary. The best fitted value of N_H is $(0.24 \pm 0.01) \times 10^{22}$ cm^{-2}, which is in agreement with the result of $N_H = 0.25 \times 10^{22}$ cm^{-2} presented by Ravasio et al. (2003), but is larger than the value of $N_H = 0.18 \times 10^{22}$ cm^{-2} from the Leiden/Argentine/Bonn (LAB) survey of galactic HI (Kalberla et al., 2005).

The UVOT cycled through each of the optical and the UV pass bands V, B, U, UVW1, UVM2 and UVW2. Data were taken in the *image mode* discarding the photon timing information. Only data from UVW2 band are shown in this work; the other bands roughly track UVW2. The photometry was computed using an aperture of 5" following the general prescription of Poole et al. (2008) and Breeveld et al. (2010). Contamination by background light arising from nearby sources was removed by introducing *ad hoc* exclusion regions. Adopting the N_H value provided by the XRT analysis and assuming $E(B-V) = 0.34$ mag (Maesano et al., 1997), we estimated $R_V = 3.2$ (Güver & Özel, 2009). Then, the optical/UV galactic extinction coefficients were applied (Fitzpatrick, 1999). The host galaxy contribution has been estimated using the PEGASE-HR code (Le Borgne et al., 2004) extended for the ultraviolet UVOT filters. Moreover, there is no pixel saturation in the source region and no significant photon loss. Therefore, it is possible to constrain the systematics to below 10%.

Optical observations of BL Lacertae

As part of the Steward Observatory spectropolarimetric monitoring project (Smith et al., 2009), BL Lacertae was observed regularly with the 2.3m Bok Telescope and the 1.54m Kuiper Telescope in Arizona. Measurements of the V-band flux density and optical linear polarization are from the Steward Observatory public data archive (`http://james.as.arizona.edu/~psmith/Fermi/`). The data were reduced and calibrated following the procedures described by Smith et al. (2009). We note that there is a 180-degree degeneracy in polarization angle, so we shifted some polarization angles by 180 degrees to minimize the change between two consecutive measurements. No corrections to the data have been made for the contribution from the host galaxy, or interstellar polarization, extinction and reddening. However, these issues have little effect on variability studies.

Radio observations of BL Lacertae

BL Lacertae was observed with the VLBA at 43 GHz, roughly once a month, as part of the monitoring program of gamma-ray bright blazars at Boston University (`http://www.bu.edu/blazars/VLBAproject.html`). Two extra epochs of imaging were added via Director's Discretionary Time on 2011 July 6 and 29. The data were correlated at the National Radio Astronomy Observatory in Socorro, NM, and then analyzed at Boston University following the procedures outlined by Jorstad et al. (2005). The calibrated total and polarized intensity images were used to investigate the jet kinematics and to calculate the polarization parameters (degree of polarization p and position angle of polarization χ) for the whole source imaged at 43 GHz with the VLBA and for individual jet components. The uncertainties of polarization parameters were computed based on the noise level of total and polarized intensity images and do not exceed 0.6% and 3.5 degrees for degree of polarization and position angle of polarization, respectively.

BL Lacertae is also in the sample of the Monitoring Of Jets in Active galactic nuclei with VLBA Experiments (MOJAVE) program. For this work, we only used results from polarization measurements at 15.4 GHz. The data reduction procedures are described by Lister et al. (2009). Briefly, the flux density of the core component is derived from a Gaussian model fit to the interferometric visibility data. Polarization properties of the core are then derived by taking the mean Stokes Q and U flux densities of the nine contiguous pixels that are centered at the Gaussian peak pixel position of the core fit. The results include fractional linear polarization, electric vector position angle (note the 180-degree degeneracy), and polarized flux densities. The flux density has an uncertainty of $\sim 5\%$, and the position angle of polarization has an uncertainty of ~ 3 degrees.

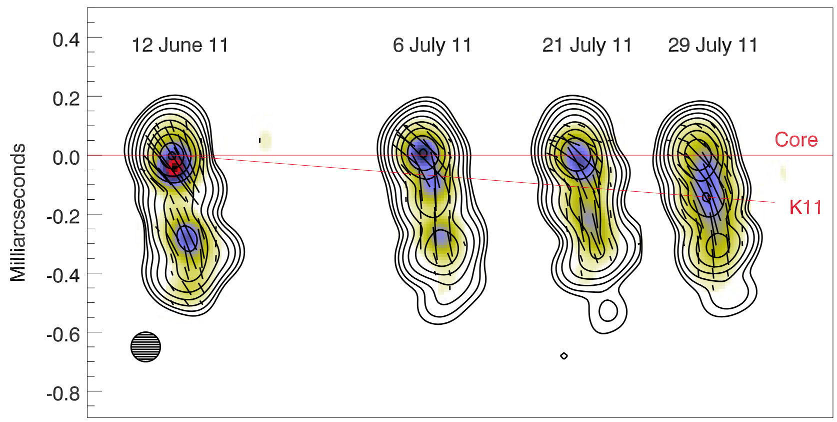

Figure 3.4.: 43 GHz VLBA images of BL Lacertae at four epochs around the time of the TeV gamma-ray flare. The images are convolved with a circular Gaussian function (represented by the circle in the bottom-left corner) that has a full width at half maximum of 0.1 mas (i.e., ∼0.15 pc at the distance of 311 Mpc), the approximate resolution of the longest baselines of the array. Contours correspond to total intensity, with levels in factors of 2 from 0.25%, plus an extra contour at 96%, of the peak intensity of 2.16 Jy beam^{-1}. Color represents linearly polarized intensity, with maximum (black) of 0.103 Jy beam^{-1} followed by red, blue, yellow, and white (no polarization detected). Red lines mark the position of the assumed stationary core and the superluminally moving knot K11, each of which has a distinct polarization position angle.

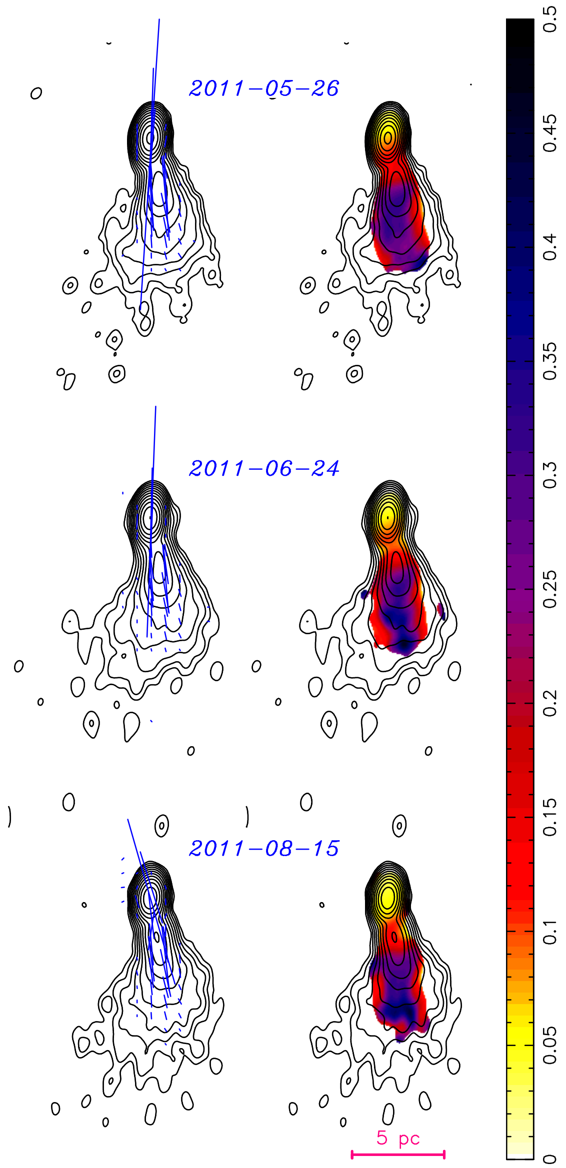

Figure 3.5.: MOJAVE 15.4 GHz VLBA images of BL Lacertae at three epochs in 2011, showing a change in core polarization after the 2011 June 28 TeV flare. The images on the left show total intensity contours, with electric polarization vectors overlaid in blue. The images on the right show total intensity contours with fractional linear polarization in color. The polarization color scale ranges from 0 to 50%. The images have been convolved with the same Gaussian restoring beam having dimensions 0.89 mas $\times$ 0.56 mas and position angle -8 degrees. The base contour levels in each image are 1.3 mJy beam^{-1} in total intensity and 1 mJy beam^{-1} in polarization. The angular scale of the image is 1.29 pc mas^{-1}.

For better sampling, we used data from blazar monitoring programs with the Owens Valley Radio Observatory (OVRO) at 15.4 GHz, with the Metsähovi Radio Observatory (MRO) at 37 GHz, and with the Submillimeter Array (SMA) at 230 and 350 GHz, respectively. The OVRO 40 m uses off-axis dual-beam optics and a cryogenic high electron mobility transistor (HEMT) low-noise amplifier with a 15.0 GHz center frequency and 3 GHz bandwidth. The two sky beams are Dicke-switched using the off-source beam as a reference, and the source is alternated between the two beams in an ON-ON fashion to remove atmospheric and ground contamination. Calibration is achieved using a temperature-stable diode noise source to remove receiver gain drifts and the flux density scale is derived from observations of 3C 286 assuming the Baars et al. (1977) value of 3.44 Jy at 15.0 GHz. The systematic uncertainty of about 5% in the flux density scale is not included in the error bars. Complete details of the reduction and calibration procedure are found in Richards et al. (2011).

The 37 GHz observations were made with the 13.7 m diameter Metsähovi radio telescope, which is a radome-enclosed paraboloid antenna situated in Finland (24 23' 38"E, +60 13' 05"). The measurements were made with a 1 GHz-band dual beam receiver centered at 36.8 GHz. The observations are ON–ON observations, alternating the source and the sky in each feed horn. A typical integration time to obtain one flux density data point is between 1200 s and 1400 s. The detection limit of the telescope at 37 GHz is on the order of 0.2 Jy under optimal conditions. Data points with a signal-to-noise ratio < 4 are treated as non-detections. The flux density scale is set by observations of DR 21. Sources NGC 7027, 3C 274 and 3C 84 are used as secondary calibrators. A detailed description of the data reduction and analysis is given in Teraesranta et al. (1998). The error estimate in the flux density includes the contribution from the measurement rms and the uncertainty of the absolute calibration.

Observations of BL Lacertae at frequencies near 230 and 350 GHz are from the Submillimeter Array (SMA), a radio interferometer consisting of eight 6-m diameter radio telescopes located just below the summit of Mauna Kea, Hawaii. These data were obtained and calibrated as part of the normal monitoring program initiated by the SMA (see Gurwell et al., 2007). Generally, the signal-to-noise ratio of these observations exceeds 50 and is often well over 100, and the true error on the measured flux density is limited by systematic rather than signal-to-noise effects. Visibility amplitudes are calibrated by referencing to standard sources of well-understood brightness, typically solar system objects such as Uranus, Neptune, Titan, Ganymede, or Callisto. Models of the brightness of these objects are accurate to within around 5% at these frequencies. Moreover, the SMA usually processes only a single polarization at one time, and there is evidence that BL Lacertae in 2011 exhibited a fairly strong ($\sim$15%) linear polarization. For a long observation covering a significant range of parallactic angle, the effect of the linear polarization would be largely washed out, providing a good measure of the flux density. However, not all observations of BL Lacertae covered a significant range of parallactic angle, and thus in some cases we would expect a potential absolute systematic error up to 10%. In most cases, we expect that the total systematic error is around 7.5%.

The results from the above observations as well as the possible connections between them are described in the following sections.

3.4.2 Mrk 421

Mrk 421 is one of the closest TeV blazars at a redshift of $z = 0.031$. It was reported in the Third EGRET Catalog (Michelson et al., 1992; Hartman et al., 1999) as one of the weakest AGNs. However, remarkably, Mrk 421 was later detected with the Whipple 10 m telescope as one of the brightest TeV sources (Punch et al., 1992). It was also the second VHE source ever detected. There has been multiple episodes of TeV outburst detected from this source, e.g. in May 1996 (Gaidos et al., 1996), February 2001 (Fossati et al., 2008), May 2008 (Swordy, 2008), February 2010 (The MAGIC Collaboration et al., 2014), April 2013 (Cortina & Holder, 2013), and April 2014. The earliest example of rapid TeV variability came from this source in

May 1996 (Gaidos et al., 1996), when its VHE flux increased by a factor of 20-25 in 30 minutes. Mrk 421 is also very active in X-ray band. X-ray flaring activity in Mrk 421 happens on all time scales, and exhibiting spectral hysteresis (Cui, 2004). With the improved sensitivity of VERITAS at VHE, it is possible to investigate if similar phenomenon exists in VHE. Mrk 421 is one of the best studied sources for its exceptional brightness in VHE band. There are many active MWL monitoring campaigns on the source covering the whole spectrum. Below I describe the TeV and X-ray observations of Mrk 421. The details of MWL observations in other bands closely resembles the descriptions in the previous subsection, including data from *Fermi*-LAT, Steward Observatory, and OVRO.

VERITAS observations of Mrk 421

Mrk 421 has been monitored by VERITAS regularly for $\sim$20 hours per observing season. The general strategy is to observe it every third day, with coordinated simultaneous X-ray observations (e.g. from Swift XRT). Due to two major VERITAS upgrades in Summer 2009 and Summer 2012, we divide all the VERITAS data into three groups: 2007-2009, 2009-2012, and 2012-2014. Even at lower flux state, VERITAS can detect the source within 10 minutes. This allows us to construct a long term TeV light curve.

Apart from the long term light curve, we also focus on the flaring episodes on Feb 17, 2010, between Apr 11 and Apr 16, 2013, and a slightly lower flaring state between Apr 29 and May 3, 2014. I have contributed to the analysis of the former two flares, but I will focus on the third one in 2014 in this work.

On Feb 17, 2010, VERITAS observed Mrk 421 with three telescopes for an exposure time of $\sim$292 minutes, yielding a significance of $\sim$206.6 with medium cuts VEGAS analysis. The average flux level of the source was at $8.6\times10^{-6}\pm9.0\times10^{-8}\mathrm{m}^{-2}\mathrm{s}^{-1}$ above 420 GeV on this night. A manuscript is being prepared by VERITAS and MWL collaborators regarding this flare. I have been involved with the secondary analysis using a modified auto-correlation function to quantify the duration of the variability.

In April 2013, a strong flare from Mrk 421 was detected by VERITAS. The TeV flare lasted for at least 5 days at the flux level above 1 C. U., varying between 2 C. U. to 6 C. U.. Very good simultaneous MWL observations was taken by Swift, NuStar, and Steward Observatory. The total VERITAS live exposure time on the six nights from Apr 11 to Apr 16 amounts to ∼1220 minutes. Two joint publications are being prepared by a large group of MWL collaborators including the VERITAS collaboration.

Table 3.2.: Summary of VERITAS observations of Mrk 421

Date	Exposure	Significance	Non	Noff	Gamma-ray rate	Background rate
	(minutes)	σ			photons min^{-1}	photons min^{-1}
2014-04-29	237.4	97.4	2481	538	10.2 ± 0.2	0.21
2014-05-01	146.4	55.3	796	168	5.3 ± 0.2	0.11
2014-05-03	131.0	74.3	1443	315	10.8 ± 0.3	0.22

On 2014 April 25, MAGIC reported an elevated flux of ∼7 times the flux of Crab Nebula (Crab Units, C.U.) from Mrk 421 according to the preliminary automatic online analysis results. This triggered a joint ToO program by XMM-Newton, VERITAS and MAGIC. With the help of the long orbital period of XMM-Newton, three ∼4-hour-long gapless and simultaneous X-ray and TeV gamma-ray observations were carried out on Apr 29, May 1 and May 3. This is the third time in eight years that the same source triggered these joint ToO observations. Comparing to the last two times in 2006 and 2008 (Acciari et al., 2009d), the source flux is the highest this time, ranging from 1 C.U. to 2.5 C.U.. In this work, we report the the results from these ToO observations and other contemporaneous MWL observations of Mrk 421.

The VERITAS data were again analyzed using the VEGAS package (described in section 2.4.2 of chapter 2). The standard data quality cuts previously optimized for medium point sources of 2-10% of the C. U. and a photon index of 2.5-3 were chosen in the analysis. The specific value of the cuts used were: an integrated charge lower cut of 700 digital counts, a distance upper cut of 1.43°, a minimum number of pixels cut of 5 for each image, inclusive, mean scaled width and length cuts $0.05 <$ MSW < 1.1, and $0.05 <$ MSL < 1.3, respectively, an upper cut on the size of the point-source search window $\theta < 0.1°$, and a lower cut of 7 km on the shower height. The lookup table and effective area files corresponding to these cuts were generated using `KASCADE` simulations. The gamma-ray spectrum was fitted with a power law model with exponential cutoff

$$\frac{dN}{dE} = K \left(\frac{E}{E_0}\right)^{-\alpha} e^{-\frac{E}{E_{cutoff}}} \tag{3.5}$$

and a log parabola model

$$\frac{dN}{dE} = K \left(\frac{E}{E_0}\right)^{-\alpha-\beta \log E/E_0}, \tag{3.6}$$

respectively.

X-ray observations of Mrk 421

Two X-ray light curves focusing on longer timescales and shorter timescales from Swift-XRT and XMM-Newton are used, respectively.

The long-term Swift-XRT light curve is produced using an online analysis tool *The Swift-XRT data products generator* (or `user_objects`) (Evans et al., 2007, 2009). This tool is publicly available and can be used to conveniently and reliably produce Swift-XRT spectra, light curves, and images for a point source. A light curve of Mrk 421 was made from all Swift-XRT observations available from 2005 Mar 1 to 2014 Apr 30, integrated between 0.3 and 10 keV, with a fixed bin width of 50 s (see Figure 3.7).

For short timescale studies, we use the X-ray Multi-Mirror (XMM-Newton) mission, which is onboard a satellite with a long orbital period (48 hr), and therefore well suited for studying sub-hour variability. The XMM-Newton satellite carries the European Photon Imaging Camera (EPIC) X-ray CCD camera (Strüder et al., 2001), including two MOS cameras and a pn camera. The reflection grating spectrometers (RGS) with high energy resolution are installed in front of the MOS detector. Incoming X-ray flux is divided into two portions for MOS and RGS detectors. The EPIC-pn (EPN) detector receives unobstructed beam and is capable of observing with very high time resolution. The Optical/UV Monitor (OM) onboard the XMM satellite provides the capability to cover a $17' \times 17'$ square region between 170 nm to 650 nm (Mason et al., 2001). The OM is equipped with six broad band filters (U, B, V, UVW1, UVM2 and UVW2).

Three ToO observations were taken simultaneously with the VERITAS observations on Apr 29, May 1, and May 3, 2014. To fully utilize the high time resolution capability of XMM-Newton in both X-ray and optical/UV band, all three ToO observations of Mrk 421 were taken in PN timing mode and OM image fast mode. MOS and RGS were also operated during the observations, but the data are not used considering the relatively low timing resolution and the lack of X-ray spectral lines from the source. The PN camera covers a spectral range of approximately 0.5 - 10 keV, and with the UVM2 filter the OM covers the range of about 200 - 270 nm.

XMM-Newton PN and OM data are analyzed using SAS software version 13.5 (Gabriel et al., 2004). The raw data are in the format of Observation Data Files (ODFs). X-ray loading correction and rate-dependent PHA correction are performed using SAS tool `epchain`. We ran the SAS task `epproc runepreject=yes withxrlcorrection=yes runepfast=no withrdpha=yes` to produce the rate-dependent pulse height amplitude (RDPHA) results, which applies calibrations using known spectral lines and are likely more accurate than the alternative charge transfer inefficiency (CTI) corrections (see `http://xmm2.esac.esa.int/docs/documents/CAL-SRN-0312-1-4.pdf`). Note that even after the RDPHA corrections, residual absorption features can still be present in the spectrum (see e.g. Pintore et al., 2014). To account for the source and the residual absorption features, the X-ray spectra were fitted with two different models using `Xspec` version `12.8.1g`. The first model includes a power law, a `wabs` photoelectric absorption component representing the Galactic neutral hydrogen absorption, an absorption `edge` component and two Gaussian components accounting for the oxygen edge at ∼0.54 keV, the silicon edge at ∼1.84 keV, and the gold M edge at ∼2.2 keV, respectively. The second model uses a broken power law instead of the single power law in the first model, and all the other absorption components remain similar. The models with power law and broken power law can be expressed as follows:

$$\frac{dN}{dE} = \begin{cases} e^{-n_H\sigma(E)}\left[K_{PL}e^{-\alpha}+\sum_i \frac{K_{G,i}}{\sqrt{2\pi}\sigma_i}e^{-\frac{(E-E_{0,i})^2}{2\sigma_i^2}}\right], & E \leqslant E_c; \\ e^{-D(E/E_c)^{-3}-n_H\sigma(E)}\left[K_{PL}e^{-\alpha}+\sum_i \frac{K_{G,i}}{\sqrt{2\pi}\sigma_i}e^{-\frac{(E-E_{0,i})^2}{2\sigma_i^2}}\right], & E \geqslant E_c; \end{cases} \tag{3.7}$$

$$\frac{dN}{dE} = \begin{cases} e^{-n_H\sigma(E)}\left[K_b e^{-\alpha_1}+\sum_i \frac{K_{G,i}}{\sqrt{2\pi}\sigma_i}e^{-\frac{(E-E_{0,i})^2}{2\sigma_i^2}}\right], & E \leqslant E_b, E \leqslant E_c; \\ e^{-n_H\sigma(E)}\left[K_b E_b^{\alpha_2-\alpha_1}e^{-\alpha_2}+\sum_i \frac{K_{G,i}}{\sqrt{2\pi}\sigma_i}e^{-\frac{(E-E_{0,i})^2}{2\sigma_i^2}}\right], & E \geqslant E_b, E \leqslant E_c; \\ e^{-D(E/E_c)^{-3}-n_H\sigma(E)}\left[K_b e^{-\alpha_1}+\sum_i \frac{K_{G,i}}{\sqrt{2\pi}\sigma_i}e^{-\frac{(E-E_{0,i})^2}{2\sigma_i^2}}\right], & E \leqslant E_b, E \geqslant E_c; \\ e^{-D(E/E_c)^{-3}-n_H\sigma(E)}\left[K_b E_b^{\alpha_2-\alpha_1}e^{-\alpha_2}+\sum_i \frac{K_{G,i}}{\sqrt{2\pi}\sigma_i}e^{-\frac{(E-E_{0,i})^2}{2\sigma_i^2}}\right], & E \geqslant E_b, E \geqslant E_c; \end{cases} \tag{3.8}$$

respectively. In the above equations, n_H is the column density of neutral hydrogen; K_{PL}, $K_{G,i}$, K_b are the normalization factor for the power law component, the ith Gaussian component, and the broken power law component, respectively; E_c, $E_{0,i}$, and σ_i are the energy of the absorption edge, the center and the standard deviation of the ith Gaussian component, respectively; E_b is the break energy in the broken power law model; and αs are the spectral indices in each model.

The count rate measured by pn camera with thin filter can be converted to flux using energy conversion factors (ECF, in the unit of 10^{11} cts cm^2 erg^{-1}), which depends on filter, spectral index, Galactic n_H absorption, and energy range (Mateos et al., 2009). The flux f in the unit of ergs cm^{-2} s^{-1} can be obtained by $f = rate/ECF$, where rate has a unit of cts s^{-1}. A similar flux conversion factor is used for OM UVM2 filter to convert each count at 2310 Å to flux density 2.20×10^{15}ergs cm^{-2} s^{-1} Å^{-1}. A 2% systematic uncertainty error was added to the OM light curve.

The results of these ToO observations of Mrk 421 in 2014 are presented in the following sections.

3.5 Variability of TeV blazars: short timescale

The observations of blazars have revealed variability on a wide range of timescales, from months down to minutes. They exhibit fast flares as well as long-term persistent variations. This section focuses on the local variability properties on short timescales, in the context of the observations described in the previous section. In subsection 3.5.1 and 3.5.2 I give a brief overview of time series, and describe some common formats of astronomical time series. In subsection 3.5.3, I present interesting results from the BL Lacertae TeV flare, and discuss what we can learn from MWL observations of such flares. In subsection 3.5.4, I present results from simultaneous observations of Mrk 421 in X-ray and TeV band, dedicated to study the sub-hour variability in both bands.

3.5.1 Time series overview

Any quantity x measured at different times t form a time series $x(t)$. Mathematically, depending on the form of time t, there are continuous and discrete time series. An astronomical time series, often called a light curve, describes the number of detected photons within a certain time interval, which is always discrete. A discrete time series can be expressed as a sequence of measurement values $\{X_1, X_2, \cdots, X_N\}$, each taken at a corresponding time in the sequence $\{t_1, t_2, \cdots, t_N\}$. A light curve can often be measured in two different ways according to the instrument: (i) discretely sampled time series $\{(X_k, t_k), k = 1, 2, \cdots, N\}$, where each t_k represents the center of a finite time interval, and X_k is the averaged number of photons, or photon count rate, or flux, during that time interval; or (ii) time-tagged events (TTE)

$\{t_k, k = 1, 2, \cdots, N\}$, where t_k is the sequence of time of an event being recorded (in this case, each element in the sequence $\{X_k\}$ all have a value of 1, therefore can be omitted). The former type of light curves are usually measured in radio to optical frequencies, since the direct measured quantity is power. However, at higher energies e.g. gamma-ray band, the latter TTE format is ubiquitous, due to the combination of low flux level and detection method.

The reason that we study time series in astronomy is that the variations of a time series contain information of physical processes of the light source. The difference between a process and a realization is worth noting: a process is an underlying rule that governs the observed time series, i.e. it determines the probability distribution of a X_k at a time t_k; while each observed time series is a realization of the process, only reflecting one specific possible outcome of the process.

A common example is periodicity in light curves, the period of emission from a pulsar is the same as its spin period. Periodicity is a deterministic process, which means the signal at a given time is perfectly predictable, as there is only one set of possible outcomes of such a process. However, a real-world time series almost always includes the contribution from one or more random processes, e.g. the Poisson counting process, shot noise process, random walk process. The signal from a random process at a given time is a random variable, whose value is not predictable. Although the probability distribution of this random variable can be determined.

The source of the randomness may lie in both the source and the instrument, the former of which are of scientific interest, e.g. the $1/f$ noise from blazars and X-ray binaries. Our goal is to recover the underlying processes by measuring time series. In statistical terms, this is done by calculating the probability of getting the measured data (the realization) if the hypothesis (the process under test) is true.

There are two different approaches to test the hypothesis based on data, and study the process from a realization: frequentist approach and Bayesian approach. The two approaches rely on probability, but view it from different aspects. Frequentist views the hypothesis as an objective proposition that is either true or false, meanwhile the data are viewed as one random realization of the true hypothesis that represent the underlying process. The goodness that the hypothesis agrees with the data is reflected by a chosen statistical property, e.g. the χ^2-test. The goodness assessment relies on the validity of the assumed distribution. On the other hand, Bayesian views the probability differently. In a nutshell, Bayesian approach considers probability as the likelihood of a hypothesis being correct. Instead of treating observed data as one realization in an ensemble, it treats a hypothesis as one possible choice among many. A introductory but comprehensive review is given by Loredo (1992). A Bayesian-based method is used to determine the bin width of light curves in the subsection below. Jeff Scargle has written a series of articles providing comprehensive reviews and innovations on the topic astronomical time series using both frequentist and Bayesian approaches (e.g. Scargle, 1981, 1982, 1989, 1998).

3.5.2 Formats of astronomical time series

Time-tagged events (TTE)

The spectrum of extragalactic background photons follows a rough power law as summarized by Ressell & Turner (1990). The number density of photons drops rapidly at higher energies (e.g. X-ray and gamma-ray), therefore the data are usually taken in a time-tagged events (TTE) format. TTE data records the arrival time (usually also the direction and energy in some form) of each incoming photon. Consider a point source within a certain energy range (e.g. for a particular instrument), all detected photons from one observations is represented by a one-dimensional vector containing the arrival times of each photon $t_k, k = 1, 2, 3, \cdots, N$. A time series in TTE format is a point process.

Ideally each event happens instantaneous at t_k, and can be described by a delta function $\delta(t_k)$. In reality, astrophysical instruments have finite time resolution (e.g. corresponding to the deadtime). However, the dead time is usually much smaller comparing to the average wait time between two events, e.g. for VERITAS the deadtime is 0.33 ms and the trigger rate is ∼400 Hz (∼2.5 ms), while the count rate from a Crab-like source within the signal region (e.g. 0.1°) is on the order of 0.1-1 Hz (wait time 1-10 s).

The advantage of using a TTE format time series is that it contains all information from a particular measurement. However, individual events are subjects to random fluctuation, leading to a very noisy light curve. Therefore the need of density estimation arises. In the next few paragraphs, I introduce a few ways to make statistical inferences from TTE format event lists.

Binned light curves (histograms)

Histogram is a simple and commonly used non-parametric method of density estimation. This is also the conventional format to present astronomical light curves. There are only two free parameters when constructing a histogram: the start time and the time intervals. The choices of these two parameters can sometimes be arbitrary, and may lead to different results when the number of events is small within each bin. The start time of the observation is usually used as the start time of the histogram. There are two schemes for choosing a set time intervals: constant widths of each interval or constant number of events within each interval. Constant widths binning scheme is widely used for its convenience. Different choices of bin width controls the tradeoff between resolution in flux and resolution in time. A coarse time bin yields a larger number of counts within each bin, thus the probability distribution of the number of counts approximately follows a Gaussian distribution according to the central limit theory. On the other hand, more detailed information (e.g. arrival time) about the events that fall in a bin is lost. Therefore, a coarse time bin offers a more reliably estimation of the rate comparing to a finer bin, at the expense of time resolution.

Motivated by the rapid variability, we are interested in light curves on short timescales. But the above bias-variance tradeoff limits the finest timescale that we can use. A generic rule for bin width choice is to have enough number (e.g. >10) of events in each interval so that the standard deviation can be used to reliably estimate the rate uncertainties in each bin. Knuth (2006) proposed an “optimal data-based binning” method, that uses a piece-wise constant model and calculates an bin-width that yield the maximum likelihood that the resulting histogram correctly estimates the underlying density distribution.

Binning schemes with variable bin widths are sometimes used, to balance the bias variance tradeoff. For example, one may require equal number of points in each bin (equal-population). This is used in z-transformed discrete cross-correlation function (see below in section 3.5.3).

For VERITAS light curve histograms, a flux estimation (instead of the rate) is needed since the rate has hardware dependency. Instead of simply counting the number of photons, a weight of $1/A_{eff}$ for “On” events and a weight of α/A_{eff} for “Off” events are applied, respectively, where A_{eff} is the effective area, and α is the ratio of exposure area and acceptance of “On” and “Off” region. Therefore the flux in a time interval Δt is

$$flux = \frac{1}{\Delta t_{live}} \left[\sum_{i=1}^{N_{on}} \frac{1}{A_{eff,i}} - \sum_{j=1}^{N_{off}} \frac{\alpha}{A_{eff,j}} \right], \tag{3.9}$$

where N_{on} and N_{off} are the number of “On” and “Off” events within Δt, and Δt_{live} is the live time ($\Delta t-$ dead-time). Also, equation 17 in Li & Ma (1983) can also be used to calculate the significance of the detection within each time bin.

Figure 3.6 and Figure 3.7 show a series of MWL light curves of BL Lacertae around the time of the 2011 TeV flare, and of Mrk 421 from the year of 2009 to 2014, respectively. The bin width are chosen to be one night.

Focusing on the two flaring VERITAS runs of BL Lacertae on 2010 Jun 28, we produced a light curve with 4-minute bins as shown in the inset of Fig. 3.8. The fluxes were computed with a lower energy threshold of 200 GeV. The observations missed the rising phase of the flare. In 4-minute bins, the highest flux that was measured is $(3.4 \pm 0.6) \times 10^{-6}$ photons m^{-2}s^{-1}, which corresponds to about 125% of the Crab

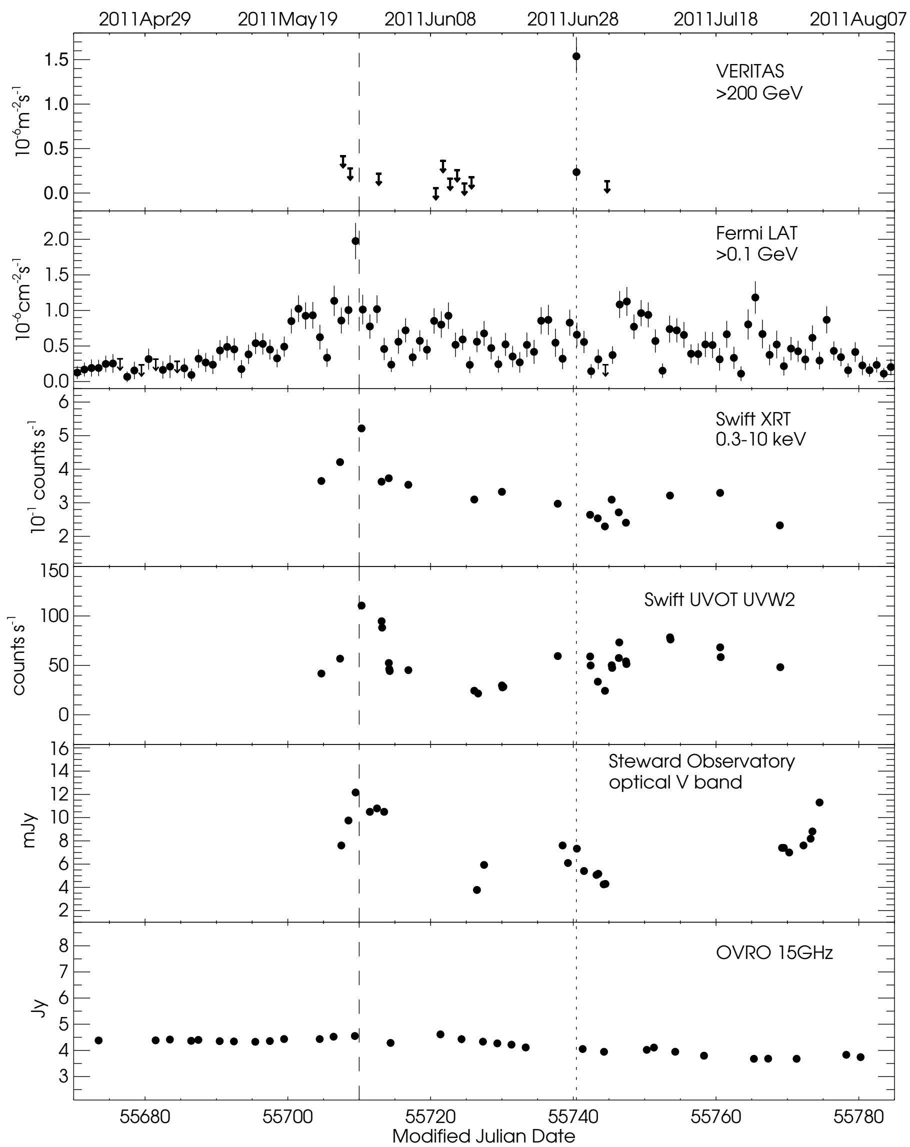

Figure 3.6.: MWL light curves of BL Lacertae from 2011 April to 2011 August.

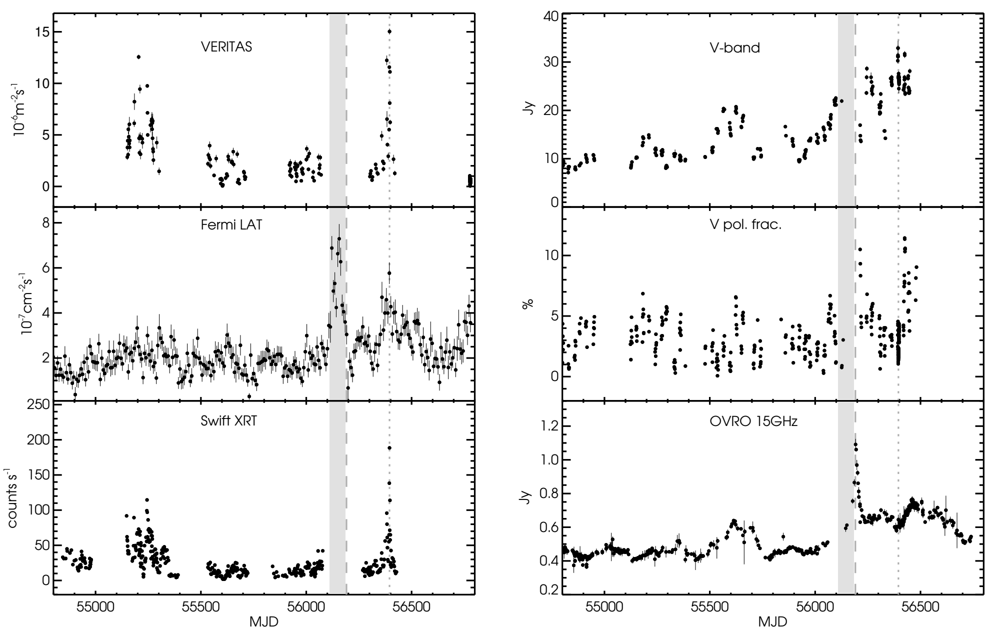

Figure 3.7.: MWL light curves of Mrk 421 from 2009 to 2013.

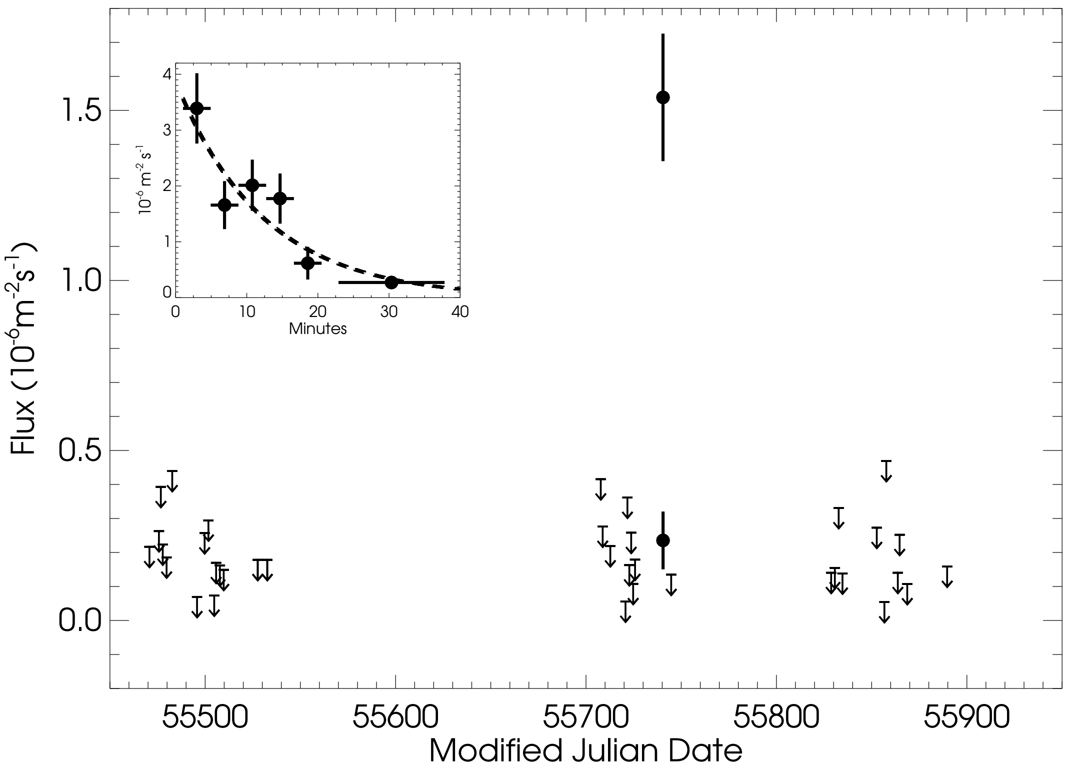

Figure 3.8.: TeV gamma-ray light curve of BL Lacertae (> 200 GeV). When the source was not significantly detected, 99% confidence upper limits are shown. The upper limits were derived by combining data from all observation runs for each night, but for the night of the flare, the fluxes derived from the two individual runs are shown separately. The inset shows the flare in detail, in 4-minute bins for the first run, and one 16-minute bin for the second run, with minute 0 indicating the start of the first run. The dashed line shows the best fit to the profile with an exponential function (see text).

Nebula flux above 200 GeV, as measured with VERITAS. To quantify the decay time, the light curve was fitted with an exponential function $I(t) = I_0 \times \exp(-t/\tau_d)$, and the best-fit decay time was $\tau_d = 13 \pm 4$ minutes. The timescale constraints the size, and provide insights on the location or the Doppler factor of the emitting region (see subsection 3.5.3 below).

For the first time, a rapid (minute-scale) TeV gamma-ray flare is seen from BL Lacertae – this is also the first such flare from an LBL. It fills an important gap between similar phenomenon observed in FSRQs and HBLs. The rapid variability poses serious challenges to the theoretical understanding of gamma-ray production in blazars. On the one hand, rapid gamma-ray variability implies very compact emitting regions that can be most naturally associated with the immediate vicinity of the central supermassive black hole. On the other hand, the regions must be sufficiently outside the BLRs that gamma rays can escape attenuation due to external radiation fields (which, for FSRQs, are particularly strong).

Kernel density estimation and Bayesian blocks

However, the use of histograms inevitably causes information loss, and introduce artificial discontinuity. Moreover, different choices of the start time and time intervals can lead to different conclusions for the same data set. These problems becomes more apparent when the bin size, and subsequently the number of events in each bin, is small.

There are many methods to overcome such limits: e.g. kernel density estimation (KDE). Given a sequence of arrival time of N events $\{t_i, i = 1, \cdot, N\}$, the kernel density estimator at a given time t is:

$$\hat{f}(t,h) = \frac{1}{Nh} \sum_{i=1}^{N} K\left(\frac{t - t_i}{h}\right),$$

where, K is the kernel and h is bandwidth. A kernel characterize the contribution of an event t_i and centers at Different shapes of kernels can be used, e.g. Gaussian, Epanechnikov, and exponential. The choice of bandwidth (h) of KDE presents a problem of tradeoff between variance and bias, which is similar to the bin width in histogram. Small bandwidth yields large variance and noisy results, and large bandwidth may over smooth the signal and lead to significant bias.

Another constraint of KDE method is the boundary effect. In KDE, an event that occurs at t_i contributes not only the flux at t_i, but also to time before and after t_i. At the boundaries when $t_i < t_1 + h$ or $t_i > t_N - h$, since there are no data point before the beginning (or after the end) of the observation, the KDE method underestimates the flux.

I use the KDE function in the publicly available python package `Scikit-learn` (Pedregosa et al., 2012) to produce light curves of VERITAS observations. A comparison of light curve estimations of BL Lacertae during the 2011 flare is shown in Figure 3.13. The red solid line shows the results using KDE method with an Epanechnikov kernel profile and band width of 2 minutes. Instead of the more rigorous way of correcting for effective area and live time as described in equation 3.9, the KDE model is estimated using only the arrival time of the photons. An averaged effective area and live time over one 30-minute observation run is used. For comparison, the light curves using regular evenly-binned histograms are also plotted. The results using different methods are in reasonable agreement.

A Bayesian block algorithm uses Bayesian approach to determine a list of N_{cp} change points, the points in time when the signal changes significantly, in a light curve (Scargle, 1998; Scargle et al., 2013). The set of change points divides the light curve into $N_{cp}+1$ segments (or "blocks"), each of which may have a different duration. A block fitness function is defined to evaluate how well a constant model describes this block. The form of block fitness function that Scargle et al. (2013) uses for TTE data is based on Bayesian likelihood of the piece-wise constant model:

$$\log L(k)(\lambda) = N(k) \log \lambda - \lambda T(k),$$

where $N(k)$ and $T(k)$ are the number of events in and the duration of the kth block, respectively, λ is the constant rate parameter within this block. This likelihood maximizes when the rate $\lambda = N(k)/T(k)$ to a value of:

$$\log L_{max}(k)(\lambda) = N(k)(\log N(k) - \log T(k)) - \log N(k).$$

Bayesian block algorithm can be conveniently realized using dynamic programming: (i) starting from the first data block, compute the fitness function for it; (ii) iterate through possible change point time, calculate the fitness function for the two blocks (or k blocks after the kth step), add a change point that maximize the fitness function for new blocks; (iii) repeat the process until all N_{cp} change points are found. It is implemented in the publicly available `PYTHON` `astroML` package by VanderPlas et al. (2012).

One important parameter of Bayesian blocks is the number of change points N_{cp}. This is the same kind of parameters as the bin width to regular histograms, or the bandwidth to KDE, which controls the tradeoff between bias and variance. A geometric prior parameter γ is adopted by Scargle et al. (2013) to balance the tradeoff.

$$P(N_{blocks}) = P_0 \gamma^{N_{blocks}} = \frac{1-\gamma}{1-\gamma^{N+1}} \gamma^{N_{blocks}},$$

where $N_{blocks} = N_{cp} + 1$, and $0 < N_{blocks} \leqslant N$, N is the total number of points (or bins) in the original input light curve. When $0 < \gamma < 1$, a smaller probability is given to large number of blocks, and a larger probability is given to smaller number of blocks. $\gamma > 1$ is allowed but will lead to over-fitting since an larger N_{blocks} will lead to a greater probability in this case, and resulting in too many narrow blocks. The above probability of the number of blocks can also be expressed as:

$$P(N_{cp}) = p_0^{N_{cp}},$$

where p_0 is the *prior* correct-detection probability (or $1 - p_0$ is the *prior* false-alarm probability). For a series with N TTE events, the expected prior N_{cp} were calculated to be $4 - 73.53 p_0 N^{-0.478}$ (equation 21 Scargle et al., 2013).

Bayesian blocks method gives an optimal, adaptive set of time bins for making a histogram. The comparisons of histograms using even-width bins, Knuth's rule and Bayesian blocks is made for simulated Poisson noise on top of a (i) sinusoidal signal as shown in Figure 3.9, (ii) exponential decay signal as shown in Figure 3.10, and (iii) a saw-tooth signal with instantly rising edge as shown in Figure 3.11. The `astroML` package (VanderPlas et al., 2012) was used for generating the histograms using Knuth's rule and Bayesian blocks. While the even-binning scheme is also able to detect the flare, the arbitrariness of the start edge of the bin leads to an uncertainty in the flare onset on the order of binwidth. Bayesian blocks tend to accurately locate the sharp rising edge in the process. We also applied the Bayesian blocks module in `astroML` to VERITAS observations of BL Lacertae and Mrk 421, as shown in Figure 3.13 and Figure 3.14 together with KDE method. A prior correct-detection probability of change point $p_0 = 0.05$ is used.

Figure 3.12 illustrates the bias variance tradeoff by changing the prior probability p_0 that controls the number of blocks in Bayesian blocks, and the band width in KDE. The underlying process is a saw-tooth signal with a peak rate of 20 cts/s on top of a Poisson sequence with a mean rate of 60 cts/s. As p_0 increases and bandwidth h decreases, both Bayesian blocks and KDE give more detailed estimations with larger noisy fluctuations.

3.5.3 Fast flares: the case of BL Lacertae

Flares are the most important local feature of a blazar light curve at VHE. If a flare from a blazar is observed, independent of any models, the timescale of the flare (T_{var}) requires that the size of the emitting region must be very small,

$$R' \leq \mathrm{c}T_{var}\delta/(1+z), \tag{3.10}$$

where z is the redshift of the source and δ is the Doppler factor of the jet.

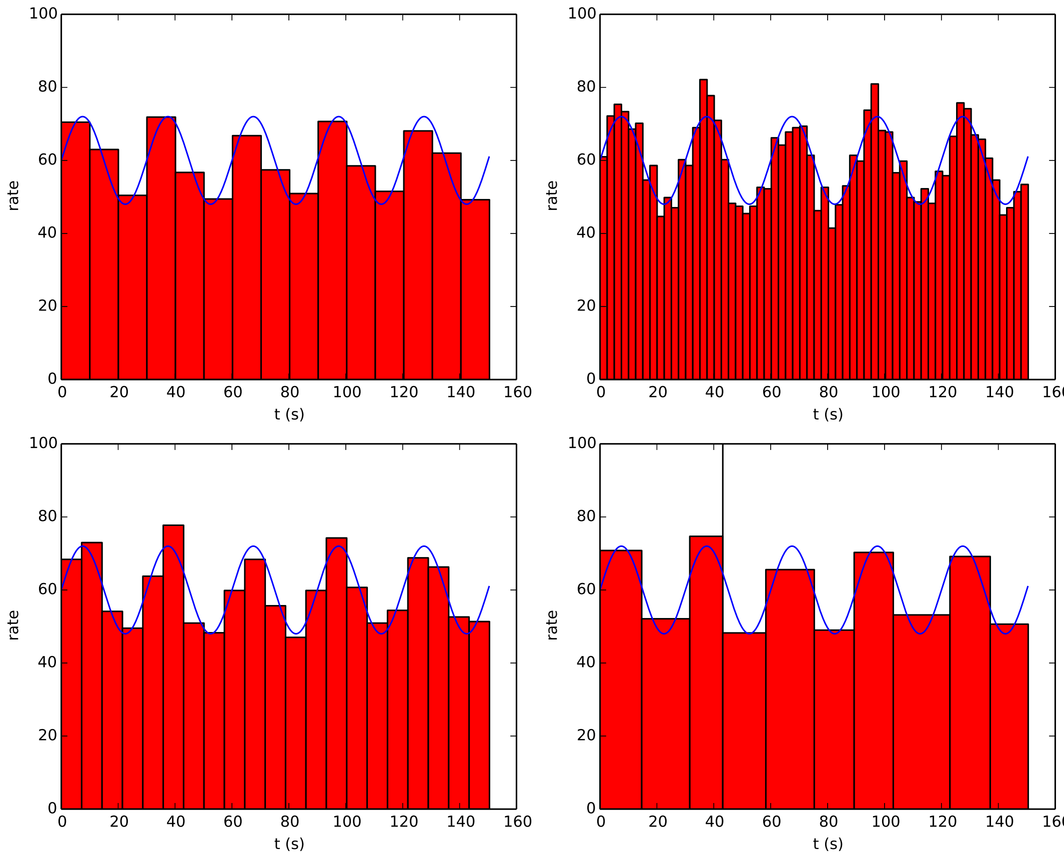

Figure 3.9.: Simulated sine wave modulation with an amplitude of 12 cts/s and a period of 30 s, on top of a Poisson noise with an expected mean count rate of 60 cts/s. The simulation was generated in TTE format with a total number of 9000 events. The resulting duration of the simulated light curve is ~150 s. Four different binning schemes are applied: the top left subplot shows the fixed bin width histogram with 15 bins; the top right subplot shows the fixed bin width histogram with 60 bins; the bottom left subplot shows the histogram made following Knuth's rule; and the bottom left subplot shows the Bayesian blocks.

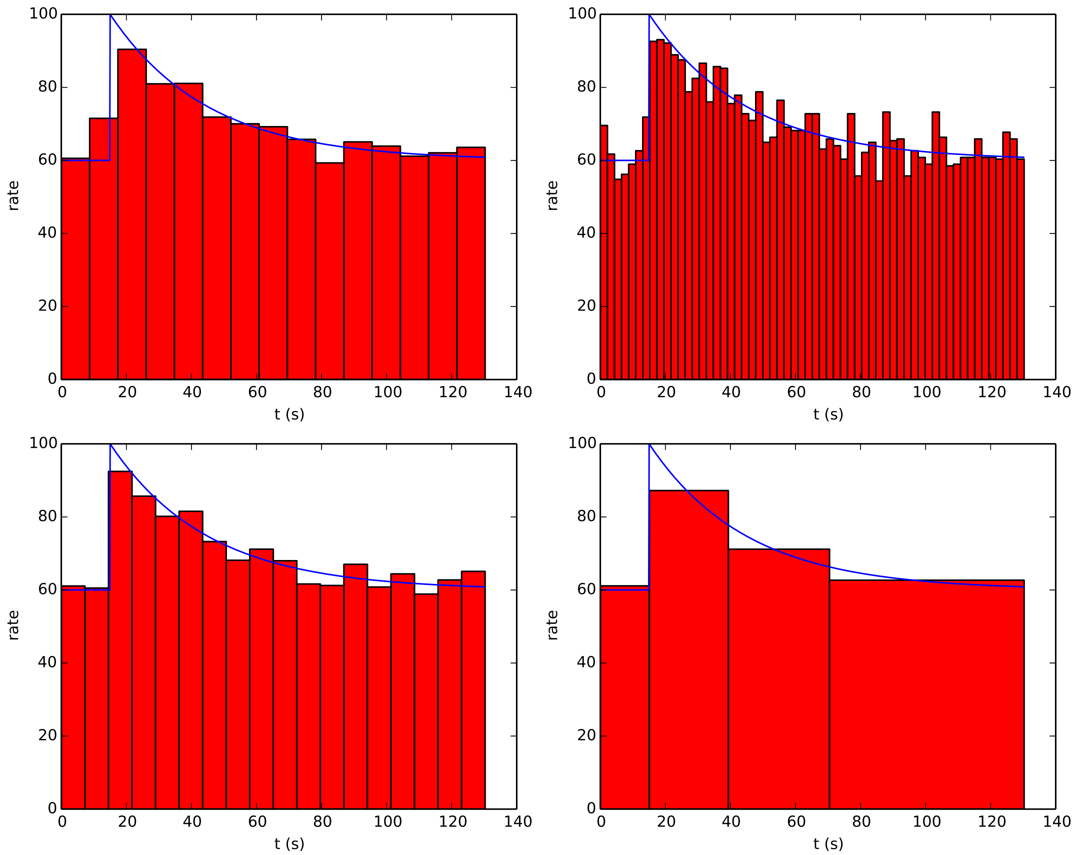

Figure 3.10.: Simulated exponential flare with an amplitude of 40 cts/s and an e-folding timescale of 30 s, on top of a Poisson noise with an expected mean count rate of 60 cts/s. The simulation was generated in TTE format with a total number of 9000 events. The resulting duration of the simulated light curve is ∼150 s. Four different binning schemes are applied: the top left subplot shows the fixed bin width histogram with 15 bins; the top right subplot shows the fixed bin width histogram with 60 bins; the bottom left subplot shows the histogram made following Knuth's rule; and the bottom left subplot shows the Bayesian blocks.

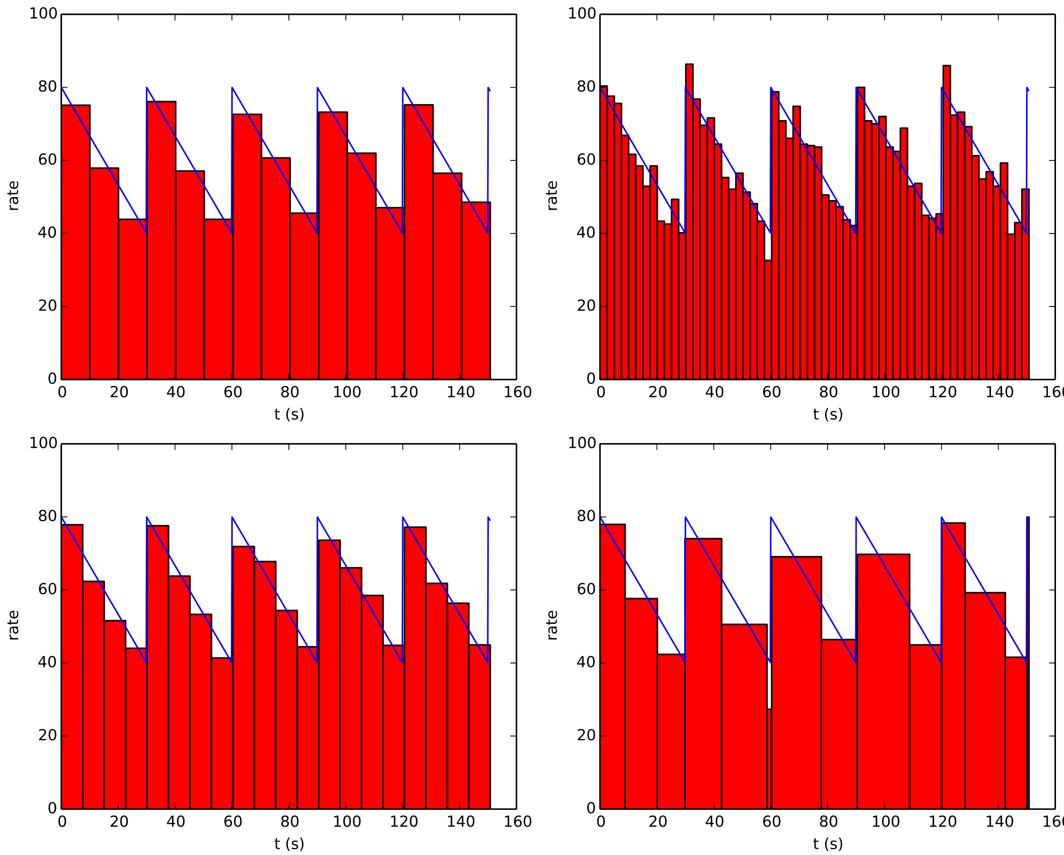

Figure 3.11.: Simulated triangle modulation with an amplitude of 40 cts/s and a period of 30 s, on top of a Poisson noise with an expected mean count rate of 60 cts/s. The simulation was generated in TTE format with a total number of 9000 events. The resulting duration of the simulated light curve is ∼150 s. Four different binning schemes are applied: the top left subplot shows the fixed bin width histogram with 15 bins; the top right subplot shows the fixed bin width histogram with 60 bins; the bottom left subplot shows the histogram made following Knuth's rule; and the bottom left subplot shows the Bayesian blocks.

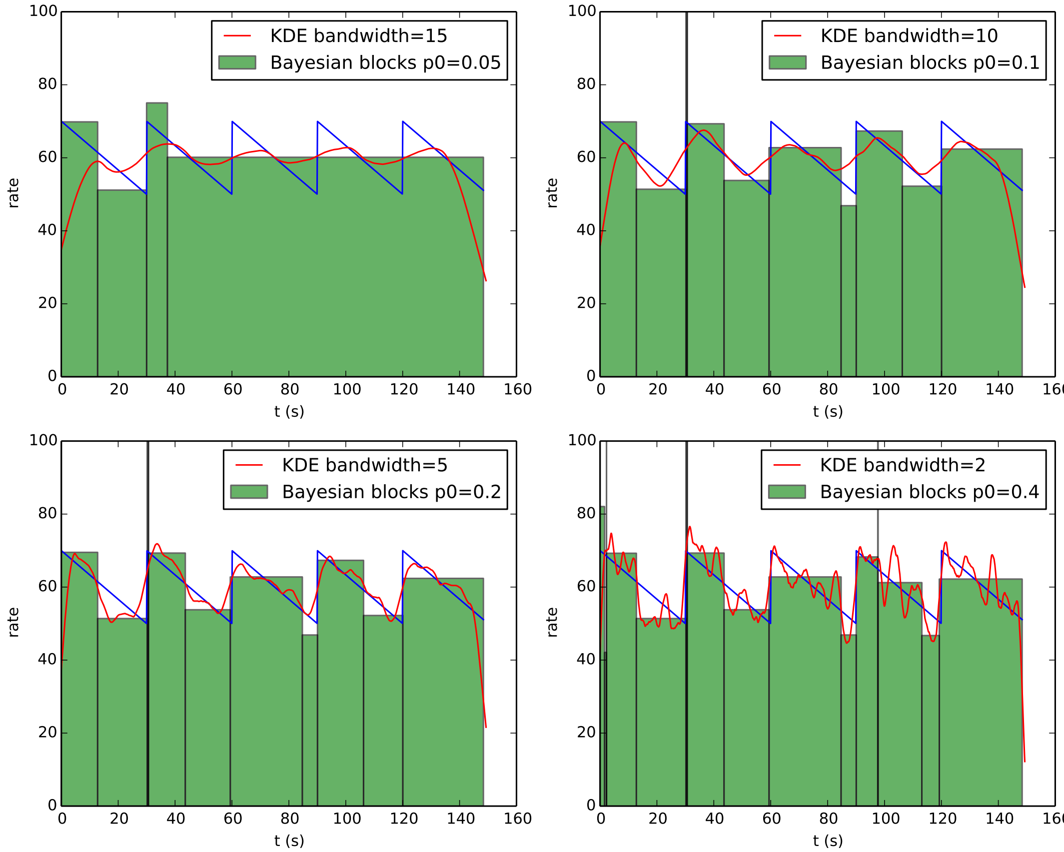

Figure 3.12.: Illustration of the bias variance tradeoff in Bayesian blocks and KDE. The siimulated light curve consists of a Poisson sequence with mean rate of 60 cts/s and a saw-tooth signal that peaks at a rate of 20 cts/s.

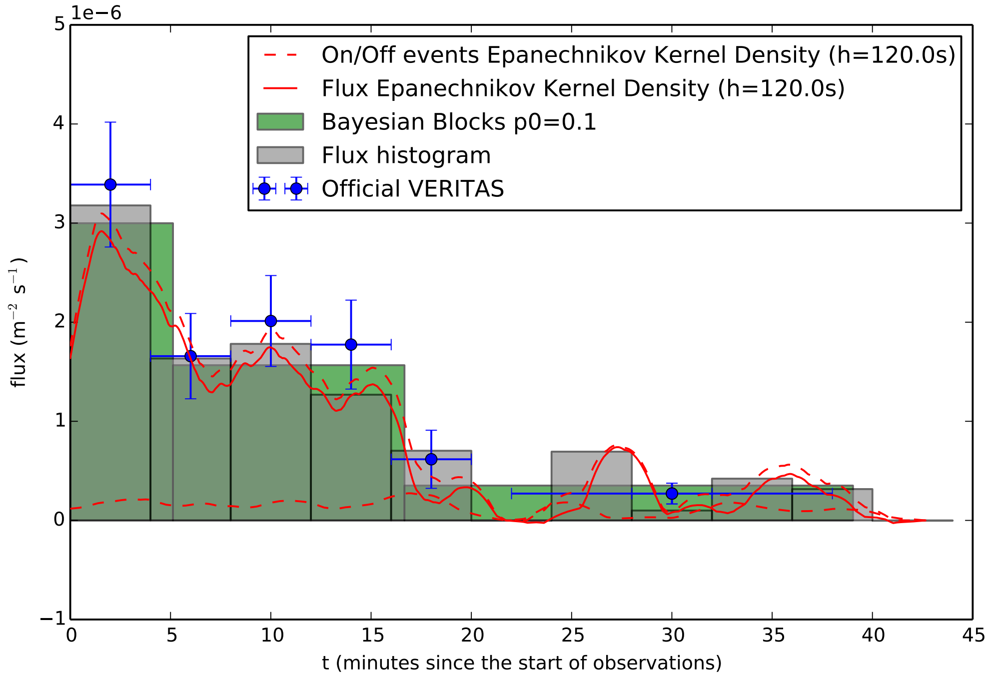

Figure 3.13.: VERITAS light curve of BL Lacertae flare on 2011 Jun 28. The red solid line is the flux estimation using KDE using bandwidth of 2 min. The green histogram is the made using the bin widths using Bayesian blocks module in `astroML` package with $p_0 = 0.1$. The gray histogram is made with fixed binwidth using average live time from the entire run. The blue points are from the standard VEGAS light curve macro `vaMoonShine`, using a more accurate estimation of the live time based on the L3 scalar.

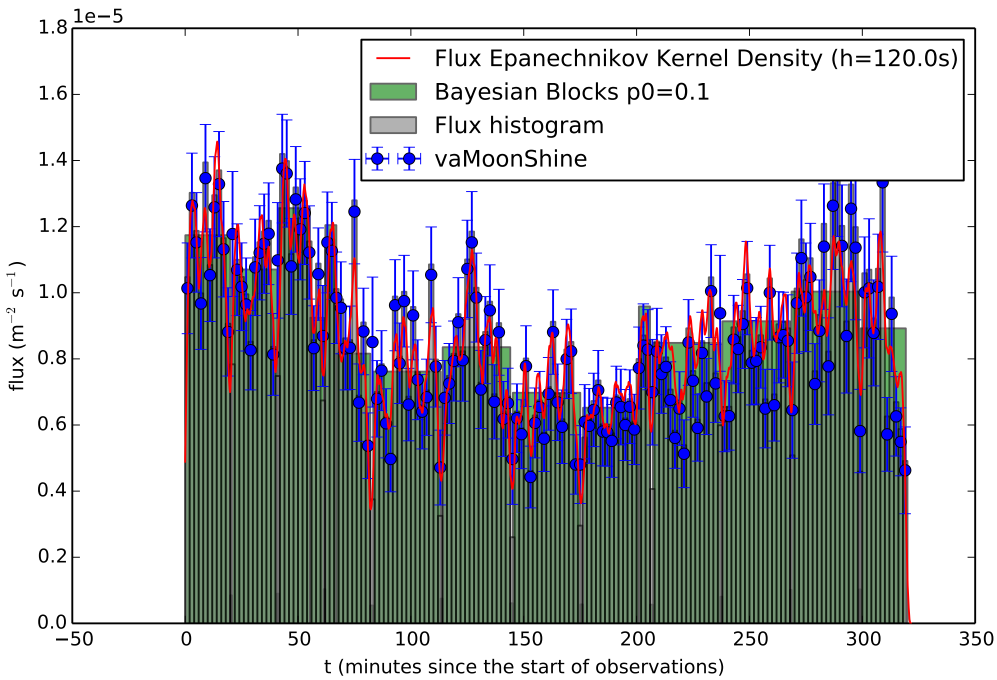

Figure 3.14.: VERITAS light curve of the Mrk 421 flare on 2010 Feb 17. Flux estimations (using run-wise averaged live time) using KDE with bandwidth of 2 min (red solid curve), Bayesian blocks with $p_0 = 0.1$ (green bars), and fixed-binwidth histogram (gray) are shown for comparison. The blue points are from the standard VEGAS light curve macro `vaMoonShine`, using a more accurate estimation of the live time based on the L3 scalar.

For the fast flare of BL Lacertae detected by VERITAS, the measured decay time of the flare (τ_d) leads to a strong constraint on the size of the emitting region:

$$R' \leq c\tau_d\delta/(1+z) \approx 2.2 \times 10^{11}\delta \text{ m} \approx 0.59\delta R_{Schwarzschild} \approx 7.1 \times 10^{-6}\delta \text{ pc}, \quad (3.11)$$

where the redshift is $z = 0.069$, δ is the Doppler factor of the jet, and $R_{Schwarzschild} \approx 3.7 \times 10^{11}$m $\approx 1.2 \times 10^{-5}$pc is the Schwarzschild radius of BL Lacertae. Note that for a typical Doppler factor of a blazar $\delta < 100$, the size of the emitting region is comparable to a few or several tens of times the size of the black hole, and much smaller than the size of BLR (~0.1-1 pc).

Location of the TeV emitting region

From the compactness of the emitting region calculated above, one may immediately wonder where the emitting region is in the jet. On the one hand, if the jet undergoes adiabatic expansion and therefore has a smaller cross section near the black hole, the compact gamma-ray emitting region can be most naturally associated with the immediate vicinity of the central supermassive black hole. On the other hand, the gamma-ray emitting regions must be sufficiently far away from the center (outside the BLRs) that gamma rays can escape attenuation due to low energy radiation fields (which are particularly strong for FSRQs). Since the TeV emitting region cannot be both close to and far away from the black hole at the same time, we discuss these two possibilities below.

If the TeV flaring region is close to the black hole, constraints on the Doppler factor δ of the TeV emitting region can be calculated, because TeV photons have to escape absorption through $\gamma - \gamma$ pair-production (as described in section 1.1.4 in chapter 1). However, such constraint depends on the knowledge of lower energy emission. Consider a gamma-ray photon with observed frequency ν, the frequency of this photon in the jet frame becomes $\nu' = \nu(1+z)/\delta$. The cross-section of the $\gamma - \gamma$

pair-production reaches a maximum of $\sigma_T/5$ when the frequency of the target photon in the jet frame is $\nu'_{target} = \nu_0[\delta/(1+z)]$, where the fiducial frequency ν_0 is defined as

$$\nu_0 = \frac{1}{\nu}\left(\frac{m_e c^2}{h}\right)^2.$$

Thus the frequency of the target photon is $\nu_{target} = \nu_0[\delta/(1+z)]^2$ in the observer frame. The assumption is made that the low-energy target photons follow a power-law distribution between ν_0 and ν_{target}, so that we can use the flux at ν_0 to estimate the flux at ν_{target}, at which the pair-production occurs.

The optical depth of this process in the context of flaring event is given by Dondi & Ghisellini (1995):

$$\tau_{\gamma\gamma} = (1+z)^{2\alpha}\delta^{-(4+2\alpha)}\frac{\sigma_T d_L^2}{5hc^2}\frac{F(\nu_0)}{T_{1/2}}, \tag{3.12}$$

where d_L is the luminosity distance; $T_{1/2}$ is the doubling time of the flare; $F(\nu_0)$ is the observed flux at ν_0; α is the spectral index between ν_0 and $\nu_0[\delta/(1+z)]^2$, under the assumption that the energy spectrum follows a power law in this frequency range. The fact that we detect TeV gamma-ray emission implies that the optical depth $\tau_{\gamma\gamma}$ cannot be too large. Without significant cutoff in the observed spectrum up to $\sim$600 GeV (as shown in Figure 3.15), we assume $\tau_{\gamma\gamma} < 1$. This requirement puts a lower limit on the Doppler factor

$$\delta \geq \left[\frac{\sigma_T d_L^2 (1+z)^{2\alpha}}{5hc^2}\frac{F(\nu_0)}{T_{1/2}}\right]^{1/(4+2\alpha)}. \tag{3.13}$$

The calculation assumes that gamma rays and target photons are both isotropic in the jet frame, so is, strictly speaking, only applicable if the gamma rays are produced via SSC scattering.

For BL Lacertae, the luminosity distance is $d_L \approx 311$Mpc, assuming $\Omega_m = 0.27$, $\Omega_\Lambda = 0.73$, and $H_0 = 70$ km s^{-1}Mpc^{-1} (Larson et al., 2011). The time that the flux dropped to half is $T_{1/2} \approx 9$ minutes. At $h\nu \approx 0.9$ TeV, which is about the highest energy of all gamma rays detected within the source region, we have $\nu_0 \approx 7 \times 10^{13}$ Hz. Unfortunately, we did not have simultaneous IR coverage during the gamma-ray flare. Interestingly, according to Raiteri et al. (2009), the IR flux of BL Lacertae did

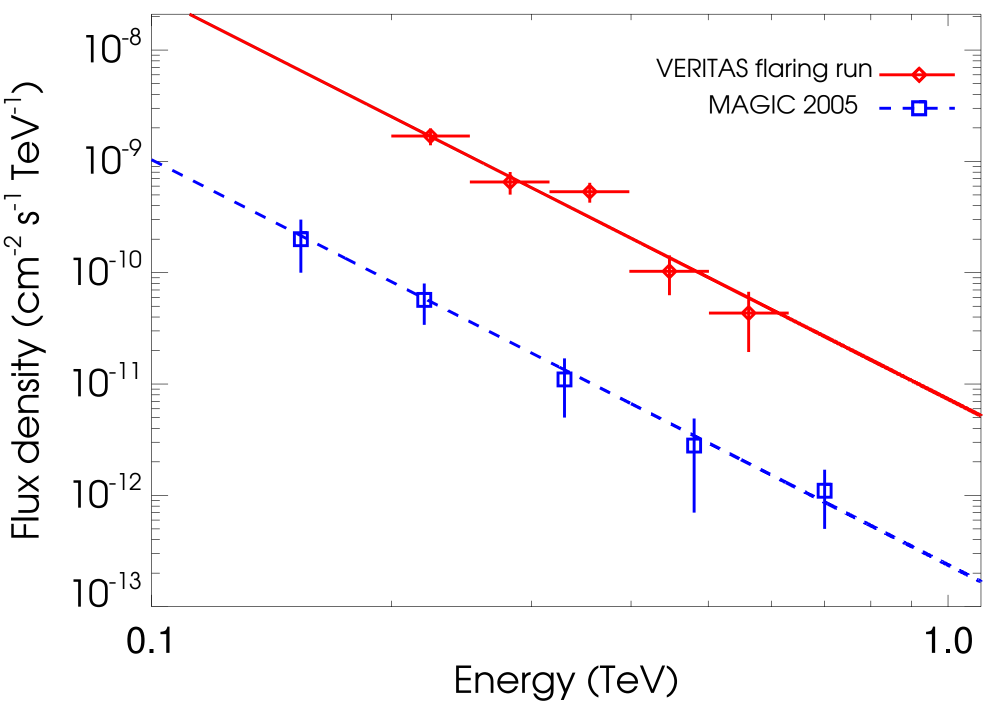

Figure 3.15.: TeV gamma-ray spectrum of BL Lacertae. The VERITAS data points are shown as red open diamonds, along with the best-fit power law (solid line). For comparison, we also show the published MAGIC spectrum of the source as blue open squares, along with the best-fit power law (dashed line). The two power laws have comparable slopes.

not vary significantly (within a factor 2) during their long-term monitoring (for over 150 days) in 2007-2008 (see also Abdo et al., 2011). It is also worth noting that the synchrotron SED peak of BL Lacertae lies in the near-IR band, and the archival SEDs between near-IR and X-ray can be roughly described by a power law (e.g., Böttcher et al., 2003; Raiteri et al., 2010; Abdo et al., 2011). The spectral index (α) varied in the range 1.34–1.40 in the frequency range 7×10^{13}–10^{17} Hz. Taking $F(\nu_0)$ and α from the archival SEDs of BL Lacertae (Raiteri et al., 2009; Abdo et al., 2011), from Eq. 3.13 we found that the lower limit on δ lies in the range 13–17.

The derived lower limits on δ can be compared with other estimates. From the radio variability of BL Lacertae, Hovatta et al. (2009) derived a value of $\delta = 7.3$. However, the uncertainty is expected to be large due to a number of assumptions involved in the analysis (especially in relation to the intrinsic brightness temperature). On the other hand, using a different method, Jorstad et al. (2005) arrived at a value of $\delta = 7.2 \pm 1.1$ for different jet components, in good agreement with Hovatta et al. (2009). These values are significantly below the lower limits imposed by gamma-ray observations, perhaps implying differences between radio and gamma-ray emitting regions in the jet or a gamma-ray optical depth of $\tau_{\gamma\gamma} \gtrsim 40$. It remains to be seen whether such a strong attenuation of TeV gamma rays can be accommodated theoretically. The efforts to model the broadband SED of BL Lacertae have generally led to Doppler factors larger than 7 (e.g., Abdo et al. 2011; see, however, Böttcher & Reimer 2004).

Rapid TeV gamma-ray flaring was first observed in HBLs. It was recognized immediately that the requisite (large) Doppler factor would be problematic (so-called "Doppler-factor crisis"), because no superluminal motion had ever been seen in any of these sources (Piner et al., 2008). This led to many jet models invoking temporal or spatial structures: the Doppler factor of the jet changes as the jet propagates (deceleration models and acceleration models); or some localized regions in the jet have a larger Doppler factor than other regions (e.g. rarefaction and jets-in-a-jet models). The observations in radio and VHE band detect different part of the jets, therefore yield different Doppler factors. Below I list a few examples of these models.

A stratified structure of the jet that consists of a fast-moving spine and slow-moving sheath with radiative feedback in between them is suggested (Ghisellini et al., 2005). The high-resolution polarization maps of the TeV gamma-ray HBLs have provided some evidence for such a configuration (Piner et al., 2008). However, for BL Lacertae, the polarization measurements do not show any stratification of the jet (for example, see Fig. 3.19). There is no evidence for a slowly-moving sheath either. A slightly altered version of this model, the "needle/jet" model, is proposed by Ghisellini & Tavecchio (2008), which predicts "orphan" TeV flares. Giannios et al. (2009) proposed a "jets-in-a-jet model", in which many fast "emitting blobs" are driven by magnetic reconnection within a slower jet with bulk Lorentz factor $\Gamma_j \sim 10$. The small blobs naturally gives the fast variability, the small energy budget associated with them plus the ubiquitous turbulent magnetic field make it possible to have many such blobs, therefore increases the probability of observing one. Deceleration models are proposed that the jet is compact and fast at the base near the black hole (where the TeV emissions are produced), while it decelerates through radiative cooling as it propagates and expands (Georganopoulos & Kazanas, 2003; Levinson, 2007; Stern & Poutanen, 2008). However, pushing the gamma-ray production region too close to the central black hole would be problematic for BL Lacertae and, even more so, for PKS 1222+21, as attenuation due to radiation from the BLRs would be strong. Also, the abundance of the low energy field inevitably leads to external Compton radiation, which cools the electrons more (on top of the SSC cooling) and may shift the peak emission to GeV energies. This may explain the intermittent detection of these sources in TeV energies.

One of the above models may explain the flaring region of the TeV gamma rays to be far upstream of the radio core (closer to the supermassive black hole), related to the emergence of a high-density region. As the region moves downstream, and along the helical magnetic field as postulated by Marscher (2012), it produces polarized optical

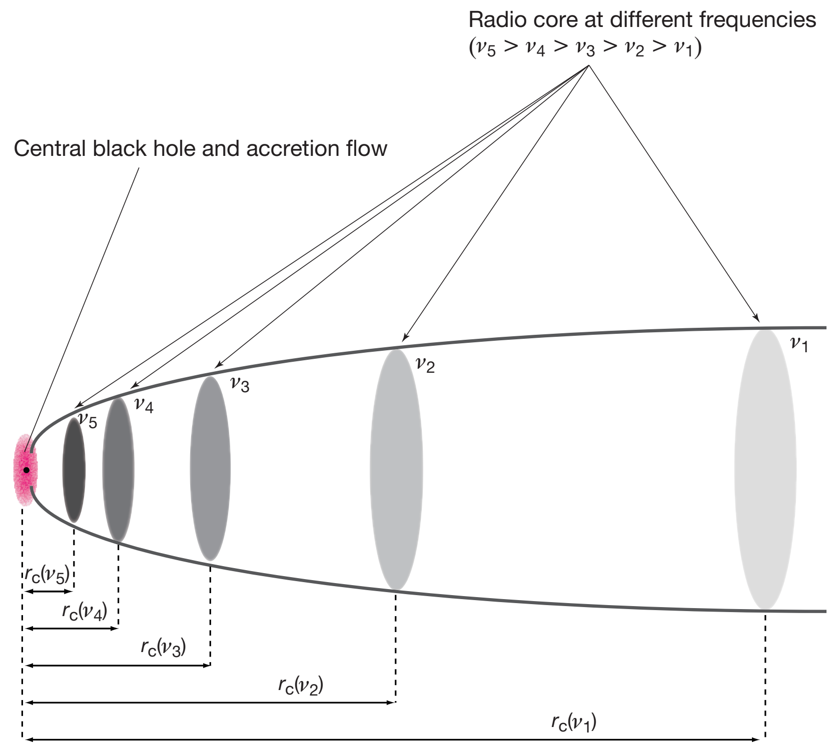

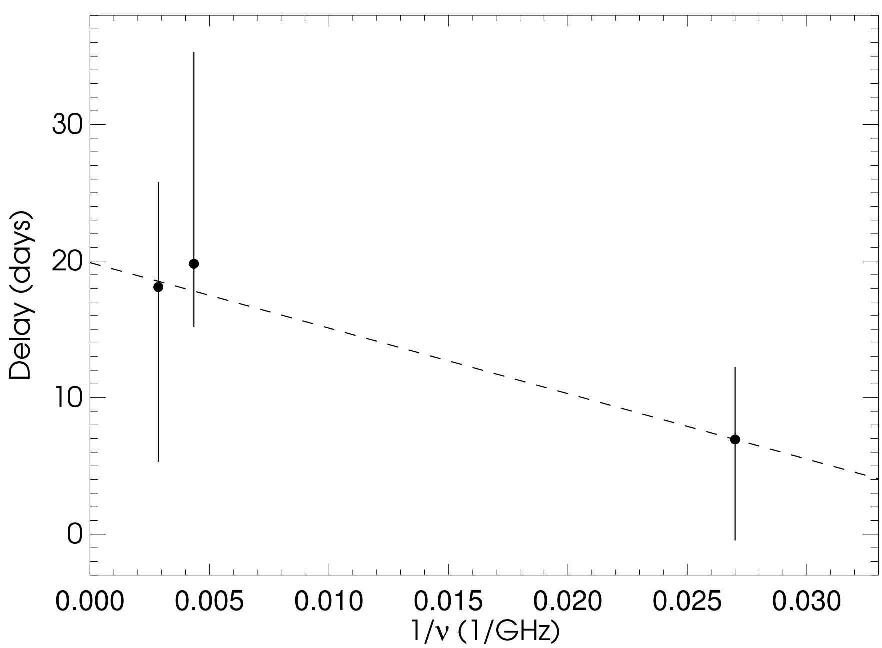

Figure 3.16.: Top plot illustrate the effect of “core shift” in radio frequencies Hada et al. (2011). The bottom plot shows the time delays of the radio flare from BL Lacertae. The time delays with respect to the OVRO band were determined from a likelihood code `PLIKE`. Positive delays indicate “lead” with respect to the OVRO band. The dashed line is drawn to guide the eye. See the text for discussion.

emission with a characteristic variation pattern of the polarization angle. When it becomes optically thin to synchrotron self-absorption further downstream at the radio core, it is seen at successively longer wavelengths. Theoretically, the optical-depth effect should lead to a radio core shift, i.e. the radius of the core r_c depends on the observed frequency ν, $r_c \propto \nu^{-1}$ (Blandford & Königl, 1979). This core shift will then lead to a ν^{-1} dependence of the time lag between different radio frequencies, as the core remains optically thick to synchrotron self-absorption up to a distance from the black hole until it reaches the radio core.

The radio core shift is able to provide constraint on the magnetic field strength in the jet. The core radius and the magnetic field is related by $r_c = (B_1^{k_b} F/\nu)^{1/k_r}$ pc assuming a ultracompact jet described in Lobanov (1998), where B_1 is the magnetic field strength, index $k_b = (3-2\alpha)/(5-2\alpha)$ and α is the spectral index of synchrotron radiation, $k_r = 1$ if azimuthal magnetic field dominates and the ratio between magnetic energy and particle energy remains constant. Zamaninasab et al. (2014) used this relation to measure the magnetic field in the jet, and reported a connection between the magnetic field and the jet power.

The observed radio flare about four months after the TeV flare from the BL Lac may be a manifestation of the radio core shift, as shown in Figure 3.17. The intense radio flare occurred roughly sequentially at 230 GHz, 37 GHz, and 15.4 GHz. Although the elevated flux is also evident at 350 GHz, the flare is poorly sampled. In order the measure the frequency dependent delay, we compute the cross-correlation functions (CF or CCF) between the four radio frequencies.

Cross-correlation function, which quantifies how much similarity (or how much overlapping area) there is between two variable time series at different time delays. Edelson & Krolik (1988) gave a popular definition of discrete cross-correlation function (DCF) between two unevenly sampled light curves a and b. The unbinned DCF between a measurement in a at time t_i (a_i) and another measurement in b at time t_j (b_j) is:

$$UDCF_{ij} = \frac{(a_i - \bar{a})(b_i - \bar{b})}{\sigma_a \sigma_b}, \tag{3.14}$$

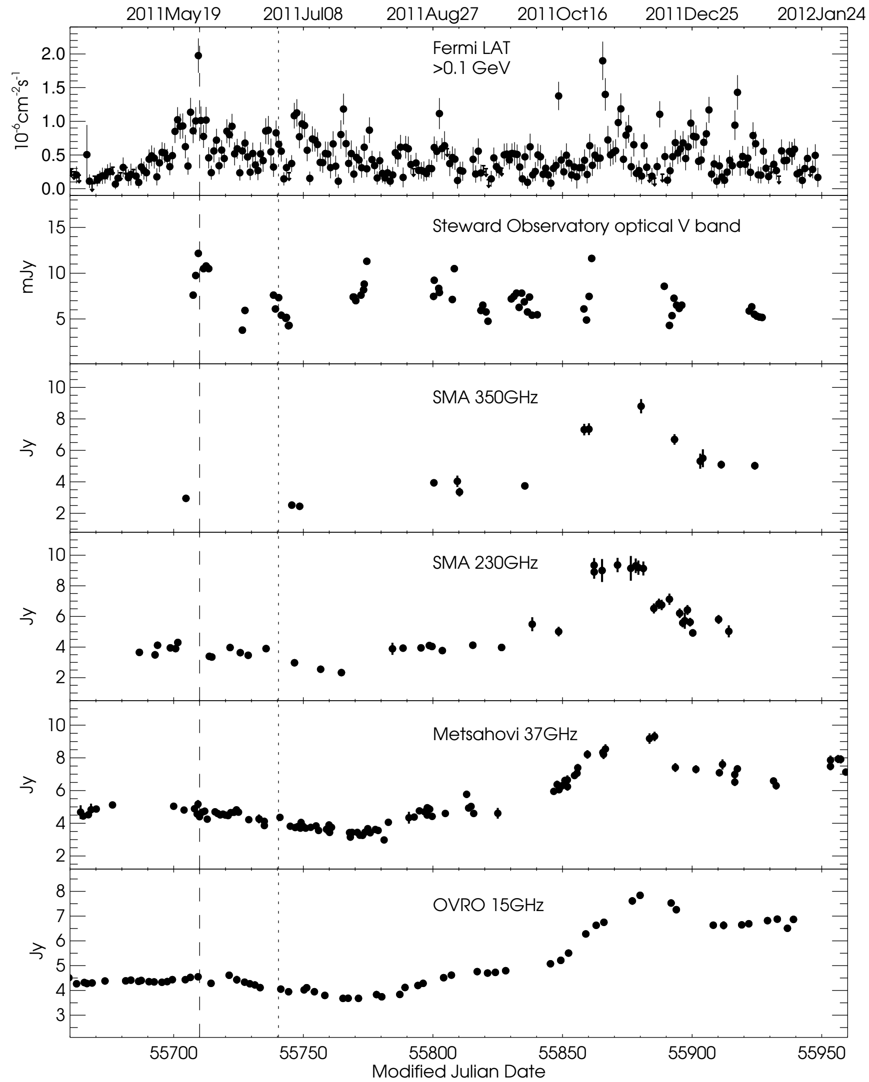

Figure 3.17.: Extended *Fermi*-LAT, optical, and radio light curves of BL Lacertae. As in Fig. 3.6, the dotted line indicates the time of the VERITAS flare, and the dashed line shows the time of the *Fermi*-LAT flare.

where ($\bar{a}$, $\bar{b}$) and (σ_a, σ_b) are the mean and variance of each light curve. For noisy measurements they also recommend using $\sqrt{\sigma_a^2 - e_a^2}$ and $\sqrt{\sigma_b^2 - e_b^2}$ instead of σ_a and

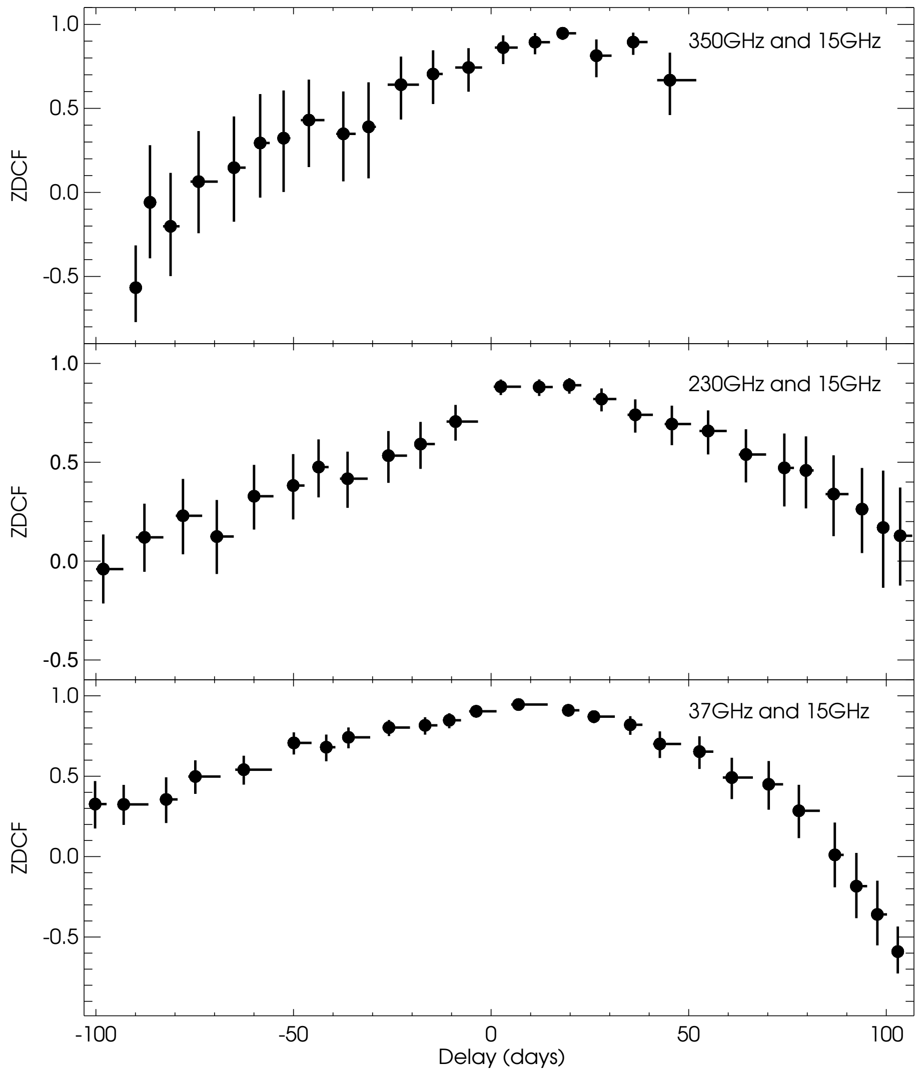

Figure 3.18.: Cross-correlation functions derived from the light curves of BL Lacertae: *top* between the SMA 350 GHz and OVRO 15 GHz bands; *middle* between the SMA 230 GHz and OVRO 15 GHz bands; and *bottom* between the Metsähovi 37 GHz and OVRO 15GHz bands. Positive delays indicate "lead" with respect to the reference (OVRO 15 GHz) band.

σ_b. By averaging all M $UDCF_{ij}$ with a delay $\tau - \Delta\tau/2 < t_j - t_i < \tau + \Delta\tau/2$, one has the DCF at time delay τ:

$$DCF(\tau) = \frac{\sum UDCF_{ij}}{M}. \tag{3.15}$$

In this work we use the z-transformed discrete correlation function (ZDCF) (Alexander, 1997). ZDCF is based on the UDCF above, but uses Fishers z-transform and equal population binning (therefore different time lag binwidth, see section 3.1). ZDCF binning provides a more robust estimation than DCF when the light curve measurements are sparse (under-sampled). The publicly available code `ZDCF_v2.2` and `plike_v4.0` developed by Alexander (1997) are used for calculating the ZDCF, and the time lag and its confidence interval, respectively.

The results are shown in Fig. 3.18, indicating high degree of correlation among the bands. From the ZDCFs, the corresponding time lags were measured, using a publicly available likelihood code (`PLIKE`), and are plotted against ν^{-1} in Fig. 3.16. Unfortunately, the measurements are not of sufficient quality to confirm such a frequency dependence.

The well-sampled *Fermi*-LAT light curve indicates some elevated and variable GeV emission in 2011 November. However, the presence of similar GeV variabilities from 2011 May to the end of the year makes it difficult to establish a correlation between GeV and radio bands. If the TeV flaring activities are related to the giant radio flare, the delay of the radio flare by four months, with respect to the gamma-ray precursor, is in line with the fact that the radio variability of blazars generally lags the gamma-ray variability by 1–8 months (e.g., Lähteenmäki & Valtaoja, 2003; Pushkarev et al., 2010; Nieppola et al., 2011; León-Tavares et al., 2012).

These difficulties might be alleviated in models that invoke subregions inside the jets that are fast moving and also sufficiently far from the black hole (Giannios et al. 2009; Narayan & Piran 2012; Nalewajko et al. 2012; Marscher 2012; see, however, Tavecchio et al. 2011). Specifically, the TeV flaring region should be outside the BLR, which has a typical size of ∼0.1-1 pc. However, this means the emitting region is smaller than the jet cross-section at such distances, and an acceleration mechanism

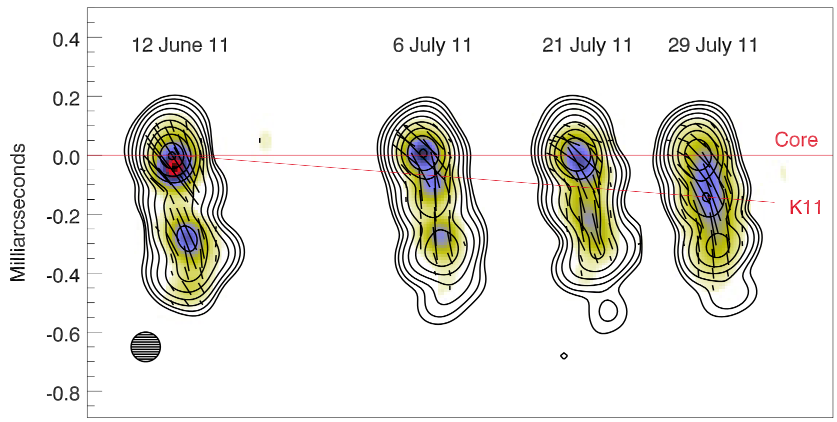

Figure 3.19.: 43 GHz VLBA images of BL Lacertae at four epochs around the time of the TeV gamma-ray flare. The images are convolved with a circular Gaussian function (represented by the circle in the bottom-left corner) that has a full width at half maximum of 0.1 mas (i.e., ∼0.15 pc at the distance of 311 Mpc), the approximate resolution of the longest baselines of the array. Contours correspond to total intensity, with levels in factors of 2 from 0.25%, plus an extra contour at 96%, of the peak intensity of 2.16 Jy beam^{-1}. Color represents linearly polarized intensity, with maximum (black) of 0.103 Jy beam^{-1} followed by red, blue, yellow, and white (no polarization detected). Red lines mark the position of the assumed stationary core and the superluminally moving knot K11, each of which has a distinct polarization position angle.

has to exist at that location to produce VHE flares. Below we discuss this possibility for the BL Lacertae flare.

A particularly interesting result from the MWL observations of BL Lacertae is the emergence of a superluminal knot (K11 in Fig. 3.19) around the time of the TeV gamma-ray flare. The knot K11 with distinct polarization angle is directly seen in the VLBA 43 GHz images, although there is a large gap in the coverage around the time of the TeV gamma-ray flare. The VLBA 15 GHz observations also show changes in the polarization angle, which supports the emergence of a new component. The coincidence in time between the emergence of K11 and the TeV flare strongly suggests a connection between them. The turbulent extreme multi-zone model proposed by Marscher (2012) offers a plausible mechanism to produce TeV flares when a compact radio knot passes the stationary radio core.

In the model of Marscher (2012), the radio core is a turbulent, conical shock that ends in a small Mach disk oriented transverse to the jet axis. The slow but highly compressed plasma in the Mach disk provides a highly variable local source of seed photons for inverse-Compton scattering by electrons in the faster plasma that passes across the conical shock. This faster plasma is divided into turbulent cells, each of which has a different magnetic field direction. If a cell of especially high density of relativistic electrons passes through the core, it can cause a sharp flare at gamma-ray energies and appear as a superluminal knot at radio frequencies (similar to Narayan & Piran, 2012).

Although the angular resolution of the VLBA is insufficient to measure the angular size of the knot during the observations, it is likely to have a diameter ~ 0.07 mas assuming that its brightness temperature is close to the value of $\sim 5 \times 10^{10}$ K needed for equipartition between the energy density in relativistic electrons and that in the magnetic field (Readhead, 1994). In this case, the knot interacted with the core over a period of 70 ± 15 days centered on MJD 55711 (i.e., from late April 2011 until early July 2011). Therefore, the knot would be near the end of the core region when the TeV gamma-ray flare erupted.

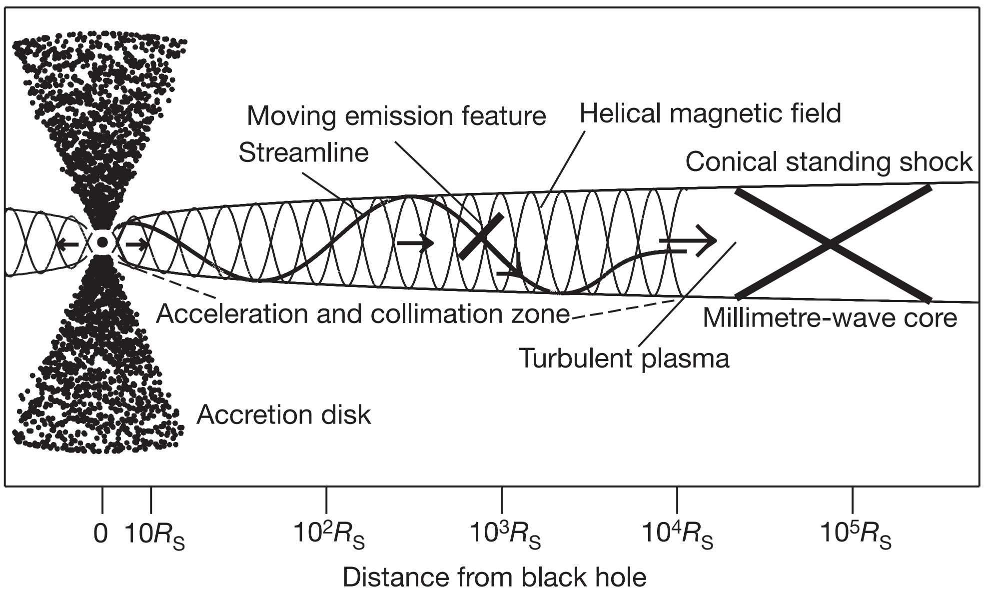

Figure 3.20.: An illustration of the inner jet model of BL Lac by Marscher et al. (2008). The TeV flare is possibly produced near the conical standing shock at $\sim 10^5 R_{Schwarzshild}$, if it is produce when K11 passes the standing shock. Figure taken from Marscher et al. (2008).

If the TeV flare and the emergence of the radio knot are connected, the TeV emitting region could be located roughly at the same distance of the radio core when the TeV flare was observed. This puts a unprecedented constraint on the location of the TeV gamma-ray emitting region. However, the distance of the radio core with respect to the central engine is also an elusive property. It can be calculated based on the distance of the object, angular size of the core, and the opening angle of the jet. These properties can be difficult to measure. While observations of several objects have shown that the radio cores are located at distances of 10^4-10^6 $R_{Schwarzshild}$ away from the central black holes (e.g. Larionov et al., 2008; Marscher et al., 2010; Agudo et al., 2011), Hada et al. (2011) reports that the 43 GHz core of M 87 is within 14-23 $R_{Schwarzshild}$ to the central black hole. Based on earlier VLBA imaging, Marscher et al. (2008) argued that the 43 GHz core of BL Lacertae is a standing shock located well downstream at a distance of $\sim 10^5 R_{Schwarzshild}$ (or $\sim$ 1 pc) from the black hole (see Figure 3.20). Their model also describes a helical magnetic field configuration upstream of the radio core, which the radiating plasma follows. This is now supported by the observed pattern of change in the optical polarization that coincides with the TeV gamma-ray flare. The new superluminal knot seems to have passed through the core on MJD 55711$\pm$15 (2011 May 30, when the brightness centroids of the knot and core coincided), close to the time when a rapid flare was seen with the *Fermi*-LAT, *Swift* XRT and UVOT, and the Steward Observatory.

The lack of similarly rapid change of significant amplitude at other wavelengths is likely due to inadequate sampling. In other words, the TeV gamma-ray flare is so rapid that pointed instruments were unlikely to be observing the source at the right time, while for other instruments (e.g., the *Fermi* LAT) it is difficult to accumulate adequate statistics. Nevertheless, around the time of the TeV gamma-ray flare, there is evidence for flux variations at optical and UV wavelengths, which would represent a response of the synchrotron emission to the VHE gamma-ray flaring.

Optical and radio polarization

The radio polarization images are already shown above in Figure 3.19, providing a great amount of information. However, even without such high-resolution images, the polarization fractions and polarization angles in optical and radio bands are still informative. Zhang et al. (2014) calculated the time-dependent polarization signatures during a blazar synchrotron/SSC flare at different wavelengths, assuming a structured, helical magnetic field in a cylindrical jet. The emissions come from a shock-in-jet model, where a cylindrical shock moves along the jet and accelerates particles. One of their proposed flaring mechanisms (amplification of toroidal magnetic field through shock compression) was able to produce (i) a simultaneous flare in synchrotron and SSC band; (ii) two sharp polarization angle changes (reaching a rotation of $\sim 180°$) on the rising and falling edge of the flare, respectively; and (iii) two dips in the polarization fraction on the rising and falling edge of the flare, respectively. However, if the magnetic field is turbulent as suggested by Marscher (2012), the polarization angles should follow the random magnetic field configuration, therefore making this effect much more chaotic.

The observations of BL Lacertae are evidence of abrupt changes of optical polarization angles, as well as a dip in polarization fraction. Fig. 3.21 shows results from optical polarization measurements. The polarized flux fraction does not vary significantly before and after the VHE gamma-ray flare. However, changes in optical polarization angle are significant around the times of both GeV and TeV gamma-ray flares and between. Over the 4-day period that included the VERITAS flare, the optical polarization position angle changed by a minimum of 38.8 deg (between MJD 55738 and 55739), -31.2 deg (between MJD 55739 and 55740), and 88.8 deg (between MJD 55740 and 55741). Therefore, at a minimum, the optical polarization angle was changing by more than one degree per hour. On the other hand, around the time of the Fermi LAT flare, the polarization fraction decreased abruptly from $\sim$11% on 2011 May 27 to $\sim$3.7% on 2011 May 28. But between these two days, the polarization

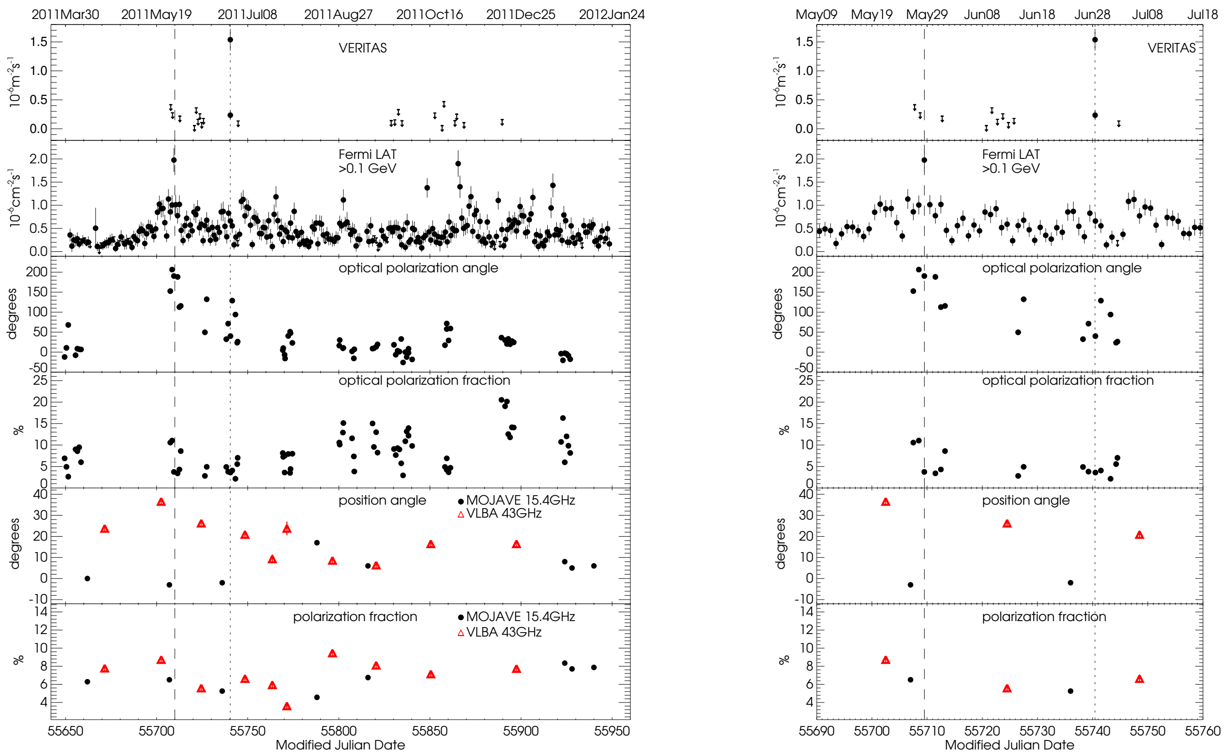

Figure 3.21.: Polarized optical and radio emission from BL Lacertae. VERITAS and *Fermi*-LAT light curves are also shown for comparison. The optical measurements were made at the Steward Observatory, while the radio measurements were made with the VLBA at 15.4 GHz (black dots) and 43 GHz (red triangles). The radio electric vector position angle has an uncertainty of about ±3 degrees, and the polarization fraction has an uncertainty of about 5%. The dotted line indicates the time of the VERITAS flare, and the dashed line shows the time of the *Fermi*-LAT flare. Right panel is a zoom-in view of the same polarization curve, with a better view of the optical polarization fraction drop at time of the Fermi-LAT flare and the optical polarization angle change at the time of the TeV flare.

angle only changed by $\sim 15°$. We did not see the simultaneous change in polarization fraction and angle, as predicted by the toroidal magnetic amplification described by Zhang et al. (2014). Instead, we observed a dramatic change in one and a less change in the other. This may be the manifestation of a turbulent, instead a helical, magnetic field.

Also shown in Fig. 3.21 are the results from radio polarization measurements. Although there is no significant variation in the average polarization fraction, the average polarization angle of the core appears to change before and after the TeV gamma-ray flare. However, the polarization angles for VLBA 15.4 GHz and 43 GHz do not agree with each other in earlier epochs (before the TeV gamma-ray flare). This discrepancy is likely due to the combination of the emergence of a new component, the Faraday rotation and the difference in beam size at the two frequencies. At the core, the Faraday rotation can be significant for BL Lacertae (Gabuzda et al., 2006; Jorstad et al., 2007), mostly affecting the 15.4 GHz measurements. It is also worth noting that the effects can be variable on timescales of months.

We note that the lack of similarly rapid change of significant amplitude at other wavelengths is likely due to inadequate sampling. In other words, the TeV gamma-ray flare is so rapid that pointed instruments were unlikely to be observing the source at the right time, while for other instruments (e.g., the *Fermi* LAT) it is difficult to accumulate adequate statistics. Nevertheless, around the time of the TeV gamma-ray flare, there is evidence for flux variations at optical and UV wavelengths, which would represent a response of the synchrotron emission to the VHE gamma-ray flaring.

Flaring profile: symmetric or asymmetric?

The flare from BL Lacertae was only caught in the decay phase, preventing us to study the skewness and kurtosis of the flaring profile. The flare profile, like many other observables in blazars, are controlled by a combination of timescales: injection timescale t_{inj}, acceleration timescale t_{acc}, cooling timescale t_c, and dynamic timescale

$t_{dyn} = R/c$. As described qualitatively in Li & Kusunose (2000), the net change in photon flux is a combination of photon production and escape. The flux increases when the photon production rate exceeds the escape rate, and reaches the peak when they are equal.

Sikora et al. (2001) showed that in external Compton model, when the electron injection is longer than the dynamic timescale ($t_{inj} > t_{dyn}$), a flat and shallow flare should be observed. Such flares have not been observed in blazars, favoring a fast injection of particles. When the injection is very fast, an asymmetric flare profile with fast flux rise and slow decay may arise, in agreement to the similar predictions on flare profile made by Kirk et al. (1998) and Li & Kusunose (2000) for SSC model.

In fast-cooling regime, it is shown that for a single, step-function particle injection, an shoulder feature is present on the rising edge of the flare, leading to a very asymmetric profile. For triangle-like injections, the flare is more symmetric. However, regardless of the injection profile, the decay edge of the flare is always governed by the light travel effect, and can be described by an exponential function that directly gives the size of the emitting region.

In the slow-cooling regime, the flare continues to rise even after the injection has stopped, due to the long cooling time of the injected particles ($t_c > t_{dyn}$). The flare decay timescale is governed by the cooling time, therefore depends on energy $T_{var} \propto E^{-1/2}$, e.g. cooling time in UV and X-ray $T_{250nm}/T_{1keV} \sim 14$. However, in the slow-cooling regime, SSC may become the dominant cooling channel as synchrotron photon density increases, and the system becomes non-linear. Moreover, for the highest energy electrons and the radiations associated with it (e.g. keV and TeV), the cooling time can still be fast enough so that the decay timescale is controlled by the size of the emitting region.

The observed flares from blazars almost always exhibits symmetric profiles, this may be due to a combination of light travel effect and multiple injections. The former smears out any asymmetry, and the latter makes the profile more symmetric since the emission tail from one injection may contribute to the rising edge of the next.

The flare profile, including its rise and decay timescales and their energy dependence, offers insights to the emitting region. However, the fact that multiple injections and light travel effect may smear out any features, and the lack of simultaneous detections of major flares, make such studies difficult.

3.5.4 Sub-hour variability in X-ray and TeV band: Mrk 421

As shown in the case of the BL Lacertae in section 3.5.3, the TeV gamma-ray flare is so rapid that pointed instruments were unlikely to be observing the source at the exactly the same time. Therefore the best strategy is to schedule the observations in different wavelengths so that they happen simultaneously. Several MWL campaigns on a few brightest TeV blazars are in place, especially focusing on X-ray and gamma-ray emissions (e.g. see `http://www.swift.psu.edu/monitoring/`). These two bands are particularly interesting because the SSC mechanism predicts highly correlated flux change in both bands, as the same electrons with the highest energies are responsible for their emissions.

A general correlation on longer timescales in X-ray and TeV flux has been observed with no systematic lags (e.g., Błażejowski et al., 2005; The MAGIC Collaboration et al., 2014). However, more questions were raised than answered by coordinated X-ray and TeV observations. The detailed relationship between X-ray and TeV bands may depend on a number of factors, including the observed timescales, the flux level, and the phase (rise or decay) of a flare.

Fossati et al. (2008) found "an intriguing hint" that the correlation between X-ray and VHE fluxes may be different between hour timescales and day timescales. Specifically, data suggest a roughly quadratic dependence of TeV flux on X-ray flux on timescales (of hours), but a less steep, close to linear relationship on longer timescales (of days) once the faster variations are smoothed out (Fossati et al., 2008).

The relation (quadratic or linear) may provide information on emitting mechanism in the context of SED (e.g. Katarzyński et al., 2005). For example, an SSC model in

Thomson regime can naturally produce a quadratic relationship, while SSC scattering in Klein-Nishina regime tend to produce a linear relationship. Note that this also depends on which parts (transition frequencies near a spectral peak vs. the falling tail after a spectral peak) in the spectrum are being compared. However, if the flare happens in slow-cooling regime, the rising edge tend to always show a linear correlation, regardless of the model and the relationship on the rising edge of the flare. Moreover, the light traveling effect also can make the relation less steep.

Petropoulou (2014) has shown from numerical simulations that a two-zone SSC model yields a weak correlation between X-ray and TeV band when the flux is low, but can exhibit a tight, linear correlation when one of the zone produces a flare.

Making it more puzzling, an "orphan" gamma-ray flare from 1ES 1959+650 was reported by Krawczynski et al. (2004) with no X-ray counterpart observed, which cannot be explained by the one-zone SSC model (see also Błażejowski et al., 2005, for a similar case in Mrk 421). Models involving multiple emitting regions and particles are likely required in this case (see Böttcher, 2005, for a plausible hybrid model).

Given the complexity in both models and observations, the details of the X-ray/TeV correlation (especially during major flares and on short timescales) still need to be addressed by future simultaneous observations. Although, simultaneous data for studying such TeV and X-ray correlation on short (sub-hour) timescales are still lacking.

In this section, I present results from the three simultaneous ToO observations of Mrk 421 with XMM-Newton and VERITAS in 2014 (see section 3.4.2). In subsection 3.5.4, light curves of the ToO observations are shown, and the variability amplitude is calculated. In subsection 3.5.4, the cross-correlation between X-ray and TeV fluxes is shown, the intraband energy-dependent time lags in X-ray and TeV are studied, the spectral hysteresis patterns are presented and compared with the energy-dependent time lags, and finally, the overall SEDs and a SSC model are shown.

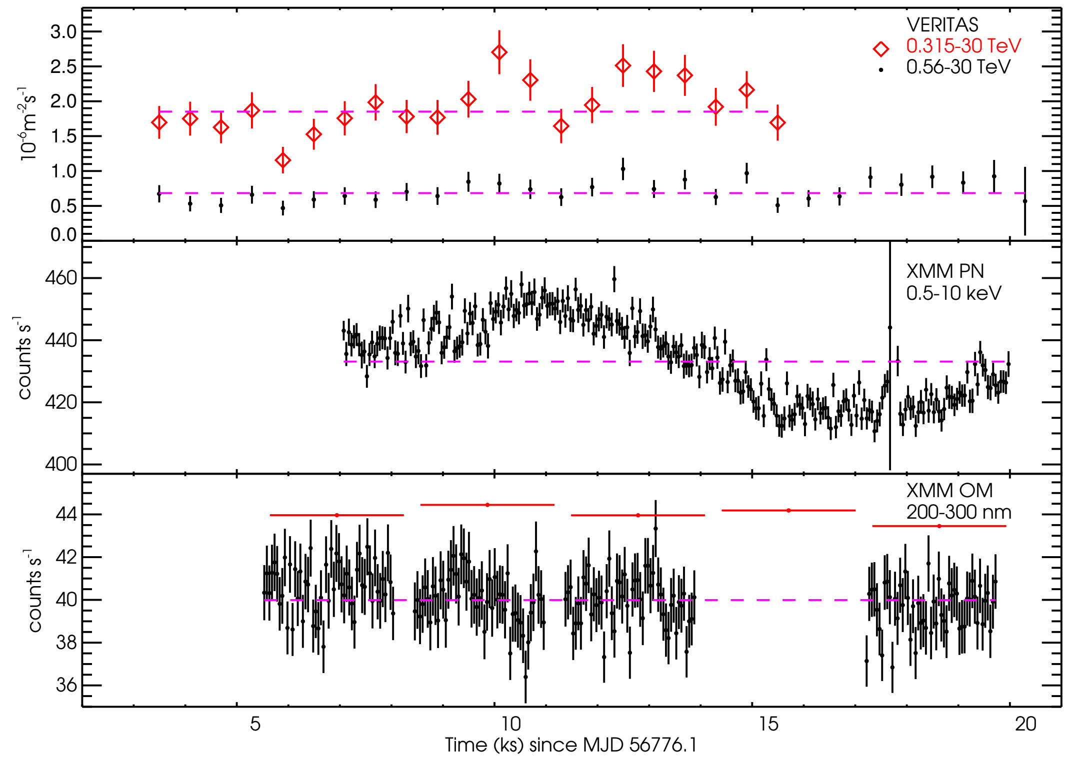

Figure 3.22.: XMM Newton and VERITAS light curves of Mrk 421 from the simultaneous ToO observations on 2014 April 29. Top panel: VERITAS light curves integrated above the highest energy threshold of all runs on that night in 10-minute bins. Middle panel: XMM-Newton PN count rates between 0.5 to 10 keV in 50-s bins. Bottom panel: XMM OM Fast mode optical count rates between 200 to 300 nm in 50-s bins.

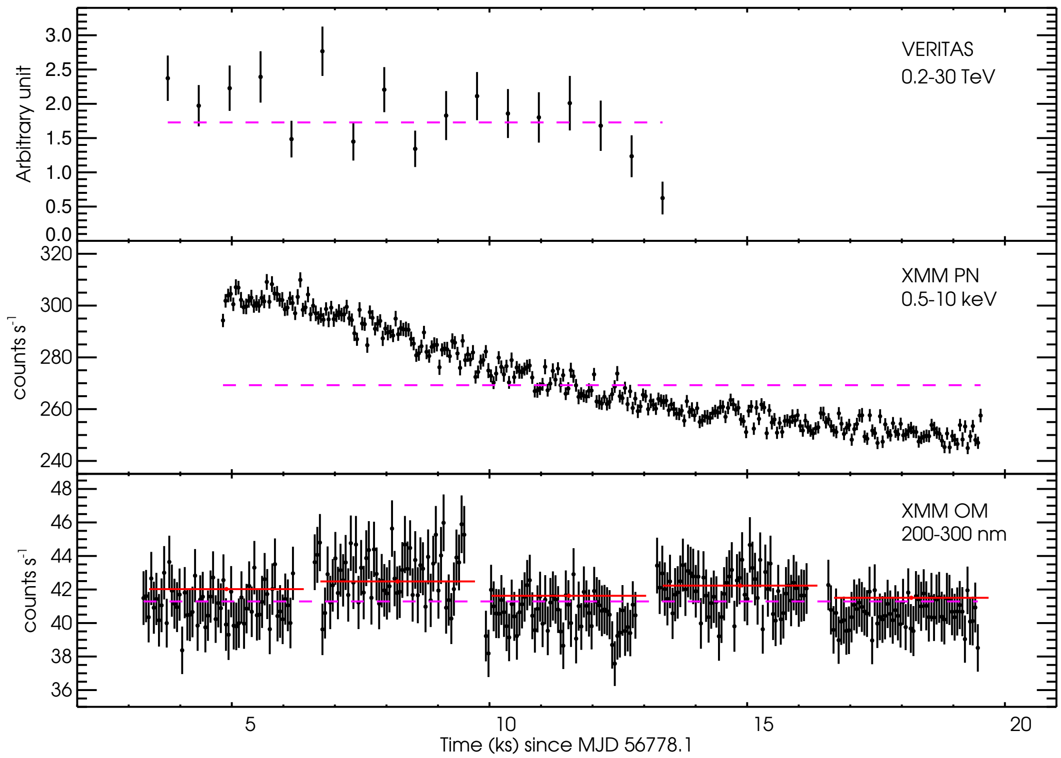

Figure 3.23.: XMM Newton and VERITAS light curves of Mrk 421 from the simultaneous ToO observations on 2014 May 1. Note that VERITAS data on May 1 was taken under poor weather condition.

Table 3.3.: Reduced χ^2 values for constant fit to light curves.

Date	VERITAS	XMM PN	XMM OM
0429	2.1 (> 315 GeV)	11.1	0.9
	1.2 (> 560 GeV)		
0501	-	48.0	0.9
0503	1.6	7.0	0.9

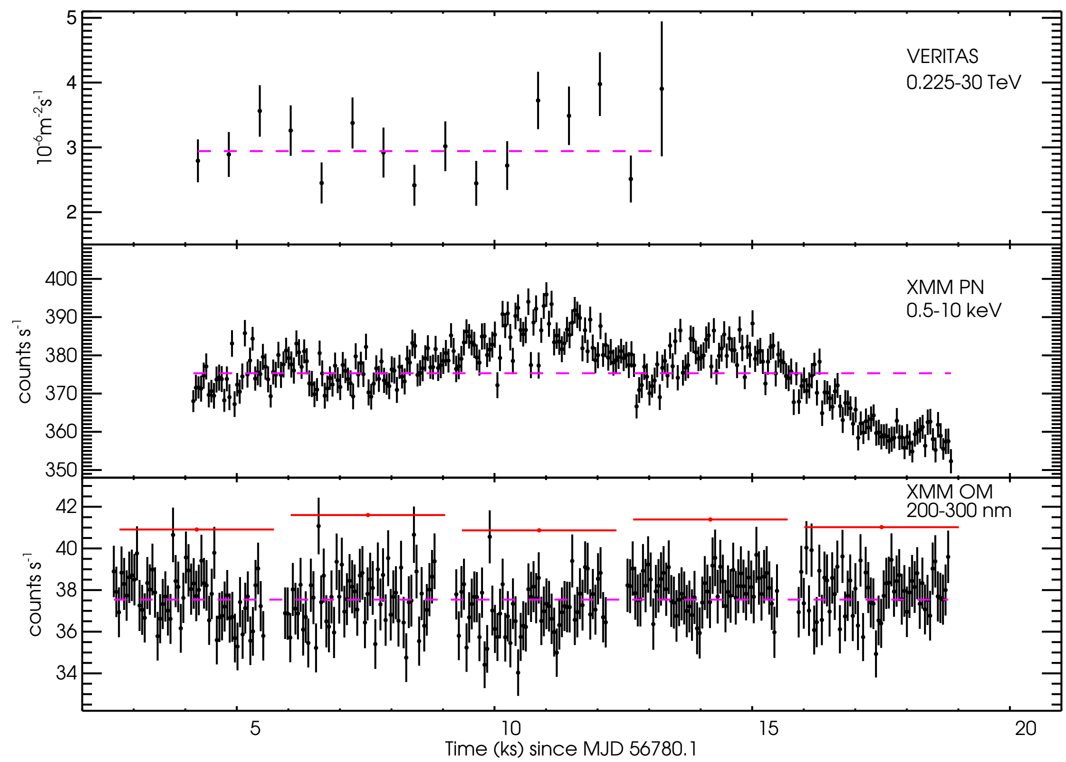

Figure 3.24.: XMM Newton and VERITAS light curves of Mrk 421 from the simultaneous ToO observations on 2014 May 3.

Light curves

Figure 3.22, 3.23, and 3.24 show simultaneous light curves in VHE, X-ray and UV bands. The VHE light curves are binned in 10-minute intervals, integrated from the highest energy threshold among all observations taken on that night, which are 560 GeV on April 29 (and 315 GeV for the first ∼3.5 hr, shown in red diamonds), 200 GeV on May 1 (arbitrary unit shown due to bad weather), and 225 GeV on May 3. The X-ray light curves in the middle panels show XMM EPN count rate between 0.5 to 10 keV binned in 50-s intervals. The bottom panels show UV light curves constructed from XMM OM count rate using UVM2 filter in both Image and Fast mode. The black points are OM Fast mode count rates binned also in 50-s intervals, and red points are OM Image mode count rates binned by exposure.

The average VERITAS integral flux above 0.4 TeV is $(1.27 \pm 0.03) \times 10^{-6}$ m^{-2}s^{-1} on Apr 29 and $(1.10 \pm 0.04) \times 10^{-6}$ m^{-2}s^{-1} on May 3. A constant fit to light curves yields relatively large reduced χ^2 values for X-ray and VHE band (see Table 3.3), rejecting constant hypothesis and suggesting intranight variability in both bands. Another quantity that describes the relative amount of variability is the fractional variability amplitude (see section 3.6). The fractional variability amplitude in X-ray band was measured to be ∼5%, and that in TeV band is ∼10% (as shown in Figure 3.46). A higher fractional variability is observed at higher frequencies, in agreement with previous results (e.g. Błażejowski et al., 2005). This may be the manifestation of the different cooling time at different energies $t_{cool} \propto E^{-1/2}$ (see section 3.5.3). In slow-cooling regime, the cooling time is faster at higher energies leading to fast variability, i.e. more variation on the same timescales. This directly leads to a higher fractional variability for higher energy emissions.

X-ray and TeV flux correlation

In the beginning of this section, we demonstrated that the correlation between X-ray and TeV emissions is of great interest. To examine the relation between the

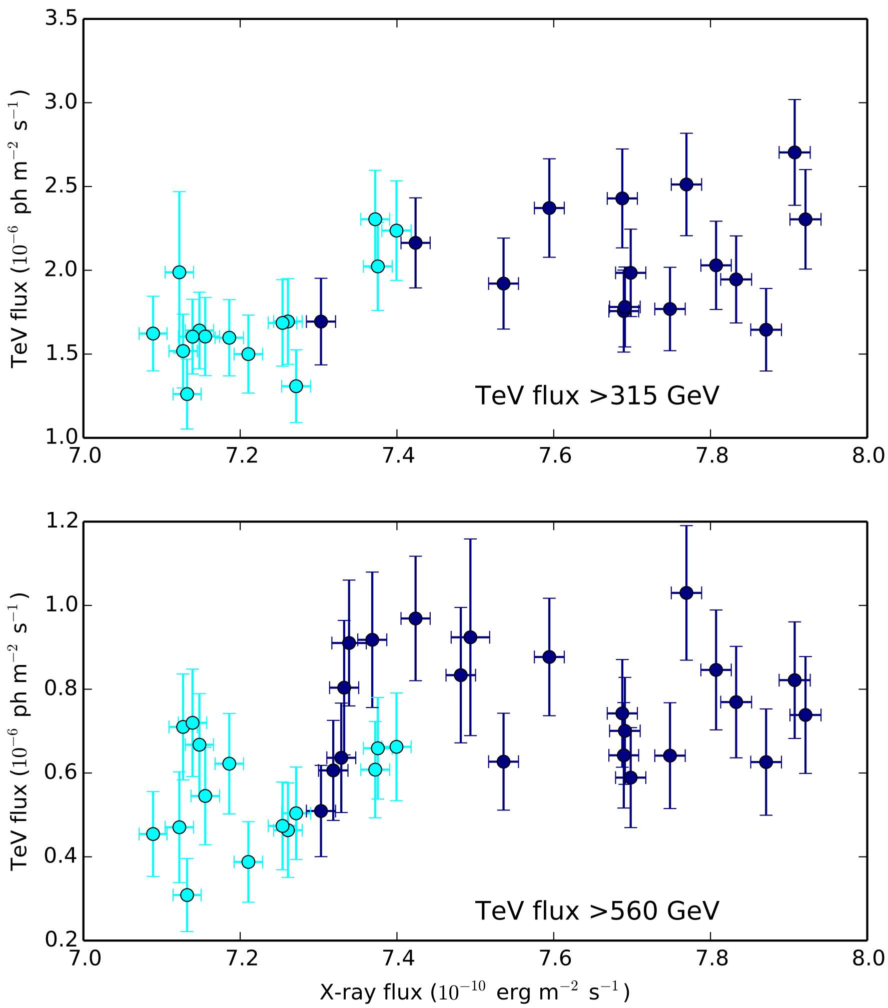

Figure 3.25.: Correlation between TeV flux and X-ray count rate from the simultaneous observations on 2014 April 29 (shown in navy) and May 3 (shown in cyan). TeV fluxes are measured by VERITAS integrated above 315 GeV (top panel) and 560 GeV (bottom panel); X-ray count rates are measured by XMM EPN. Both X-ray and TeV data are binned in 10-minute intervals.

two bands, we first plot VHE flux above 315 GeV and 560 GeV against X-ray flux in Figure 3.25. To convert XMM-Newton count rate to flux, the energy conversion factors (ECF) (see section 3.4.2) are calculated using `WebPIMMS` and the best-fit spectral model in Table 3.7. The correlation is not as strong as one would expect from a one-zone SSC model. Although this may be because that the dynamic range in VHE flux is small, it is consistent with the two-zone SSC model in Petropoulou (2014). As already shown in the observations of BL Lacertae in the previous section, we can also use cross-correlations for such studies. ZDCFs between X-ray and VHE light curves are calculated using `ZDCF_v2.2`, as shown in Figure 3.26. The lack of a peak in ZDCFs indicates that no strong correlation between these two bands can be detected in our data, in agreement with Figure 3.25. A significant dip in ZDCF on Apr 29 seemingly suggests an strong anti-correlation between the two bands at a X-ray lag of $\sim$5 ks, but this is most likely an artifact due to the one-cycle "sinusoidal" shape of the X-ray light curve.

To test the effect of the "sinusoidal" shape of the X-ray light curve, we calculate the auto-correlation function (ACF) also using `ZDCF_v2.2`, as shown in Figure 3.27. A negative peak also showed up in the ACF of the X-ray light curves on Apr 29 and May 3 at $\sim$6 ks. This confirms that the dip in ZDCF between X-ray and TeV data should not indicate a anti-correlation between the two band. We note that CCF and ACF are prone to non-stationary features (e.g. a strong flare) on the timescales comparable to the duration of the light curve. Longer light curve measurements may help avoid this problem, however, gaps that inevitably associated with long measurements also cause significant bias in CCF/ACF as well as power spectrum.

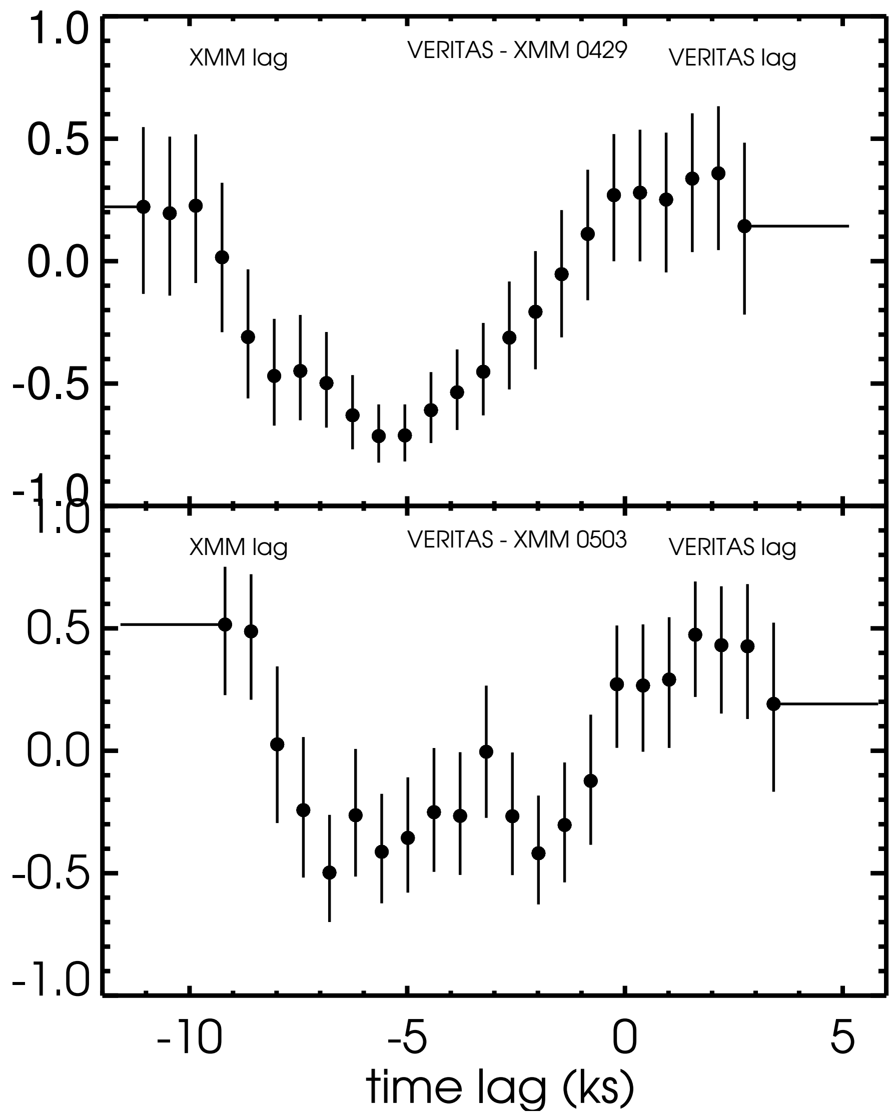

Figure 3.26.: Z-transformed discrete correlation function between X-ray count rate and TeV flux from the simultaneous observations on 2014 April 29 (upper panel) and May 3 (lower panel). Positive lag values represent VHE lag behind X-ray.

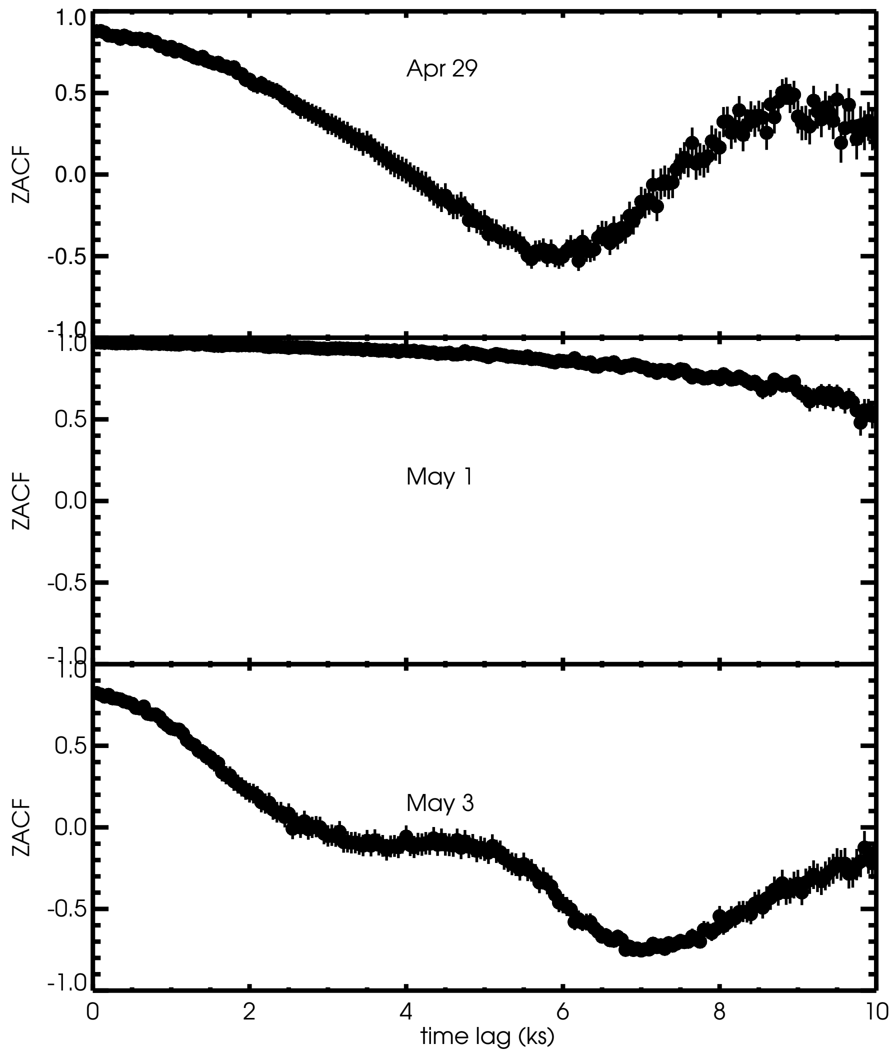

Figure 3.27.: Z-transformed discrete auto-correlation function (ZACF) of X-ray light curves on 2014 April 29 (upper panel), May 1 (middle panel), and May 3 (lower panel), respectively.

Hard/soft X-ray correlation

To study intraband variability at different X-ray bands, we further divide XMM PN X-ray light curves into three energy bands, 0.5-1 keV, 1-3 keV, and 3-10 keV, as shown in the left panels of Figure 3.28, 3.29, and 3.30. ZDCFs are calculated between X-ray light curves at these three bands, as shown in the right panels of the same figures. From the ZDCFs, the corresponding time lags are calculated using `PLIKE v4.0` (see Table 3.4).

Table 3.4 show evidence of hard X-rays 3-10 keV lagging soft X-ray 0.5-1 keV emission (so-called "hard lag") by 0.8-1.8 ks on Apr 29. However, on May 1 and May 3 the opposite "soft lag" scenario is more likely to be the case. Although we note that on May 1 the X-ray count rate monotonously decrease, making it difficult to reliably determine the time lag. Such energy dependent time lag could be the result of two competing timescales, the acceleration timescale and the cooling timescale (e.g. Kirk et al., 1998; Li & Kusunose, 2000; Sato et al., 2008). Higher energy electrons cool faster (through both synchrotron and IC), t_{cool} is smaller. But it also takes a longer time to accelerate an electron to higher energies, i.e. t_{acc} is longer at higher energies (see section 1.1.3 in chapter 1 for a review of t_{cool} and t_{acc} for different processes). Kirk et al. (1998) found that at lower energies (with respect to the highest possible energy for electrons when $t_{cool} = t_{dyn}$), the cooling timescale controls the spectral shape when the flux changes. In this case, the flux change propagates from high energy to low energy, leading to a "soft lag" and clockwise spectral hysteresis loops. On the contrary, at higher energies (close to the maximum), the flux changes are more dominated by the acceleration timescale, and a "hard lag" as well as counter-clockwise spectral hysteresis loops are predicted. We examine the spectral hysteresis patterns in subsection section 3.5.4 Hardness flux correlation and spectral hysteresis.

Table 3.4.: Time lags calculated from ZDCF between hard/soft X-ray light curves. For each night and pair of energy bands, the most likely time lag (peak), its likelihood, and the 1-sigma maximum likelihood interval of the time lag are shown.

Date	1-3 keV lag 0.5-1 keV			3-10 keV lag 1-3 keV			3-10 keV lag 0.5-1 keV		
	peak(s)	likelihood	range(s)	peak(s)	likelihood	range(s)	peak(s)	likelihood	range(s)
0429	50	0.18	−87 - 283	−50	0.14	−213 - 684	1350	0.15	767 - 1776
0501	−800	0.11	−1412 - −124	−3350	0.06	−3753 - −2016	−1650	0.06	−2410 - −1044
0503	−50	0.33	−166 - 83	−750	0.10	−821- −68	−450	0.13	−796- −79

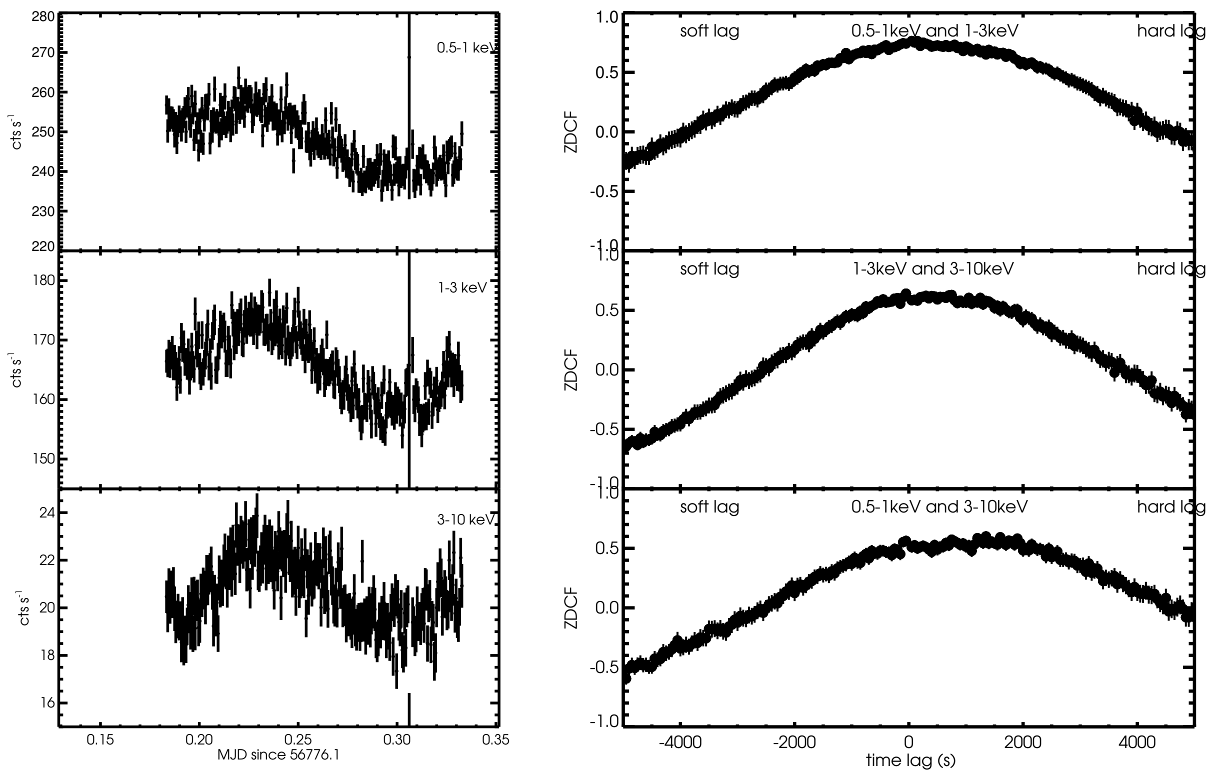

Figure 3.28.: Left panel: Light curves of Mrk 421 observed with XMM Newton EPIC pn on 2014 Apr 29. Count rates binned in 50 s time intervals in three energy bands, 0.5-1 keV, 1-3 keV, and 3-10 keV, are shown from top to bottom panel, respectively. Right panel: the ZDCF between these three X-ray band. Positive lag values indicate “hard lag”.

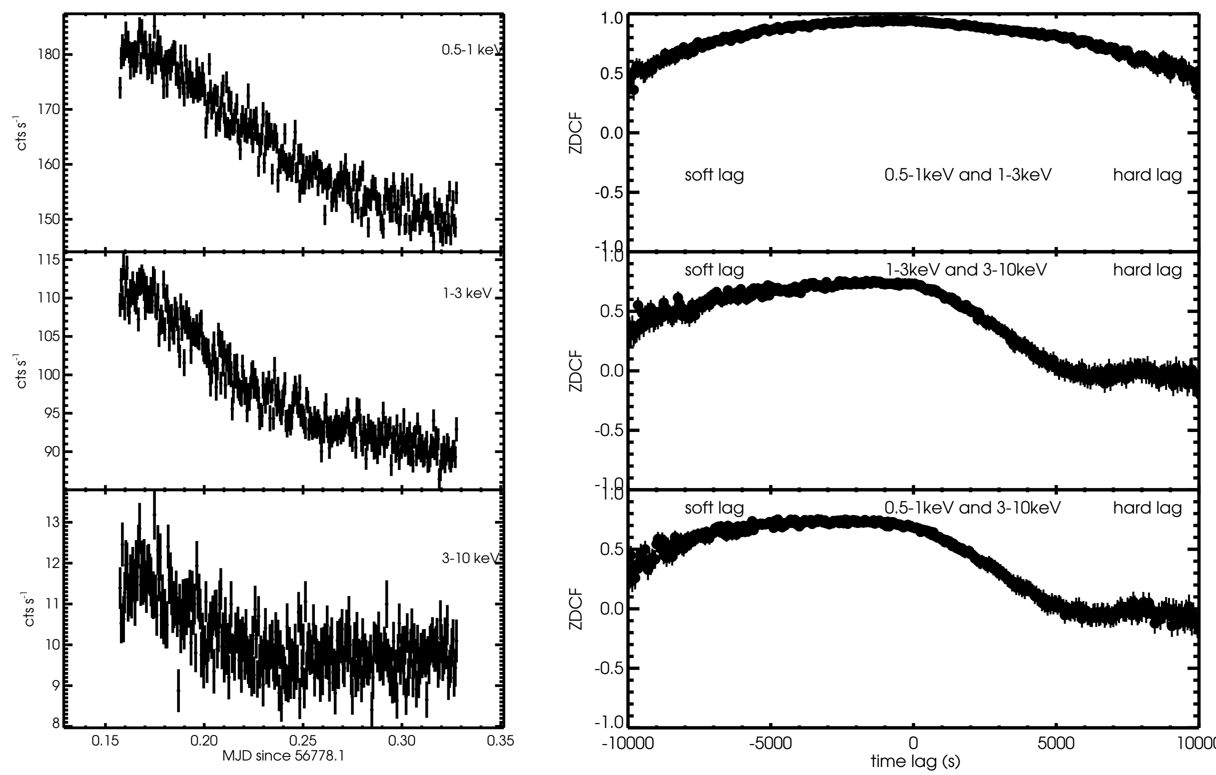

Figure 3.29.: Left panel: Light curves of Mrk 421 observed with XMM Newton EPIC pn on 2014 May 1. Count rates binned in 50 s time intervals in three energy bands, 0.5-1 keV, 1-3 keV, and 3-10 keV, are shown from top to bottom panel, respectively. Right panel: the ZDCF between these three X-ray band. Positive lag values indicate “hard lag”.

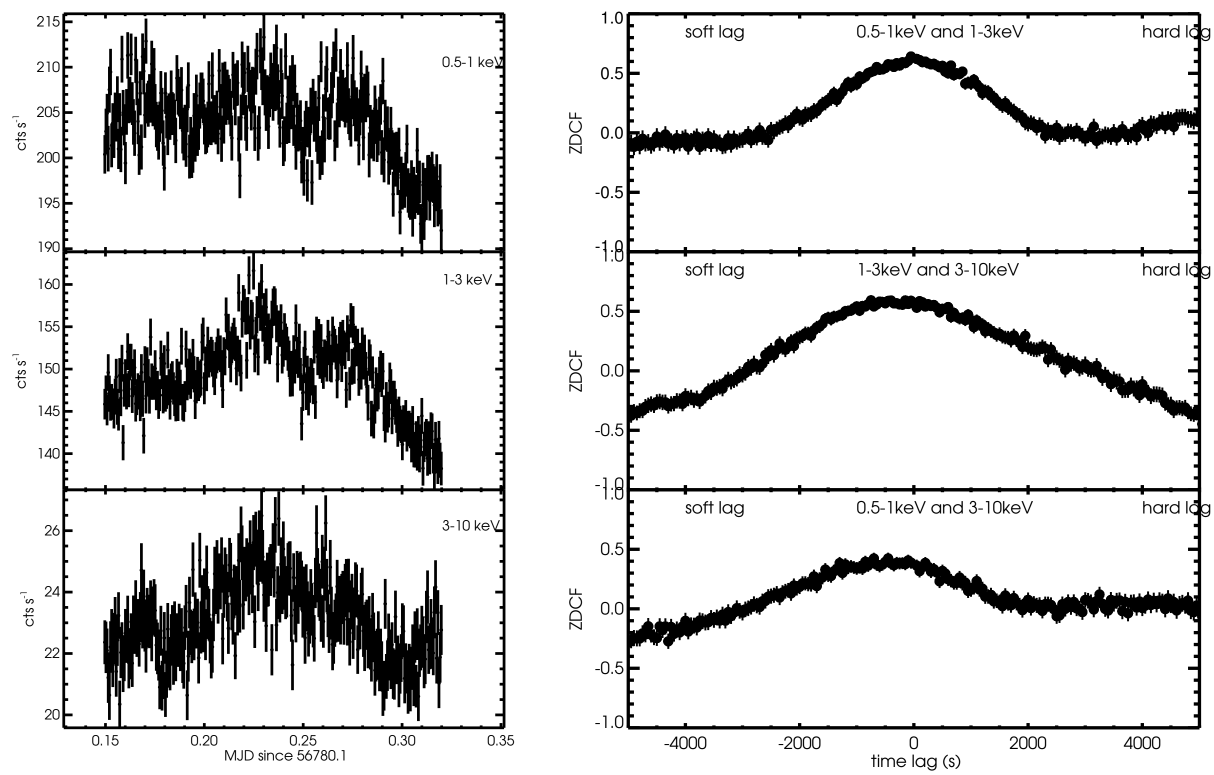

Figure 3.30.: Left panel: Light curves of Mrk 421 observed with XMM Newton EPIC pn on 2014 May 3. Count rates binned in 50 s time intervals in three energy bands, 0.5-1 keV, 1-3 keV, and 3-10 keV, are shown from top to bottom panel, respectively. Right panel: the ZDCF between these three X-ray band. Positive lag values indicate "hard lag".

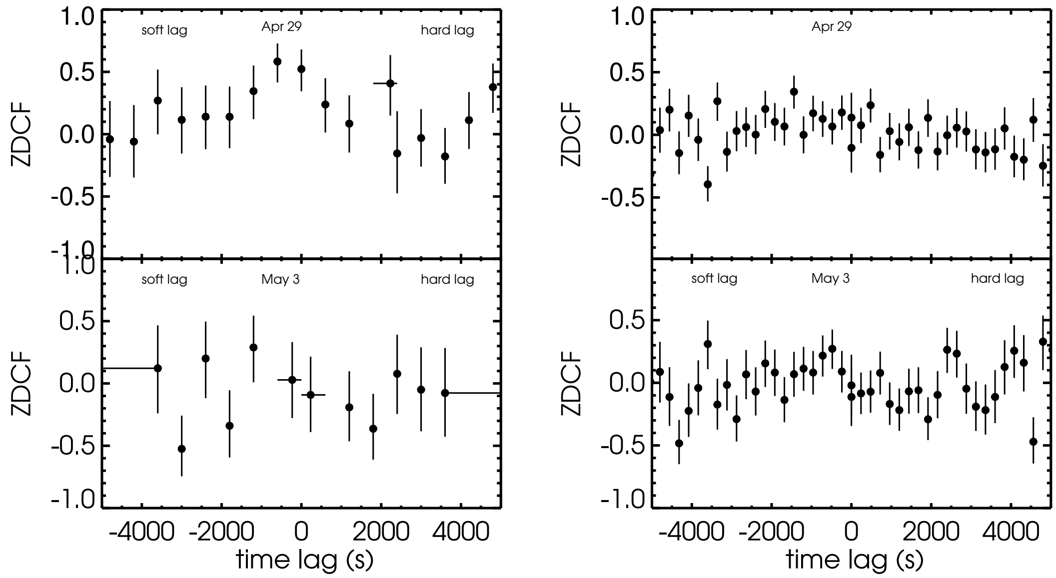

Figure 3.31.: VERITAS ZDCFs between light curves integrated below and above 560 GeV of Mrk 421 on 2014 Apr 29 and May 3. Left panel shows the ZDCF calculated using 10-min binned light curves, and right panel using 4-min binned LCs.

Table 3.5.: Time lags calculated from ZDCF between VERITAS light curves. Negative lag indicates "soft lag" (315/225-560 GeV lags 560 GeV-30 TeV).

Date	bin width (min)	peak (s)	likelihood	1σ interval (s)
0429	10	0	0.38	-480 - $+1330$
0503	10	-1200	0.28	-1470 - $+400$
0429	4	-1440	0.35	-1570 - -6
0503	4	-480	0.24	-1005 - -30

Gamma-ray intraband correlation

The cross-correlations between light curves of blazars at TeV energies are particularly interesting, not only because they can provide insight to the particle acceleration and radiation, but also thanks to their potential to test Lorentz invariance violation which predicts an energy-dependent speed of light at Planck scale. In a similar fashion to X-ray, we divide gamma-ray light curves into two bands, and compute ZDCFs and time lags as shown in Table 3.5 and Figure 3.31. The chosen bands are 315-560 GeV and 560 GeV-30 TeV on Apr 29, and 225-560 GeV and 560 GeV-30 TeV on May 3. The 1-σ confidence interval of the time lag of maximum likelihood is calculated between -2000 s and 2000 s using `plike_v4.0`. The results of the time lags and their probabilities are shown in Table 3.5. ZDCFs are calculated using light curves binned by 10 minutes and 4 minutes, respectively. The results are consistent with no time lags between the two gamma-ray bands, since the 1-σ confidence level covers a wide range of both positive and negative lags. However, the peak likelihood and the 1σ interval seems to prefer a negative time lag on both nights, indicating a possible "soft lag", although not statistically significant.

One limitation of the ZDCFs (also for other DCFs) is that the time lags smaller than the bin width cannot be resolved. The VERITAS light curves used to calculate the ZDCFs have relatively large bin width (4 min), restricting the resolution of the ZDCF. A modified cross-correlation function(MCCF) method is proposed by Li (2001) and Li et al. (2004) to achieve a better time lag resolution. Different from regular CCF or DCF, MCCF does not take a histogram as the input format. Instead it takes a TTE-format input time series, and then applies two different bin-width δt (micro-bin) and Δt (macro-bin) to the events. The time resolution δt can be infinitely small theoretically, but in practice is restricted to be longer than the dead-time of the instrument by which the events are recorded (in the case of VERITAS, $\sim$0.33 ms). The macro-bin timescale $\Delta t = M\delta t$ is the bin width with which a regular histogram is made. There are M micro-bins within each macro-bin. The choice of Δt together with the duration of the light curve determines the timescale being probed.

The key idea of MCCF is to shift the start time of the histogram (with a macro-bin width of Δt) by steps of micro-bin size δt. Therefore, M different histograms $x_m(i; \Delta t)$ can be made, where the index for the start time of the mth histogram is $m = 1, \cdots, M$, indicating the start time of the histogram is at $t_0, t_0 + \delta t, t_0 + 2\delta t, \cdots, t_0 + (M-1)\delta t$ (note that $\Delta t = M\delta t$), and the index i labels the ith macro-bin with a bin width of Δt.

Now instead of regular DCF that is calculated for time lags $k\Delta T$ in steps of Δt, MCCF propose to calculate DCF for time lags $k\delta t$ in steps of δt. For two series X and Y, M histograms can be made for each series as described above: $x_m(i; \Delta t)$ and $y_m(i; \Delta t)$. If we shift one of the light curve e.g. $y_m(i; \Delta t)$ by $k\delta t$, it becomes $y_{m+k}(i; \Delta t)$. Then the MCCF at lag $k\delta t$ is the average of DCFs at $k\delta t$ from the M pairs of light curve, the formula is given by Li et al. (2004):

$$MCCF(k\delta t; \Delta t) = \frac{1}{M} \sum_{m=1}^{M} \sum_{i} \frac{(x_m(i; \Delta t) - \bar{x})(y_{m+k}(i; \Delta t) - \bar{y})}{\sigma(x)\sigma(y)}. \tag{3.16}$$

The shift and average method used in MCCF balances the bias-variance tradeoff, and is able to estimate cross-correlation on a much shorter timescale comparing to the timescales on which a histogram can be made.

The autocorrelation function $ACF(\tau)$ of x(t) is the cross correlation of the signal x(t) and itself with a delay of τ $x(t + \tau)$, defined as:

$$ACF(\tau) = \langle x(t)x(t + \tau)\rangle \tag{3.17}$$

$ACF(\tau)$ is useful for detecting periodicity in the signal, and the length of the memory of a stochastic process. A modified autocorrelation function (MACF) can be defined similarly between a time series $x_m(i; \Delta t)$ and a delayed copy of itself $x_m(i; \Delta t)$. The full width half maximum (FWHM) of the MACF function shows the duration of the variability on the probed timescale ΔT (how far back the process has memory of).

A `C` program wrote by a VERITAS collaborator Nicola Galante is modified and used to compute MCCF. For verification purposes, I generate simulated TTE light

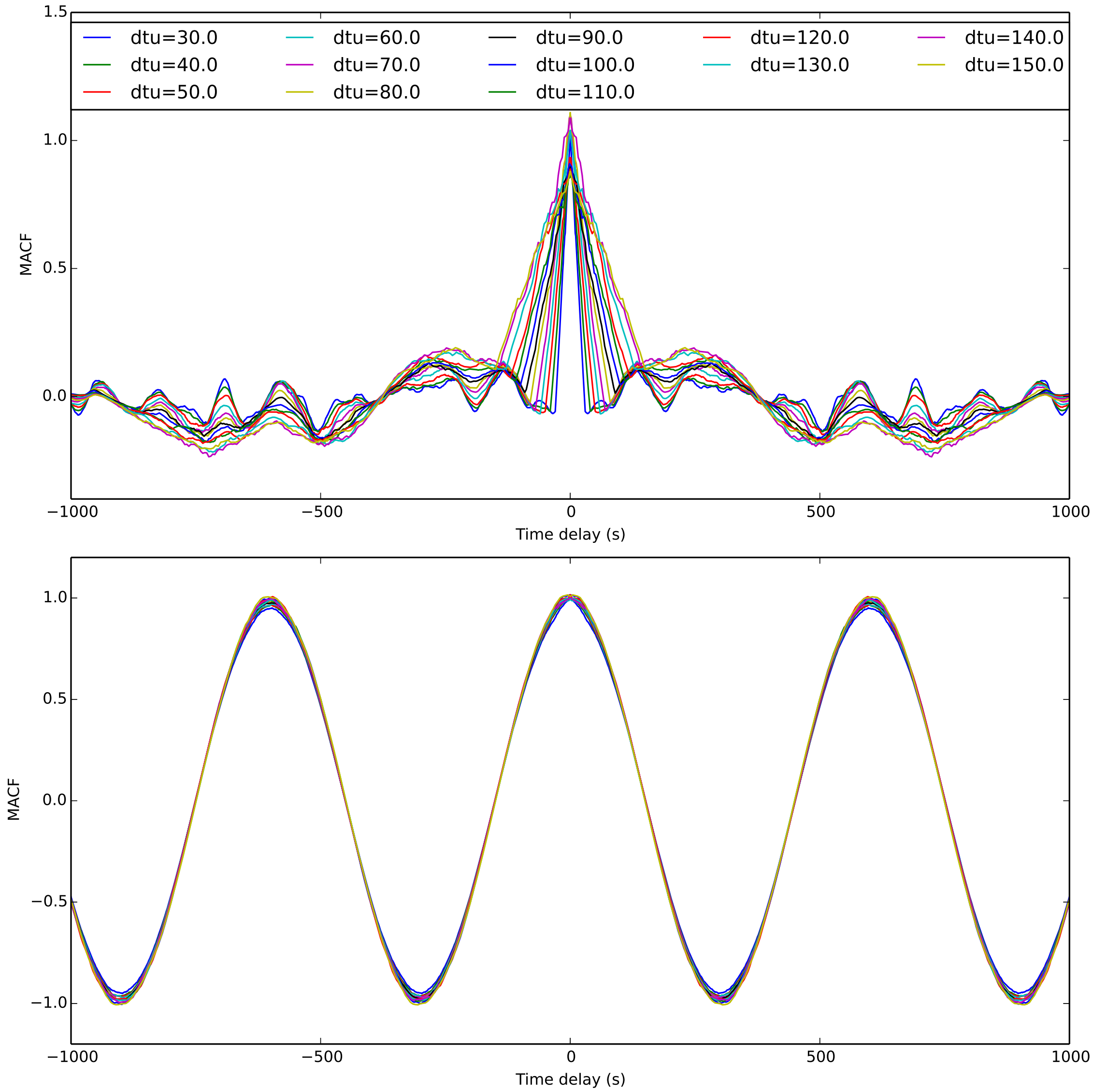

Figure 3.32.: MACF calculated for a simulated Poisson sequence (top panel) and a sinusoidal signal on top of the Poisson noise. Different timescales Δt from 30 s to 150 s are used.

curves containing Poisson noise and sinusoidal signal, and compute the MACF with different timescale Δt ranging from 30 s to 150 s (as shown in Figure 3.32). While the periodicity is well detected by MACF, the FWHM of MACF for Poisson noise depends on the choice of Δt. This is as expected since MCCF/MACF uses overlapping

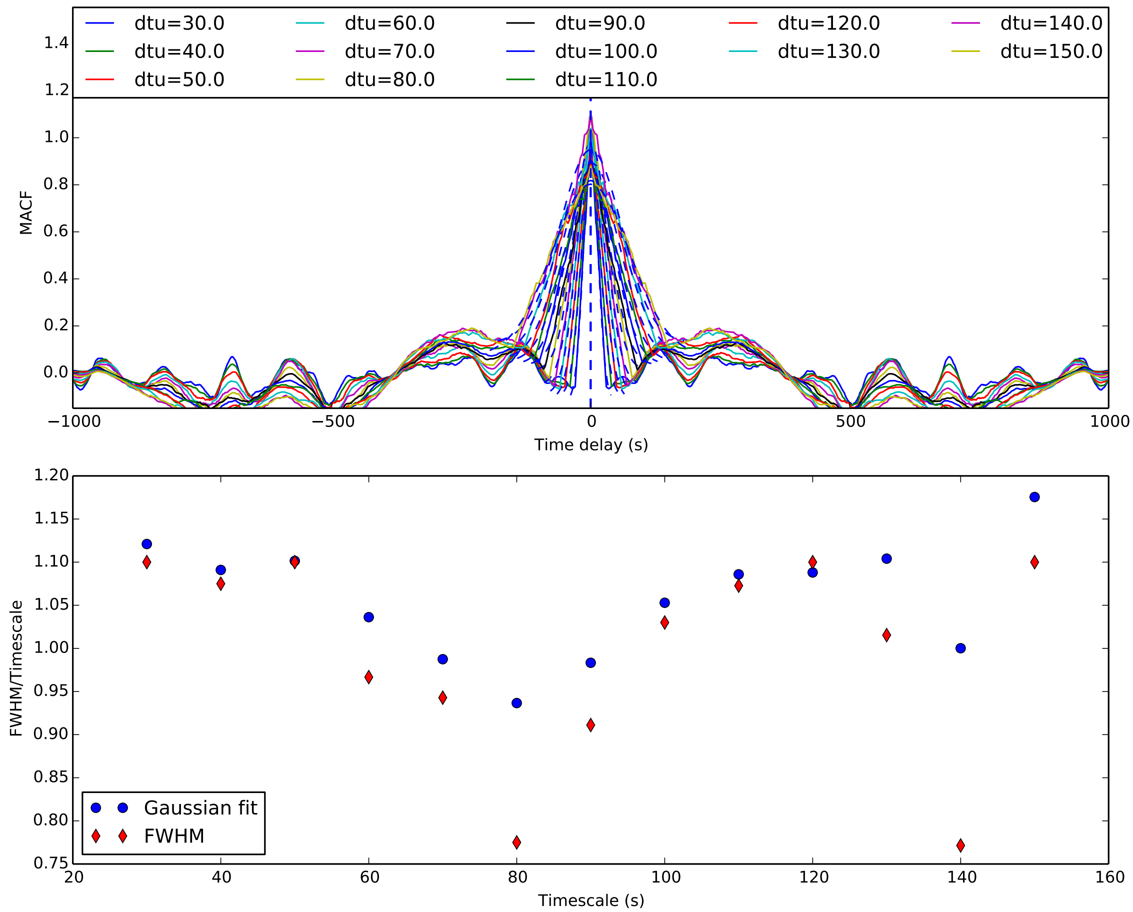

Figure 3.33.: MACF calculated for a simulated Poisson sequence (top panel). The ratio of FWHM and timescale Δt as a function of Δt is plotted in the bottom panel. Different timescales Δt from 30 s to 150 s are used.

segments in a TTE light curve multiple times to get an average, leading to correlation between MCCF/MACF for neighboring time lag values $k\delta t$ within Δt. However, if the FWHM of the MACF is significantly larger than studied timescale Δt, it indicates that the duration of the variation in the light curve on the studied timescale is longer than Δt, i.e. the flux at a given macro-bin Δt_i is correlated with the flux at previous times $\Delta t_{i-1}, \cdots$, which is a feature of autoregressive process and $1/\mathrm{f}^{\alpha}$ noise. Such flickr noise is a signature of blazars. The ratio between FWHM and timescale Δt as a function of Δt is shown in Figure 3.33. The widths of the MACF calculated from

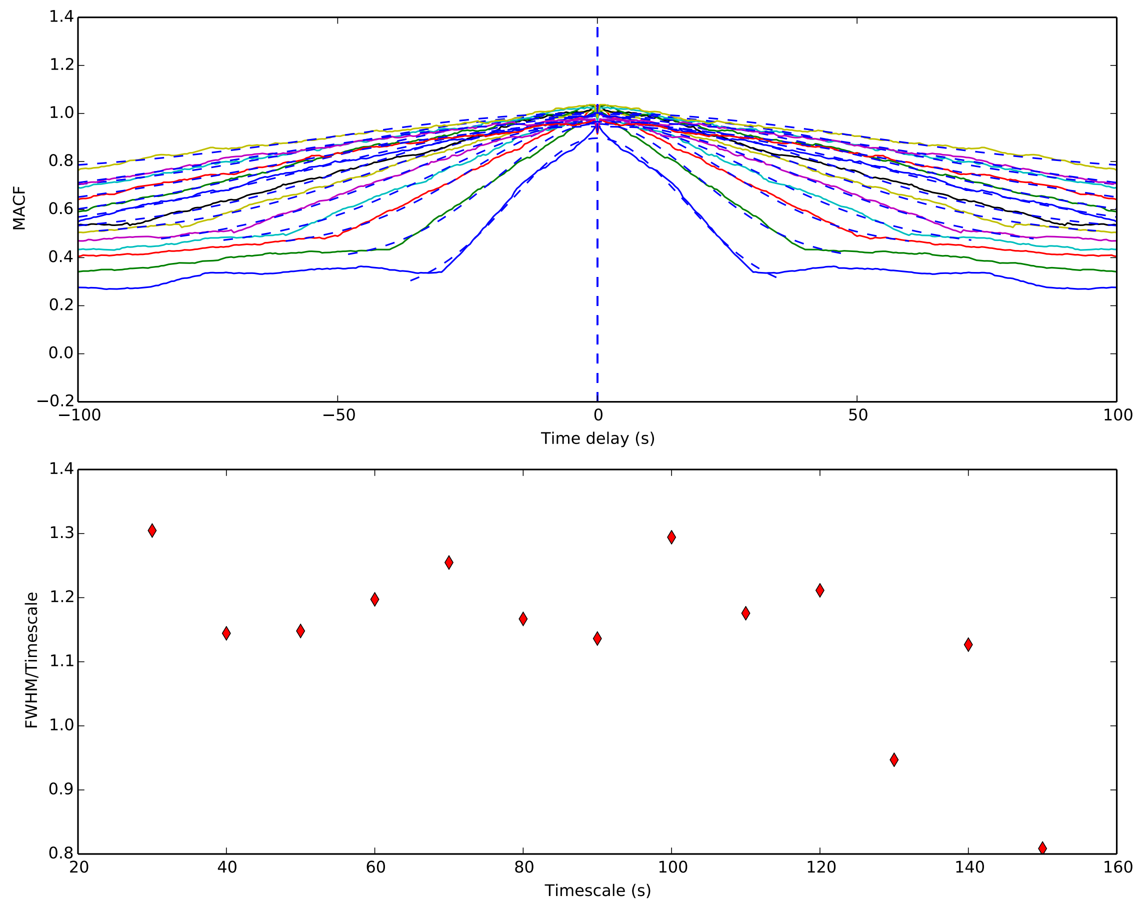

Figure 3.34.: MACF calculated from VERITAS observations of Mrk 421 on 2014 Apr 29 (top panel). The energy interval selected is 560 GeV-30 TeV. The ratio of FWHM and timescale Δt as a function of Δt is plotted in the bottom panel. Different timescales Δt from 30 s to 150 s are used.

both the FWHM and Gaussian plus constant fit are shown. The results are consistent except for Δt =140 s.

Figure 3.34 and 3.35 show the MACF computed for VERITAS TTE list on Apr 29 and May 3. The bottom panel of Figure 3.35 shows the ratio of FWHM and timescale. For the VERITAS observations on May 3, the ratio FWHM/timescale peaks at Δt ~50 s. Although we note that the variation amplitude in FWHM ratio is comparable to that in simulated Poisson noise. A similar study for the VERITAS

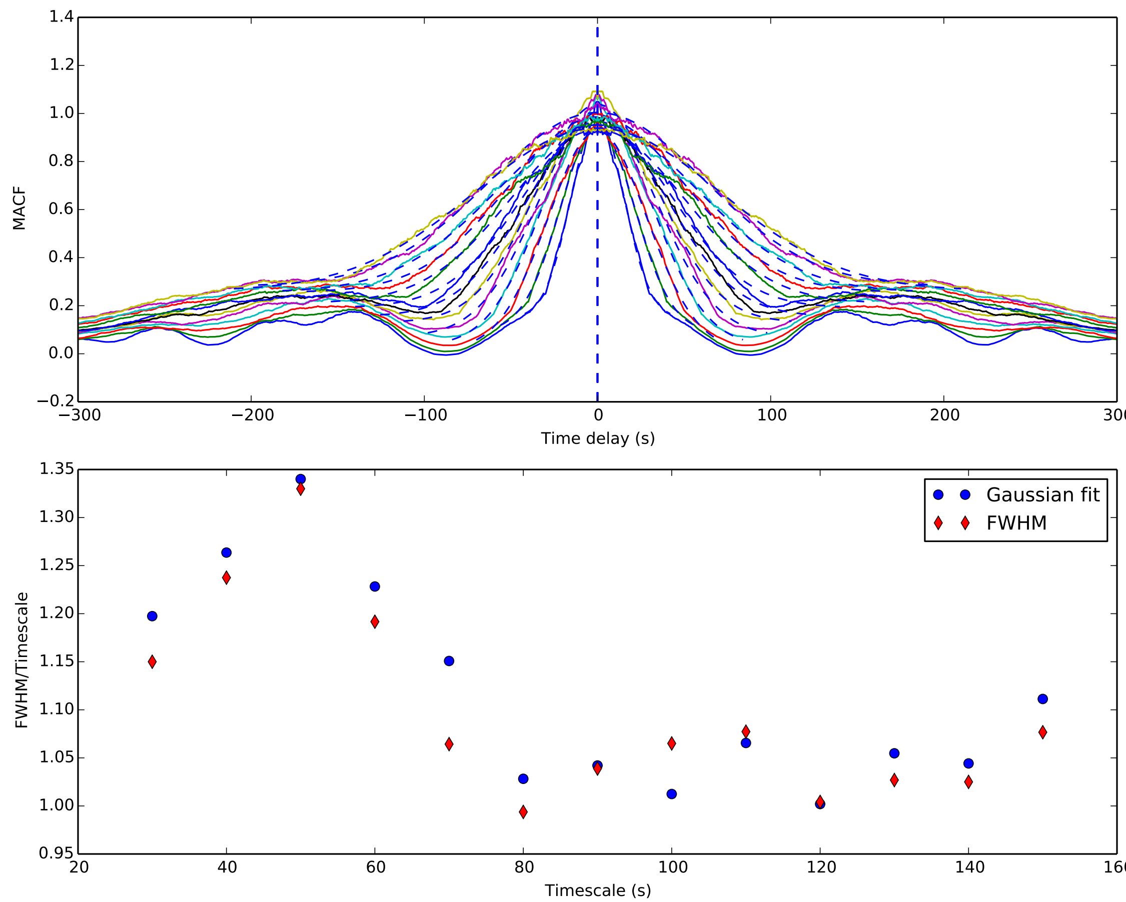

Figure 3.35.: MACF calculated from VERITAS observations of Mrk 421 on 2014 May 3 (top panel). The energy interval selected is 225 GeV-30 TeV. The ratio of FWHM and timescale Δt as a function of Δt is plotted in the bottom panel. Different timescales Δt from 30 s to 150 s are used.

observations of Mrk 421 in 2010 is being done as a part of a VERITAS publication in preparation.

To study the time lags at different gamma-ray energies, we calculate the MCCFs. We first test the MCCFs on 100 pairs of simulated light curves. Each light curve is simulated following the procedures below:

1. simulate a red-noise light curve with a power-law power spectral density distribution (PSD$\propto 1/f$), at a mean rate of 0.15 cts/s, with a bin-width of 0.67 s

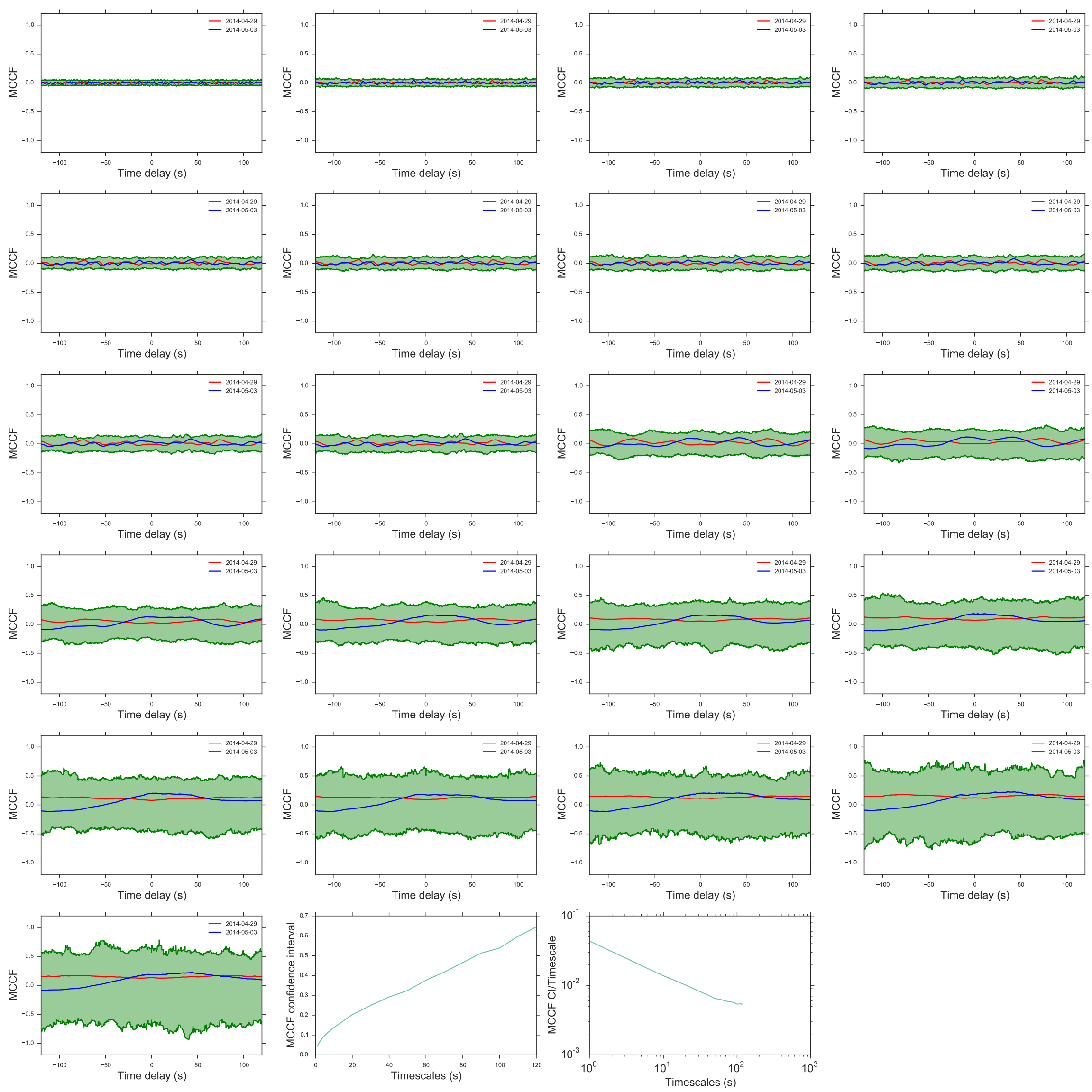

Figure 3.36.: The green shaded regions show the 95% confidence intervals (CI) calculated from 100 MCCFs between simulated pairs of red-noise Poisson sequences. From top left to bottom right, different timescales (Δt_u) ranging from 1.0 s to 10 s in 1 s steps, and from 10 s to 120 s in 10 s steps were used in the MCCF calculation, respectively. The MCCFs calculated from the VERITAS data at the corresponding timescale between energy above/below 800 GeV on Apr 29 and May 3 are shown in red and blue, respectively. The last two panels in the bottom row show the relation between the MCCF CIs and the timescales.

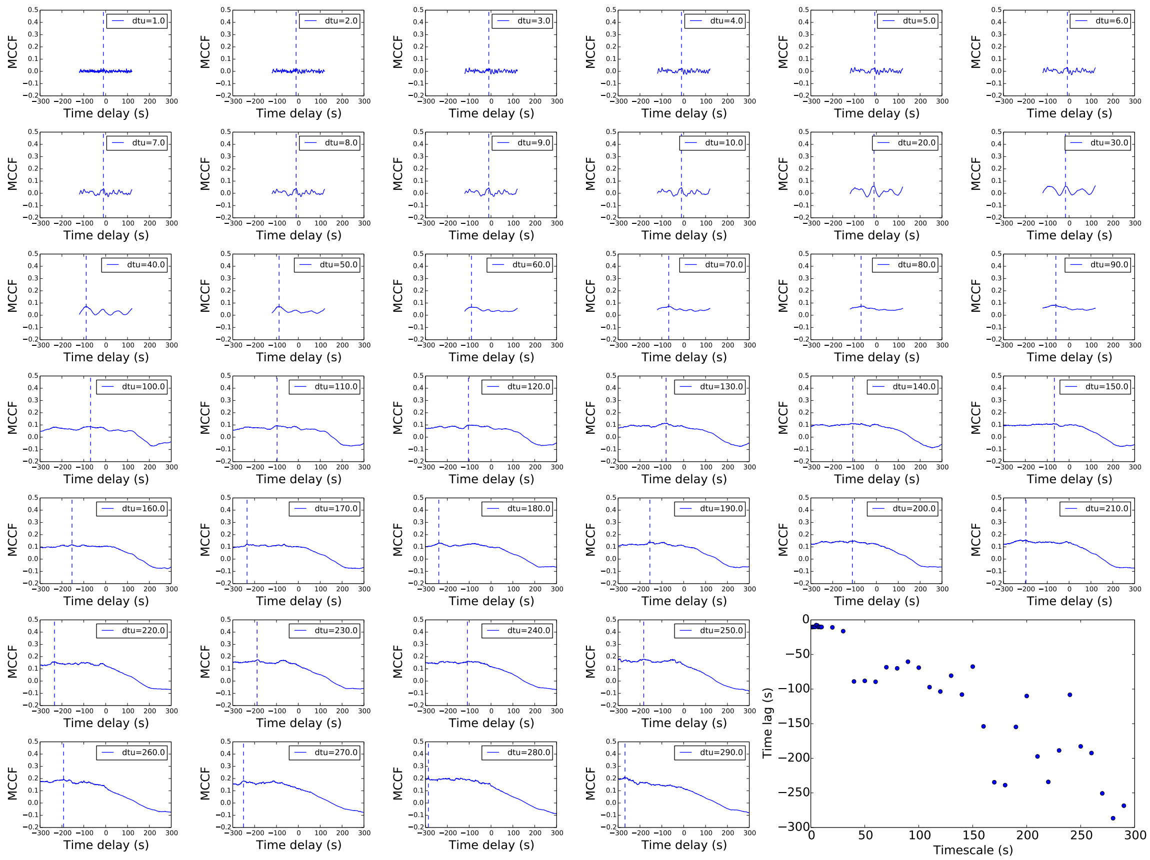

Figure 3.37.: The MCCFs calculated between two TeV bands, 560-800 GeV and 800 GeV to 30 TeV, measured on 2014 Apr 29. Time steps δt=0.1 s and different timescales (Δt_u) ranging from 1.0 s to 190 s were used. Positive lag values indicate "hard lag". Bottom panel: the MCCF between two TeV bands. The vertical lines are drawn at the time lags with the maximum MCCF value.

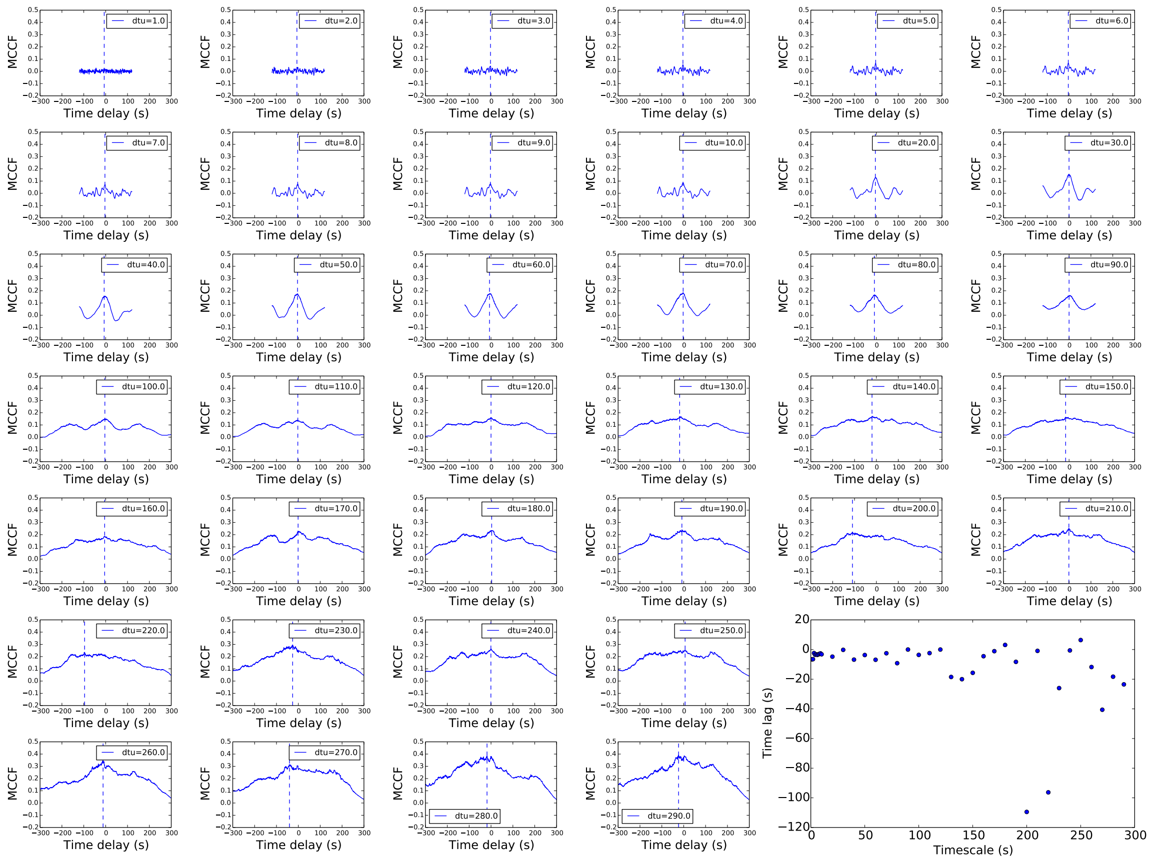

Figure 3.38.: The MCCFs calculated between two TeV bands, 225-600 GeV and 600 GeV to 30 TeV, measured on 2014 May 3. Time steps δt=0.1 s and different timescales (Δt_u) ranging from 1.0 s to 190 s were used. Positive lag values indicate “hard lag”. Bottom panel: the MCCF between two TeV bands. The vertical lines are drawn at the time lags with the maximum MCCF value.

and a duration of ∼16 ks that are comparable to the VERITAS observations of Mrk 421;

2. within each time bin, we use the rate generated from the previous step as the expected rate, and simulated a Poisson sequence with arrival time between the start and end of this bin, the total number of events in each simulated light curve is ∼2400, comparable to the observed ones;

3. we assign an energy taken from an "On" event observed by VERITAS on Apr 29 to each simulated event, to ensure the simulated light curve has the same spectrum as the observed one.

The 95% confidence intervals from the MCCFs calculated from 100 pairs of simulated red-noise Poisson sequences are shown as the green shaded regions in Figure 3.36. The confidence interval becomes wider as the timescales increases (as shown in the second panel of the last row of Figure 3.36). As a result, no significant cross-correlation can be established from the VERITAS data between the energy range below and above 800 GeV.

Figure 3.37 and 3.38 show the results of MCCF computed for the VERITAS observations between two TeV bands, 560GeV to 800 GeV and 800 GeV - to 30 TeV on Apr 29, and 225 GeV to 600 GeV and 600 GeV to 30 TeV on May 3, respectively. All events in the 0.1° "On" region that passed the quality and shower cuts are used. The MCCFs show evidence of a "soft lag" in VHE band on Apr 29, peaking at a negative time lag (560GeV to 800 GeV lags 800 GeV - to 30 TeV) increasing from ∼0 s to ∼300 s as timescale Δt becomes longer. However, we note the peak value of the MCCF is around 0.2, which is not strong enough to claim a correlation between the two band. The MCCF on Apr 29 is also consistent with a "soft" lag scenario, although the time lag is even smaller at around 20 s, while the peak MCCF value is slightly higher, reaching 0.4.

Combining the ZDCF and the MCCF results, no statistically significant conclusions can be reached for the gamma-ray time lag. However, both methods seem to suggest a "soft" lag in TeV gamma-ray band. If a time lag (e.g. "soft" lag here) can be established, it has several important implications on cooling and acceleration timescales, or alternatively on Lorentz invariance violation.

Hardness flux correlation and spectral hysteresis

Besides the time lags at different energies, the spectral evolutions during blazar flares are also informative. A general trend that the spectrum is harder when the flux is higher is observed in blazars in both X-ray and gamma-ray band (e.g. Albert et al., 2007b; Fossati et al., 2008; Acciari et al., 2011b; Aleksić et al., 2011). Several possibilities can lead to such a trend if they are located at the synchrotron and IC tail of the SED peaks, e.g. an increase of the maximum electron energy or a hardening in the electron energy distribution (see 3.3). If the X-ray and gamma-ray are sampling the emissions near the peak of the SED, the "harder-when-brighter" effect could also be the result of an increase of the SED peak frequency, which could arise from an increase in magnetic field strength or Doppler factor.

Apart from the "harder-when-brighter" trend in the hardness-flux relation, the competition between acceleration timescale and the cooling timescale can lead to spectral hysteresis, i.e. the hardness of the spectrum is different on the rising edge of the flux comparing to that on the falling edge (e.g. Kirk et al., 1998; Li & Kusunose, 2000; Sato et al., 2008). If one plots the hardness-flux relation so that the spectrum is harder toward positive y-axis, and the flux is higher toward positive x-axis, the spectral hysteresis are seen as loop patterns. Since the spectral hysteresis is driven by the same timescales that determine the time lags at different energies, the direction of the hysteresis loop should be consistent with the sign of the time lag. Specifically, a "hard lag" should correspond to counter-clockwise hysteresis loops (see section 3.5.4), while a "soft lag" will lead to clockwise hysteresis loops. Therefore the hardness-flux plot offers an alternative view on the timescales in the system, and can be compared with the time lags studies presented in the previous section. We divide the

Table 3.6.: VERITAS spectral fit results for a power law model with exponential cutoff and a log parabola model.

Power law with exponential cutoff model (see equation 3.5)				
Date	α	Cutoff energy (TeV)	Normalization K (at 1 TeV, $10^{-7}\mathrm{m}^{-2}\mathrm{s}^{-1}$)	Reduced χ^2
0429	2.38 ± 0.10	1.94 ± 0.4	8.1 ± 1.2	3.7
0503	2.38 ± 0.12	2.1 ± 0.8	7.1 ± 1.4	1.7

Log parabola model (see equation 3.6)					
Date	α	β	Reference energy E_0 (TeV)	Normalization K (at E_0 TeV, $10^{-7}\mathrm{m}^{-2}\mathrm{s}^{-1}$)	Reduced χ^2
0429	2.87 ± 0.06	0.23 ± 0.05	0.79 ± 0.10	9.7 ± 2.9	4.5
0503	2.82 ± 0.08	0.23 ± 0.06	0.77 ± 0.10	9.3 ± 3.4	1.24

Table 3.7.: XMM-Newton EPIC pn spectral fit results and ECFs.

Absorbed power law model (see equation 3.7)				
Parameter	Unit	Value on 0429	Value on 0501	Value on 0503
α		2.657 ± 0.003	2.830 ± 0.003	2.451 ± 0.002
n_H	10^{20}cm^{-2}	3.33 ± 0.04	3.62 ± 0.04	1.98 ± 0.03
K_{PL}	at 1 keV	0.2765 ± 0.0004	0.1750 ± 0.0003	0.2264 ± 0.0003
Reduced χ^2		8.4	6.6	7.9
ECF	10^{11} cts cm^2 erg^{-1}	5.74	6.15	5.30

Absorbed power law model plus three absorption features (see 3.7)				
Parameter	Unit	Value on 0429	Value on 0501	Value on 0503
E_c	keV	0.563 ± 0.008	0.572 ± 0.009	$K_G = 0.5$
D		0.078 ± 0.009	0.059 ± 0.007	$\sigma_G = 0.1$
n_H	10^{20} cm^{-2}	2.37 ± 0.11	2.85 ± 0.10	1.89 ± 0.06
α		2.654 ± 0.003	2.827 ± 0.003	2.450 ± 0.002
K_{PL}		0.2732 ± 0.0006	0.1732 ± 0.0004	0.2251 ± 0.0005
$E_{0,1}$	keV	1.88 ± 0.02	1.88 ± 0.02	1.87 ± 0.03
σ_1	keV	1.8×10^{-7}	6.7×10^{-6}	2×10^{-7}
$K_{G,1}$	10^{-4}	2.1 ± 0.4	0.9 ± 0.2	0.9 ± 0.3
$E_{0,2}$	keV	2.264 ± 0.003	2.254 ± 0.007	2.26 ± 0.10
σ_2	keV	0.043 ± 0.008	0.04 ± 0.01	6×10^{-5}
$K_{G,2}$	10^{-4}	8.0 ± 0.4	3.2 ± 0.3	5.9 ± 0.5
Reduced χ^2		1.51	1.27	2.3

Table 3.8.: XMM-Newton EPIC pn rate and spectral index results for data on 2014 Apr 29.

MJD (Day)	rate (cts s^{-1})	index	norm (at 1 keV)
56776.1866251	438.15 ± 1.09	2.70 ± 0.01	0.283 ± 0.002
56776.1935696	439.62 ± 1.10	2.74 ± 0.01	0.290 ± 0.002
56776.200514	439.03 ± 1.12	2.68 ± 0.01	0.283 ± 0.002
56776.2074585	442.04 ± 1.11	2.69 ± 0.01	0.285 ± 0.002
56776.2144029	444.98 ± 1.11	2.65 ± 0.01	0.284 ± 0.002
56776.2213474	451.28 ± 1.14	2.63 ± 0.01	0.286 ± 0.002
56776.2282918	451.90 ± 1.13	2.63 ± 0.01	0.286 ± 0.002
56776.2352362	449.26 ± 1.12	2.64 ± 0.01	0.286 ± 0.002
56776.2421807	446.69 ± 1.13	2.62 ± 0.01	0.281 ± 0.002
56776.2491251	442.98 ± 1.11	2.65 ± 0.01	0.283 ± 0.002
56776.2560696	438.21 ± 1.10	2.63 ± 0.01	0.278 ± 0.002
56776.263014	433.23 ± 1.09	2.65 ± 0.01	0.276 ± 0.002
56776.2699585	430.08 ± 1.09	2.66 ± 0.01	0.274 ± 0.002
56776.2769029	422.98 ± 1.06	2.67 ± 0.01	0.271 ± 0.002
56776.2838474	416.70 ± 1.06	2.67 ± 0.01	0.266 ± 0.002
56776.2907918	417.77 ± 1.07	2.68 ± 0.01	0.268 ± 0.002
56776.2977362	418.08 ± 1.06	2.69 ± 0.01	0.270 ± 0.002
56776.3046807	419.63 ± 1.26	2.71 ± 0.01	0.274 ± 0.002
56776.3116251	417.70 ± 1.06	2.68 ± 0.01	0.268 ± 0.002
56776.3185696	419.99 ± 1.06	2.67 ± 0.01	0.268 ± 0.002
56776.325514	426.88 ± 1.08	2.63 ± 0.01	0.271 ± 0.002
56776.3324585	426.90 ± 1.40	2.67 ± 0.01	0.275 ± 0.002

Table 3.9.: XMM-Newton EPIC pn rate and spectral index results for data on 2014 May 1.

MJD (Day)	rate (cts s^{-1})	index	norm (at 1 keV)
56778.1606338	301.93 ± 0.80	2.83 ± 0.01	0.198 ± 0.001
56778.1675782	302.92 ± 0.81	2.83 ± 0.01	0.199 ± 0.001
56778.1745226	300.68 ± 0.81	2.82 ± 0.01	0.196 ± 0.001
56778.1814671	296.48 ± 0.80	2.83 ± 0.01	0.193 ± 0.001
56778.1884115	293.23 ± 0.79	2.86 ± 0.01	0.193 ± 0.001
56778.195356	290.81 ± 0.79	2.85 ± 0.01	0.191 ± 0.001
56778.2023004	284.72 ± 0.77	2.88 ± 0.01	0.187 ± 0.001
56778.2092449	282.00 ± 0.77	2.87 ± 0.01	0.186 ± 0.001
56778.2161893	276.54 ± 0.75	2.85 ± 0.01	0.179 ± 0.001
56778.2231338	275.05 ± 0.75	2.87 ± 0.01	0.180 ± 0.001
56778.2300782	270.59 ± 0.75	2.86 ± 0.01	0.175 ± 0.001
56778.2370226	268.19 ± 0.73	2.89 ± 0.01	0.178 ± 0.001
56778.2439671	265.64 ± 0.73	2.87 ± 0.01	0.174 ± 0.001
56778.2509115	263.14 ± 0.73	2.85 ± 0.01	0.171 ± 0.001
56778.257856	260.46 ± 0.71	2.84 ± 0.01	0.167 ± 0.001
56778.2648004	258.21 ± 0.71	2.84 ± 0.01	0.168 ± 0.001
56778.2717449	258.75 ± 0.71	2.82 ± 0.01	0.165 ± 0.001
56778.2786893	256.96 ± 0.71	2.84 ± 0.01	0.166 ± 0.001
56778.2856338	254.61 ± 0.71	2.83 ± 0.01	0.164 ± 0.001
56778.2925782	254.08 ± 0.70	2.81 ± 0.01	0.162 ± 0.001
56778.2995226	252.94 ± 0.70	2.83 ± 0.01	0.164 ± 0.001
56778.3064671	251.53 ± 0.69	2.81 ± 0.01	0.161 ± 0.001
56778.3134115	250.45 ± 0.69	2.81 ± 0.01	0.160 ± 0.001
56778.320356	249.03 ± 0.70	2.79 ± 0.01	0.157 ± 0.001
56778.3273004	250.38 ± 0.91	2.80 ± 0.01	0.159 ± 0.002

Table 3.10.: XMM-Newton EPIC pn rate and spectral index results for data on 2014 May 3.

MJD (Day)	rate (cts s^{-1})	index	norm (at 1 keV)
56780.1528554	371.95 ± 0.94	2.49 ± 0.01	0.227 ± 0.001
56780.1597998	375.11 ± 0.95	2.49 ± 0.01	0.229 ± 0.002
56780.1667442	375.46 ± 0.96	2.46 ± 0.01	0.225 ± 0.002
56780.1736887	377.58 ± 0.96	2.47 ± 0.01	0.228 ± 0.002
56780.1806331	374.14 ± 0.95	2.50 ± 0.01	0.229 ± 0.002
56780.1875776	374.57 ± 0.94	2.48 ± 0.01	0.227 ± 0.001
56780.194522	374.75 ± 0.95	2.47 ± 0.01	0.227 ± 0.002
56780.2014665	378.54 ± 0.96	2.46 ± 0.01	0.231 ± 0.002
56780.2084109	380.87 ± 0.96	2.44 ± 0.01	0.229 ± 0.002
56780.2153554	381.24 ± 0.97	2.44 ± 0.01	0.230 ± 0.002
56780.2222998	387.21 ± 0.97	2.43 ± 0.01	0.234 ± 0.002
56780.2292442	387.55 ± 0.98	2.43 ± 0.01	0.234 ± 0.002
56780.2361887	386.21 ± 0.97	2.43 ± 0.01	0.233 ± 0.002
56780.2431331	380.53 ± 0.96	2.44 ± 0.01	0.229 ± 0.002
56780.2500776	374.18 ± 0.95	2.44 ± 0.01	0.226 ± 0.001
56780.257022	377.89 ± 0.96	2.43 ± 0.01	0.226 ± 0.001
56780.2639665	381.10 ± 0.96	2.44 ± 0.01	0.229 ± 0.002
56780.2709109	381.33 ± 0.96	2.45 ± 0.01	0.231 ± 0.002
56780.2778554	379.76 ± 0.97	2.45 ± 0.01	0.229 ± 0.002
56780.2847998	373.50 ± 0.95	2.48 ± 0.01	0.227 ± 0.002
56780.2917442	370.96 ± 0.93	2.48 ± 0.01	0.226 ± 0.001
56780.2986887	363.23 ± 0.94	2.47 ± 0.01	0.219 ± 0.001
56780.3056331	359.62 ± 0.91	2.48 ± 0.01	0.218 ± 0.001
56780.3125776	358.71 ± 0.91	2.45 ± 0.01	0.214 ± 0.001
56780.319522	356.84 ± 1.21	2.45 ± 0.01	0.213 ± 0.002

Table 3.11.: VERITAS flux and spectral index results for data on 2014 Apr 29.

MJD (Day)	Flux>560GeV 10^{-6} m $^{-2}$ s^{-1}	Index	Flux 315-560GeV 10^{-6} m $^{-2}$ s^{-1}
56776.1420065	0.67 ± 0.12	-2.43 ± 0.17	1.02 ± 0.20
56776.1489509	0.53 ± 0.11	-2.69 ± 0.22	1.22 ± 0.22
56776.1558953	0.51 ± 0.11	-2.36 ± 0.22	1.12 ± 0.20
56776.1628398	0.66 ± 0.13	-2.66 ± 0.22	1.21 ± 0.23
56776.1697842	0.47 ± 0.11	-2.99 ± 0.25	0.69 ± 0.16
56776.1767287	0.59 ± 0.12	-2.68 ± 0.23	0.94 ± 0.19
56776.1836731	0.64 ± 0.13	-2.60 ± 0.17	1.11 ± 0.21
56776.1906176	0.59 ± 0.12	-2.70 ± 0.16	1.40 ± 0.23
56776.197562	0.70 ± 0.13	-2.75 ± 0.17	1.08 ± 0.20
56776.2045065	0.64 ± 0.13	-2.56 ± 0.25	1.13 ± 0.21
56776.2114509	0.85 ± 0.14	-2.77 ± 0.16	1.18 ± 0.22
56776.2183953	0.82 ± 0.14	-2.67 ± 0.16	1.88 ± 0.28
56776.2253398	0.74 ± 0.14	-2.49 ± 0.21	1.56 ± 0.26
56776.2322842	0.63 ± 0.13	-2.72 ± 0.25	1.02 ± 0.21
56776.2392287	0.77 ± 0.13	-2.76 ± 0.21	1.18 ± 0.22
56776.2461731	1.02 ± 0.16	-2.59 ± 0.21	1.48 ± 0.26
56776.2531176	0.74 ± 0.13	-2.45 ± 0.22	1.69 ± 0.27
56776.260062	0.88 ± 0.14	-2.60 ± 0.21	1.49 ± 0.26
56776.2670065	0.63 ± 0.12	-2.56 ± 0.20	1.29 ± 0.25
56776.2739509	0.97 ± 0.15	-2.85 ± 0.36	1.19 ± 0.22
56776.2808953	0.51 ± 0.11	-2.60 ± 0.42	1.18 ± 0.23
56776.2878398	0.61 ± 0.12	-2.72 ± 0.28	-
56776.2947842	0.64 ± 0.13	-2.82 ± 0.34	-
56776.3017287	0.91 ± 0.15	-2.56 ± 0.70	-
56776.3086731	0.80 ± 0.16	-3.46 ± 0.46	-
56776.3156176	0.92 ± 0.16	-3.69 ± 0.67	-
56776.322562	0.83 ± 0.16	-4.17 ± 0.97	-

Table 3.12.: VERITAS flux and spectral index results for data on 2014 May 3.

MJD (Day)	Flux>225GeV 10^{-6} m $^{-2}$ s^{-1}	Index	Flux 225-560GeV 10^{-6} m $^{-2}$ s^{-1}
56780.1507007	2.79 ± 0.33	-2.33 $\pm$ 0.16	2.15 ± 0.31
56780.1576452	2.89 ± 0.35	-2.39 $\pm$ 0.17	2.30 ± 0.33
56780.1645896	3.56 ± 0.40	-2.53 $\pm$ 0.21	2.96 ± 0.38
56780.1715341	3.26 ± 0.39	-2.77 $\pm$ 0.18	2.61 ± 0.37
56780.1784785	2.45 ± 0.32	-2.71 $\pm$ 0.19	1.86 ± 0.29
56780.1854229	3.38 ± 0.39	-3.00 $\pm$ 0.20	2.89 ± 0.38
56780.1923674	2.92 ± 0.39	-2.69 $\pm$ 0.35	2.43 ± 0.37
56780.1993118	2.41 ± 0.32	-2.24 $\pm$ 0.23	1.77 ± 0.29
56780.2062563	3.02 ± 0.38	-3.06 $\pm$ 0.22	2.70 ± 0.37
56780.2132007	2.44 ± 0.35	-2.75 $\pm$ 0.21	1.85 ± 0.32
56780.2201452	2.72 ± 0.38	-2.63 $\pm$ 0.25	2.27 ± 0.36
56780.2270896	3.72 ± 0.44	-2.75 $\pm$ 0.25	2.98 ± 0.42
56780.2340341	3.49 ± 0.45	-2.95 $\pm$ 0.22	2.87 ± 0.43
56780.2409785	3.98 ± 0.49	-2.90 $\pm$ 0.26	3.39 ± 0.48
56780.2479229	2.51 ± 0.36	-2.85 $\pm$ 0.29	2.07 ± 0.35

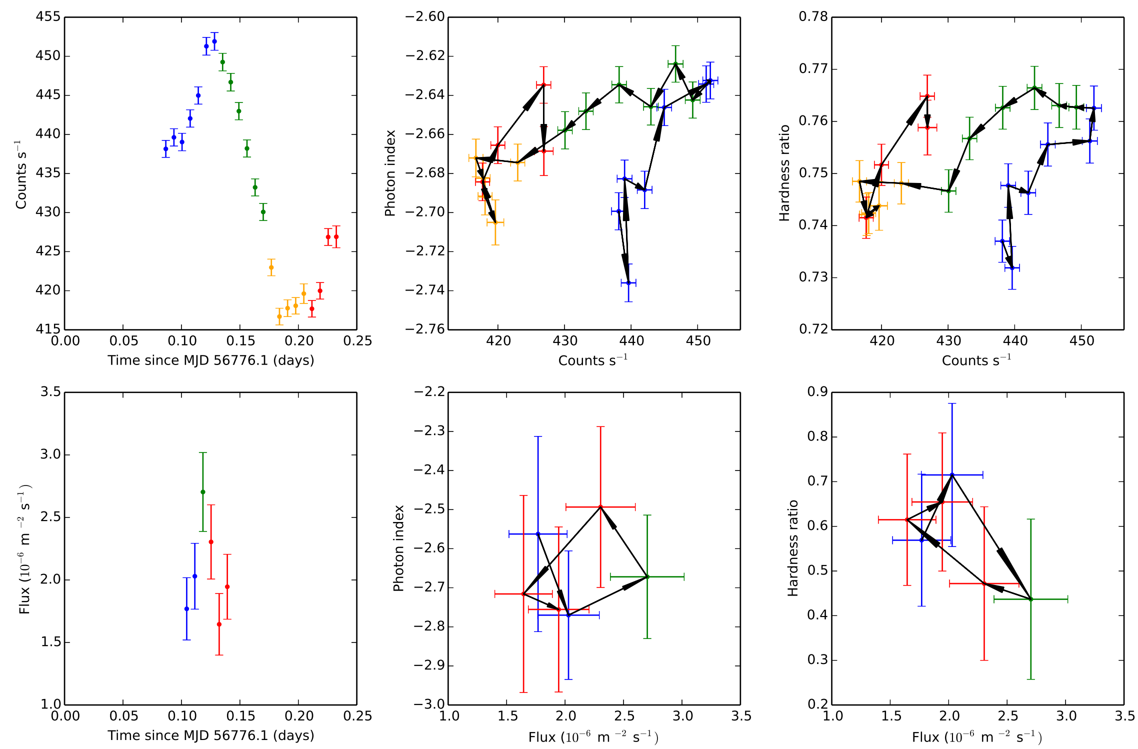

Figure 3.39.: Spectral hysteresis of Mrk 421 on 2014 April 29. The top and bottom rows show results from X-ray and TeV observations, respectively. In each row, the left plot shows a light curve segment that contains a bump in flux, the middle plot shows the relationship between flux (or counts) and best-fit spectral index, and the right plot shows the relationship between flux (or counts) and the hardness ratio. Each point of flux, HR, and index measurements is from a 10-min interval. The hardness ration for X-ray is the ratio between the count rates in 1-10 keV and 0.5-1 keV; and for TeV between 560 GeV-30 TeV and 315-560 GeV.

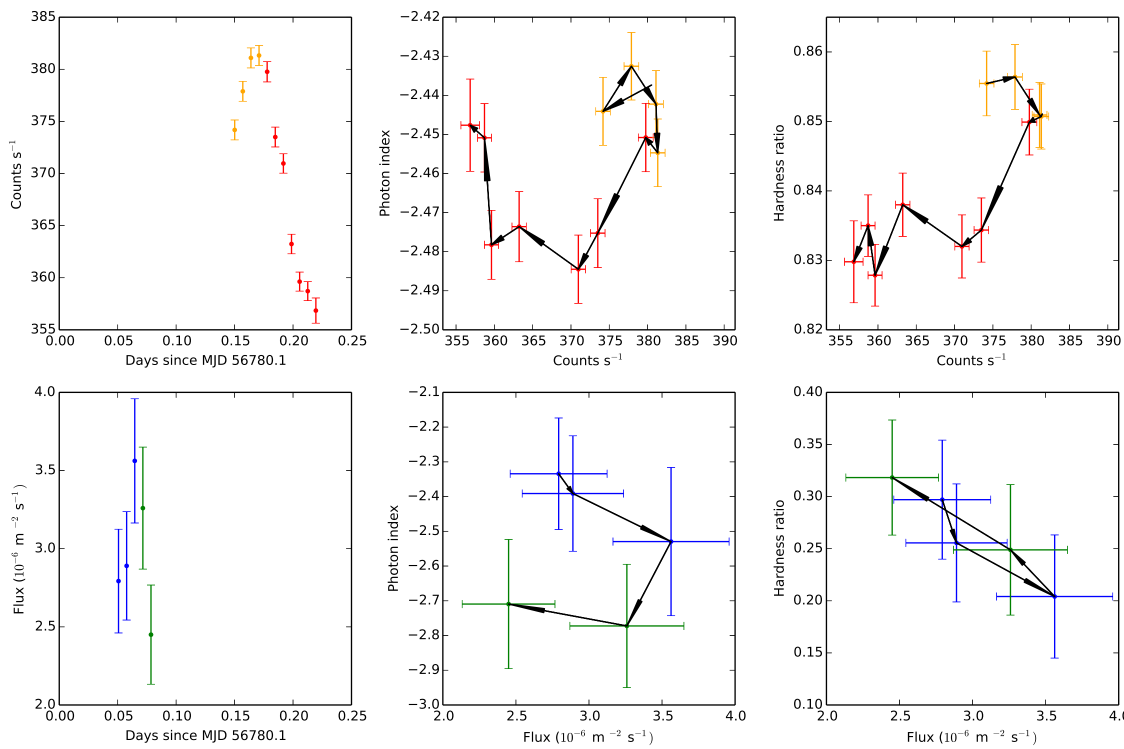

Figure 3.40.: Spectral hysteresis of Mrk 421 on 2014 May 3. The top and bottom rows show results from X-ray and TeV observations, respectively. In each row, the left plot shows a light curve segment that contains a bump in flux, the middle plot shows the relationship between flux (or counts) and best-fit spectral index, and the right plot shows the relationship between flux (or counts) and the hardness ratio. Each point of flux, HR, and index measurements is from a 10-min interval. The hardness ration for X-ray is the ratio between the count rates in 1-10 keV and 0.5-1 keV; and for TeV between 560 GeV-30 TeV and 225-560 GeV.

three XMM-Newton and VERITAS observations of Mrk 421 into simultaneous 10-minute intervals, and performed spectral fitting for each interval. The XMM-Newton EPIC pn X-ray spectra are fit first using a power law model with neutral hydrogen absorptions, the results are shown in the top table in Table 3.7. We note that the large reduced χ^2 values were likely due to absorption features caused by oxygen, silicon, and gold. We add these three absorption features to the spectral model following equation 3.7 in section 3.4.2. The oxygen absorption at $\sim$0.54 keV was described using the `edge` model in `Xspec` for the first two observations, and using `Gauss` model for the third observation. As shown in the bottom table in Table 3.7, the fit was significantly improved with the extra absorption features since the reduced χ^2 was close to 1 (slightly worse for the spectrum on May 3). We note that the spectral indices α remained unchanged within the uncertainty range of $\sim$0.1% between these two spectral models. Therefore we are confident that the hardness ratios and the spectral indices derived for each 10-min interval are robust, and are not severely affected by the absorption features. We also use two models, a power law model with exponential cutoff and a log parabola model, to fit the VERITAS TeV gamma-ray spectra, as described in equation 3.5 and 3.6 in section 3.4.2. The fit results for both models are shown in Table 3.6. For the following hysteresis analyses, we use absorbed power law model for X-ray data, and power law with exponential cutoff for gamma-ray data.

The spectral fit results for each 10-min intervals are listed in Table 3.8, 3.9, 3.10, 3.11 and 3.12. For a comparison, we note that the column density of galactic neutral hydrogen toward the direction of Mrk 421 is measured by the Leiden/Argentine/Bonn (LAB) survey to be $N_H \approx 1.9 \times 10^{20}$ cm^{-2} (Kalberla et al., 2005).

We identify several "bumps" with a rise and a subsequent fall of flux in the light curves, and plot spectral index and hardness ratio against flux (or count rate) for these bumps (see Figure 3.39 and Figure 3.40). Black arrows indicate the order of time for each point. Measurements taken at different times are also color coded to guide the eye. A "harder-when-brighter" effect can be identified on some individual

X-ray branches, (e.g. the blue and green points in the top right panel in Figure 3.39). The observed "soft lag" on May 3 indicates a harder spectrum when flux rises, and a softer spectrum when flux falls, corresponding to a clockwise loop (in orange color) in the bottom right panel of the spectral hysteresis plot in Figure 3.40. Similarly, for the "hard lag" scenario on Apr 29, a counter-clockwise loop is predicted and observed, as shown in Figure 3.39. It is interesting to note that the time lag and loop direction changes in a few days, even the source flux levels are similar.

The same analysis are carried out for VHE data, and similar plots are shown. Although the uncertainty in VHE flux, hardness ratio and index are large, we note that the direction of the VHE index-flux evolution in the bottom middle panels in Figure 3.39 and Figure 3.40 is consistent with the ZDCF/MCCF results on both days. Especially, on May 3, ZDCF/MCCF results seem to suggest a "soft" lag, while the index-flux diagram shows evolution along clockwise direction. The two signatures are consistent with each other. We note that the VHE spectrum of Mrk 421 is likely curved, therefore the index alone may not be a good indicator of the spectral shape. The hardness ratio pattern offers a more crude but less model-dependent estimation of the same signature. However, the hardness-flux diagram of the VERITAS observations is of large uncertainty. At the flux level of roughly 1 to 2 Crab Unit, such spectral hysteresis studies with current VERITAS instrument is still difficult. This offers a reference for the future criteria for target-of-opportunity observations aiming for similar goals.

Broadband SEDs

The SED of simultaneous VERITAS and XMM-Newton data, as well as contemporaneous MWL data are shown in Figure 3.41. Daily averaged high energy (HE) gamma-ray spectra are constructed from *Fermi*-LAT data between 100 MeV and 300 GeV, and butterfly regions of 95% confidence level are shown. Note that the uncertainty is large because the scarcity of HE photons in the one-day window. Optical spectra from Steward Observatory between 400 and 750 nm on May 3, radio data from CARMA at 93 GHz taken on both nights, and from OVRO at 15 GHz on other nights within the week are also shown.

X-ray and VHE emission are each located on the falling slope of their own spectral bump. The synchrotron peak is between the UV measurement at $\sim 10^{15}$ Hz and the soft end of the X-ray spectrum at $\sim 10^{17}$ Hz. Although *Fermi*-LAT spectrum is not very constraining, but the high-energy spectral peak is likely just below 100 GeV as suggested by the TeV spectrum.

We use a static SSC model described in Krawczynski et al. (2002) to study the observed SEDs (see also section 3.3). The set of parameters used are listed in Table 3.13. The static one-zone SSC model describes the data reasonably well, despite that the correlation between X-ray and gamma-ray is not strong. The synchrotron peak frequency given by the model is $\sim 4 \times 10^{16}$Hz, while the inverse-Compton peak lies at $\sim 5 \times 10^{25}$Hz. According to the relation given in equation 3.1, we can quickly estimate the strength of the magnetic field to be ~ 1.8 Gauss assuming the Doppler factor is 20.3. Note that this is considerably larger than the value given in Table 3.13. From Apr 29 to May 3, the change in SED can be described by an increase in the radius of the emitting region R, along with an increase in the maximum energy E_{max}, and a slight decrease in break energy E_{break} of the electron distribution (see Table 3.13).

This evolution of the SED is consistent with the results of an expansion of the emitting region. The direct results of such an expansion is an increase in the dynamic timescale $t_{dyn} = R/c$. Moreover, this will lead to a higher maximum energy of the electrons E_{max}, since a maximum possible gyro-radius has increased (see equation 1.2). Also, the synchrotron cooling break, which occurs at the electron energy that satisfies $t_{syn} = t_{dyn}$, decreases since $t_{syn} \propto \gamma$, where γ is the Lorentz factor of the electron.

An expansion of the emitting region is also consistent with the X-ray "hard lag" on Apr 29 and "soft lag" on May 3. Since the maximum electron energy E_{max} is lower on Apr 29, the observed X-ray frequencies is closer to the maximum frequencies, therefore

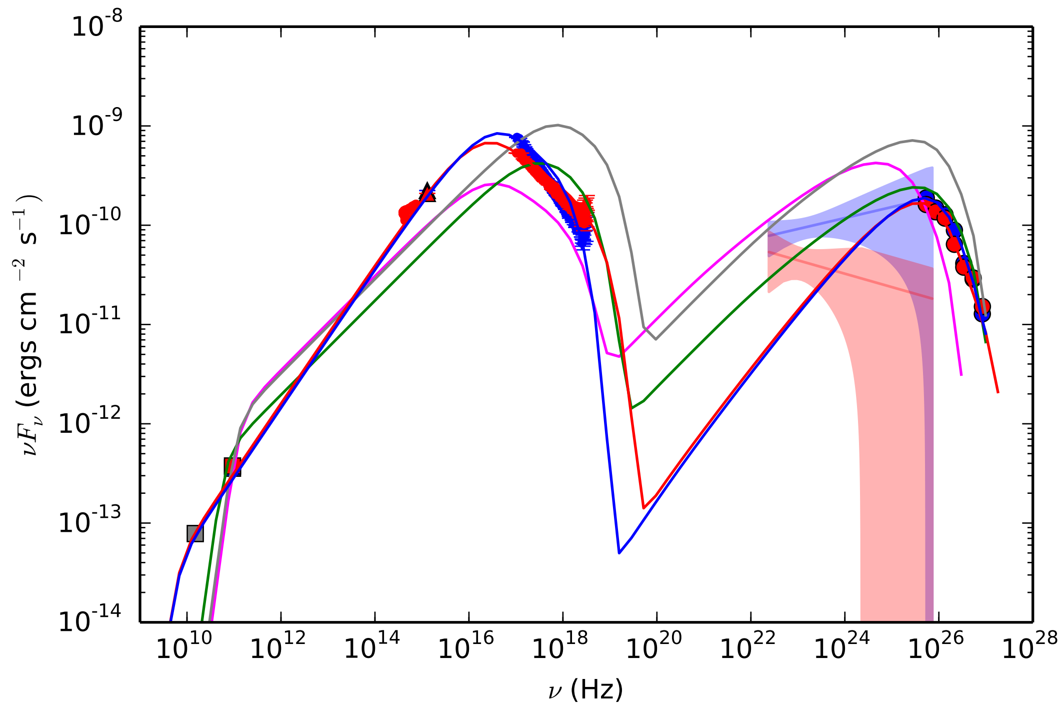

Figure 3.41.: Broadband SED of Mrk 421 on 2014 April 29 (shown in blue) and May 3 (shown in red). See text for details of the measurements shown. The results from previous observations are also shown for comparison: the gray, green, and magenta line corresponds to models used for high, medium, and low flux as described in Błażejowski et al. (2005).

the change in flux propagates from high to low frequencies. On the other hand, on May 3, the observed X-ray frequencies is relatively farther away from the highest-energy electrons due to the larger E_{max}, therefore the change in flux propagates from low to high energy (see e.g. Kirk et al., 1998).

Table 3.13.: Parameters used for the SSC model in Figure 3.41. B05 refers to Błażejowski et al. (2005).

Model	z	Γ	θ	B	Radius	w_e	$\log E_{min}$	$\log E_{max}$	$\log E_{break}$	p_1	p_2
			deg	T	m	ergs m^{-3}	eV	eV	eV		
0429	0.031	23.0	2.8	0.025e-4	9.45e+14	0.00025	6.5	11.6	10.82	1.6	3.7
0503	0.031	23.0	2.8	0.025e-4	9.5e+14	0.00025	6.5	11.9	10.72	1.6	3.7
B05 low	0.031	19.48	5.01	4.05e-05	7e+13	0.13777	6.5	11.22	10.34	2.05	3.6
B05 med	0.031	20.05	3.2	1.02e-05	1e+14	0.03192	6.5	11.55	10.98	2.05	3.4
B05 high	0.031	20.0	3.905	2.6e-05	7e+13	0.086	6.5	11.6	11.0	2.05	3.4

3.6 Persistent variability from blazars: global properties on long timescales

Apart from the local flaring structures described above, a couple of interesting global properties in time domain are discussed below. These include stationarity, linearity, fractional variability amplitude, autocorrelation, timescale spectrum, power spectrum, and some time frequency representations.

Stationarity and linearity

Although there are no compelling reasons that empirical time series should be linear and stationary, many theories and tools for treating time series are based on linear and stationary models.

The n-th order moment of a set of events $X_i, i = 1, 2, \cdot, N$ is defined as

$$\frac{1}{N}\sum_{i=1}^{N} X_i^n.$$

The first order moment is the mean μ, and second order moment is the variance σ. The mean and the variance are the most important properties of a light curve. As they quantify the intensity and the variability.

A light curve is called stationary if the joint distribution of a sub-series of a fixed length is time-invariant, i.e. $F_{t+\tau}(x) = F_t(x)$. Some basic second-moments (autocorrelation and power spectrum) are insensitive to non-stationary signals. Note that the linear combination of a stationary time series is also stationary. We know that blazars are variable and non-stationary, especially on a longer timescale. This remains a caveat in many widely used temporal and spectral analysis focusing on the global features of a time series, e.g. autocorrelation and power spectrum. However, many analyses subdivide the light curves to segments. Within each segment, the light curve can sometimes be loosely stationary. The segmentation improves the quality of estimations by improving statistics at the expense of narrower covered timescales/frequencies.

Sometimes Monte Carlo simulation is necessary to determine the best fit model for a time series (frequentist approach). This assumes ergodicity, meaning that the properties of an ensemble of light curves is the same as the light curve over a long period of time. The test of ergodicity is beyond the scope of this thesis.

A time series is called linear if it can be expressed as follows:

$$X_i = \sum_{k=-\infty}^{\infty} a_k Z_{i-k},$$

where Z_i is a zero-mean stationary process with finite variance, and a_k is a sequence of coefficients. The bispectrum $B(\omega_j, \omega_k)$ can be used as an estimator of linearity of a time series (see e.g. Hinich, 1982; Maccarone, 2013). Consider a time series $\{X(t_i)\}$ evenly sampled at $t_i = 0, 1, \cdot, N$, the bispectrum can be estimated as follows:

$$B(\omega_j, \omega_k) = E\left[X(\omega_j)X(\omega_k)X^*(\omega_j + \omega_k)\right],$$

where $\omega_j = 2\pi j/N, \omega_k = 2\pi k/N,\ j = 0, 1, \cdot, N$ and $k = 0, 1, \cdot, j$. Bicoherence is defined as the normalized bispectrum:

$$b(\omega_j, \omega_k) = \frac{|B(\omega_j, \omega_k)|}{\sqrt{|X(\omega_j)X(\omega_k)|^2 |X^*(\omega_j + \omega_k)|^2}},$$

A definition of biphase is given by Kim & Powers (1979):

$$\beta(\omega_j, \omega_k) = arctan\left[\frac{Im(B(\omega_j, \omega_k))}{Re(B(\omega_j, \omega_k))}\right].$$

The bispectrum is a third-order moment that reflects the skewness and reversibility of a time series. Time reversibility quantifies if the probability distribution of X_i at t_i is the same as that of X_{-i} at $-t_i$. A time-reversible process has a strictly-zero imaginary part of the spectrum (power spectrum or bispectrum), and therefore a zero biphase.

I have implemented the bispectrum calculation using `Python`, the procedures of which include segmentation, calculation of bispectrum, and averaging. No windowing was applied. The top four plots in Figure 3.42 shows a sanity test of the bispectral analysis following Choudhury et al. (2008). A coupled sinusoidal signal is used $t =$

$cos(\omega_b t+\theta_b)+cos(\omega_c t+\theta_c)+0.5cos(\omega_d t+\theta_d)+cos(\omega_e t+\theta_e)+\beta_{random}$, where $\omega_b = 2\pi 0.12$ Hz, $\omega_c = 2\pi 0.18$ Hz, $\omega_d = \omega_b + \omega_c$, $\omega_e = \omega_b + \omega_d$, $\theta_b = \pi/3$, $\theta_c = \pi/12$, $\theta_d = \pi/4$, $\theta_e = 3\pi/8$, and β_{random} is a zero-mean normal random number of variance 0.2. The bicoherence shows two significant peaks at the bifrequencies of $(0.18, 0.12)$ Hz, and $(0.30, 0.12)$ Hz as expected.

Three simulated exponential light curves and their bispectral products are calculated, as shown in the bottom four plots in Figure 3.42 and Figure 3.43. Exponential flares with (i) symmetric rising and falling profile, (ii) sharp rise and exponential decay, and (iii) exponential rise and sharp decay are studied. While the symmetric flares do not exhibit any feature in bicoherence, both asymmetric flares (case ii and iii) show triangle-zone features in the bicoherence. This demonstrates that the bispectrum is sensitive to asymmetry of the flare profiles.

However, it is important to note that unlike autocorrelation and power spectrum, bispectrum is sensitive to white noise. This is challenging for practical detections of non-linearity like asymmetry. I calculated the bispectra of a Fermi-LAT weekly- and daily-binned light curves of Mrk 421 that cover a duration of ∼2100 days, as shown in Figure 3.44. On 73 days out of the 2100 days there were no significant detections of Mrk 421 from Fermi-LAT likelihood analysis, and cubic spline interpretation was made to estimate the flux on those days. No apparent features are present in the bicoherence and biphase. No conclusion of any non-linearity can be made, probably due to the low signal-to-noise ratio of the LAT light curves.

Is there variability?

As mentioned above, variance offers a good estimation on the variability of a light curve. However, it does not take measurement error into account. Fractional variability amplitude is essentially the variance of the light curve with the measurement

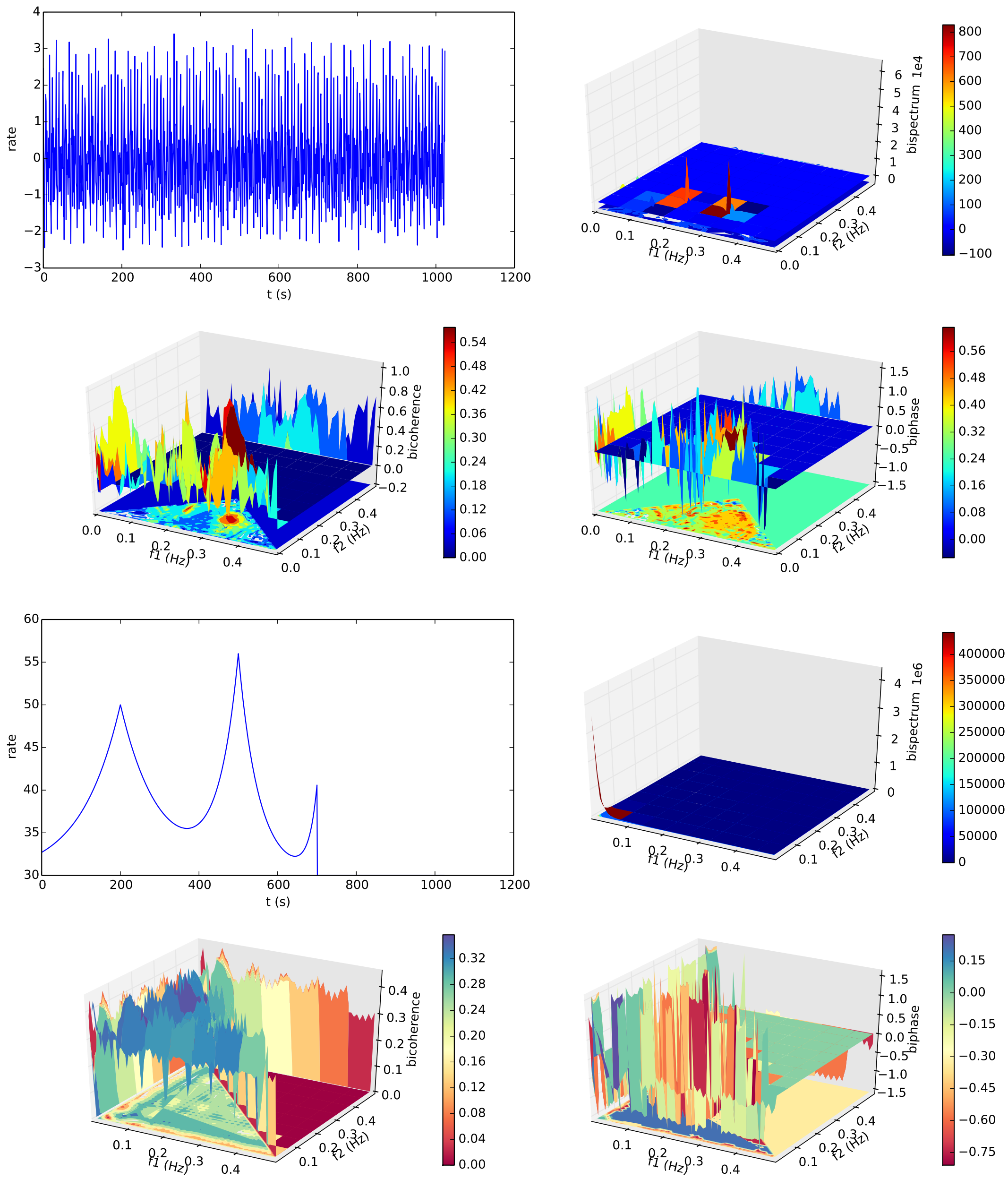

Figure 3.42.: Bispectrum, bicoherence, and biphase calculated from simulated light curves. The top four plots show results from a simulated light curve consists of four correlated sine components and a white noise component, two significant peaks are present in the bicoherence. The bottom four plots show three flares with symmetric exponential rise and decay. There are no apparent features in bispectral products for this case.

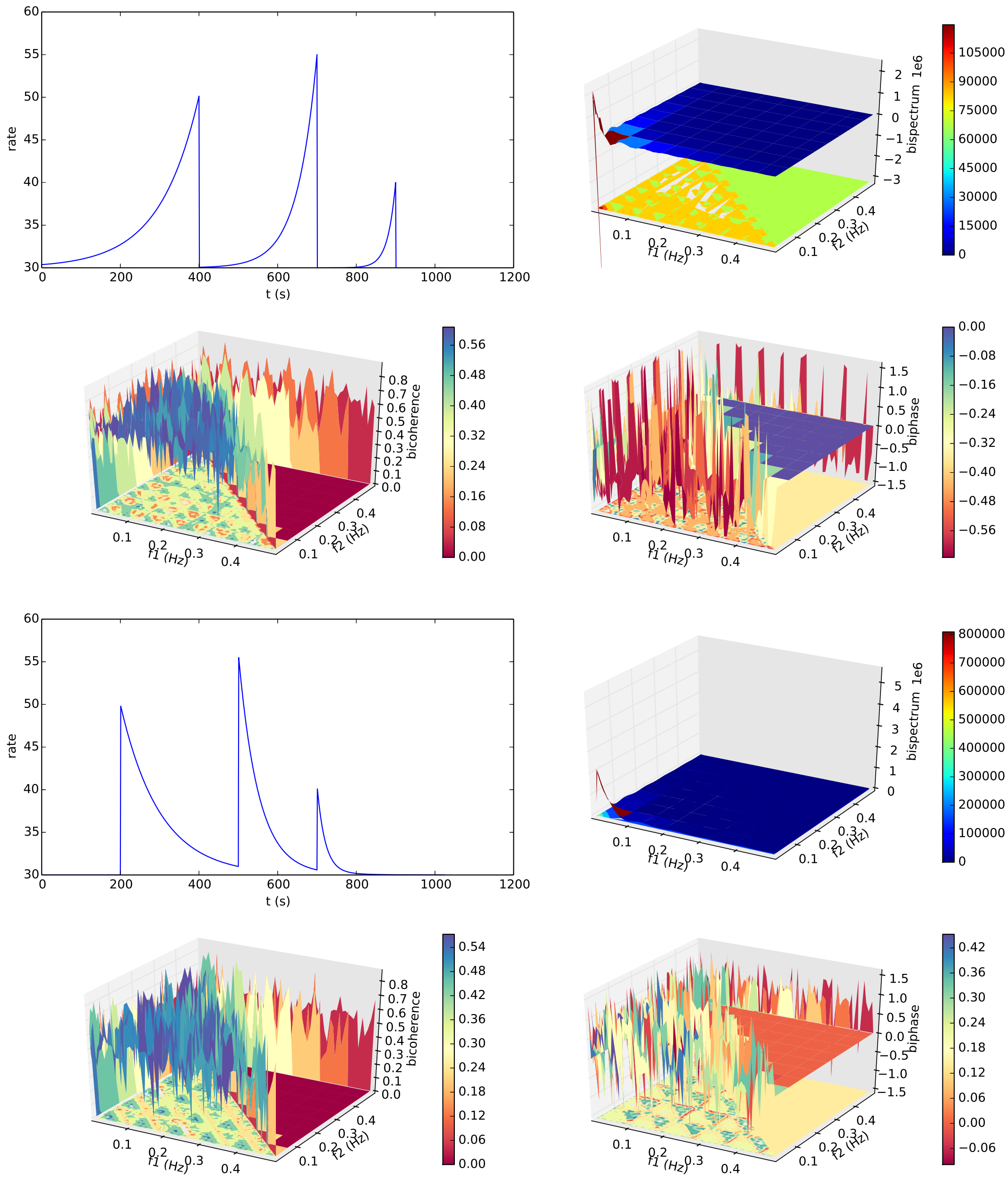

Figure 3.43.: Bispectrum, bicoherence, and biphase calculated from simulated light curves. The top four figures show three exponentially rising flares with a sharp cutoff. The bottom four plots show three flares with sharp rising edge and exponential decay. Triangular features are apparent in the bicoherence plots for both cases, showing evidence for skewness.

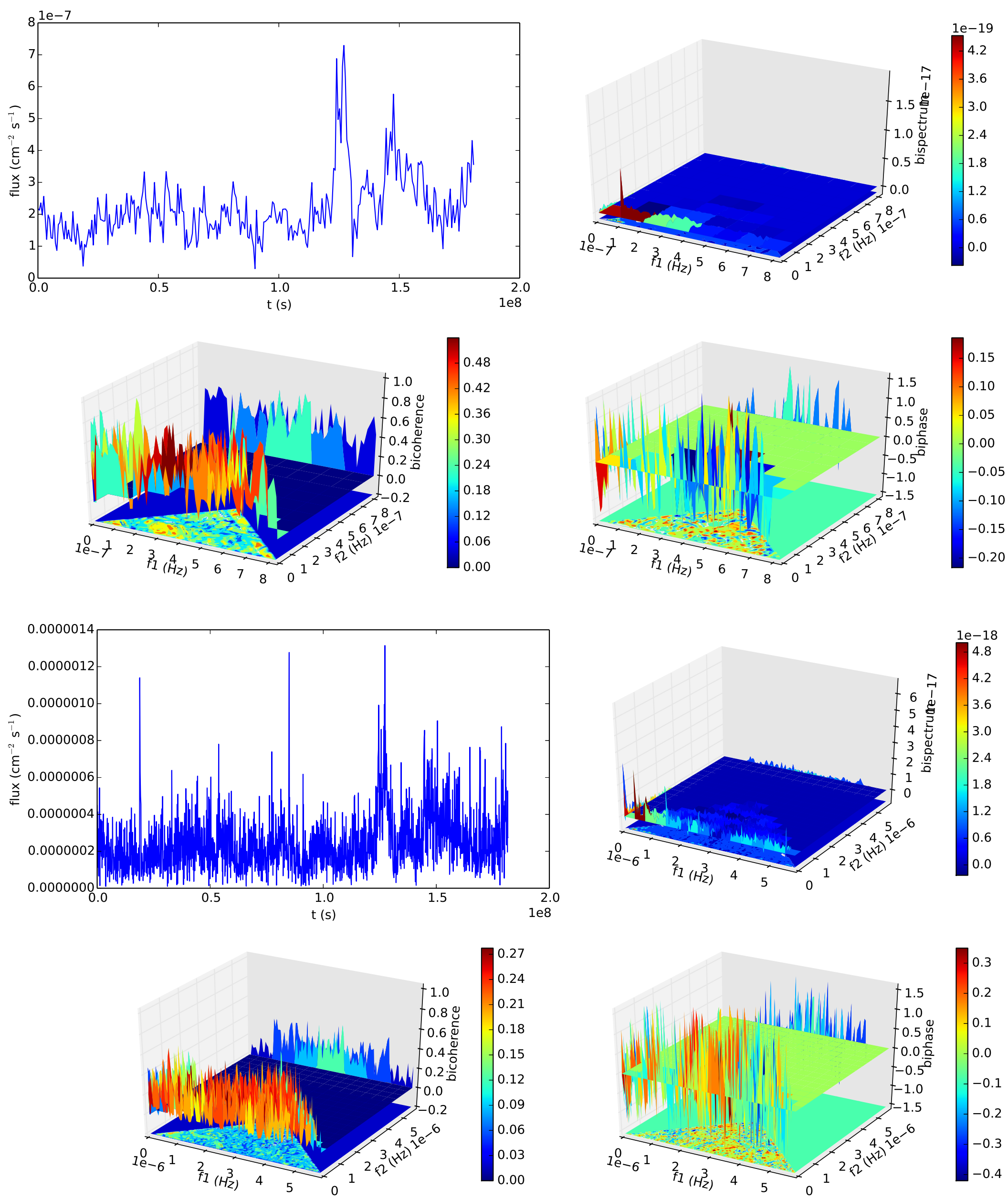

Figure 3.44.: Bispectrum, bicoherence, and biphase calculated from weekly- and daily-binned Fermi-LAT light curve. Top four plots are results using the weekly-binned light curve, which is divided into 25 overlapping segments each has a duration of 128 weeks. The bottom four plots are results from the daily light curve, which is divided into 100 overlapping segments each has a duration of 256 days. The bispectrum, bicoherence, and biphase are calcaulated for each segment and averaged over all segments.

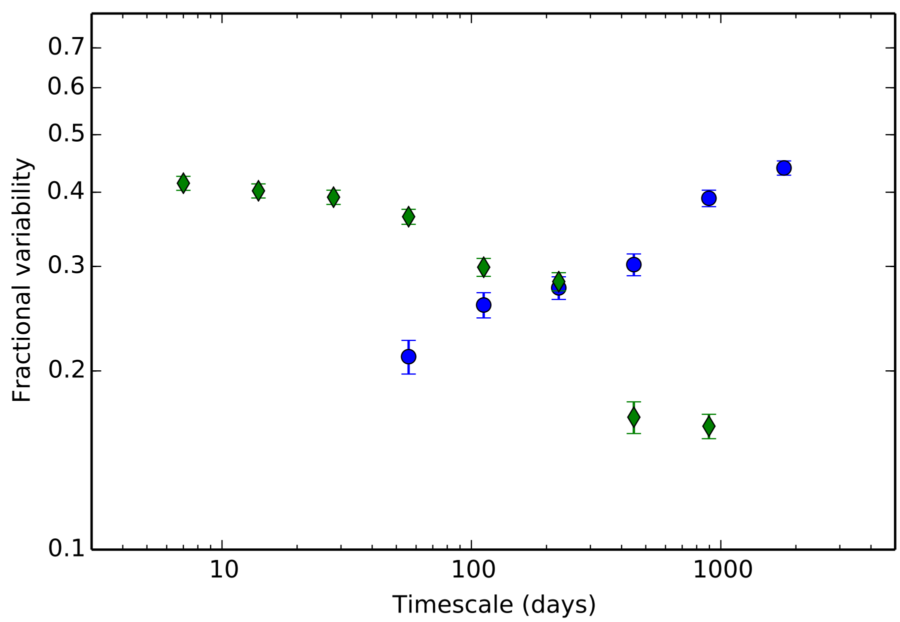

Figure 3.45.: Tthe fractional variability as a function of timescales. We use *Fermi*-LAT weekly binned light curve of Mrk 421 that covers ~300 weeks. The green filled circles are fractional variabilities calculated from the LC with a binwidth equal to the timescale and a duration of the entire duration; while the blue shows the calculations using weekly binned LC that has a duration equal to the timescale.

errors taken out. Following the descriptions in Vaughan et al. (2003) and Poutanen et al. (2008), fractional variability F_{var} and its error $\sigma_{F_{var}}$ are calculated as follows:

$$F_{var} = \sqrt{\frac{S^2 - \langle \sigma_{err}^2 \rangle}{\langle F \rangle^2}}$$

and

$$\sigma_{F_{var}} = \sqrt{F_{var}^2 + \sqrt{\frac{2\langle \sigma_{err}^2 \rangle^2}{N\langle F \rangle^4} + \frac{4\langle \sigma_{err}^2 \rangle F_{var}^2}{N\langle F \rangle^2}}} - F_{var},$$

where S is the standard deviation of the N flux measurements, $\langle \sigma_{err}^2 \rangle$ is the mean squared error of these flux measurements, $\langle F \rangle$ is the mean flux. Note that the fractional variability represents the power between the timescale of the time bin width t_{bin} and the duration t_{dur} of the light curve, and depends on these two parameters $F_{var} = F_{var}(t_{bin}, t_{dur})$. So when comparing fractional variability between different instruments, care needs to be taken if the durations and bin widths are different.

Figure 3.45 shows the fractional variability as a function of timescale, using a *Fermi*-LAT weekly binned light curve of Mrk 421 that covers ∼300 weeks. Two different effects are shown: (i) use only weekly bin width t_{bin} = 7days, and cut the light curves into equal-length segments with a duration of $t'_{dur} = t_{dur}/2^i$, then calculate $F_{var}(t_{bin}, t'_{dur})$ and $\sigma_{F_{var}}$; (ii) using the full light curve of duration t_{dur}, but rebin the light curve using bin widths of $t'_{bin} = 2^i t_{bin}$, then calculate $F_{var}(t'_{bin}, t_{dur})$ and $\sigma_{F_{var}}$. This plot quantifies the amount of variability at a range of timescales from t_{bin} to t_{dur}, which achieves the same task of power spectrum (see subsection 3.6.2). It is similar to the "timescale spectrum" (Li, 2001; Li et al., 2004). The advantage of studying variability power on different timescales (at different frequencies) in time domain offers several advantages comparing to frequency domain. For example, no FFT is necessary in time domain, therefore avoiding possible biases associated with FFT.

The fractional variability results from simultaneous XMM and VERITAS data, as well as from contemporaneous MWL data are shown in Figure **??**. The VHE fractional variability is only computed for the light curve of energy threshold 315 GeV

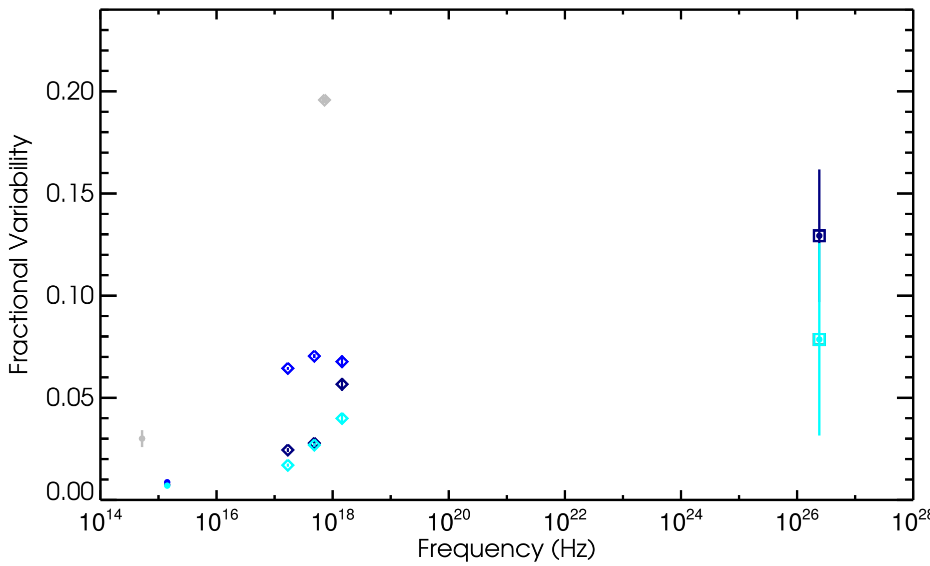

Figure 3.46.: Fractional variability amplitude of Mrk 421 at different wavelengths around the time of the three simultaneous ToO observations of Mrk 421 in 2014. Open squares are from VERITAS measurements and open diamonds are from XMM EPN measurements. The results from three energy intervals (0.5-1 keV, 1-3 keV, and 3-10 keV) in X-ray band are shown. Navy points represents measurements on April 29, blue ones for May 1, and cyan for May 3. On April 29 the VERITAS fractional variability is calculated from data from the first ~3.5 hr at energy threshold of 315 GeV. Gray point is calculated from contemporaneous data from Apr 28 to May 4. Gray diamond is from XRT data and gray points are from Steward Observatory.

from data in the first ∼3.5 hr on April 29, since the standard deviation is smaller than the uncertainty of the measurements ($S^2 < \langle \sigma_{err}^2 \rangle$) if the last one-hour data are included, probably due to the relatively large uncertainty caused by the higher energy threshold of 560 GeV.

The fractional variability of X-ray flux is low but well measured (with small error bars) in three different energy intervals 0.5-1 keV, 1-3 keV and 3-10 keV. An increase in variability amplitude from lower energy to higher energy is apparent on April 29 (navy open diamonds) and on May 3 (cyan open diamonds), but not on May 1 (blue open diamonds). Comparing April 29 and May 3, the overall X-ray fractional variability is similar, but the hard X-ray flux (3-10 keV) is more variable on April 29, while on the same night the VHE flux is less variable. The XMM OM fractional variability are almost zero, likely because of the added 2% systematic error being larger than the variance from the measurements, probably indicating a slight overestimate in the uncertainty. Also the longer cooling time at optical frequency may also lead to less variability on shorter timescales.

Are there different states?

Since flares are detected repeatedly from blazars like Mrk 421, one may ask if there exists a "flaring state" and a "quiescent state", similar to X-ray binaries. Evidence for different states has been suggested since EGRET observations show a systematic spectral hardening when blazars flare (Stecker & Salamon, 1996). A simple test for whether the two states exist is to search for bimodality in the flux distribution. Figure 3.47 shows the flux histograms of Mrk 421 from long-term observations using VERITAS, Fermi-LAT, and Swift-XRT, with both evenly-spaced and Bayesian blocks binning. The VERITAS light curves were nightly binned integrated from the energy threshold of the observation to 30 TeV, the Fermi-LAT flux were weekly binned integrated from 100 MeV to 30 GeV, and the Swift-XRT counts are binned by 50 s

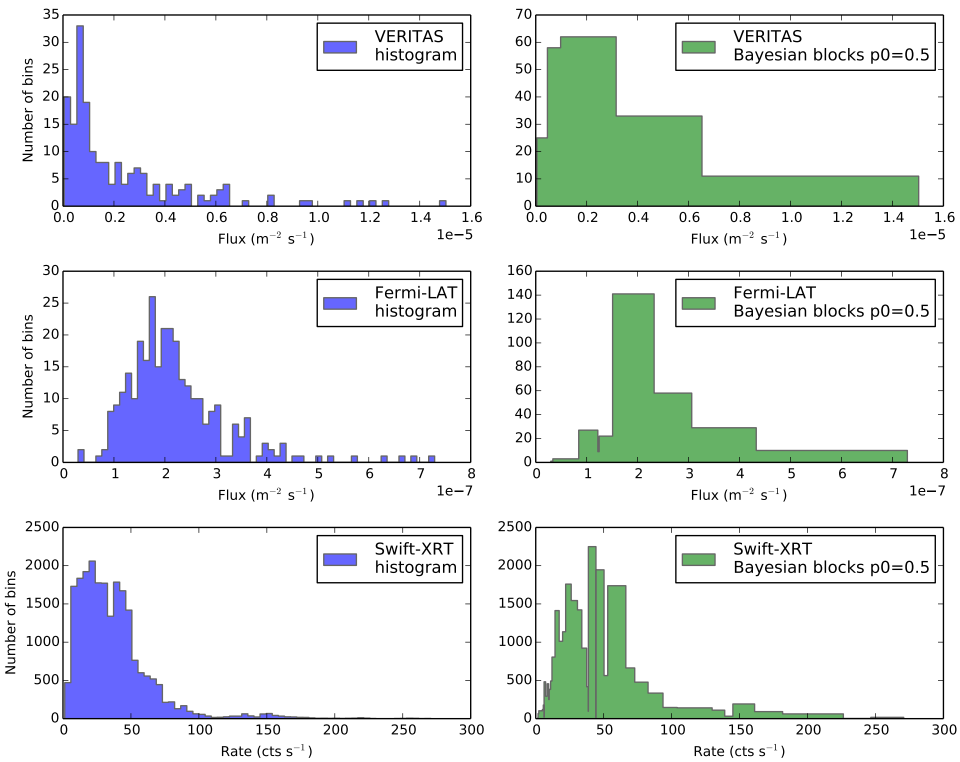

Figure 3.47.: Flux (or rate) histogram of Mrk 421 from long-term observations using VERITAS (top), Fermi-LAT (middle), and Swift-XRT (bottom). Both histograms with 60 evenly spaced bins (left) and Bayesian blocks using a prior correct-detection probability $p_0 = 0.5$ (right) are shown.

intervals integrated from 0.3 keV to 10 keV. No strong evidence for bimodality is apparent.

3.6.1 Simulating light curves

As mentioned above, many statistical properties of a time series can only be calculated exactly if the series itself is infinitely long and is stationary. The real-world estimations of these properties heavily rely on the comparison between data and simulations generated from a specific underlying process. We have used simulated light curves, in both TTE and histogram formats, in the previous section to test the performance of different statistical tools. Simulations are even more important in the estimation of power spectral density, which has a non-Gaussian probability distribution (see section 3.6.2 below). In this section, I describe the methods that I used for generating simulated light curves from different processes in various formats.

Poisson sequence: A Poisson sequence is a fundamental stochastic time series. It represents a series of independent events arriving randomly in time, with the expected number of events being constant in a fixed interval. A poisson sequence is a specific type of white noise, with constant power density at all frequencies. Following Scargle (1981), it can be formalized by a sequence of impulses (Dirac delta functions) arriving at times t_i as follows:

$$X_{Poisson} = \sum_i \delta(t - t_i). \tag{3.18}$$

The probability to count k events in a time interval Δt follows a Poisson distribution:

$$P_k(\Delta t) = \frac{e^{-\lambda \Delta t}(\lambda \Delta t)^k}{k!}, \tag{3.19}$$

where λ is a parameter that describes the mean count rate over a long period of time. Note that $\lambda \Delta t$ is both the mean and the variance of $P_k(\Delta t)$, giving the expected number of events and fluctuation in the interval of Δt. The probability density of the waiting time between two occurrences of events, which is equivalent to an time interval with zero event, follows an exponential distribution

$$P_0(t_{\rm wait}) = e^{-\lambda t_{wait}}, \tag{3.20}$$

where $t_{\rm wait} = t_{i+1} - t_i$ is the wait time. When sampling is much faster than the expected rate ($\lambda\Delta t \ll 1$), $P_k(\Delta t)$ can be approximated by

$$P_k(\Delta t) \approx \begin{cases} 1 - \lambda\Delta t, & k = 0; \\ \lambda\Delta t, & k = 1; \\ 0, & k > 1. \end{cases} \tag{3.21}$$

Under the assumption of $\lambda\Delta t \ll 1$, (i) there is a constant small probability ($\lambda\Delta t$) of receiving one event with in each interval Δt, and the process has no memory of the past; (ii) a large probability ($1-\lambda\Delta t$) of receiving zero event; and (iii) zero probability to receive more than one events arriving in the same interval Δt. On the other hand, since the mean and variance of a Poisson distribution are given by $\lambda\Delta t$, the signal to noise ratio of photon counting is given by the ratio of expected mean and standard deviation:

$$S/N = \frac{\lambda\Delta t}{\sqrt{\lambda\Delta t}} = \sqrt{\lambda\Delta t}. \tag{3.22}$$

This shows that by increasing the bin width Δt for photon counting, the signal to noise ratio can be increased. This has an important implication for the choice of bin width for astronomical time series. A desirable bin width should result in a large number ($\gg 1$) of counts in each bin. Note that when $\lambda\Delta t$ is large, i.e. there are a large number of events arriving in Δt, a Poisson distribution becomes similar to a Gaussian distribution according to the central limit theory.

Correctly simulating Poisson counting noise is important for studying astronomical time series. Especially, when short time bins are used to study fast variability, due to the low signal to noise ratio, Poisson noise may be important. For binned I have used the `numpy.random.poisson` routine in `python` to simulate a Poisson sequnce, as shown in Figure 3.48. I first generated a list of 3×10^6 Poisson samples with

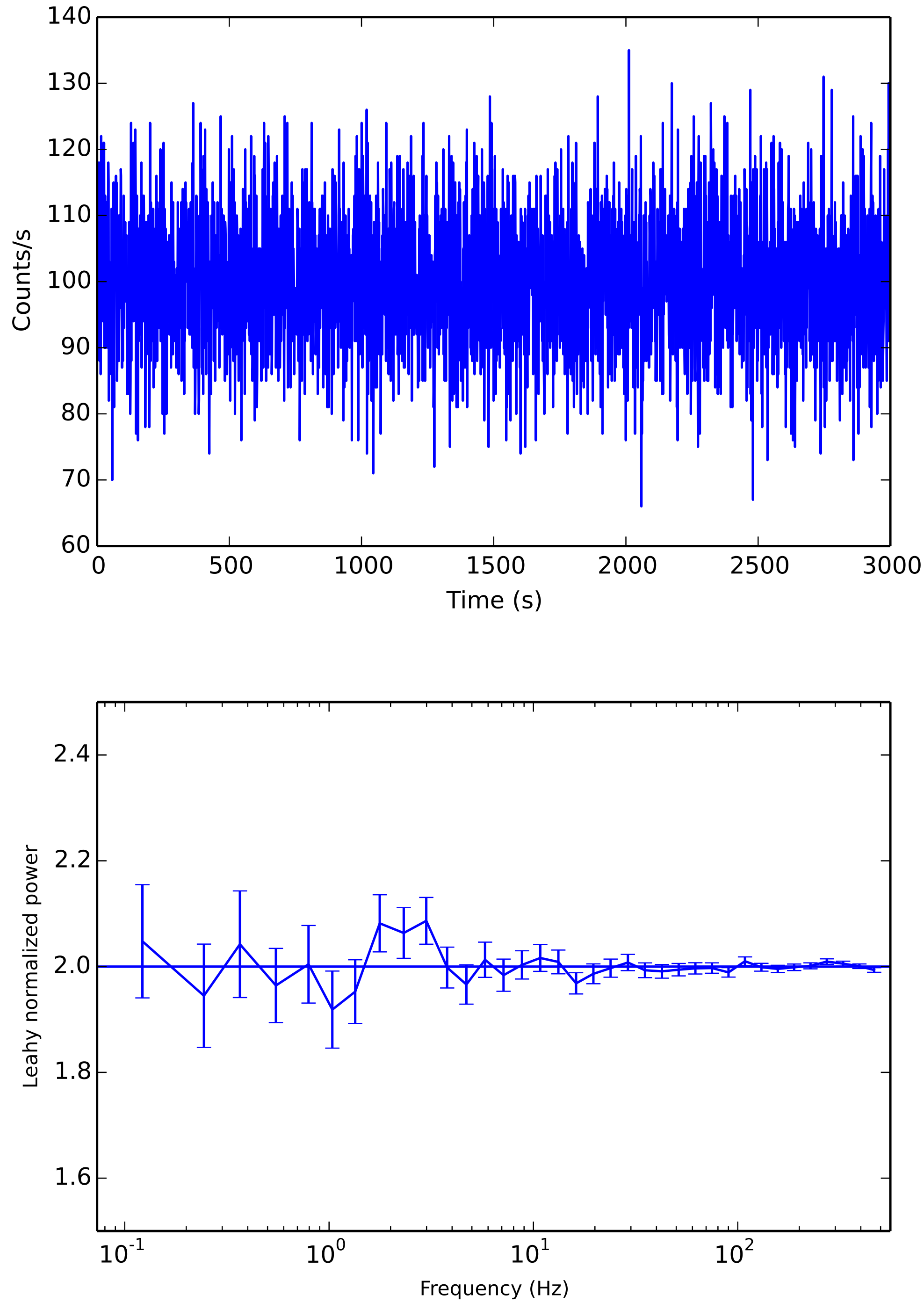

Figure 3.48.: Simulated Poisson noise with an expected mean count rate of 100 cts/s, time resolution of 1 ms, and duration of 3000 s. Top subplot is the rebinned light curve of the simulated Poisson sequence with a bin width of 1 s. Bottom subplot is the power density distribution using the raw simulated

$\lambda\Delta t = 0.1$, with the time resolution of $\Delta t = 1$ms, resulting in a Poisson sequence with mean rate of $\sim$100 cts/s. Then I rebinned this sequence into a light curve of a time resolution of 1 s, as shown in the top subplot in Figure 3.48. I calculated the power spectral density (PSD) using the `ftool powspec` to validate the white noise nature of the simulated light curve. The raw simulated light curve is divided into 367 segments, each of which contains 8192 samples. A PSD with is calculated for each segment, and averaged for all 367 segments, and then rebinned by a geometrical series of step 1.2 in frequency domain. The PSD result is shown in the bottom subplot in Figure 3.48. A constant fit yields the Leahy normalized power density to be 2.00, consistent with the expected noise level. The reduced χ^2 of the fit is $27.49/35 \approx 0.79$, with 35 being the degree of freedom.

Correctly simulating Poisson counting noise is important for studying astronomical time series. Especially, when short time bins are used to study fast variability, due to the low signal to noise ratio, Poisson noise may be important. For binned I have used the `numpy.random.poisson` routine in `python` to simulate a Poisson sequnce, as shown in Figure 3.48. I first generated a list of 3×10^6 Poisson samples with $\lambda\Delta t = 0.1$, with the time resolution of $\Delta t = 1$ms, resulting in a Poisson sequence with mean rate of $\sim$100 cts/s. Then I rebinned this sequence into a light curve of a time resolution of 1 s, as shown in the top subplot in Figure 3.48. I calculated the power spectral density (PSD) using the `ftool powspec` to validate the white noise nature of the simulated light curve. The raw simulated light curve is divided into 367 segments, each of which contains 8192 samples. A PSD with is calculated for each segment, and averaged for all 367 segments, and then rebinned by a geometrical series of step 1.2 in frequency domain. The PSD result is shown in the bottom subplot in Figure 3.48. A constant fit yields the Leahy normalized power density to be 2.00, consistent with the expected noise level. The reduced χ^2 of the fit is $27.49/35 \approx 0.79$, with 35 being the degree of freedom.

Shot noise model and the more general power-law (or $1/f^\alpha$) noise: Shot noise model is the convolution of a Poisson impulse sequence with an impulse response filter $h(t)$ (e.g. exponential shot profile $h(t) = h_0 e^{-t/\tau}, t \geqslant 0$). Similar to a Poisson process, the impulses of a shot noise process occur randomly in time at t_{shot_i}. However, the pulse shape of a shot noise process is different from Poisson process. Instead of being a Dirac delta function in a Poisson process, each pulse (or shot) in a shot noise process has a rising and decaying profile over a period of time. Shot noise process was used by Schottky (1918) to describe the variance of the direct current flow in a vacuum tube. Due to the discrete nature of the current carriers (electrons or holes), on microscopic level a DC current is the superposition of the flow of many individual charges. The flow of each charge (a single shot of current) can be described by a function of time, e.g. a square pulse or exponential pulse, the later of which defines a common shot noise model, the exponential shot noise (ESN) process. Shot noise has been observed ubiquitously in many different systems, and long applied to describe emissions from astrophysical object, e.g. to the optical emission from 3C 273 (Terrell & Olsen, 1970).

When the probed timescales are much longer than the relaxation timescale of the shot pulses, the shot noise process is well approximated by a Poisson process, and has a flat power spectral distribution (white noise). However, as the probed timescale becomes shorter (higher frequencies), the shot noise process becomes a $1/\mathrm{f}^{\alpha}$ type noise ($\alpha \ll 2$). $1/\mathrm{f}^{\alpha}$ noise has a power spectral density distribution that is proportional to $1/\mathrm{f}^{\alpha}$ (see section 3.6.2), and is also called flickr noise, or red noise, or pink noise, depending on the value of α ($\alpha > 0$). It contains more power on longer timescales (at lower frequencies), and has memory of the past. These two features describe the same property of $1/\mathrm{f}^{\alpha}$ noise in frequency domain and time domain, respectively. Based on these two features, $1/\mathrm{f}^{\alpha}$ type noise can be studied in frequency domain using tools like power spectrum, or in time domain using models like autoregressive and moving average. We primarily focus on the frequency domain in this work.

$1/\mathrm{f}^{\alpha}$ noise can be simulated following the widely-used prescriptions given by Timmer & Koenig (1995). I have implemented their algorithm in `IDL` and produced a simulations. They propose a frequentist approach that follows:

1. Assume a underlying power law spectrum $S(\nu) \sim \nu^{-\beta}$ (as defined in equation 3.23).

2. At each frequency ν_i, generate a pair of Gaussian random number, and weigh them by $\sqrt{S(\nu_i)/2} \sim \nu^{-\beta/2}$. The results are the real and imaginary of the Fourier coefficient at frequency ν_i.

3. Reflect the Fourier components generated above to negative frequencies following $F(-\nu_i) = F^*(\nu_i)$, so that the final time series is real.

4. Inverse Fourier transform the obtained Fourier components to time domain to get the simulated time series.

Note that the power spectrum is exponentially distributed, so that individual power spectrum can fluctuate wildly (as its mean and variance is the same), and the error bar is non-Gaussian. Therefore simulation of $1/\mathrm{f}^{\alpha}$ is very important in estimating the shape of power spectrum.

3.6.2 Power Spectral Density

Blazars not only exhibit rapid flares, which may be of transient nature, but also show persistent variability on all timescales. Power spectral density (PSD) provides a useful tool to quantify the amount of contribution to the variance from different frequencies/timescales of a time series. The same as many other time frequency analyses, PSD connects time domain and frequency domain through Fourier transform. Essentially, Fourier transform uses sine and cosine functions as a set of bases and expands a input signal in this new set of bases. Consider a time series x(t), the Fourier transform is defined as

$$F(\nu) = \int_{-\infty}^{\infty} x(t) e^{-2\pi i \nu t}\, \mathrm{d}t.$$

Note that this definition requires x(t) to be absolute integrable and does not apply to periodic function (Deeming, 1975). Thus it is useful to define finite Fourier transform

$$F_T(\nu) = \int_{-T/2}^{T/2} x(t)e^{-2\pi i\nu t}\,\mathrm{d}t,$$

and discrete Fourier transform (DFT)

$$F_N(\nu) = \sum_{i=1}^{N} x(t_i)e^{-2\pi i\nu t_i} = \sum_{i=1}^{N} \left[x(t_i)cos(2\pi\nu t_i) - ix(t_i)sin(2\pi\nu t_i)\right].$$

The frequencies ν in $F_N(\nu)$ in DFT are only physically meaningful within a finite range. The lowest frequency $\nu_{min} = T_{dur}^{-1}$ is determined by the duration of time $T_{dur} = t_N - t_1$. The highest frequency is the Nyquist frequency $\nu_{Nyq} = \Delta T^{-1}$, which is determined by the sampling interval, or bin width in most of the astronomical time series, ΔT. The inverse of DFT is defined as:

$$x(t) = \sum_{j=1}^{N} F_N(\nu_j)e^{2\pi i\nu_j t} = \sum_{j=1}^{N} \left[F_N(\nu_j)cos(2\pi\nu_j t) + iF_N(\nu_j)sin(2\pi\nu_j t)\right].$$

Astronomical time series are discretely measured and measurements are of finite length (although the duration of the actual time series from the source is much longer and may be considered infinite). Thus we only consider discrete time series and DFT. DFT is widely used by many scientists and engineers, and a fast Fourier transform (FFT) algorithm is widely used for rapidly computing DFT and inverse DFT.

Recall that the autocorrelation function $ACF(\tau)$ of x(t) at a delay of τ is defined in equation 3.17 as:

$$ACF(\tau) = \langle x(t)x(t+\tau)\rangle.$$

The spectrum of x(t), closely related to autocorrelation function, is defined as the Fourier transform of the autocorrelation function

$$S(\nu) = \sum_{i=1}^{N} ACF(\tau_i)e^{-2\pi i\nu t_i}. \tag{3.23}$$

As stressed in Timmer & Koenig (1995), spectrum and ACF are the intrinsic properties of the underlying process which are not related to each realization. This means a infinitely long time series that are sampled faster than the smallest variation timescale is needed to calculate spectrum and ACF, making them impractical. However, there are many practical ways to estimate spectrum.

A common way to estimate spectrum is the periodogram, the modulus squared of the Fourier transform of a time series, which is defined as

$$Per(\nu) = |F_N(\nu)|^2 = \left[\sum_{i=1}^{N} x(t_i) cos(2\pi\nu t_i)\right]^2 + \left[\sum_{i=1}^{N} x(t_i) sin(2\pi\nu t_i)\right]^2.$$

$Per(\nu)$ represents the the energy per unit frequency at frequency ν, and is also called energy spectrum. The integral/sum of $P(\nu)$ from ν_1 to ν_2 yields the fractional energy in the frequency range between ν_1 and ν_2. Now it is clear that $P(\nu)$ quantifies the amount of variability at different frequencies.

According to Parseval's theorem, the sum of $P(\nu)$ over all ν and the sum of $|x(t_i)|^2$ are equal to each other:

$$\sum_{i=1}^{N} |x(t_i)|^2 = \sum_{j=1}^{N} |F_N(\nu_j)|^2,$$

and both represents the total energy of the time series. Therefore, periodogram can be normalized so that it reflect the variability power. Two common normalizations are the Leahy normalization

$$A_{Leahy} = \frac{2\Delta T_{sample}}{N\bar{x}},$$

and the RMS normalization

$$A_{RMS} = \frac{2\Delta T_{sample}}{N\bar{x}^2}.$$

According to the shape of the PSD, stochastic processes can be classified. The most common noise is white noise, which is defined as process with a zero mean and a constant, finite variance in time domain. In frequency domain, white noise has constant power over all frequencies. Note that the probability distribution is not specified, which means there are different types of white noise. Poisson noise described in section 3.6.1 is a common type of white noise. Gaussian distributed white noise is also common.

In section 3.6.1, we have introduced a common and interesting type of noise, the $1/f^{\alpha}$ noise, which exhibits a power spectral density distribution as follows:

$$P(\nu) \propto \nu^{-\alpha}.$$

Such a power-law noise can have different origins, but always indicate scale-invariant processes. For example, Lu & Hamilton (1991) demonstrated that self-organized criticality, i.e. a local rule for a system to reconfigure after reaching a critical condition, can lead to a global PSD distribution that follows $1/\mathrm{f}^{\alpha}$. Interestingly, the slope of the PSD does not depend on the critical value of the system.

Extensive studies on black hole binaries (BHBs) in X-ray wavelengths have shown evidence for red-noise style variability, with one or two bends in PSD distribution depending on state (see McHardy, 2010, for a review). The bending frequency were found to scale roughly with the accretion rate, and inversely with the black hole mass. Similar to BHBs, AGNs also show red-noise type of variability in X-ray band, sometimes also with a bending feature in PSD (e.g. Uttley et al., 2002; Cui, 2004; Chatterjee et al., 2008). The bending frequency of AGNs is much lower than BHBs, due to their large masses. This makes the bending features in AGN much harder to study because of the much longer time scale and the consequent unevenness of data. However, this scaling relation provides an opportunity to examine the relation between accretion process of stellar mass black holes and supermassive black holes.

Having demonstrated the importance of PSDs, we now look at the practical challenges in the estimation of PSDs. Like other methods that focus on the global properties of a time series, PSDs are affected by uneven sampling of the measurements. The finite duration and time resolution, as well as the gaps in the light curve measurements lead to distortion effects known as red-noise leak and aliasing (e.g. Papadakis & Lawrence, 1993). Simulation is needed for estimating the shape of the PSD as well as the distortion from sampling patterns. I have generated simulated power-law noise time series following Timmer & Koenig (1995) (see also section 3.6.1). I contaminate the simulated light curve by rebinning and resampling. Resampling leads to the well known aliasing problem, since faster variations on shorter timescales are contributing

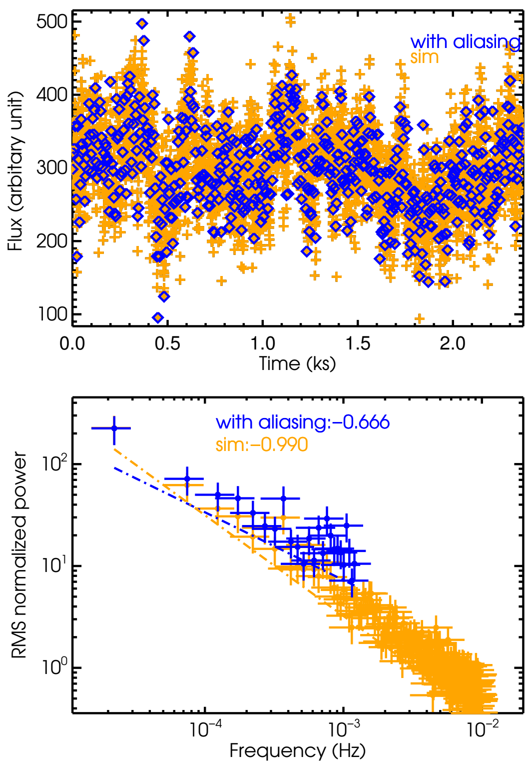

Figure 3.49.: PSDs from simulated light curves generated from a PSD distribution $P(\nu) \propto \nu^{-1}$ (i.e. $\alpha = 1$), in comparison with the PSD after a sparser sampling. The simulated light curve is normalized so that it has a mean rate of 300 cts/s and a standard deviation of 60 cts/s. The top panels show the original simulated light curves (orange), and the resampled light curve (blue), sampled at every 8 original bins (left) and every 16 original bins (right). Bottom panels show the PSDs from the simulated LCs in top panels. Aliasing leads to a much flatter PSD.

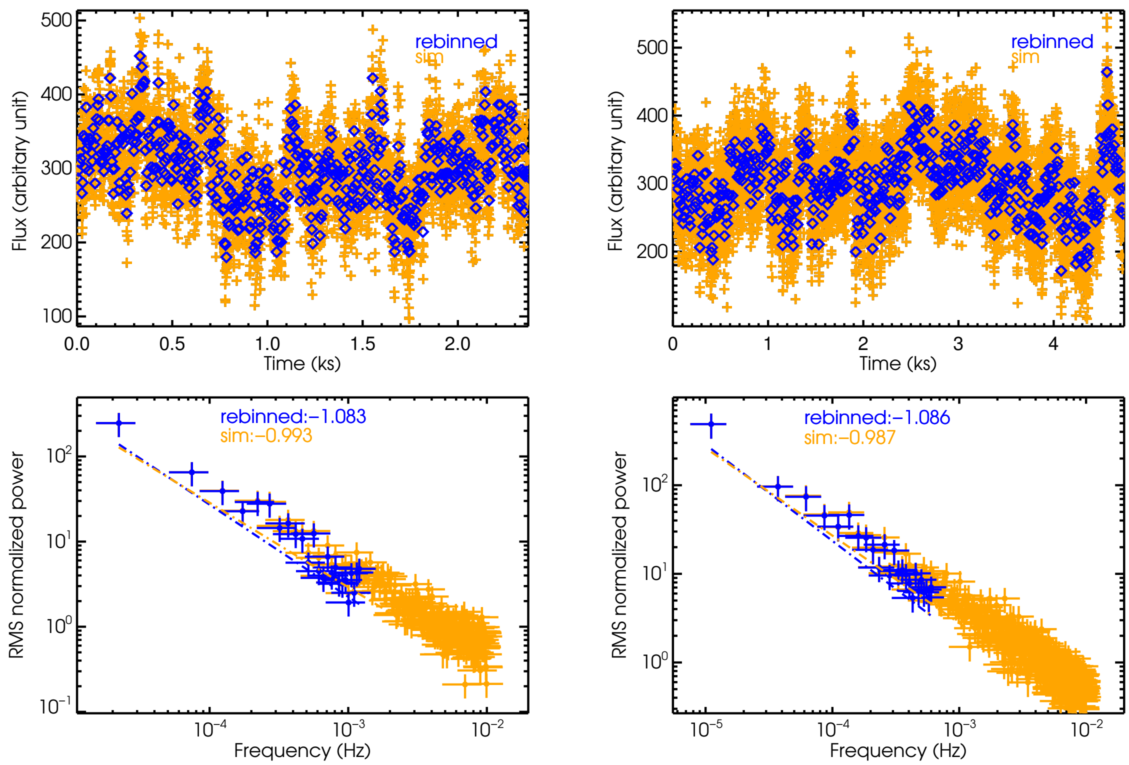

Figure 3.50.: PSDs from simulated light curves generated from a PSD distribution $P(\nu) \propto \nu^{-1}$ (i.e. $\alpha = 1$), in comparison with the PSD after time averaging. The simulated light curve is normalized so that it has a mean rate of 300 cts/s and a standard deviation of 60 cts/s. The top panels show the original simulated light curves (orange), and the time-averaged light curves (blue), rebinned with a coarse time interval of 8 times (left) and 16 times (right) the original bin width. Bottom panels show the PSDs from the simulated LCs in top panels. Time-averaging leads to a slightly steeper PSD.

to the longer timescales due to inadequate sampling. Therefore aliasing leads to a flatter PSD, as shown in Figure 3.49. This is the case for "snapshot" observations arranged evenly over a long period of time, e.g. the weekly to monthly blazar snapshots in the VERITAS blazar long term plan.

On the other hand, for continuous observations that do not suffer from aliasing, the effect of time-averaging is rarely discussed in literature. The common light curve format is the histogram, which averages out the variability on timescales shorter than the bin width. However, similar to the red noise leak, this time-averaging affects PSD at lower frequencies (just below the Nyquist frequency), leading to a slightly steeper PSD as shown in Figure 3.50. Another distorting effect is the red noise leak, i.e. power from below the minimum frequency can leak in to the observed frequency. This effect is particularly severe if the PSD is very steep, e.g. when $\alpha > 2$.

Effects from red noise leak, aliasing, and time-averaging can be corrected, by applying them to simulated light curves and comparing with the observations PSD_{obs}. A success fraction (SuF) method is described by Uttley et al. (2002); Chatterjee et al. (2008), the steps are:

1. Calculate the PSD of the observed light curve PSD_{obs}.

2. Simulate a large number (M) of light curves assuming a underlying PSD shape, and calculate their $PSD_{sim,i}, i = 1, \cdot, M$.

3. Calculate a function similar to χ^2 for each PSD:

$$\chi^2_x = \sum_{\nu} \frac{(PSD_x - PS\bar{D}_{sim})^2}{(\Delta PSD_{sim})^2},$$

   where PSD_x can be PSD_{obs} or $PSD_{sim,i}$.

4. Count the number of occurrences (m) of $\chi^2_{obs} < \chi^2_{sim,i}$, and m/M is the success fraction.

We have tested the SuF method with simulated light curves generated from $1/f^{\alpha}$ processes with known index α, as shown in Figure 3.51. We simulated 100 LCs

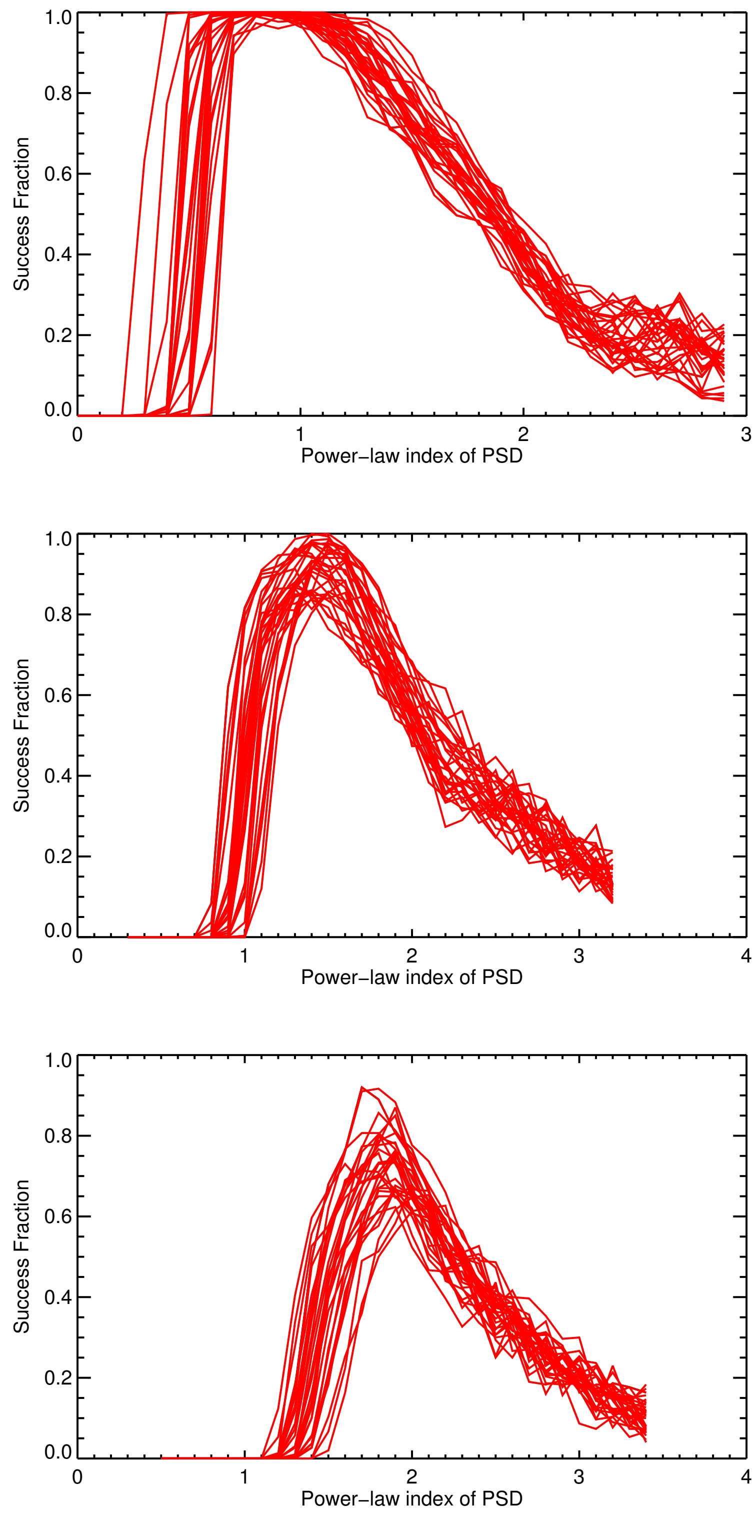

Figure 3.51.: SuF values calculated for simulated light curves as a function of the index α in $1/f^{\alpha}$ processes. From top to bottom, the indices used for generating the simulated LCs are 1.0, 1.5, and 2.0, respectively. Each panel shows the SuF distribution for 100 simulated LCs. For each simulated LC, at every α value (incremented in steps of 0.1), 1024 LCs are generated to calculated the χ^2 and SuF.

with α each being 1.0, 1.5, and 2.0, respectively, and calculated SuF for each of the simulated LCs (treating them as an observed LC and following the steps listed above). At each tested index that we scanned through (as shown in the x-axis in Figure 3.51), we generated M=1024 LCs to calculated the χ^2s and SuFs. The SuF can reconstruct the underlying PSD shape reasonably well with relatively small bias, but the uncertainty (variance) is quite large, especially for smaller α values (flatter PSD distribution).

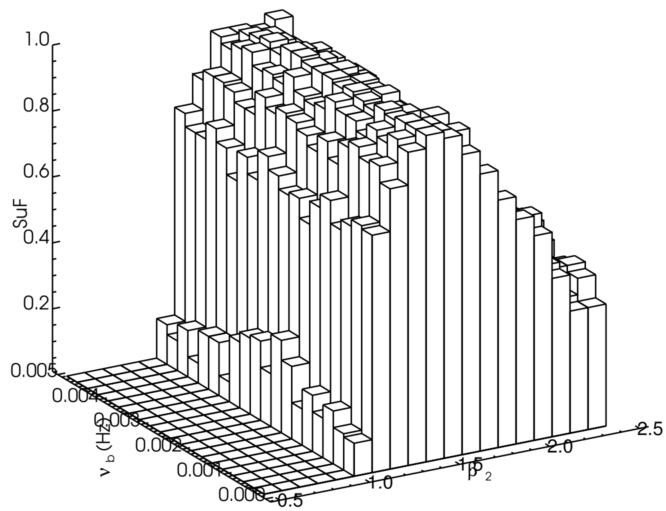

Figure 3.52.: SuF values for a simulated LC with broken power-law distributed PSD. The break frequency $\nu_b = 0.002$Hz, the index α_1=1.0 below ν_b, and α_2=2.5 above ν_b. Each grid in the plot corresponds to a combination of α_2 and ν_b, while α_1 fixed at 1.0. We simulate 100 LCs in each grid to calculate the SuF.

We have also tested the SuF method with simulated LCs with broken power-law distributed PSDs, and found that the method is insensitive to break frequencies. For example, we calculated the SuF distribution for a simulated LC generated with the following PSD:

$$P(\nu) \propto \begin{cases} \nu^{-\alpha_1}, & \nu \leqslant \nu_b, \\ \nu^{-\alpha_2}, & \nu \geqslant \nu_b, \end{cases}$$

where $\nu_b = 2 \times 10^{-3}$Hz is the break frequency, $\alpha_1 = 1.0$ and $\alpha_2 = 1.5$ are the power-law index below and above the break frequency, respectively. We fixed α_1 at 1.0, and scanned through different combinations of α_2 (from 0.5 to 2.5 in steps of 0.1) and ν_b (from 2.5×10^{-4}Hz to 5×10^{-3}Hz in steps of 2.5×10^{-4}Hz), at each of which we simulated 100 LCs to calculated the SuF. Figure 3.52 shows the SuF distribution as a function of α_2 and ν_b. The SuF distribution is quite flat along the ν_b-axis, and therefore not sensitive to the break frequency.

Figure 3.53, 3.54, and 3.55 show PSDs calculated from X-ray light curves of Mrk 421 measured by XMM-Newton EPIC pn on 2014 Apr 29, May 1, and May 3, respectively. The light curves is first binned by 50 s intervals, then divided into equal-length segments each has 128 bins. A raw power spectrum is calculated for each segment and averaged over all segments. Then, the power spectrum is rebinned geometrically with step factor 1.2, i.e. a bin edge in frequency is the previous bin edge multiplied by a factor of 1.2. The PSDs cover a frequency range of 4×10^{-4} to 0.01 Hz. At higher frequency, the shape of PSDs becomes flatter due to Poisson noise. However, we note that the PSD is well above the Poisson noise level up to $\sim$$10^{-3}$ Hz on all three days, which is less than an hour. On May 1, the variability is still present reaching $\sim 2 - 3 \times 10^{-3}$ Hz, which is shorter than 10 minutes.

We simulated 1000 light curves of for each underlying $1/f^{\alpha}$ noise with different α. Then we calculated the SuF following the descriptions above, as an estimation for the power-law index α. The results are plotted in Figure 3.56. The SuF peaks at the PSD indices of $\sim$1.1 on Apr 29, $\sim$1.4 on May 1, and $\sim$1.0 on May 3.

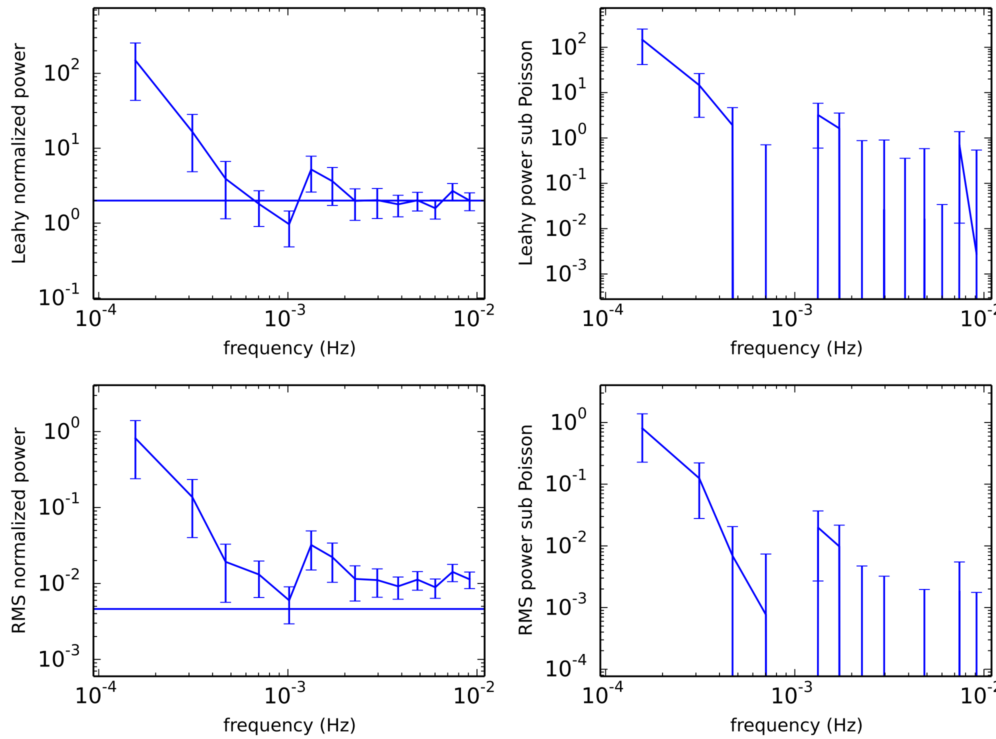

Figure 3.53.: Power spectral density of Mrk 421 calculated from the XMM-Newton EPIC pn observations on 2014 Apr 29. The light curves is first binned by 50 s intervals, then divided into equal-length segments each has 128 bins. A raw power spectrum is calculated for each segment and averaged over all segments. Finally, the power spectrum is rebinned geometrically with step factor 1.2, i.e. a bin edge in frequency is the previous bin edge multiplied by a factor of 1.2. The top left panel shows the PSD with Leahy normalization, a constant line indicates the Poissoin noise level. The top right panel shows the PSD with Leahy normalization but subtract the Poisson noise constant floor. Similarly, the bottom two panels show the PSD with rms normalization, with and without Poisson noise.

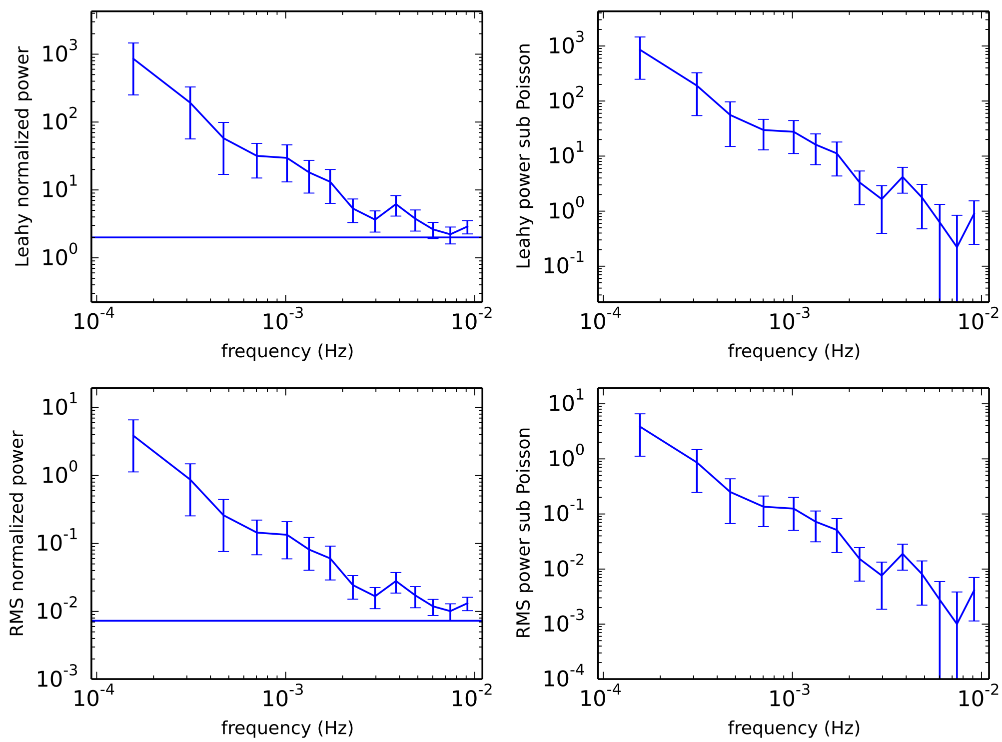

Figure 3.54.: Power spectral density of Mrk 421 calculated from the XMM-Newton EPIC pn observations on 2014 May 1. The PSDs are calculated in a similar fashion described in Figure 3.53.

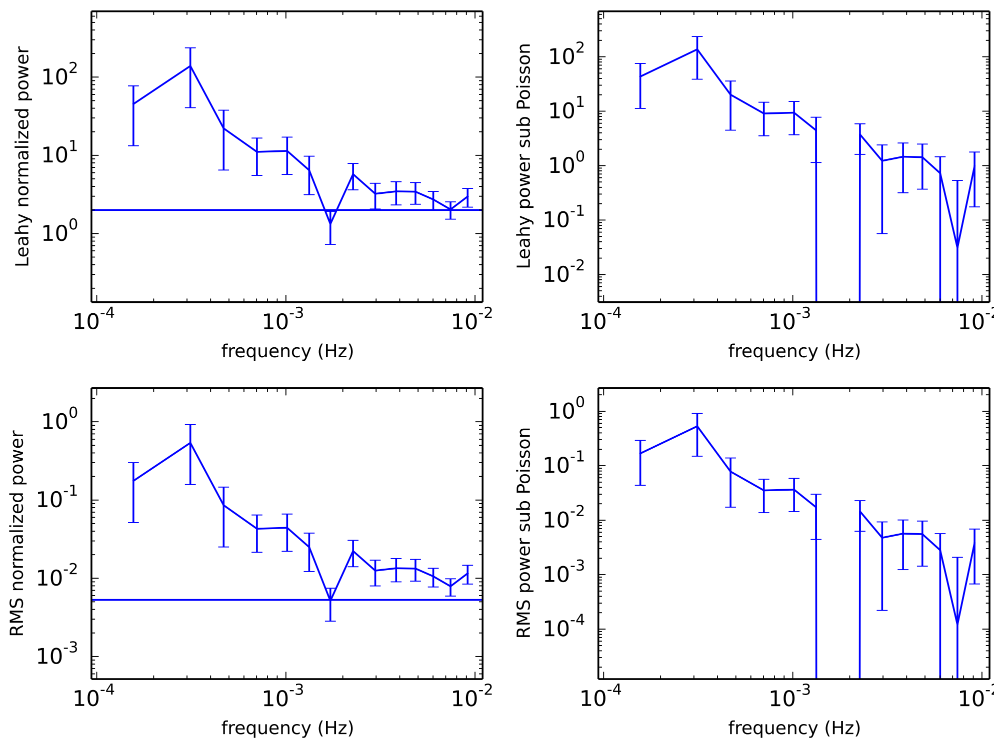

Figure 3.55.: Power spectral density of Mrk 421 calculated from the XMM-Newton EPIC pn observations on 2014 May 3. The PSDs are calculated in a similar fashion described in Figure 3.53.

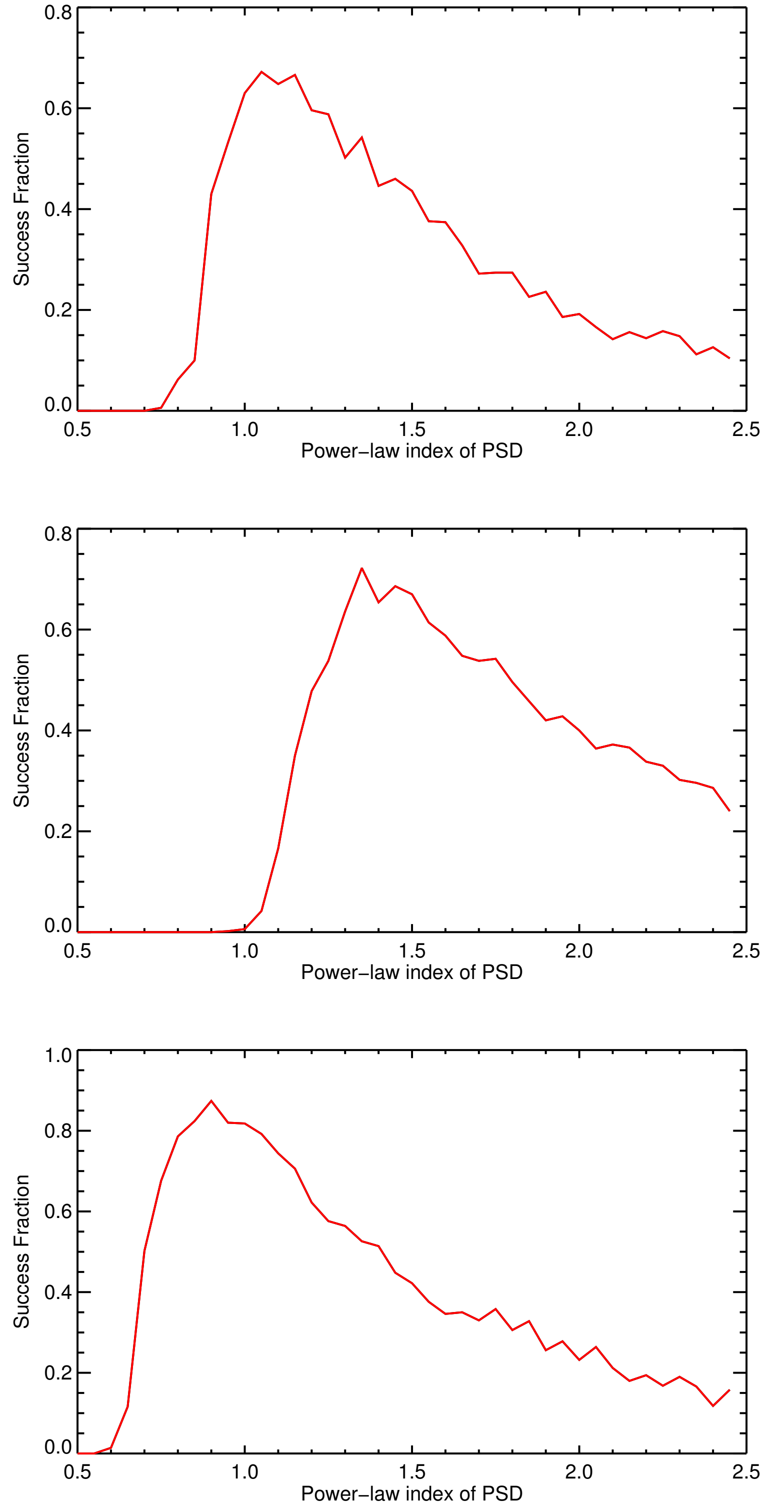

Figure 3.56.: The SuF results calculated from simulated light curves assuming a power-law underlying power spectrum following Timmer & Koenig (1995). The index of the PSD goes from 0.5 to 2.5 in 0.05 steps. 1000 simulated light curves are generated at each index.

3.6.3 Hilbert-Huang Transform

PSD has been the most common tool for finding characteristic timescales in persistent variability in astrophysics. However, it has severe limitations, since it expands the input time series using trigonometric basis, which is only localized in frequency domain. Thus it only works for stationary and linear system. For example, it does not distinguish between (i) the superposition of two signals at two different frequencies and (ii) an intermittent signal periodically switching between the two frequencies. To analyze such a non-stationary time series, one needs a set of basis that is localized both in frequency and time domain, to produce a spectrogram that quantifies the power at a certain time and a certain frequency. The simplest time-frequency analysis is the short time Fourier transform, which calculates the FT of fixed-duration segments (windows) of the time series. A popular and more flexible time-frequency analysis method is the wavelet transform. It decomposes a time series using wavelet basis functions that are both localized in frequency (scale) and time. However, the decomposition in wavelet analysis relies on a priori, fixed set of basis (wavelets), therefore only suitable for linear time series. Adaptive basis is needed for treating non-linear time series. In this subsection I introduce the Hilbert-Huang Transform (HHT Huang et al., 1998a; Huang & Wu, 2008), a technique similar to wavelet analysis but using adaptive basis, demonstrate its applicability to astrophysical time series, and present as well as interpret the HHT results for light curves of TeV blazars.

HHT contains two steps: The first step is empirical mode decomposition (EMD), which acts like a set of band-pass filters with adaptive passband and bandwidth, and produces a set of sub series, each of which are locally narrowband. The second step is Hilbert spectral analysis (HSA), which calculate the instantaneous frequency of a sub series produced by the first step. HHT is a useful tool since it works well with non-stationary and non-linear processes.

Empirical mode decomposition (EMD): EMD is a method to decompose a signal to a series of intrinsic mode functions (IMFs), i.e. to find out sub-components of different frequencies from a signal $Signal = IMF_1 + IMF_2 + IMF_3 + ... + IMF_n + Trend$. The steps to obtain each IMF is depicted below:

1. Determine all the local extrema of the input signal.
2. Connect maxima and minima respectively using a cubic spine line, forming an upper envelope and a lower envelope.
3. Compute the average of upper envelope and lower envelope.
4. Subtract the average from the input signal, and get a high frequency residual.
5. If this residual satisfies two conditions: (1) number of extrema and number of zero crossings is the same or differs by one; and (2) local average of the upper and lower envelop is zero; this residual is an IMF. Otherwise use this residual as input signal and repeat steps above until an IMF is found.

After finding an IMF, subtract it from the original signal and get a residual signal, then perform the above steps again (so-called "sift"). The process stops when there is only one extrema left in the residual. The sub-component of the highest frequency (IMF_1) will be found first, and it contains the fastest variability in the signal.

A time series can usually be represented by less than ten IMFs, much more efficient than FFT or wavelet representations. The sum of all IMFs (including the residual trend) is precisely the input signal, illustrating the advantage of empirical bases comparing to priori bases. Each IMF is locally narrow-band and zero-mean, therefore the frequency of the IMF is data-driven and physically meaningful. The IMFs thus form a good set of basis for separating the amplitude modulation (AM) and frequency modulation (FM) components of a time series.

Hilbert spectral analysis (HSA): To take use of the good properties of the IMFs and convert a time series from time domain to time-frequency domain, Huang

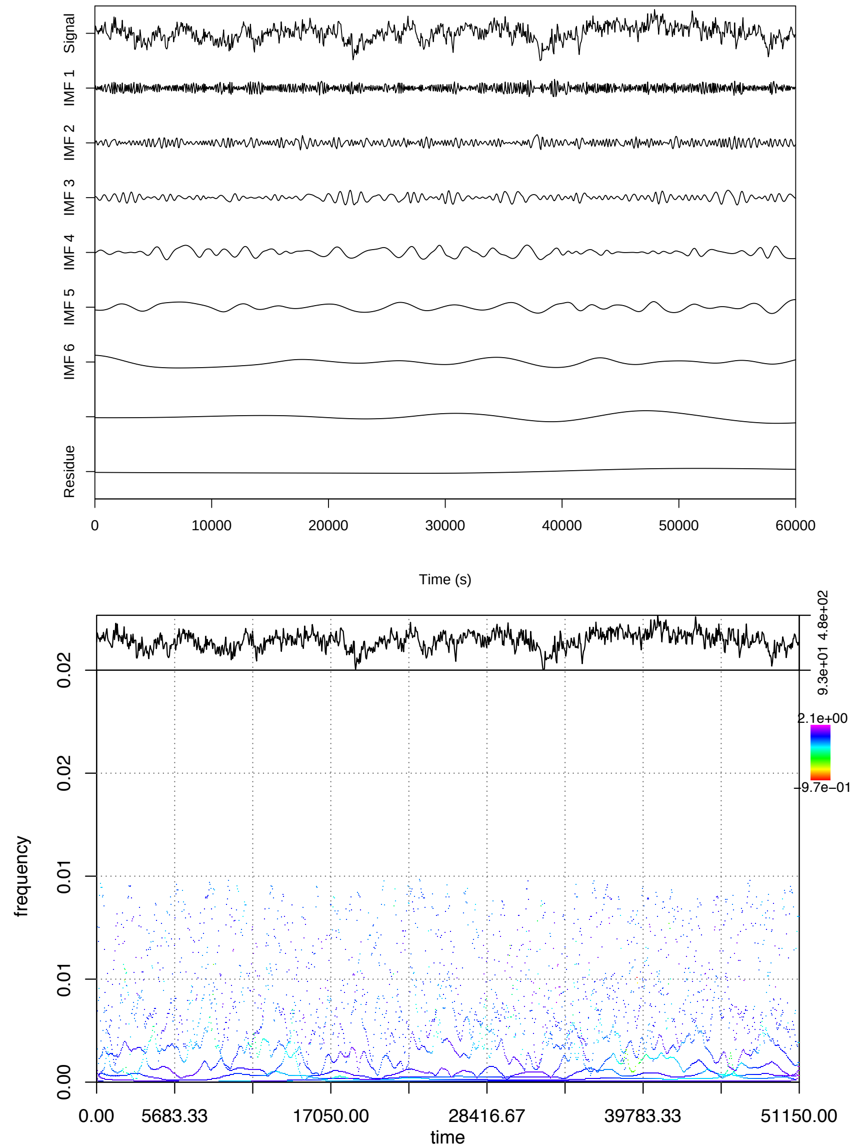

Figure 3.57.: The IMFs (top) and the Hilbert spectra $H(\nu, t)$ for each IMF (bottom) of a simulated 1/f noise ($\alpha = 1$). The simulated light curve is normalized so that it has a mean rate of 300 cts/s and a standard deviation of 60 cts/s (similar to Figure 3.49). A white noise of amplitude 0.1 is used for EEMD to prevent mode mixing (see below).

& Wu (2008) proposed the use of Hilbert transform (HT). The HT of a given function $x(t)$ is defined as:

$$H[x(t)] = \frac{1}{\pi} P.V. \int_{-\infty}^{\infty} \frac{x(\tau)}{t-\tau} d\tau,$$

where $P.V.$ is the Cauchys principal value. With this definition of HT, an analytical function can be represented by:

$$z(t) = x(t) + iH[x(t)] = a(t)e^{i\theta(t)},$$

where $a(t)$ is the instantaneous amplitude function, and $\theta(t)$ is the instantaneous phase function that is related to both instantaneous frequency (IF) $\nu(t)$ and time t. The IF is defined as:

$$\nu(t) = \frac{d\theta(t)}{2\pi dt}.$$

Note that the HT has a similar form to Fourier transform, with the important difference that the frequency in HT depends on time, while each components of FT only has a constant frequency.

However, the IFs obtained by HT only have physical meaning when the input time series are both locally narrow-band and zero-mean. IMFs obtained from EMD method automatically satisfies these two criteria. As a result, we can obtain meaningful IFs by performing HT to the IMFs to obtain the expansion in following format:

$$IMF_j(t) = a_j(t)e^{i\theta_j(t)}.$$

For each IMF_j, $a_j(\nu_j, t)$ gives its Hilbert amplitude spectrum (also known as Hilbert spectrogram, or Hilbert spectrum) $H(\nu_j, t)$, the square of which is the Hilbert energy spectrum, at frequency ν_j and time t. A marginal Hilbert spectrum, similar to power spectrum, can be obtained by integrating the Hilbert spectrum over all time:

$$h(\nu) = \int_{T_{\text{start}}}^{T_{\text{end}}} H(\nu, t).$$

A publicly available `R` package 'hht' (R Core Team, 2014; Bowman & Lees, 2013) is used to compute IMFs and Hilbert spectra. Figure 3.57 shows the IMFs and the Hilbert spectrogram of a simulated 1/f noise with a power-law index $\alpha = 1$. As shown

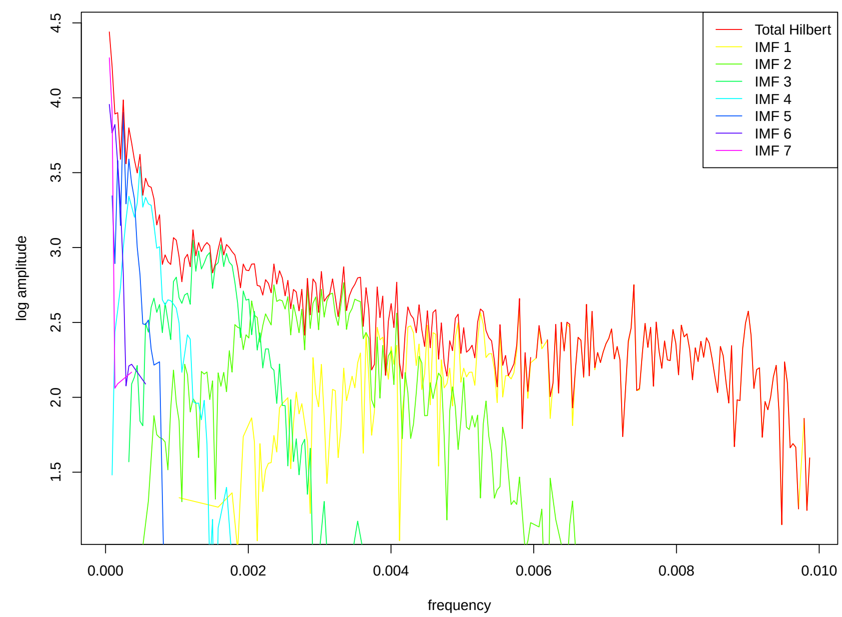

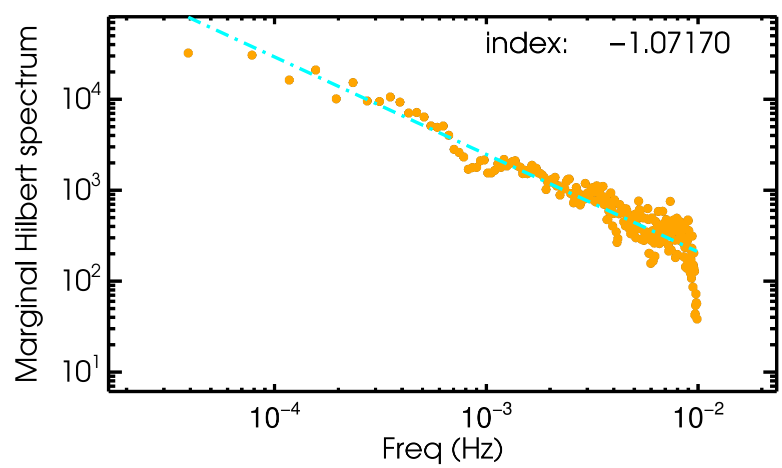

Figure 3.58.: Top panel: the marginal Hilbert spectra $h(\nu)$ obtained by integrating $H(\nu,t)$ of each IMF over all time. The amplitude is shown in log scale, while the frequency is shown in linear scale. The same simulated 1/f light curve as that in Figure 3.57 was used. Bottom panel: the total Hilbert spectra, as the sum of $h(\nu)$ for all IMFs, shown in log frequency (in the unit of Hz) and log amplitude.

in the top panel, seven IMFs and a residual are necessary to decompose the input series. Each IMF is locally zero-mean, and shows variability over a range of overall frequencies. But at any given time, the only variability on a particular timescale corresponding to the IF is significant. As a result, these IMFs show up as narrow traces in the Hilbert spectra as plotted in the bottom panel of Figure 3.57, with well defined IF. The color along the traces indicates the instantaneous amplitude. The marginal Hilbert spectra of each IMF are shown in the top panel of Figure 3.58. The total marginal spectrum of all IMFs (shown in bottom panel in Figure 3.58) recovers the simulated power-law index very well.

Intermittency: Intermittency of a signal, e.g. a large gap with no measurements, may lead to severe bias in the IMF. Recall that the IMF are constructed using adjacent extrema, therefore intermittency directly causes a strong fake signal at low frequency. As a result, the instantaneous frequencies calculated from such IMFs lose physical meanings. This is a particularly important issue in astrophysical time series, which usually consists of numerous gaps. Fig. 3.59 illustrates the effect of intermittency caused by the annual gap in a VERITAS light curve of Mrk 421. The light curve is made with all VERITAS observations between 2009 and 2014, and are binned nightly. Strong and slowly-varying (on comparable timescales as the length of the gap) artificial features in the IMFs during the yearly gaps are clearly visible. These features also shows up in the Hilbert spectrum as shown in Figure 3.60, as the strong (bright yellow and red) segments during the gaps at low frequencies.

Such effect of intermittence has been identified by Huang et al. (1998b). To treat intermittence, they provided a method called ensemble empirical mode decomposition (EEMD). EEMD creates an ensemble of time series by adding white noise to the input time series. IMFs are produced for each resulting "trial" series with the added white noise. The average of all trial IMFs are used as the final IMF. The amplitude of the white noise and the number of trials can be adjusted. Figure 3.61 shows the EEMD results for the five-year nightly-binned VERITAS light curve of Mrk 421. The

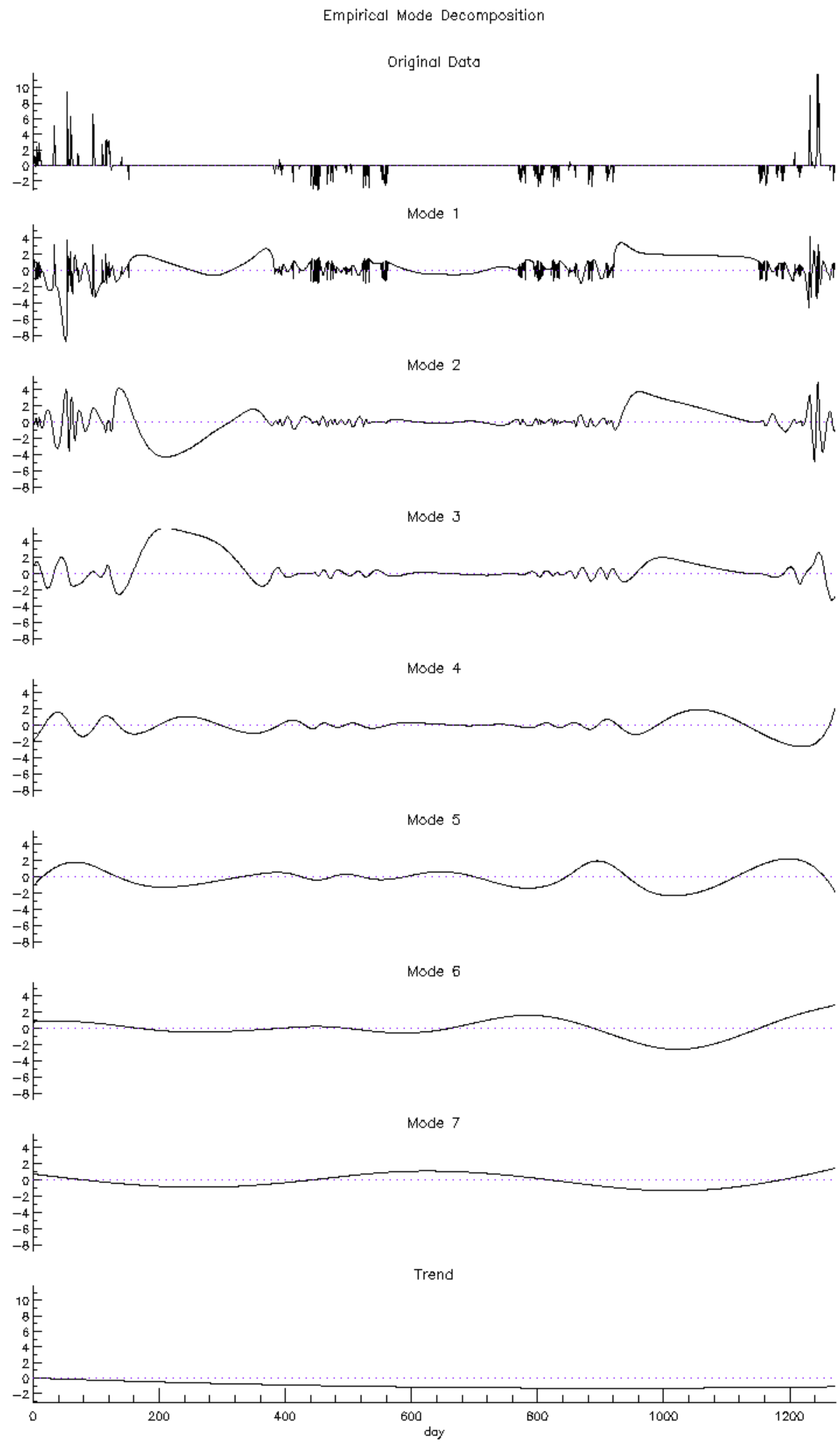

Figure 3.59.: An example of the effect of annual intermittence on IMFs for a VERITAS light curve of Mrk 421. The input light curve has a time span of four years and bin width of one day. Days without data are padded with zero flux values.

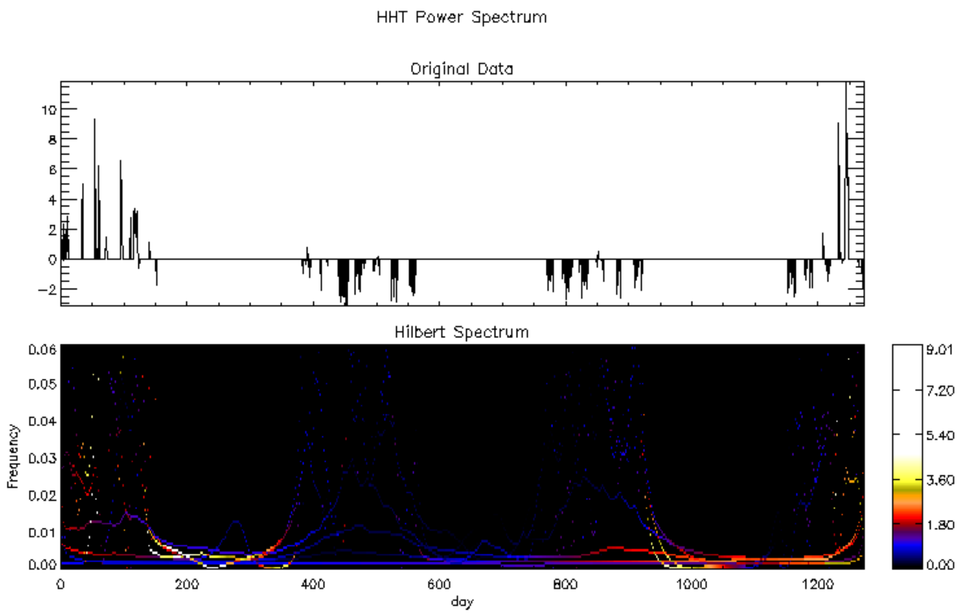

Figure 3.60.: The corresponding Hilbert spectrum calculated from the IMFs shown in Fig. 3.59. The effect of annual gaps in the light curve reflects in the Hilbert spectrum as strong power during the gaps.

gaps between observations are first padded with zeroes, and a white noise of variance 1×10^{-8}photons m^{-2} s^{-1} is added to the entire light curve to create a trial series, and a total number of 10 trials are made. Note that for most IMFs produced by EEMD, the amplitude lies at zero during the gaps of the observations, which is a great improvement from the EMD. However, for IMF_3, IMF_4, IMF_5, and lower-frequency IMFs, there are still some bias at the end of the fourth season. Figure 3.62 shows the Hilbert spectra and marginal Hilbert spectra of the above IMFs obtained from EEMD. The artificial power during the gaps of the observations are much weaker comparing to that with the EMD.

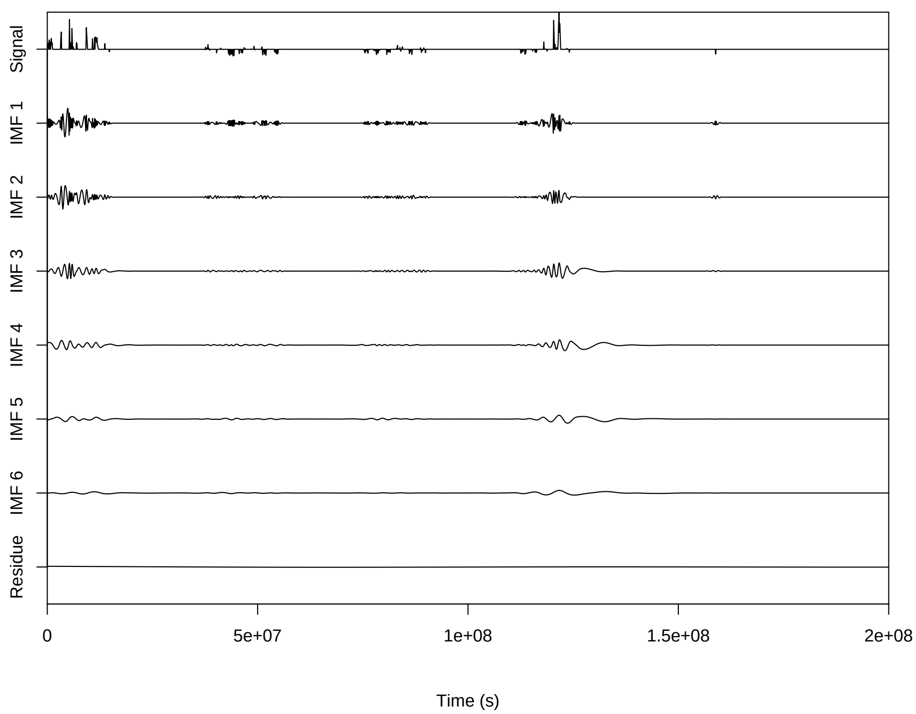

Figure 3.61.: IMFs generated by EEMD method from the same VERITAS light curve of Mrk 421 as shown in Fig. 3.59. The artificial features in IMFs during the annual gaps are much weaker comparing to that in Figure 3.59, although it still exists.

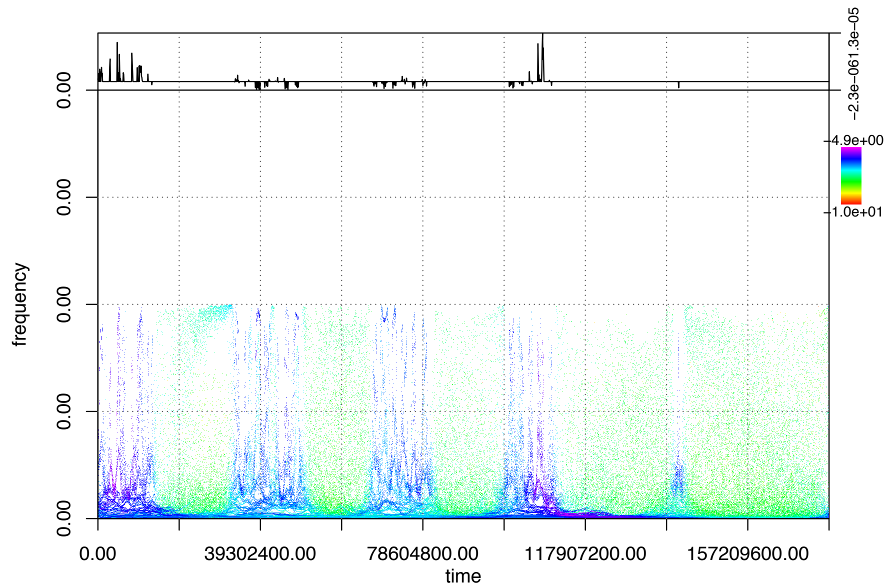

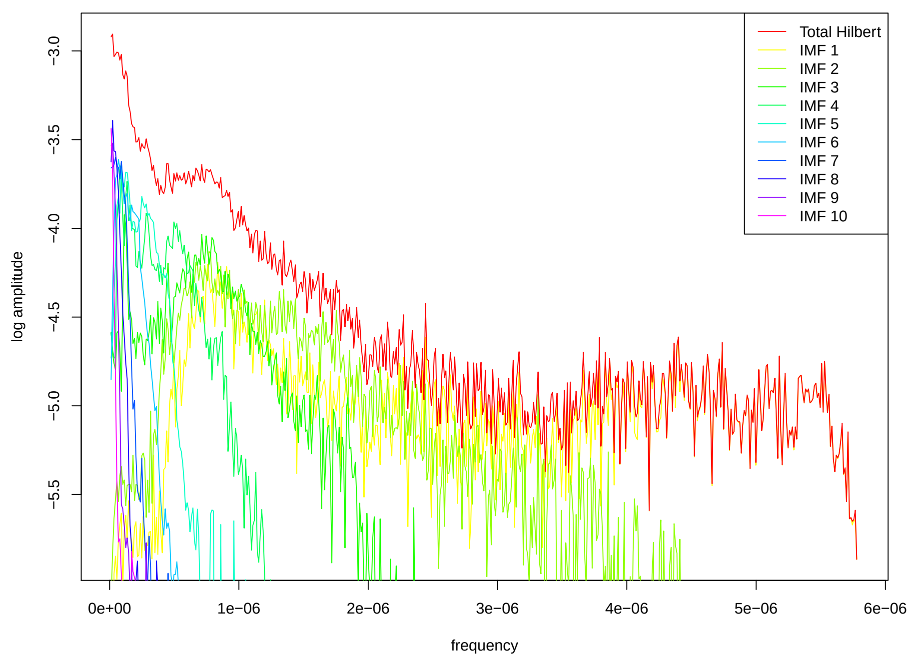

Figure 3.62.: Top panel: the corresponding Hilbert spectrum $H(\nu, t)$ calculated from the IMFs shown in Fig. 3.61. The effect of annual gaps in the light curve are ameliorated comparing to Figure 3.60. Bottom panel: the marginal Hilbert spectrum of all IMFs obtained by integrating $H(\nu, t)$ of each IMF over all time. The unit of x-axis is Hz.

3.7 Conclusions

1. For the first time, a rapid TeV gamma-ray flare on the timescale of minutes is observed from an low-frequency peaked blazar, BL Lacertae. It fills an important gap between similar phenomenon observed in FSRQs and HBLs. The flare timescale provides a model-independent constraint on the size of the emitting region.

2. The compactness of the emitting region suggests that the flare from BL Lacertae is either produced at the base of the jet near the central black hole, or at a local region that is smaller than the jet cross section downstream of the jet (further away from the central black hole). If the former case is true, the Doppler factor of the emitting region needs to be larger than ∼13 in order to avoid pair-production attenuation; if the latter case is true, the gamma-ray emitting region for the flare is most likely located at the radio core (see below).

3. Several facts from the polarization observations lend support to the model proposed by Marscher et al. (2008), which suggests that a gamma-ray flare can be produced when a knot in the jet crosses a conical standing shock (the radio core) further downstream in the jet. Especially interesting is the emergence of a compact knot structure revealed by radio observations at 43 GHz contemporaneous with the TeV flare, and a sharp jump in the optical polarization angle (also an earlier dip in the optical polarization fraction). If the connection between the TeV flare and the emergence of the radio knot is true, the location of the gamma-ray emitting region can be constrained to an unprecedented precision at the distance of the radio core, i.e. ∼1 pc away from the black hole.

4. Several important timescales in blazars, cooling time t_{cool}, acceleration time t_{acc}, dynamic timescale t_{dyn}, and injection timescale t_{inj} control many observable quantities, especially the energy-dependent trend in their variability. For example, if the cooling timescale controls the flare timescale (slow-cooling regime),

shorter decay timescale and greater fractional variability will be observed at higher energies, a "soft-lag" and clockwise spectral hysteresis loop will be observed. Although these observables can also be affected by other factors (e.g. the light travel time effect), and TeV gamma rays are limited by statistics, examinations of both the energy dependent time lag and the direction of spectral hysteresis loop can help validate each other. We study simultaneous and gapless observations of Mrk 421 in both X-ray and TeV gamma-ray band as an example. We demonstrated that the time lag and spectral hysteresis loop directions are consistent with each other using the X-ray data with better statistics. However, at the flux level roughly between 1 and 2 Crab Unit, such studies in TeV gamma-ray band with VERITAS are still difficult. Future gamma-ray observations at higher flux level are needed to reach statistically significant conclusions.

5. The evolution of the observed SED suggests a possible expansion of the emitting region in Mrk 421 from 2014 Apr 29 to 2014 May 3. Such an expansion will lead to an increase in the dynamic timescale $t_{dyn} = R/c$, a higher maximum energy of the electrons E_{max}, and a lower-frequency synchrotron cooling break. This scenario is also consistent with the X-ray time lags and the spectral hysteresis patterns. Since a lower maximum electron energy E_{max} on Apr 29 indicates that the observed X-ray frequencies is closer to the maximum frequencies, thus the change in flux propagates from high to low frequencies, leading to a "hard lag" and counter-clockwise spectral hysteresis pattern. On the other hand, a higher E_{max} on May 3 indicates that the observed X-ray frequencies is relatively farther away from the highest-energy electrons, therefore the change in flux propagates from low to high energy (see e.g. Kirk et al., 1998).

6. No strong correlation between X-ray and TeV are found from the 2014 observations of Mrk 421 in X-ray and TeV, which suggests a more complex picture than a one-zone SSC model. For example, in a two-zone SSC model (e.g.

Petropoulou, 2014), the X-ray/TeV correlation is expected to be weaker when the flux is lower.

7. We examine a variety of methods for time series analysis: (i) Kernel density estimations and Bayesian blocks are data-driven density estimation methods and have the potential to better balance the bias and variance; (ii) Power spectrum and autocorrelation measure the memory of a time series, but suffers bias when the signal is non-stationary and non-linear; (iii) Modified cross-correlation can probe fast timescale correlations that are much shorter than regular bin interval; (iv) Bispectrum tests for linearity and reversibility, but it is prone to noise; (v) Hilbert-Huang transform offers a data-driven, adaptive method that can deal with non-linear and non-stationary time series. The above tools are implemented and/or applied to simulations and blazar data, and the results are compared with other methods.

8. Blazars exhibit $1/f^{\alpha}$ type of red noise extending to timescales as fast as minutes. However, the lower frequency PSD is difficult to measure, due to the limited duration of the light curves and the gaps between observations, e.g. the time averaging leads to an opposite effect (slightly steeper PSD shape) compared to aliasing. The distorting effect due to irregular sampling can be estimated by simulations, which are important for determining the shape of the power spectrum. We examine the distortion effects with simulations, and use simulation-based "success fraction" method (e.g. Chatterjee et al., 2008) to estimate PSD shapes of the Mrk 421 observations. We note that the "success fraction" is insensitive to spectral breaks in PSDs.

9. Many of the observable signatures mentioned above are subtle, future observations with larger collecting area, higher sensitivity, and better spectral coverage and resolution will shed more light on the puzzles in blazars.

BIBLIOGRAPHY

Bibliography

A. Weinstein for the VERITAS Collaboration. 2014, ArXiv e-prints

Abdo, A. A., Ackermann, M., Agudo, I., et al. 2010, ApJ, 716, 30

Abdo, A. A., Ackermann, M., Ajello, M., et al. 2011, ApJ, 730, 101

Acciari, V. A., Beilicke, M., Blaylock, G., et al. 2008, ApJ, 679, 397

Acciari, V. A., Aliu, E., Arlen, T., et al. 2009a, ApJLett, 703, L6

—. 2009b, ApJ, 700, 1034

—. 2009c, ApJLett, 698, L133

Acciari, V. A., Aliu, E., Aune, T., et al. 2009d, ApJ, 703, 169

Acciari, V. A., Aliu, E., Arlen, T., et al. 2010a, ApJ, 714, 163

Acciari, V. A., Arlen, T., Aune, T., et al. 2010b, ApJ, 720, 1174

Acciari, V. A., Aliu, E., Arlen, T., et al. 2011a, ApJLett, 730, L20

—. 2011b, ApJ, 738, 25

—. 2011c, ApJ, 743, 62

Acero, F., Aharonian, F., Akhperjanian, A. G., et al. 2009, Science, 326, 1080

Ackermann, M., Albert, A., Atwood, W. B., et al. 2014, ApJ, 793, 64

Agudo, I., Jorstad, S. G., Marscher, A. P., et al. 2011, ApJLett, 726, L13

Aharonian, F., Anchordoqui, L., Khangulyan, D., & Montaruli, T. 2006a, Journal of Physics Conference Series, 39, 408

Aharonian, F., Essey, W., Kusenko, A., & Prosekin, A. 2013, Phys. Rev. D, 87, 063002

Aharonian, F., Akhperjanian, A., Barrio, J., et al. 2001, A&A, 370, 112

Aharonian, F., Akhperjanian, A. G., Bazer-Bachi, A. R., et al. 2006b, Nature, 440, 1018

—. 2006c, Science, 314, 1424

—. 2006d, Physical Review Letters, 97, 221102

—. 2007, ApJLett, 664, L71

Aharonian, F., Akhperjanian, A. G., Barres de Almeida, U., et al. 2008a, Physical Review Letters, 101, 170402

Aharonian, F., Akhperjanian, A. G., Anton, G., et al. 2009a, ApJLett, 695, L40

—. 2009b, A&A, 502, 749

—. 2009c, ApJLett, 696, L150

—. 2009d, A&A, 503, 817

Aharonian, F. A. 2000, New Astronomy, 5, 377

—. 2002, MNRAS, 332, 215

Aharonian, F. A., Khangulyan, D., & Costamante, L. 2008b, MNRAS, 387, 1206

Albert, J., Aliu, E., Anderhub, H., et al. 2007a, ApJLett, 666, L17

—. 2007b, ApJ, 669, 862

—. 2008a, ApJLett, 685, L23

—. 2008b, ApJ, 674, 1037

Aleksić, J., Antonelli, L. A., Antoranz, P., et al. 2011, ApJLett, 730, L8

Alexander, T. 1997, in Astrophysics and Space Science Library, Vol. 218, Astronomical Time Series, ed. D. Maoz, A. Sternberg, & E. M. Leibowitz, 163

Aliu, E., Archambault, S., Arlen, T., et al. 2013, ApJ, 764, 38

Aliu, E., Aune, T., Barnacka, A., et al. 2014a, ApJLett, 795, L3

Aliu, E., Archambault, S., Aune, T., et al. 2014b, ApJ, 780, 168

Aliu, E., Aune, T., Behera, B., et al. 2014c, ApJ, 788, 78

Aliu, E., Archambault, S., Archer, A., et al. 2015, ApJ, 800, 61

Aller, H. D., Aller, M. F., & Hughes, P. A. 1985, ApJ, 298, 296

Amenomori, M., Ayabe, S., Bi, X. J., et al. 2006, Science, 314, 439

Angelakis, E., Fuhrmann, L., Nestoras, I., et al. 2011, The Astronomer's Telegram, 3380, 1

Archambault, S., Aune, T., Behera, B., et al. 2014, ApJLett, 785, L16

Arlen, T., Aune, T., Beilicke, M., et al. 2012, ApJ, 757, 123

—. 2013, ApJ, 762, 92

Atwood, W. B., Abdo, A. A., Ackermann, M., et al. 2009, ApJ, 697, 1071

Baade, W., & Minkowski, R. 1954, ApJ, 119, 215

Baars, J. W. M., Genzel, R., Pauliny-Toth, I. I. K., & Witzel, A. 1977, A&A, 61, 99

Barkov, M. V., Aharonian, F. A., & Bosch-Ramon, V. 2010, ApJ, 724, 1517

Barth, A. J., Ho, L. C., & Sargent, W. L. W. 2003, ApJ, 583, 134

Beilicke, M., & VERITAS Collaboration. 2012, Nuclear Instruments and Methods in Physics Research A, 692, 208

Bell, A. R., & Lucek, S. G. 2001, MNRAS, 321, 433

Berezhko, E. G. 1996, Astroparticle Physics, 5, 367

Berge, D., Funk, S., & Hinton, J. 2007, A&A, 466, 1219

Bernlöhr, K. 2008, Astroparticle Physics, 30, 149

Bhabha, H. J., & Heitler, W. 1937, Royal Society of London Proceedings Series A, 159, 432

Biretta, J. A., Sparks, W. B., & Macchetto, F. 1999, ApJ, 520, 621

Blandford, R., Simeon, P., & Yuan, Y. 2014, ArXiv e-prints

Blandford, R. D., & Königl, A. 1979, ApJ, 232, 34

Blandford, R. D., & Znajek, R. L. 1977, MNRAS, 179, 433

Błażejowski, M., Blaylock, G., Bond, I. H., et al. 2005, ApJ, 630, 130

Bloom, S. D., & Marscher, A. P. 1996, ApJ, 461, 657

Bonning, E., Urry, C. M., Bailyn, C., et al. 2012, ApJ, 756, 13

Böttcher, M. 2005, ApJ, 621, 176

Böttcher, M., Mause, H., & Schlickeiser, R. 1997, A&A, 324, 395

Böttcher, M., & Reimer, A. 2004, ApJ, 609, 576

Böttcher, M., Reimer, A., Sweeney, K., & Prakash, A. 2013, ApJ, 768, 54

Böttcher, M., Marscher, A. P., Ravasio, M., et al. 2003, ApJ, 596, 847

Bowman, D. C., & Lees, J. M. 2013, Seismological Research Letters, 84, 1074

Breeveld, A. A., Curran, P. A., Hoversten, E. A., et al. 2010, MNRAS, 406, 1687

Bregman, J. N., Glassgold, A. E., Huggins, P. J., et al. 1990, ApJ, 352, 574

Broderick, A. E., Chang, P., & Pfrommer, C. 2012, ApJ, 752, 22

Carrasco, L., Carraminana, A., Escobedo, G., et al. 2011, The Astronomer's Telegram, 3375, 1

Chatterjee, R., Jorstad, S. G., Marscher, A. P., et al. 2008, ApJ, 689, 79

Cheung, C. C., Harris, D. E., & Stawarz, Ł. 2007, ApJLett, 663, L65

Choudhury, S. A. A., Shah, S., & Thornhill, N. 2008, in Diagnosis of Process Nonlinearities and Valve Stiction, Advances in Industrial Control (Springer Berlin Heidelberg), 29–41

Cirelli, M. 2012, Pramana, 79, 1021

Cogan, P. 2008, in International Cosmic Ray Conference, Vol. 3, International Cosmic Ray Conference, 1385–1388

Corbett, E. A., Robinson, A., Axon, D. J., et al. 1996, MNRAS, 281, 737

Cortina, J., & Holder, J. 2013, The Astronomer's Telegram, 4976, 1

Cui, W. 2004, ApJ, 605, 662

—. 2009, Research in Astronomy and Astrophysics, 9, 841

Cui, W., Zhang, S. N., Focke, W., & Swank, J. H. 1997, ApJ, 484, 383

Curtis, H. D. 1918, Publications of Lick Observatory, 13, 9

Cutini, S. 2011, The Astronomer's Telegram, 3368, 1

D. B. Kieda for the VERITAS Collaboration. 2013, ArXiv e-prints

Daniel, M. K. 2008, in International Cosmic Ray Conference, Vol. 3, International Cosmic Ray Conference, 1325–1328

Daugherty, J. K., & Harding, A. K. 1983, ApJ, 273, 761

Daum, A., Hermann, G., Heß, M., et al. 1997, Astroparticle Physics, 8, 1

Davies, J. M., & Cotton, E. S. 1957, Solar Energy, 1, 16

Daylan, T., Finkbeiner, D. P., Hooper, D., et al. 2014, ArXiv e-prints

de Naurois, M., & Rolland, L. 2009, Astroparticle Physics, 32, 231

Deeming, T. J. 1975, Ap&SS, 36, 137

Dermer, C. D., Murase, K., & Takami, H. 2012, ApJ, 755, 147

Dimitrakoudis, S., Petropoulou, M., & Mastichiadis, A. 2014, Astroparticle Physics, 54, 61

Dole, H., Lagache, G., Puget, J.-L., et al. 2006, A&A, 451, 417

Domínguez, A., Primack, J. R., Rosario, D. J., et al. 2011, MNRAS, 410, 2556

Dondi, L., & Ghisellini, G. 1995, MNRAS, 273, 583

Drake, J. F., Swisdak, M., Che, H., & Shay, M. A. 2006a, Nature, 443, 553

Drake, J. F., Swisdak, M., Schoeffler, K. M., Rogers, B. N., & Kobayashi, S. 2006b, Geophys. Res. Lett., 33, 13105

Dwek, E., & Krennrich, F. 2013, Astroparticle Physics, 43, 112

Edelson, R. A., & Krolik, J. H. 1988, ApJ, 333, 646

Essey, W., Kalashev, O., Kusenko, A., & Beacom, J. F. 2011, ApJ, 731, 51

Essey, W., Kalashev, O. E., Kusenko, A., & Beacom, J. F. 2010, Physical Review Letters, 104, 141102

Evans, P. A., Beardmore, A. P., Page, K. L., et al. 2007, A&A, 469, 379

—. 2009, MNRAS, 397, 1177

F. Hess, V. 1912, Physikalische Zeitschrift, 13, 1084

Fazio, G. G., & Stecker, F. W. 1970, Nature, 226, 135

Fermi, E. 1949, Physical Review, 75, 1169

Fermi-LAT collaboration, & Fermi-GBM collaboration. 2013, ArXiv e-prints

Finke, J. D., Dermer, C. D., & Böttcher, M. 2008, ApJ, 686, 181

Fitzpatrick, E. L. 1999, PASP, 111, 63

Forman, W., Jones, C., Churazov, E., et al. 2007, ApJ, 665, 1057

Fossati, G., Maraschi, L., Celotti, A., Comastri, A., & Ghisellini, G. 1998, MNRAS, 299, 433

Fossati, G., Buckley, J. H., Bond, I. H., et al. 2008, ApJ, 677, 906

Furniss, A., Williams, D. A., Danforth, C., et al. 2013, ApJLett, 768, L31

Gabriel, C., Denby, M., Fyfe, D. J., et al. 2004, in Astronomical Society of the Pacific Conference Series, Vol. 314, Astronomical Data Analysis Software and Systems (ADASS) XIII, ed. F. Ochsenbein, M. G. Allen, & D. Egret, 759

Gabuzda, D. C., Rastorgueva, E. A., Smith, P. S., & O'Sullivan, S. P. 2006, MNRAS, 369, 1596

Gaensler, B. M., & Slane, P. O. 2006, ARA&A, 44, 17

Gaidos, J. A., Akerlof, C. W., Biller, S., et al. 1996, Nature, 383, 319

Gaisser, T. K., & Stanev, T. 1989, Physics Letters B, 219, 375

Gallant, Y. A., & Achterberg, A. 1999, MNRAS, 305, L6

Gehrels, N., Chincarini, G., Giommi, P., et al. 2004, ApJ, 611, 1005

Georganopoulos, M., & Kazanas, D. 2003, ApJLett, 594, L27

Ghisellini, G., Maraschi, L., & Treves, A. 1985, A&A, 146, 204

Ghisellini, G., & Tavecchio, F. 2008, MNRAS, 386, L28

Ghisellini, G., Tavecchio, F., & Chiaberge, M. 2005, A&A, 432, 401

Giannios, D. 2010, MNRAS, 408, L46

Giannios, D., Uzdensky, D. A., & Begelman, M. C. 2009, MNRAS, 395, L29

Gillessen, S., Eisenhauer, F., Trippe, S., et al. 2009, ApJ, 692, 1075

Goldreich, P., & Julian, W. H. 1969, ApJ, 157, 869

Gould, R. J., & Schréder, G. 1966, Physical Review Letters, 16, 252

Greisen, K. 1966, Physical Review Letters, 16, 748

Guo, F., Li, H., Daughton, W., & Liu, Y.-H. 2014, Physical Review Letters, 113, 155005

Gurwell, M. A., Peck, A. B., Hostler, S. R., Darrah, M. R., & Katz, C. A. 2007, in Astronomical Society of the Pacific Conference Series, Vol. 375, From Z-Machines to ALMA: (Sub)Millimeter Spectroscopy of Galaxies, ed. A. J. Baker, J. Glenn, A. I. Harris, J. G. Mangum, & M. S. Yun, 234

Güver, T., & Özel, F. 2009, MNRAS, 400, 2050

Hada, K., Doi, A., Kino, M., et al. 2011, Nature, 477, 185

Hall, J., Vassiliev, V. V., Kieda, D. B., et al. 2003, International Cosmic Ray Conference, 5, 2851

Hanna, D., McCann, A., McCutcheon, M., & Nikkinen, L. 2010, Nuclear Instruments and Methods in Physics Research A, 612, 278

Hartman, R. C., Bertsch, D. L., Bloom, S. D., et al. 1999, ApJS, 123, 79

H.E.S.S. Collaboration, Abramowski, A., Acero, F., et al. 2013, A&A, 551, A94

Hillas, A. M. 1984, ARA&A, 22, 425

Hinich, M. J. 1982, Journal of Time Series Analysis, 3, 169

Hoffmeister, C. 1929, Astronomische Nachrichten, 236, 233

Hovatta, T., Valtaoja, E., Tornikoski, M., & Lähteenmäki, A. 2009, A&A, 494, 527

Huang, N., Shen, Z., Long, S., et al. 1998a, Proceedings of the Royal Society of London Series a-Mathematical Physical and Engineering Sciences, 454, 903

—. 1998b, Proceedings of the Royal Society of London Series a-Mathematical Physical and Engineering Sciences, 454, 903

Huang, N. E., & Wu, Z. 2008, Reviews of Geophysics, 46, 2006

Inoue, Y., Kalashev, O. E., & Kusenko, A. 2014, Astroparticle Physics, 54, 118

Jacob, U., & Piran, T. 2008, Phys. Rev. D, 78, 124010

Jauch, J. M., & Rohrlich, F. 1955, The theory of photons and electrons

Jelley, J. V., & Porter, N. A. 1963, QJRAS, 4, 275

Jokipii, J. R. 1987, ApJ, 313, 842

Jones, T. W., O'dell, S. L., & Stein, W. A. 1974, ApJ, 188, 353

Jorstad, S. G., Marscher, A. P., Lister, M. L., et al. 2005, AJ, 130, 1418

Jorstad, S. G., Marscher, A. P., Stevens, J. A., et al. 2007, AJ, 134, 799

Kalberla, P. M. W., Burton, W. B., Hartmann, D., et al. 2005, A&A, 440, 775

Katarzyński, K., Ghisellini, G., Tavecchio, F., et al. 2005, A&A, 433, 479

Kertzman, M. P., & Sembroski, G. H. 1994, Nuclear Instruments and Methods in Physics Research A, 343, 629

Kifune, T. 1999, ApJLett, 518, L21

Kim, Y. C., & Powers, E. J. 1979, IEEE Transactions on Plasma Science, 7, 120

Kirk, J. G., Rieger, F. M., & Mastichiadis, A. 1998, A&A, 333, 452

Klebesadel, R. W., Strong, I. B., & Olson, R. A. 1973, ApJLett, 182, L85

Knuth, K. H. 2006, ArXiv Physics e-prints

Krawczynski, H., Coppi, P. S., & Aharonian, F. 2002, MNRAS, 336, 721

Krawczynski, H., Hughes, S. B., Horan, D., et al. 2004, ApJ, 601, 151

Lacki, B. C., Thompson, T. A., Quataert, E., Loeb, A., & Waxman, E. 2011, ApJ, 734, 107

Lähteenmäki, A., & Valtaoja, E. 2003, ApJ, 590, 95

Larionov, V. M., Larionova, E. G., Efimova, N. V., Villata, M., & Raiteri, C. M. 2011, The Astronomer's Telegram, 3371, 1

Larionov, V. M., Jorstad, S. G., Marscher, A. P., et al. 2008, A&A, 492, 389

Larson, D., Dunkley, J., Hinshaw, G., et al. 2011, ApJS, 192, 16

Le Bohec, S., Degrange, B., Punch, M., et al. 1998, Nuclear Instruments and Methods in Physics Research A, 416, 425

Le Borgne, D., Rocca-Volmerange, B., Prugniel, P., et al. 2004, A&A, 425, 881

León-Tavares, J., Valtaoja, E., Giommi, P., et al. 2012, ApJ, 754, 23

Levinson, A. 2007, ApJLett, 671, L29

Li, H., & Kusunose, M. 2000, ApJ, 536, 729

Li, T.-P. 2001, ChJAA, 1, 313

Li, T.-P., & Ma, Y.-Q. 1983, ApJ, 272, 317

Li, T.-P., Qu, J.-L., Feng, H., et al. 2004, ChJAA, 4, 583

Lister, M. L., Aller, H. D., Aller, M. F., et al. 2009, AJ, 137, 3718

Lobanov, A. P. 1998, A&A, 330, 79

Longair, M. S. 1992, High energy astrophysics. Vol.1: Particles, photons and their detection

Loredo, T. J. 1992, in Statistical Challenges in Modern Astronomy, ed. E. D. Feigelson & G. J. Babu, 275–297

Lu, E. T., & Hamilton, R. J. 1991, ApJLett, 380, L89

Lyutikov, M. 2003, New Astron. Rev., 47, 513

Lyutikov, M., Otte, N., & McCann, A. 2012, ApJ, 754, 33

Maccarone, T. J. 2013, MNRAS, 435, 3547

Madau, P., & Pozzetti, L. 2000, MNRAS, 312, L9

Maesano, M., Massaro, E., & Nesci, R. 1997, IAU Circ., 6700, 3

MAGIC Collaboration, Albert, J., Aliu, E., et al. 2008, Science, 320, 1752

Maier, G. 2013, in European Physical Journal Web of Conferences, Vol. 52, European Physical Journal Web of Conferences, 10001

Mannheim, K. 1993, A&A, 269, 67

Marscher, A. P. 2012, ArXiv e-prints

Marscher, A. P., Jorstad, S. G., D'Arcangelo, F. D., et al. 2008, Nature, 452, 966

Marscher, A. P., Jorstad, S. G., Larionov, V. M., et al. 2010, ApJLett, 710, L126

Marshall, H. L., Harris, D. E., Grimes, J. P., et al. 2001, ApJLett, 549, L167

Mason, K. O., Breeveld, A., Much, R., et al. 2001, A&A, 365, L36

Mastichiadis, A., & Kirk, J. G. 1997, A&A, 320, 19

Mastichiadis, A., Petropoulou, M., & Dimitrakoudis, S. 2013, MNRAS, 434, 2684

Mastichiadis, A., Protheroe, R. J., & Kirk, J. G. 2005, A&A, 433, 765

Mateos, S., Saxton, R. D., Read, A. M., & Sembay, S. 2009, A&A, 496, 879

McHardy, I. 2010, in Lecture Notes in Physics, Berlin Springer Verlag, Vol. 794, Lecture Notes in Physics, Berlin Springer Verlag, ed. T. Belloni, 203

Mészáros, P. 2013, Astroparticle Physics, 43, 134

Meyer, M., Horns, D., & Raue, M. 2013, Phys. Rev. D, 87, 035027

Michelson, P. F., Lin, Y. C., Nolan, P. L., et al. 1992, IAU Circ., 5470, 2

Miller, J. S., French, H. B., & Hawley, S. A. 1978, ApJLett, 219, L85

Mücke, A., & Protheroe, R. J. 2001, Astroparticle Physics, 15, 121

Nalewajko, K., Begelman, M. C., Cerutti, B., Uzdensky, D. A., & Sikora, M. 2012, MNRAS, 425, 2519

Narayan, R., & Piran, T. 2012, MNRAS, 420, 604

Navarro, J. F., Frenk, C. S., & White, S. D. M. 1996, ApJ, 462, 563

Neshpor, Y. I., Chalenko, N. N., Stepanian, A. A., et al. 2001, Astronomy Reports, 45, 249

Nieppola, E., Tornikoski, M., Valtaoja, E., et al. 2011, A&A, 535, A69

Ohm, S., van Eldik, C., & Egberts, K. 2009, Astroparticle Physics, 31, 383

Palmer, I. D. 1982, Reviews of Geophysics and Space Physics, 20, 335

Papadakis, I. E., & Lawrence, A. 1993, MNRAS, 261, 612

Pedregosa, F., Varoquaux, G., Gramfort, A., et al. 2012, ArXiv e-prints

Perkins, J. S., Maier, G., & The VERITAS Collaboration. 2009, ArXiv e-prints

Petropoulou, M. 2014, A&A, 571, A83

Piano, G., Tavani, M., Pittori, C., et al. 2011, The Astronomer's Telegram, 3387, 1

Pierre Auger Collaboration, Abraham, J., Abreu, P., et al. 2007, Science, 318, 938

Piner, B. G., Pant, N., & Edwards, P. G. 2008, ApJ, 678, 64

Pintore, F., Sanna, A., Di Salvo, T., et al. 2014, MNRAS, 445, 3745

Piran, T. 1999, Phys. Rep., 314, 575

Plotnikov, I., Pelletier, G., & Lemoine, M. 2013, MNRAS, 430, 1280

Pohl, M. 1994, A&A, 287, 453

Pohl, M., & Schlickeiser, R. 2000, A&A, 354, 395

Poole, T. S., Breeveld, A. A., Page, M. J., et al. 2008, MNRAS, 383, 627

Poutanen, J., Zdziarski, A. A., & Ibragimov, A. 2008, MNRAS, 389, 1427

Prosekin, A., Essey, W., Kusenko, A., & Aharonian, F. 2012, ApJ, 757, 183

Punch, M., Akerlof, C. W., Cawley, M. F., et al. 1992, Nature, 358, 477

Pushkarev, A. B., Kovalev, Y. Y., & Lister, M. L. 2010, ApJLett, 722, L7

R Core Team. 2014, R: A Language and Environment for Statistical Computing, R Foundation for Statistical Computing, Vienna, Austria

Raiteri, C. M., Villata, M., Capetti, A., et al. 2009, A&A, 507, 769

Raiteri, C. M., Villata, M., Bruschini, L., et al. 2010, A&A, 524, A43

Raiteri, C. M., Villata, M., D'Ammando, F., et al. 2013, MNRAS, 436, 1530

Ravasio, M., Tagliaferri, G., Ghisellini, G., et al. 2003, A&A, 408, 479

Readhead, A. C. S. 1994, ApJ, 426, 51

Rees, M. J. 1978, MNRAS, 184, 61P

Ressell, M. T., & Turner, M. S. 1990, Comments on Astrophysics, 14, 323

Richards, J. L., Max-Moerbeck, W., Pavlidou, V., et al. 2011, ApJS, 194, 29

Rieger, F. M., Bosch-Ramon, V., & Duffy, P. 2007, Ap&SS, 309, 119

Rieger, F. M., & Duffy, P. 2004, ApJ, 617, 155

Roache, E., Irvin, R., Perkins, J. S., & et al. 2008, International Cosmic Ray Conference, 3, 1397

Rolke, W. A., López, A. M., & Conrad, J. 2005, Nuclear Instruments and Methods in Physics Research A, 551, 493

Rosswog, S., & Brüggen, M. 2007, Introduction to High-Energy Astrophysics

Ruan, J. J., Anderson, S. F., Plotkin, R. M., et al. 2014, ApJ, 797, 19

Rybicki, G. B., & Lightman, A. P. 1979, Radiative processes in astrophysics

Sahu, S., Oliveros, A. F. O., & Sanabria, J. C. 2013, Phys. Rev. D, 87, 103015

Sánchez-Conde, M. A., Paneque, D., Bloom, E., Prada, F., & Domínguez, A. 2009, Phys. Rev. D, 79, 123511

Sari, R., & Esin, A. A. 2001, ApJ, 548, 787

Sato, R., Kataoka, J., Takahashi, T., et al. 2008, in American Institute of Physics Conference Series, Vol. 1085, American Institute of Physics Conference Series, ed. F. A. Aharonian, W. Hofmann, & F. Rieger, 447–450

Scargle, J. D. 1981, ApJS, 45, 1

—. 1982, ApJ, 263, 835

—. 1989, ApJ, 343, 874

—. 1998, ApJ, 504, 405

Scargle, J. D., Norris, J. P., Jackson, B., & Chiang, J. 2013, ApJ, 764, 167

Schlickeiser, R. 1996, Space Sci. Rev., 75, 299

Schmidt, M. 1963, Nature, 197, 1040

Schmitt, J. L. 1968, Nature, 218, 663

Schottky, W. 1918, Annalen der Physik, 362, 541

Sikora, M., Błażejowski, M., Begelman, M. C., & Moderski, R. 2001, ApJ, 554, 1

Smith, P. S., Montiel, E., Rightley, S., et al. 2009, ArXiv e-prints

Spada, M., Ghisellini, G., Lazzati, D., & Celotti, A. 2001, MNRAS, 325, 1559

Stawarz, Ł., Aharonian, F., Kataoka, J., et al. 2006, MNRAS, 370, 981

Stecker, F. W., & Salamon, M. H. 1996, ApJ, 464, 600

Stern, B. E., & Poutanen, J. 2008, MNRAS, 383, 1695

Strüder, L., Briel, U., Dennerl, K., et al. 2001, A&A, 365, L18

Swordy, S. 2008, The Astronomer's Telegram, 1506, 1

Tajima, T., & Dawson, J. M. 1979, Physical Review Letters, 43, 267

Takeda, M., Hayashida, N., Honda, K., et al. 1999, ApJ, 522, 225

Tammi, J., & Duffy, P. 2009, MNRAS, 393, 1063

Tavecchio, F., Becerra-Gonzalez, J., Ghisellini, G., et al. 2011, A&A, 534, A86

Taylor, A. M., Vovk, I., & Neronov, A. 2011, A&A, 529, A144

Teraesranta, H., Tornikoski, M., Mujunen, A., et al. 1998, A&AS, 132, 305

Terrell, J., & Olsen, K. H. 1970, ApJ, 161, 399

The Fermi-LAT Collaboration, :, Ackermann, M., et al. 2013, ArXiv e-prints

The MAGIC Collaboration, Aleksić, J., Ansoldi, S., et al. 2014, ArXiv e-prints

The Pierre Auger Collaboration. 2014, ArXiv e-prints

Timmer, J., & Koenig, M. 1995, A&A, 300, 707

Urry, C. M., & Padovani, P. 1995, PASP, 107, 803

Urry, C. M., & Shafer, R. A. 1984, ApJ, 280, 569

Uttley, P., McHardy, I. M., & Papadakis, I. E. 2002, MNRAS, 332, 231

VanderPlas, J., Connolly, A. J., Ivezic, Z., & Gray, A. 2012, in Proceedings of Conference on Intelligent Data Understanding (CIDU), pp. 47-54, 2012., 47–54

Vaughan, S., Edelson, R., Warwick, R. S., & Uttley, P. 2003, MNRAS, 345, 1271

VERITAS Collaboration, Acciari, V. A., Aliu, E., et al. 2009, Nature, 462, 770

VERITAS Collaboration, Aliu, E., Arlen, T., et al. 2011, Science, 334, 69

Vermeulen, R. C., Ogle, P. M., Tran, H. D., et al. 1995, ApJLett, 452, L5

Voelk, H. J., & Biermann, P. L. 1988, ApJLett, 333, L65

Wakely, S. P., Cui, W., Pizlo, F., et al. 2003, International Cosmic Ray Conference, 5, 2839

Weekes, T. C., Cawley, M. F., Fegan, D. J., et al. 1989, ApJ, 342, 379

Weinstein, A. f. 2009, ArXiv e-prints

Weniger, C. 2012, J. Cosmology Astropart. Phys., 8, 7

Yamada, M., Kulsrud, R., & Ji, H. 2010, Rev. Mod. Phys., 82, 603

Zamaninasab, M., Clausen-Brown, E., Savolainen, T., & Tchekhovskoy, A. 2014, Nature, 510, 126

Zatsepin, G. T., & Kuz'min, V. A. 1966, Soviet Journal of Experimental and Theoretical Physics Letters, 4, 78

Zemcov, M., Smidt, J., Arai, T., et al. 2014, Science, 346, 732

Zhang, H., Chen, X., & Böttcher, M. 2014, ApJ, 789, 66

Zheng, Y. G., & Kang, T. 2013, ApJ, 764, 113

Zitzer, B., & for the VERITAS Collaboration. 2013a, ArXiv e-prints

—. 2013b, ArXiv e-prints

Zweibel, E. G., & Yamada, M. 2009, ARA&A, 47, 291

APPENDICES

Appendix A: Notes on Harvester and Quicklook

A.1 Compile Harvester and Quicklook

Download

In the directory that you want to put Harvester folder, run:

```
cvs login
cvs co -d Harvester_head software/online/Harvester
```

Dependencies

Read the file "DEPENDENCIES" in the Harvester directory for detailed information regarding the software needed before installing Harvester/Quicklook. All dependencies need to be compiled in **32 bit mode** and installed in /usr/local/veritas/. There is no configure file for Harvester/Quicklook, the paths (e.g. /usr/local/veritas) are hard wired into the Makefiles. The packages listed in this file are **GCC, STL, MySQL, CppUnit, omniORB, HDF5, boost, and Slalib**. However, there are a few things that are not listed in this file:

1. Qt: Use earlier versions of Qt4, e.g. qt-4.2.3 (original) or qt-4.3.5 (tested), there will be errors if later versions (e.g. qt-4.8.5) is used. Set the environment properly for Qt4 instead of Qt-3.3. This can be set in ~/.bashrc file, e.g. on Control03:

```
export QTDIR=/usr/lib/qt4
export QTINC="-DQT_NO_DEBUG -DQT_GUI_LIB -DQT_CORE_LIB -
    DQT_SHARED -I/usr/lib/qt4//mkspecs/default -I. -I/usr/
    include/QtCore -I/usr/include/QtGui -I/usr/local/veritas/
    include -I."
export QTLIB="-L/usr/lib -lQtGui -lQtCore"
```

2. ruby

3. tsf, there is a tar file in Harvester directory. If complaints regarding tsf_internal.h appear while compileing, add the following line to tsf_internal.h: #undef stpcpy

4. ImageMagick, Magick++-config, can be obtained at `http://www.imagemagick.org/download/`

5. glib-2.0

6. fftw

7. omni-config: check if there is a omni-config around. If not, copy the one in directory Comms/omni4-config.linux to /usr/local/veritas/bin.

Compile

Once all packages are listed above are properly installed, to compile Harvester/Quick-look is easy. Simple run "make" and "make install" in the Harvester directory. If there is a problem regarding dependencies, specific error message will pop up on screen. Usually such problems are related to libraries either not compiled in 32 bit mode or not from a compatible software version.

It is possible to change individual sub-programs in sub-directories. To bring the changes to effect, first run `make` in the involved subdirectories, and run `make` in the Harvester directory. This will only recompile and update the changed code. To make the change effective system-wide, use `make install` or copy the updated `harvester` binary file to directory /usr/local/veritas/libexec, where the binary files to start and stop harvester daemon are located. The other `QLtools` are located in directory /usr/local/veritas/bin.

Database and QLtools configuration

If there is a ~/.vdbconf, four parameters should be properly set in this file: host (db.vts), user (readwrite), database (VERITAS), and password (**** not shown for safety).

```
host = "db.vts";
user = "readwrite";
database = "VERITAS";
passwd = "****";
```

Also a configuration file for QLtools is needed as /usr/local/veritas/etc/qltools.conf or ~/.qltoosconf. An example is in Harvester_head/support-files/QLtools/ directory.

Copy config files in Harvester_head/support-files directory to /usr/local/veritas/etc/ directory or current directory. The needed config files are: instrument configuration file, camera config files, MSW/MSL tables, pedwin, chargewin, and gain config files.

If you don't have root permission to create a folder called /usr/local/veritas/etc/, it is possible to put some conf files in your home directory with names like: .pedwin0, .pedwin1 etc. Some files can be fed to QL tools through command line options, e.g. -instrument SOMEPATH/instrument.conf, -msw-table SOMEPATH/msw%.dat (note here the % is in place for telescope id and the program can interpret that).

QLtools

QLtools are programs that monitor, analyze, and visualize VERITAS data both real time and offline. The default harvester hostname is set to be localhost (127.0.0.1). If running those tools that communicate with harvester (e.g. ql_monitor) on machines other than harvester machine and quicklook machine, you should tell the tool the correct harvester hostname (10.0.0.134). So instead of running "ql_monitor", now run:

```
ql_monitor -harvester-host 10.0.0.134
```

To analyze data in cvbf format offline in the real time Quicklook style, follow this example:

```
ql_param -rtql -config qltools.conf xxxxx.cvbf
ql_param -rtql -config qltools.conf yyyyy.cvbf
ql_param -rtql -config qltools.conf zzzzz.cvbf
...
ql_wobble -config qltools.conf off0.5 noff5 rad0.15 N xxxxx.param
    S yyyyy.param E zzzzz.param ...
ql_wobble -config qltools_size600.conf -msw-table $PathToTables/
    msw%.dat off0.5 noff5 rad0.15 N xxxxx.param S yyyyy.param E
    zzzzz.param ...
```

A.2 The elevation dependence of Quicklook results

The gamma-ray rate and significance reported by Quicklook serve an important role in the process of automatic target-of-opportunity observation triggers of VERITAS. A rough estimation of the TeV flux of a source (often in the unit of the flux of the Crab Nebula) based on the rates and/or significance is necessary. However, the rates/significance depends on many factors, e.g. the elevation and night sky background level. The elevation is the most important factor. Below I present the Quicklook results of the Crab in Figure A.1 and Table A.1 and A.2. These results can be used to conveniently estimate the flux in Crab Unit at a given elevation.

Table A.2.: Table of QL results for Crab dark runs at different elevation.

date	run	wobble	EL	Hz	QL significance	QL rate
<40 deg EL:						
20130307	67142	0.5E	35	315	6.714	1.931 +- 0.288
20131102	70453	0.5E	31	299	4.815	1.358 +- 0.282
40-50 deg EL:						
20130307	67140	0.5N	48	373	15.443	5.386 +- 0.349

20130307	67141	0.5S	41	347	12.395	4.182 +- 0.337
20130308	67231	0.5E	43	354	12.322	4.081 +- 0.331
20131028	70314	0.5N	40	335	9.698	3.003 +- 0.310
20131104	70482	0.5S	49	372	11.879	3.702 +- 0.312
50-60 deg EL:						
20130213	66735	0.5W	59	420	20.508	8.057 +- 0.393
20130307	67139	0.5W	54	390	16.119	6.001 +- 0.372
20130311	67253	0.5S	58	420	19.378	7.956 +- 0.411
20130311	67254	0.5E	52	407	17.272	6.575 +- 0.381
20130315	67374	0.5S	52	371	16.489	6.189 +- 0.375
20131031	70373	0.5S	56	386	15.160	4.906 +- 0.324
20131109	70604	0.5W	51	362	13.090	4.054 +- 0.310
60-70 deg EL:						
20130105	65776	0.5E	64	433	21.225	8.454 +- 0.398
20130307	67138	0.5E	62	403	18.440	7.411 +- 0.402
20130311	67252	0.5N	65	425	21.477	9.260 +- 0.431
20130312	67271	0.5W	69	433	22.476	9.818 +- 0.437
20130312	67272	0.5N	64	416	18.617	7.681 +- 0.413
20130313	67292	0.5S	67	415	22.693	10.119 +- 0.446
20130313	67293	0.5E	61	401	18.533	7.471 +- 0.403
20130314	67332	0.5W	67	403	23.002	9.765 +- 0.425
20131030	70351	0.5N	63	398	17.873	6.637 +- 0.371
20131102	70458	0.5E	60	388	19.535	7.103 +- 0.364
20131106	70530	0.5W	61	369	17.087	5.858 +- 0.343
70-80 Deg EL:						
20121208	65311	0.5E	74	437	21.313	8.747 +- 0.410
20121208	65312	0.5W	79	438	21.937	9.426 +- 0.430
20121210	65370	0.5N	73	425	20.137	8.082 +- 0.401
20121210	65371	0.5S	77	428	21.305	8.954 +- 0.420

20121211	65404	0.5E	79	449	21.673	9.366 +- 0.432
20121213	65474	0.5W	79	452	22.949	10.055 +- 0.438
20130105	65777	0.5W	71	438	17.858	6.933 +- 0.388
20130105	65778	0.5N	76	442	18.354	7.410 +- 0.404
20130105	65779	0.5S	79	443	23.728	10.331 +- 0.435
20130113	66002	0.5N	73	458	18.230	7.009 +- 0.385
20130113	66003	0.5S	77	460	22.081	9.479 +- 0.429
20130116	66112	0.5E	77	467	22.234	10.332 +- 0.465
20130201	66534	0.5S	79	456	22.497	9.720 +- 0.432
20130205	66556	0.5E	79	436	21.374	9.114 +- 0.426
20130205	66557	0.5W	74	432	24.319	10.394 +- 0.427
20130301	67044	0.5E	78	424	20.179	8.716 +- 0.432
20130307	67135	0.5N	75	430	20.604	9.327 +- 0.453
20130311	67251	0.5W	71	439	24.545	11.439 +- 0.466
20131003	69884	0.5N	75	402	18.869	7.182 +- 0.381
20131004	69914	0.5S	76	438	20.035	7.880 +- 0.393
20131004	69915	0.5S	79	401	21.988	9.068 +- 0.412
20131030	70356	0.5S	77	460	20.543	8.376 +- 0.408
20131030	70357	0.5E	72	463	18.609	7.293 +- 0.392
20131207	70997	0.5S	75	439	21.411	8.903 +- 0.416
20131225	71224	0.5E	78	449	21.392	8.713 +- 0.407
20140102	71428	0.5W	77	423	21.862	9.066 +- 0.415
20140102	71429	0.5N	73	423	20.333	7.712 +- 0.379
20140126	71802	0.5N	73	414	20.769	7.623 +- 0.367
>80 deg EL:						
20130116	66113	0.5W	80	460	23.275	10.671 +- 0.458
20131225	71223	0.5S	80	448	23.192	10.100 +- 0.435
20140102	71427	0.5E	80	423	20.701	8.626 +- 0.417

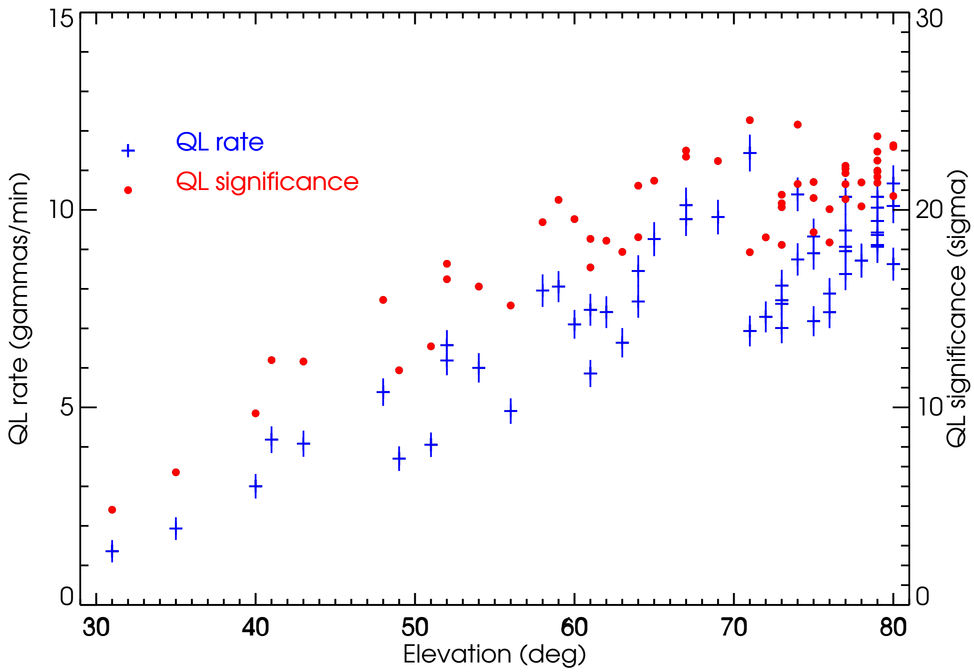

Figure A.1.: Quicklook significance and rates as a function of elevation for Crab runs during dark time. The averaged results in each elevation range and the standard deviations are shown in Table A.1. Detailed information and results of each individual run can be found in Table A.2.

A.3 QL analysis with a lower size cut for moonlight observations

VERITAS observations under moonlight are taken in special modes accommodating for the high current caused by moonlight. These special modes include runs (1) with UV filters in font of the PMTs, (2) at reduced high voltage, or (3) at raised CFD threshold. As a result, the charges deposited in the PMTs become smaller, and a lower size cut is necessary to optimize the results. I have scanned through different size cuts for Quicklook offline analysis to determine an optimal choice for the filter runs and the reduced HV runs. The runs used for the size cut optimization is listed in Table A.5, and the results are presented in Table A.3 and A.4, as well as Figure A.2. Note that the optimal size cut differs for sources of different flux and spectrum. I have

Table A.1.: Quicklook significance and rates at different elevation for Crab runs during dark time.

EL	mean EL	mean sig	stddev sig	mean rate	stddev rate
<40	33.0	5.8	1.3	1.6±0.3	0.4
40-49	44.2	12.4	2.1	4.1±0.3	0.9
50-59	54.6	16.9	2.5	6.2±0.4	1.5
60-69	63.9	20.0	2.1	8.1±0.4	1.4
70-79	75.9	21.1	1.7	8.8±0.4	1.2
>79	80	22.4	1.5	9.8±0.4	1.1

implemented an automated offline analysis that provides Quicklook results with size cuts of 200 dc and 400 dc for every run. Observers can conveniently use commands `nightsum200` and `nightsum400` to print out the results.

Table A.5.: List of run numbers of all observations analyzed under moonlight conditions. Non-Crab runs were chosen based on a relatively higher QL significance.

Non-Crab reduced HV runs:		
source	run	comments
J2239.3+6116	64310	90% reduced HV
Cas A	64311	90% reduced HV
Cas A	64312	90% reduced HV
1ES2344+514	64343	81% HV, 30mV CFD
1ES0229+200	64580	81% HV, 25mV CFD
Non-Crab filter runs:		
source	run	
1ES1959+650	63695	

1ES2344+514	63700
1ES2344+514	64426
B3 0133+388	64428
Cas A	64452
X Per	64462
Crab reduced HV 25mV:	70322
	70323
	70324
	70690
	71197
	71198
Crab reduced HV 35mV:	70754
	70755
	71547
Crab filter runs:	69662
	69663
	69681
	69682
	69683
	70750
	70751
	70752
	71107
	71108
	72492
	72493

Table A.3.: Example of cuts optimization results for a subset of three Crab runs taken with reduced HV.

size cuts	significance				rate			
(dc)	70322	70323	70324	total	70322	70323	70324	total
700	11.8	15.9	13.4	23.9	1.6 ± 0.1	2.8 ± 0.2	2.3 ± 0.2	2.2 ± 0.1
600	13.6	17.6	14.2	26.2	2.2 ± 0.2	3.4 ± 0.2	2.6 ± 0.2	2.7 ± 0.1
500	15.9	18.7	15.6	28.9	3.0 ± 0.2	4.2 ± 0.2	3.3 ± 0.2	3.5 ± 0.1
450	16.6	19.2	16.3	30.2	3.4 ± 0.2	4.6 ± 0.2	3.7 ± 0.2	3.9 ± 0.1
400	17.9	19.9	17.6	32.0	4.0 ± 0.2	5.2 ± 0.3	4.3 ± 0.2	4.5 ± 0.1
350	18.0	20.8	18.2	33.0	4.4 ± 0.2	6.0 ± 0.3	4.8 ± 0.3	5.1 ± 0.2
300	17.8	21.6	18.9	33.7	4.8 ± 0.3	6.9 ± 0.3	5.6 ± 0.3	5.8 ± 0.2
250	19.1	22.5	18.9	35.0	6.2 ± 0.3	8.3 ± 0.4	6.5 ± 0.3	7.0 ± 0.2
200	18.4	21.9	18.9	34.3	6.7 ± 0.4	8.8 ± 0.4	7.2 ± 0.4	7.5 ± 0.2
100	18.1	22.0	18.4	33.9	6.9 ± 0.4	9.3 ± 0.4	7.4 ± 0.4	7.9 ± 0.2

Table A.4.: Example of cuts optimization results for a subset of two Crab runs taken with filters.

size cuts	significance			rate		
(dc)	69663	69683	total	69663	69683	total
700	6.08	5.86	8.44	0.67 ± 0.11	0.63 ± 0.11	0.65 ± 0.08
600	5.91	5.91	8.36	0.72 ± 0.12	0.72 ± 0.12	0.72 ± 0.09
500	5.76	6.07	8.36	0.84 ± 0.15	0.87 ± 0.14	0.85 ± 0.10
450	5.88	6.57	8.81	0.89 ± 0.15	1.04 ± 0.16	0.96 ± 0.11
400	6.06	6.19	8.66	1.01 ± 0.17	1.02 ± 0.16	1.01 ± 0.12
350	5.68	5.57	7.95	1.02 ± 0.18	1.01 ± 0.18	1.02 ± 0.13
300	5.77	5.29	7.81	1.12 ± 0.20	1.06 ± 0.20	1.09 ± 0.14
200	5.56	5.03	7.49	1.14 ± 0.20	1.05 ± 0.21	1.09 ± 0.15
100	5.56	5.16	7.58	1.14 ± 0.20	1.08 ± 0.21	1.11 ± 0.15

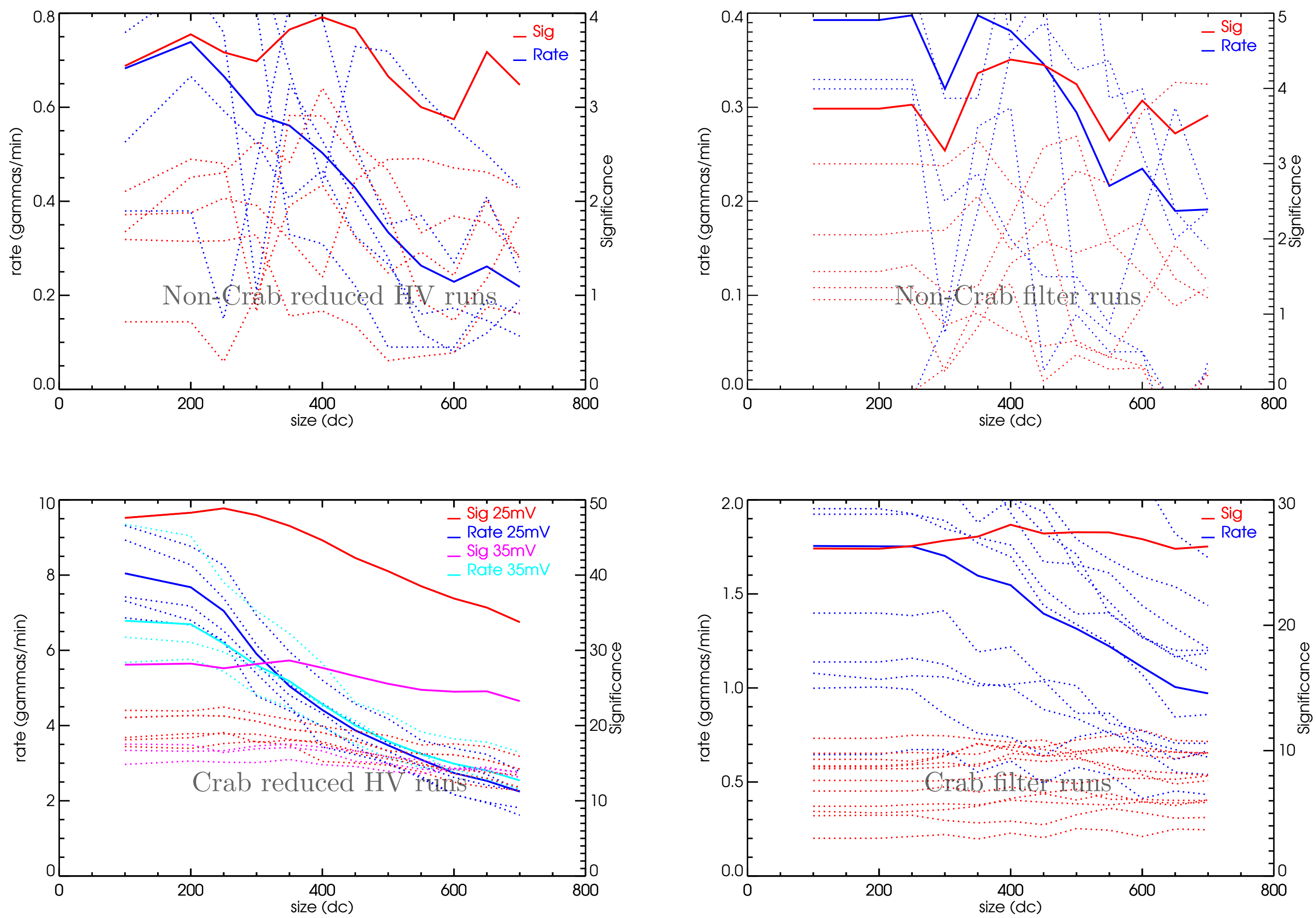

Figure A.2.: QL significance values and rates as a function of size cuts. Offline analysis were done to all runs listed in Table A.5. Solid lines are the combined results from all runs, while dashed lines are the results from each individual run.

VITA

VITA

Qi Feng was born in Gansu, China, on July 6, 1987. After five years of study at Wuhan Foreign Languages School, he transferred to Shenzhen Senior High School in June 2004, and graduated in June 2005. Between August 2005 and June 2009, he studied physics at the University of Science and Technology of China in Hefei, China, where he received a Bachelor of Science in June 2009. He then pursued graduate studies at Purdue University, and received a Doctorate of Philosophy in physics in 2015. He has received a postdoctoral fellowship from Centre de Recherche en Astrophysique du Quebec, and will continue his work in high energy astrophysics at McGill University in Montreal, Canada.